

**İSTANBUL TECHNICAL UNIVERSITY ★ EURASIA INSTITUTE OF EARTH SCIENCES**

**A COMPREHENSIVE STUDY OF THE MAGNETOSHEATH CAVITIES**

**Ph. D. Thesis by  
Filiz TÜRK KATIRCIOĞLU**

**Department : Climate and Marine Sciences**

**Programme : Earth System Sciences**

**SEPTEMBER 2010**



**A COMPREHENSIVE STUDY OF THE MAGNETOSHEATH CAVITIES**

**Ph.D. Thesis by  
Filiz TÜRK KATIRCIOĞLU  
(602022015)**

**Date of submission : 13 September 2010  
Date of defence examination: 15 September 2010**

**Supervisor : Prof. Dr. Zerefşan KAYMAZ (ITU)  
Co-supervisor : Prof. Dr. Mehmet KARACA (ITU)  
Members of the Examining Committee : Prof. Dr. Nüzhet DALFES (ITU)  
Prof. Dr. Zafer ASLAN (IAU)  
Prof. Dr. Atila ÖZGÜÇ (BU)  
Assoc. Prof. Sibel MENTEŞ (ITU)  
Asst. Prof. Cuma YARIM (ITU)**

**SEPTEMBER 2010**



**MANYETİK ÖRTÜ ÇÖKELME BÖLGELERİNİN DETAYLI İNCELENMESİ**

**DOKTORA TEZİ**  
**Filiz TÜRK KATIRCIOĞLU**  
**(602022015)**

**Tezin Enstitüye Verildiği Tarih : 13 Eylül 2010**

**Tezin Savunulduğu Tarih : 15 Eylül 2010**

**Tez Danışmanı : Prof. Dr. Zerefşan KAYMAZ (İTÜ)**  
**Tez Eş-Danışmanı : Prof. Dr. Mehmet KARACA (İTÜ)**  
**Diğer Jüri Üyeleri : Prof. Dr. Nüzhet DALFES (İTÜ)**  
**Prof. Dr. Zafer ASLAN (İAÜ)**  
**Prof. Dr. Atila ÖZGÜÇ (BÜ)**  
**Doç. Dr. Ş. Sibel MENTEŞ (İTÜ)**  
**Yard. Doç. Dr. Cuma YARIM (İTÜ)**

**EYLÜL 2010**



*Babama, anneme, eřime ve ođluma,*





## FOREWORD

My curiosity and wonder in Space Sciences, which ended up in pursuing a higher degree, go back to the times when I sat in the courses like Physics of the Upper Atmosphere followed by Planetary Atmospheres in the Department of Meteorology. I am indebted to my advisor Prof. Dr. Zerefşan Kaymaz who took me from there and showed me the way how I can enjoy the wonders of the research world in the fascinating space. I appreciate her teaching me the corner stones of the space sciences and leading me to become a good scientist. I sincerely thank her for all her efforts in this dissertation and standing with me during the hard times. She was an excellent advisor, friend, and colleague during different stages of this work. Secondly, I would like to extend my sincere thanks to my co-advisor Prof. Dr. Mehmet Karaca who accepted to be a co-advisor in this dissertation and supported me in many ways when I anytime needed, both bureaucratically in the Eurasia Institute and scientifically during the thesis committee meetings. I always appreciated his positive and encouraging attitude throughout this study.

I wish to give my special thanks to Dr. David Sibeck, who is our collaborator at NASA, for helping us with the spacecraft data and supporting me financially during my research at NASA. He contributed in many ways to my progress in space sciences and helped me to gain a broader understanding of space physics. My discussions with him and his continuous encouragements raised my confidence in my studies when I was working at NASA. My special thanks also go to Dr. Nick Omid of Solana Scientific Inc. of California who runs his kinetic-hybrid model specifically for our study and I am very happy to see that the model results support our observations. He helped me to understand the details of his model and interpreting the results when I visited him, for which I appreciate very much.

I would like to give my thanks to the members of the thesis committee, Prof. Dr. Nüzhet Dalfes, Prof. Dr. Zafer Aslan, Prof. Dr. Mete Tayanç, Prof. Dr. Atilla Özgüç, Assoc. Prof. Sibel Menteş and Asst. Prof. Cuma Yarım for their very useful comments in my dissertation, which certainly improved the quality of my work.

I would like to thank to Dr. Steven Petrinc at the Lockheed Martin Advanced Technology Center for his valuable helps on the calculation of Theta Bn, Prof. Dr. Karel Kudela and Jana Stetiarova at Slovak Academy of Sciences for the high resolution data of Interball-1, Dr. Ionnis Dandouras at Centre d'Etude Spatiale des Rayonnements and Centre National de la Recherche Scientifique.

I would like to thank to PIs and teams of the instruments on CLUSTER, INTERBALL, WIND and ACE, (the magnetometer FGM, plasma CIS, and energetic particle RAPID on Cluster, and MFI-M/PRAM, CORALL, and DOK-2 on INTERBALL-1, and MFI and SWE on ACE and WIND), for providing data via NASA's CDAWeb. Chapter 4 of this thesis was published in *Annales Geophysicae* in 2009. We thank to the journal, *Annales Geophysicae*, for allowing us to use our paper in this thesis study.

I also would like to thank to all my professors in the Department of Meteorological Engineering and Eurasia Institute of Earth Sciences from whom I have learned in

their courses. The knowledge that I received from them contributed me to develop myself in many directions and helped me to form a synthesis in my studies.

I want to thank to all my colleagues, roommates and friends, especially to the members of Room 211 at the Faculty of Aeronautics and Astronautics. I specially thank to Emine Ceren Kalafatođlu who is one of my talented colleagues as a young space science researcher, for her helps and nice discussions.

My thanks also go to the staff in the Faculty of Aeronautics and Astronautics and Eurasia Institute of Earth Sciences.

I would like to give my very special, wholeheartedly thanks to my parents whose endless love, support and encouragement made me to overcome the difficulties in my life.

Finally, I would like to thank my husband and my soul mate, İsmet Güçlü Katırcıođlu. His support was continuous and he was always there for me. My thanks go to him for his precious love, encouragement and patience throughout my studies. Last but the least, I would like to thank one more person in my life, to my little son. He has been an incredible surprise for me at the end of second year of my Ph.D. studies. He made me very happy with his love from his little hearth during the most stressful times of my study.

This study was supported by Turkish Scientific and Technological Council, project # TÜBİTAK-104Y039. Work at NASA/GSFC was supported by NASA's SR&T program, TÜBİTAK and Istanbul Technical University.

September 2010

Filiz Türk Katırcıođlu

## TABLE OF CONTENTS

	<u>Page</u>
<b>FOREWORD</b> .....	<b>vii</b>
<b>TABLE OF CONTENTS</b> .....	<b>ix</b>
<b>ABBREVIATIONS</b> .....	<b>xi</b>
<b>LIST OF TABLES</b> .....	<b>xii</b>
<b>LIST OF FIGURES</b> .....	<b>xv</b>
<b>SUMMARY</b> .....	<b>xix</b>
<b>ÖZET</b> .....	<b>xxi</b>
<b>1. INTRODUCTION</b> .....	<b>1</b>
1.1 Solar Terrestrial Environment.....	1
1.2 Sun: Source of High Energy Particles .....	1
1.3 The Bow Shock .....	4
1.4 Upstream Bow Shock (The Foreshock) .....	6
1.5 The Magnetosheath .....	8
1.6 The Magnetopause .....	9
1.7 Terminology and Concepts .....	10
1.7.1 Definitions.....	10
1.7.1.1 Plasma parameters .....	10
Gyrofrequency ( $\omega_g$ ) .....	10
Plasma frequency ( $\omega_p$ ).....	11
Ion skin dept (Plasma skin dept) ( $c/\square_p$ ).....	11
Thermal velocity ( $V_{th}$ ) .....	11
Sound speed ( $C_S$ ).....	11
Alfvén velocity ( $V_A$ ).....	12
Mach number ( $M$ ) .....	12
Alfven mach number ( $M_A$ ) .....	12
Suprathermal (or high energetic) ions .....	12
Cone angle ( $\Phi$ ) .....	12
Clock angle ( $\Theta$ ) .....	13
Flux.....	13
Electric flux.....	15
Magnetic flux .....	16
Maxwellian speed distribution (MSD) .....	16
Kinetic temperature .....	19
1.7.2 Concepts.....	19
1.7.2.1 Maxwell’s equations .....	19
1.7.2.2 Velocity moments and fluid approach.....	21
1.7.2.3 Measurements of plasma macroscopic quantities .....	22
1.7.2.4 Modeling of the plasmas .....	25
Analytical models.....	26
Numerical models .....	26
1.7.2.5 Measurements in space .....	27

Spacecraft Magnetometers .....	28
Plasma Instruments .....	28
1.7.2.6 Solar terrestrial effects.....	29
<b>2. ENERGETIC PARTICLES IN THE MAGNETOSHEATH .....</b>	<b>31</b>
2.1 Literature Survey .....	31
2.2 Purpose of the Dissertation.....	39
<b>3. RESULTS FROM INTERBALL SPACECRAFT DATA .....</b>	<b>41</b>
3.1 Interball Spacecraft, Instruments, and Data .....	41
3.2 March 10, 1996.....	41
3.2.1 Normalization with solar wind data .....	62
3.2.2 Median analysis of ion flux using 100, 200, and 500 PFU flux steps ...	66
3.2.3 Z-Score analysis.....	68
3.3 IMF and Solar Wind Plasma Connection.....	73
3.4 Discussion and Summary on Interball Search.....	76
<b>4. CLUSTER SEARCH AND MAGNETOSHEATH CAVITIES.....</b>	<b>81</b>
4.1 Cluster Spacecraft, Instruments and Data .....	81
4.2 Event Selection .....	87
4.2.1 Case 1: January 2, 2002.....	88
4.2.2 Case 2: March 11, 2002.....	98
4.2.1 Case 3: February 4, 2003.....	106
4.3 Comparison with the Foreshock Cavities.....	112
4.4 Summary from the Cluster Search.....	116
<b>5. STATISTICAL RESULTS BASED ON CLUSTER CASES.....</b>	<b>119</b>
5.1 Plasma and Magnetic Field Structure of the Magnetosheath in the Presence of Energetic Particles.....	119
5.2 Fluctuation Levels in the Presence of Energetic Particles .....	122
5.3 Dependence on IMF and Solar Wind Plasma.....	123
5.4 Effects on Magnetopause Location.....	125
5.5 Duration of the Magnetosheath Cavities .....	125
5.6 Summary of the Statistical Results .....	127
<b>6. MODELING THE MAGNETOSHEATH CAVITIES .....</b>	<b>129</b>
6.1 Introducing Kinetic Hybrid Model .....	129
6.2 Kinetic-Hybrid Model for Magnetosheath Cavities .....	129
6.2.1 Model definition.....	130
6.2.1 Model results for magnetosheath cavities .....	133
6.3 Summary and Conclusions.....	146
<b>7. CONCLUSION AND FUTURE RESEARCH .....</b>	<b>149</b>
7.1 Thesis Summary and Conclusions.....	149
7.2 Future Research .....	154
<b>REFERENCES .....</b>	<b>157</b>
<b>APPENDICES .....</b>	<b>163</b>
<b>CURRICULUM VITAE .....</b>	<b>165</b>

## ABBREVIATIONS

<b>3DP</b>	: 3 Dimensional Plasma
<b>ACE</b>	: Advanced Composition Explorer
<b>CDAWeb</b>	: Coordinated Data Analysis Web
<b>CIS</b>	: Cluster Ion Spectrometer
<b>DVD</b>	: Digital Versatile Disc
<b>FBE</b>	: Flux Burst Event
<b>FGM</b>	: Flux Gate Magnetometer
<b>FLO</b>	: Fast Linearly Oblique
<b>GIC</b>	: Geomagnetically Induced Currents
<b>GPS</b>	: Global Positioning System
<b>GSE</b>	: Geocentric Solar Ecliptic
<b>GSFC</b>	: Goddard Space Flight Center
<b>GSM</b>	: Geocentric Solar Magnetospheric
<b>HFA</b>	: Hot Flow Anomalies
<b>HIA</b>	: Hot Ion Analyzer
<b>HEOS</b>	: Highly Eccentric Orbit Satellite
<b>IMF</b>	: Interplanetary Magnetic Field
<b>IMP</b>	: Interplanetary Monitoring Platform
<b>keV</b>	: KiloElectronVolt
<b>MFI</b>	: Magnetic Field Investigation
<b>MHD</b>	: Magnetohydrodynamic
<b>MIT</b>	: Massachusetts Institute of Technology
<b>MK</b>	: Mega Kelvin
<b>MSD</b>	: Maxwell Speed Distribution
<b>nT</b>	: NanoTesla
<b>NASA</b>	: National Aeronautics and Space Administration
<b>PDL</b>	: Plasma Depletion Layer
<b>PDL</b>	: Plasma Depletion Layer
<b>PECVD</b>	: Plasma Enhanced Chemical Vapor Deposition
<b>PESA-L</b>	: Proton Electrostatic Analyzer-Low
<b>PFU</b>	: Proton Flux Unit
<b>PIC</b>	: Particle-In-Cell
<b>RAPID</b>	: Research with Adaptive Particle Imaging Detectors
<b>RAST</b>	: Recent Studies in Space Technologies
<b>SR&amp;T</b>	: Supporting Research and Technology
<b>SSCWeb</b>	: Satellite Situation Center Web
<b>SST</b>	: Solid State Telescope
<b>SWE</b>	: Solar Wind Experiment
<b>TÜBİTAK</b>	: Türkiye Bilimsel ve Teknolojik Araştırma Kurumu
<b>UHUK</b>	: Ulusal Havacılık ve Uzay Konferansı
<b>ULF</b>	: Ultra Low Frequency
<b>URL</b>	: Uniform Resource Locator
<b>UT</b>	: Universal Time



## LIST OF TABLES

	<u>Page</u>
<b>Table 1.1:</b> Maxwell's equations in microscopic form .....	20
<b>Table 3.1:</b> Instruments carried on Interball spacecraft and their characteristics. ....	43
<b>Table 3.2:</b> Types of the structures seen in Interball magnetosheath data .....	49
<b>Table 3.3:</b> Calculated correlation coefficients, t-values, and significance of relationship for March 10, 1996 case.....	64
<b>Table 3.4:</b> Calculated correlation coefficients, t-values, and significance of relationship for March 10, 1996 case by using normalized data .....	68
<b>Table 3.5:</b> Calculated correlation coefficients, t-values, and significance for March 10, 1996 case for the median tests with bandwidths of 100, 200, and 500 PFU corresponding to different critical values .....	73
<b>Table 3.6 :</b> Calculated correlation coefficients, t-values, and significance of relationship for March 10, 1996 case by using standartized data .....	75
<b>Table 3.7 :</b> Average IMF and solar wind parameters for each magnetosheath cavity type .....	75
<b>Table 4.1 :</b> Statistics for Flux Burst Events (FBE) determined in two years of Cluster data.....	85
<b>Table 5.1 :</b> Average characteristics of the magnetosheath plasma and magnetic field seen in 267 events.....	120
<b>Table 6.1 :</b> The characteristics of the magnetic field and plasma parameters for radial and inclined IMF cases at all selected points .....	144





## LIST OF FIGURES

	<u>Page</u>
<b>Figure 1.1</b> : The inner and atmospheric layers of the Sun .....	2
<b>Figure 1.2</b> : Magnetic reconnection process on the Sun's corona.....	3
<b>Figure 1.3</b> : A schematic diagram of near-Earth space environment .....	4
<b>Figure 1.4</b> : Propagating and stationary shocks.....	5
<b>Figure 1.5</b> : A bow shock crossing on day November 7, 1977 .....	6
<b>Figure 1.6</b> : A schematic figure of foreshock region.....	7
<b>Figure 1.7</b> : Upstream sinusoidal waves in foreshock region .....	7
<b>Figure 1.8</b> : A sketch of principal currents and flows around the Earth's magnetosphere. ....	8
<b>Figure 1.9</b> : A schematic definition of cone angle.....	13
<b>Figure 1.10</b> : A schematic definition of clock angle.....	13
<b>Figure 1.11</b> : Schematic illustrating the flux concept.....	14
<b>Figure 1.12</b> : Illustrations of the electric flux on plane and curved surface.....	16
<b>Figure 1.13</b> : Illustration of the magnetic flux .....	16
<b>Figure 1.14</b> : A diagram of MSD function versus Molecular speed.....	18
<b>Figure 1.15</b> : The electronic schematic and picture of the Mars Global Surveyor Magnetometer .....	28
<b>Figure 2.1</b> : Results of kinetic simulation of cavities by Thomas and Brecht .....	32
<b>Figure 2.2</b> : Example of an energetic particle event as seen by IMP-8 in the foreshock region .....	33
<b>Figure 2.3</b> : Average locations of diamagnetic cavities in XY-plane.....	34
<b>Figure 2.4</b> : Wind 3DP phase space densities versus time.....	36
<b>Figure 2.5</b> : Wind 3DP plasma and magnetic field parameters versus time .....	37
<b>Figure 2.6</b> : Simulations of foreshock region using 2.5-D global hybrid model.....	38
<b>Figure 3.1</b> : 7-day example of Interball spacecraft trajectory .....	42
<b>Figure 3.2</b> : An illustration for the orbits for 51 magnetosheath.....	46
<b>Figure 3.3</b> : An example of a magnetosheath crossing of Interball spacecraft on May 12, 1998.....	47
<b>Figure 3.4</b> : The trajectory of Interball spacecraft in May 12, 1998.....	48
<b>Figure 3.5</b> : Type-1 example of Interball in June 1, 1996.....	50
<b>Figure 3.6</b> : Trajectory of Interball spacecraft for June 1, 1996.....	51
<b>Figure 3.7</b> : The scatter plots of magnetosheath plasma and magnetic field parameters for June 1, 1996 .....	52
<b>Figure 3.8</b> : Type-2 example of Interball observed in June 1-2, 1996.....	53
<b>Figure 3.9</b> : Trajectory of Interball spacecraft for June 1-2, 1996 .....	54
<b>Figure 3.10</b> : The scatter plots of magnetosheath plasma and magnetic field parameters for June 1-2, 1996 .....	55
<b>Figure 3.11</b> : Type-3 example of Interball observed in March 29, 1996.....	56
<b>Figure 3.12</b> : Trajectory of Interball spacecraft for March 29, 1996.....	57
<b>Figure 3.13</b> : The scatter plots of magnetosheath plasma and magnetic field parameters for March 29, 1996.....	58

<b>Figure 3.14</b> : Type-4 example of Interball in March 17, 1998 .....	59
<b>Figure 3.15</b> : Trajectory of Interball spacecraft for March 17, 1998 .....	60
<b>Figure 3.16</b> : The scatter plots of magnetosheath plasma and magnetic field parameters for March 17, 1998 .....	61
<b>Figure 3.17</b> : Time series of magnetosheath plasma and magnetic field parameters for March 10, 1996.....	62
<b>Figure 3.18</b> : The scatter plots of magnetosheath plasma and magnetic field parameters for March 10, 1996 .....	63
<b>Figure 3.19</b> : Normal distribution with significant correlation regions specified by critical values for significance level of 0.05 .....	65
<b>Figure 3.20</b> : The scatter plots of normalized plasma and magnetic parameters of the magnetosheath for March 10, 1996 .....	67
<b>Figure 3.21</b> : Scatter plots of unnormalized and median values of magnetosheath magnetic field.....	69
<b>Figure 3.22</b> : Scatter plots of unnormalized and median values of magnetosheath density .....	70
<b>Figure 3.23</b> : Scatter plots of unnormalized and median values of magnetosheath ion density .....	71
<b>Figure 3.24</b> : Scatter plots of unnormalized and median values of magnetosheath velocity.....	72
<b>Figure 3.25</b> : Scatter plots of standardized magnetosheath plasma and magnetic field parameters .....	74
<b>Figure 3.26</b> : Solar activity cycle from 1985 to 2005.....	76
<b>Figure 3.27</b> : Average locations of all 51 magnetosheath cases of Interball .....	78
<b>Figure 4.1</b> : An example of a high latitude trajectory of Cluster spacecraft for May 10-11, 2002.....	82
<b>Figure 4.2</b> : The trajectories of Cluster and ACE spacecrafts for May 10-11, 2002 .	83
<b>Figure 4.3</b> : Particle flux and corresponding magnetic field variations in different time resolutions .....	86
<b>Figure 4.4</b> : The expanded time interval from 14:20 UT to 15:12 UT of March 11, 2002 .....	87
<b>Figure 4.5</b> : Trajectories of Cluster spacecraft in four different planes for January 2, 2002, March 11, 2002, and February 4, 2003.....	88
<b>Figure 4.6</b> : Time series of magnetosheath particle flux, magnetic field, and plasma parameters for Case 1 .....	89
<b>Figure 4.7</b> : Plot of the expanded time interval for Burst 1 in Case 1 .....	90
<b>Figure 4.8</b> : Scatter plots of magnetosheath parameters from 00:00 UT to 07:00 UT of Case 1.....	92
<b>Figure 4.9</b> : Plot of particle flux, magnetosheath magnetic field components, and magnetic latitude ( $B_{\theta}$ ) for Case 1 .....	93
<b>Figure 4.10</b> : Scatter plots of magnetic latitude versus magnetic longitude of three bursts for Case 1 .....	94
<b>Figure 4.11a</b> : ACE magnetic field data for Case 1 .....	95
<b>Figure 4.11b</b> : ACE solar wind plasma data for Case 1 .....	96
<b>Figure 4.12</b> : Scatter plots of IMF clock angle versus IMF longitude for Case 1 .....	97
<b>Figure 4.13</b> : Theta $B_n$ angle for Case 1 .....	98
<b>Figure 4.14</b> : Time series of magnetosheath particle flux, magnetic field, and plasma parameters for Case 2 .....	99
<b>Figure 4.15</b> : Time series of magnetosheath particle flux, magnetic field, and plasma parameters of the expanded time interval for Case 2 .....	100

<b>Figure 4.16</b> : Spectral plot for Flux Burst 1 from 14:15 to 15:15 UT for Case 2.....	101
<b>Figure 4.17a</b> : ACE magnetic field data for Case 2.....	103
<b>Figure 4.17b</b> : ACE solar wind plasma data for Case 2 .....	104
<b>Figure 4.18</b> : Scatter plots of magnetic latitude versus magnetic longitude for within and the ambient magnetosheath of Case 2 .....	105
<b>Figure 4.19</b> : Scatter plots of IMF clock angle versus IMF longitude for within and the ambient magnetosheath of Case 2.....	105
<b>Figure 4.20</b> : Theta Bn angle for Case 2 .....	106
<b>Figure 4.21</b> : Time series of magnetosheath particle flux, magnetic field, and plasma parameters of the expanded time interval for Case 3.....	107
<b>Figure 4.22</b> : Time series of magnetosheath particle flux and magnetic field of the expanded time interval for Burst 1 in Case 3 .....	108
<b>Figure 4.23</b> : Scatter plots of magnetic latitude versus magnetic longitude within Bursts 1 and 2, and in the ambient magnetosheath for Case 3 .....	109
<b>Figure 4.24a</b> : Plot of particle flux, magnetosheath magnetic field components, and IMF clock angle for Case 3 .....	110
<b>Figure 4.24b</b> : ACE solar wind plasma data for Case 3 .....	111
<b>Figure 4.25</b> : Time variation of total pressure and the magnetopause ratio for Jan. 2, 2002.....	114
<b>Figure 4.26</b> : Scatter plots of total pressure in the magnetosheath and magnetopause ratio versus particle flux for January 2, 2003 .....	115
<b>Figure 5.1</b> : Average positions of the Cluster trajectories in the magnetosheath for 267 FBE in four different planes .....	120
<b>Figure 5.2</b> : Histograms of total magnetic field within the cavities and for ambient magnetosheath of the cavities of 267 Burst Events .....	121
<b>Figure 5.3</b> : Histograms of magnetosheath plasma parameters for cavities and ambient magnetosheath for 267 Burst Events .....	122
<b>Figure 5.4</b> : The scatter plots of IMF strength versus total magnetic field for cavities and ambient magnetosheath for all Burst Events .....	123
<b>Figure 5.5</b> : IMF clock angle- $\Phi$ and cone angle- $\theta$ dependence of the magnetosheath cavities .....	124
<b>Figure 5.6</b> : Comparison of magnetopause size calculated using the magnetosheath and upstream solar wind parameters.....	125
<b>Figure 5.7</b> : Time durations of 267 flux burst events .....	126
<b>Figure 5.8</b> : Time durations of foreshock cavities seen in the upstream bow shock region .....	126
<b>Figure 6.1</b> : A model box in the kinetic hybrid model.....	131
<b>Figure 6.2</b> : Illustration of the domain used in the global hybrid model .....	132
<b>Figure 6.3</b> : Simulation box of the model including the boundaries .....	134
<b>Figure 6.4</b> : Simulated total magnetic field views at different times for inclined and radial IMF.....	135
<b>Figure 6.5</b> : Simulated ion densities views at different times for inclined and radial IMF .....	136
<b>Figure 6.6</b> : Simulated ion temperature views at different times for inclined and radial IMF.....	137
<b>Figure 6.7</b> : Model magnetic field in a selected plane for inclined IMF conditions	138
<b>Figure 6.8</b> : Profiles of magnetic field magnitude, density, and temperature of along a selected path for inclined IMF conditions.....	139
<b>Figure 6.9</b> : Profiles of magnetic field magnitude, density, and temperature of along a selected path for radial IMF conditions .....	140

<b>Figure 6.10 :</b> Profiles of magnetic field magnitude, density, and temperature of along a selected path for inclined IMF conditions again .....	141
<b>Figure 6.11 :</b> Locations of the four selected points in the magnetosheath .....	142
<b>Figure 6.12 :</b> Time series plots of density, temperature, and magnetic field magnitude at the selected points.....	143
<b>Figure 6.13 :</b> Simulations of magnetic field magnitude during inclined, radial, and again inclined IMF orientations .....	146

## A COMPREHENSIVE STUDY OF THE MAGNETOSHEATH CAVITIES

### SUMMARY

In this study, we investigate the effects of energetic particles and magnetic field, and plasma structure of the magnetosheath. Energetic particles are important in space environment as their presence can give us important information about the region where they come from, what mechanisms create them, how they interact with the environment. Foreshock cavities are formed as a result of the interaction between the energized ions reflected from bow shock and the incoming solar wind particles in the region just upstream of the Earth's bow shock. This study explores whether similar structures are present in the magnetosheath region, if so, how they formed and what controls their formation and characteristics, and what are their role on the interaction between the solar wind, magnetopause and ionosphere. These questions are addressed in this study in a comprehensive and systematic way. Observationally, four years of Interball and Cluster spacecraft data were searched for the high flux intervals of energetic particles as the spacecraft travel in the magnetosheath. We determined 267 energetic particle flux burst events and investigated the variations in the magnetosheath magnetic field and plasma in the presence of these particles in the magnetosheath flow. Our search results showed that the magnetic field and density were depressed up to 50% while the temperature increased in the presence of the energetic particles. We named these structures as the magnetosheath cavities as analogous to the foreshock cavities. Thus, the depressed magnetic fields and densities characterize the magnetosheath cavities. The fact that the temperature increases within these cavities indicates that the cavities were heated by the energetic particles within them. This also supplies the gas pressure that allows them to stay alive in the magnetosheath. All parameters become highly fluctuating within the magnetosheath cavities. Our statistical results showed that the magnetosheath cavities last typically 15-30 min. It is seen that the magnetopause moves locally outward from the Earth and is found to be larger by about 25-30% with respect to the solar wind driven magnetopause in the presence of the cavities. Magnetosheath cavities appear to occur during the low IMF cone angles which is the key finding of our research. The interaction between the magnetosheath cavities and magnetopause results in the expansion of the magnetopause away from the Earth. We compare observational findings with those obtained from kinetic-hybrid model simulations. Model results confirm the observational findings but also present new enlightening results on the formation and sources of the magnetosheath cavities. The model runs for radial IMF, for which IMF cone angle is  $0^\circ$ , clearly indicate that the magnetosheath cavities form when the IMF cone angle is low. Model cavities display highly structured and turbulent features depending on the location in the magnetosheath. These periodic, high amplitude fluctuating fields indicate wave activity within the magnetosheath cavities. This study is a first in displaying the relationship between the high energy particles and the magnetic field and density structure of the magnetosheath. The name "magnetosheath cavities" is introduced in

the literature for the first time in this study. Results of this study are crucial for the understanding of the interaction between the magnetosheath flow and the magnetopause, ionosphere and upper atmosphere of the Earth.

# MANYETİK ÖRTÜ ÇÖKELME BÖLGELERİNİN DETAYLI İNCELENMESİ

## ÖZET

Bu çalışmada yüksek enerjili parçacıkların manyetik örtünün manyetik alan ve yoğunluk yapısına olan etkileri çok kapsamlı bir şekilde incelenmektedir. Yüksek enerjili parçacıklar, geldikleri bölgeler hakkında önemli bilgi taşıdıkları ve onları oluşturan fiziksel ve dinamik mekanizmalar hakkında önemli bilgi verdikleri için uzay çevresi çalışmalarındaki önemi çok büyüktür. Yüksek enerjili parçacıklar çok farklı yerlerden Dünya çevresine gelebilirler. Dünya'nın şok sınırının güneş tarafında yer alan "ön şok" bölgesinde şokta enerjileri artan parçacıkların yansıyarak gelmekte olan güneş rüzgarı ile etkileşmesi sonucunda "ön şok çökme bölgeleri" meydana gelmektedir. Bu çalışmanın ana amaçlarından bir tanesi bu tip çökme bölgelerinin manyetik örtü içerisinde de oluşup oluşmadığını araştırmaktır. Eğer oluşuyorsa, bunların özelliklerinin ne olduğunu, hangi şartlar altında oluştuğunu, hangi faktörlerden etkilendiğini, oluşmalarını ve gelişmelerini kontrol eden parametrelerin neler olduğunu, manyetopoz ile etkileşiminin nasıl olduğunu vb belirlemek çalışmamızın diğer amaçlarıdır. Bunları araştırmak için Interball ve Cluster uzay uydularının verilerini kullanarak 267 tane manyetik örtü içerisinde yüksek akılı enerjetik parçacık aralıklarını içeren vakalar tesbit ettik. Bu vakaların kapsamlı analizi sonucunda, bu parçacıklar görüldüğünde, manyetik örtünün manyetik alan ve yoğunluk yapısındaki değişimleri saptadık. Gözlemsel olarak yüksek enerjili parçacıkların manyetik alan ve yoğunlukta %50'e varan düşüslere sebep olduğunu gördük. Bu düşüşlerin olduğu bölgeleri manyetik örtü çökme bölgeleri olarak adlandırdık. Manyetik örtü çökme bölgelerinin içinde sıcaklığın arttığını bulduk. Bunun nedeni çökme bölgesi içerisindeki yüksek enerjili parçacıkların yer almasıdır. Bu parçacıkların uyduladıkları basınç sayesinde de çökme bölgeleri manyetik örtü içerisinde uzun süre kalabilmektedirler. Tipik kalma süreleri 15-30 dakika olarak belirlenmiştir. Çökme bölgeleri içerisinde tüm parametrelerin çok türbülanslı ve yüksek değişimler gösterdikleri görülmüştür. Çökme bölgelerinin güneşin manyetik alanının (IMF) ekliptik düzleminde x-ekseni ile yaptığı açının düşük olduğu zamanlarda yani IMF radyal olarak geldiği zamanlarda oluştukları görülmüştür. Çökme bölgeleri var olduğunda, manyetopozun lokal olarak Dünya'dan uzaklaşacak şekilde hareket ettiği ve yaklaşık olarak normal güneş rüzgarı şartlarına göre %25-30 arasında büyük olduğu görülmüştür. Kinetik-hibrid model sonuçları gözlemleri desteklemektedir. IMF radyal yönde olduğunda model manyetik örtüsü düşük manyetik alan ve düşük yoğunluk göstermiştir. Böylece manyetik örtü çökme bölgelerinin kaynağına yönelik bir ipucu vermiştir. Bu, ön şok bölgesindeki çökme bölgelerinin güneş rüzgarı ile manyetik örtüye taşındığına işaret etmektedir. Model sonuçları manyetik örtü çökme bölgelerinin özelliklerinin manyetik örtü içerisinde bulunulan noktaya göre değiştiğini ortaya koymaktadır. Gözlemlerdeki gibi, manyetik örtü çökme bölgeleri içerisinde manyetik alan ve yoğunlukta yüksek çalkantılı yapılar saptanmıştır. Model sonuçları, bu periyodik, yüksek çalkantıların çökelmeler içerisinde oluşan dalga aktiviteleri olduğunu öne sormaktadır. Bu çalışma konusunda Türkiye'deki doktora araştırması düzeyindeki ilk

arařtırmadır. Bunun yanı sıra aynı zamanda Dünya’da yüksek enerjili paracıklar ile manyetik rtnn yapısı zerindeki etkileřmeyi gsteren alıřmadır. Pek ok terim ve konsept ilk defa bu alıřmada literatre sunulmuřtur. “Manyetik rt kelme Blgeleri” adı ilk defa bu tez ile literatre girmiřtir. Bu alıřmanın sonuları manyetik rt akıřı, manyetopoz ve ionosfer arasındaki etkileřimi daha iyi anlayabilmek iin ok nemli olup ve bu sonuların modellere ve teorik alıřmalara integre edilmesi bu konulardaki geliřmeleri hızlandıracaktır.



## **1. INTRODUCTION**

### **1.1 Solar Terrestrial Environment**

Solar-Terrestrial environment encompasses the Earth, the Sun, and the space between them. The solar wind, which is a plasma flowing out supersonically from the Sun, fills this space. The interaction between the Earth and solar wind causes many of the physical and dynamical changes in the Near-Earth space environment and has many technological consequences on the spacecraft and ground systems on the Earth. This study focuses on examining a part of this system, the magnetosheath, using most recent available spacecraft data and describes a new phenomenon, which we call as the magnetosheath cavities, and study the characteristics of these phenomenon. Below, first we introduce the basic regions and elements of the solar-terrestrial environment, which have significance in our research.

### **1.2 Sun: Source of High Energy Particles**

The source of the Sun's energy is the thermonuclear reactions, which produce helium atoms out of four hydrogen atoms. The mass difference is converted into the energy through the Einstein's relativity law. At the core of the Sun, the temperature is very high, around  $10^7$  °K, which allow these reactions to occur. The temperature decreases outward from the core and reaches a minimum of 4000 °K at the surface of the Sun, the photosphere. The heat energy produced within the core is carried by radiation in the radiative zone and by convection in the hydrogen convection zone. Figure 1.1 from NASA's image gallery (Url-1) illustrates this point and the inner and atmospheric structure of the Sun. The atmospheric regions of the Sun, the photosphere at the base, and outward, the chromosphere and the corona are seen in the figure. The temperature at the base of the corona increases rapidly to  $10^6$  °K again and stays almost constant within the solar system. Due to scarce observations close to the Sun, this rapid increase in temperature is one of the major issues in solar research. The theories have been proposed which involve the dissipation of the sound waves, spicules reaching out into the corona, various wave breakings, ohmic

dissipation, which converts magnetic energy to kinetic energy of the particles via magnetic reconnections that result in the solar flare activity on the Sun, etc.

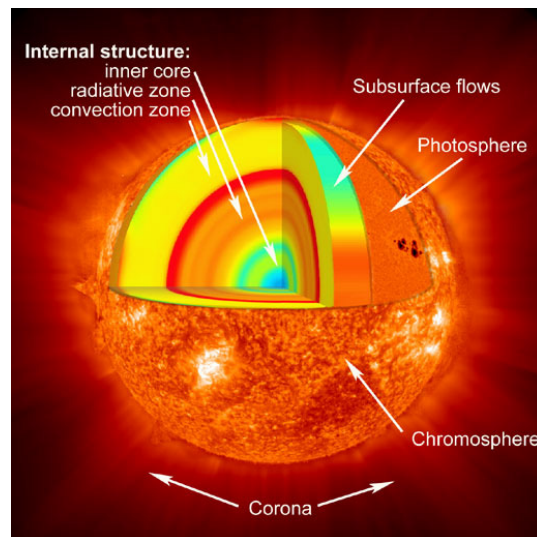


**Figure 1.1:** The inner and atmospheric layers of the Sun. Internal structure elements are inner core, radiative zone, and convective zone. The atmospheric layers of the Sun are photosphere, chromosphere, and corona (Url-1).

The structure of the corona is formed by the large magnetic loops extending from the surface of the Sun up to large distances as far as one or two solar radius into the corona. The magnetic energy, which is created and destroyed in the magnetic loops plays an important role in the high temperature of coronal gases. This high magnetic energy is also a source of the energy for acceleration of the charged particles carried by the solar wind which moving at speeds of 400-450 km/sec on the average. Although few, the particles carried by the solar wind are very hot being the protons about  $10^5$  °K and electrons  $10^6$  °K at the Earth's orbit. The solar wind particles are energized and accelerated through the magnetic reconnection in the corona or at lower distance of the Sun's atmosphere (Figure 1.2). Magnetic reconnection occurs when two oppositely directed magnetic field lines are connected. This process releases lots of X-ray energy into the space and accelerates the solar wind particles. The phenomena occurring as a result of the magnetic reconnection on the Sun is called Solar Flare. Thus, the solar flares put out huge amounts of X-ray and extreme UV energy and accelerated particles which are carried by the solar wind.

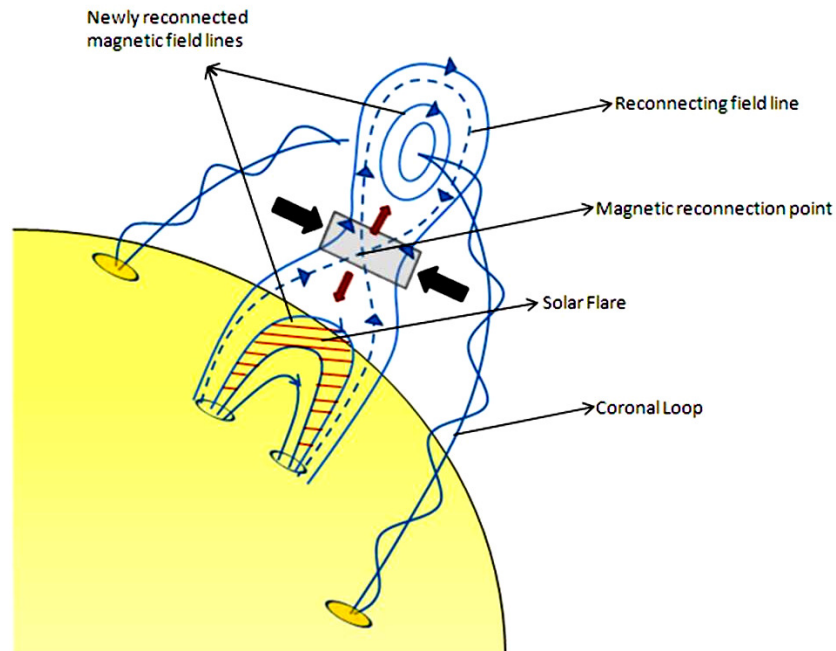


**Figure 1.2:** Magnetic reconnection (grey box) process due to the oppositely directed magnetic field lines in the corona or at lower distance of the Sun's atmosphere. The reconnected magnetic field lines of solar flares produce huge amount of energy and put out accelerated particles carried by the solar wind.

The solar wind transfers mass, momentum and energy between the Sun and the Earth. While flowing towards Earth, it encounters several regions and boundaries that play significant role in determining the physical and dynamical processes that result in the variations in these quantities, i.e. mass, momentum, and energy. Figure 1.3 exhibits the important elements of near-Earth space environment. In the figure, the Sun is placed on left and the red arrow represents the solar wind moving towards the Earth. The dark and light blue lines show interplanetary magnetic field, interconnected magnetic field (open magnetic field), and geomagnetic field lines (closed magnetic field) respectively. The important boundaries for near-Earth space environment are the bow shock (purple) and the magnetopause (red). The magnetosheath is an intermediate region between these two boundaries, while the foreshock (represented with red circles) is the region just in front of the bow shock in which the back-streaming ions and the inflowing solar wind particles interact with each other. In the figure, as our studies showed, we have added the grey areas with irregular shape to illustrate the magnetosheath cavities occurring when the high fluxes of energetic particles have been observed in the magnetosheath.

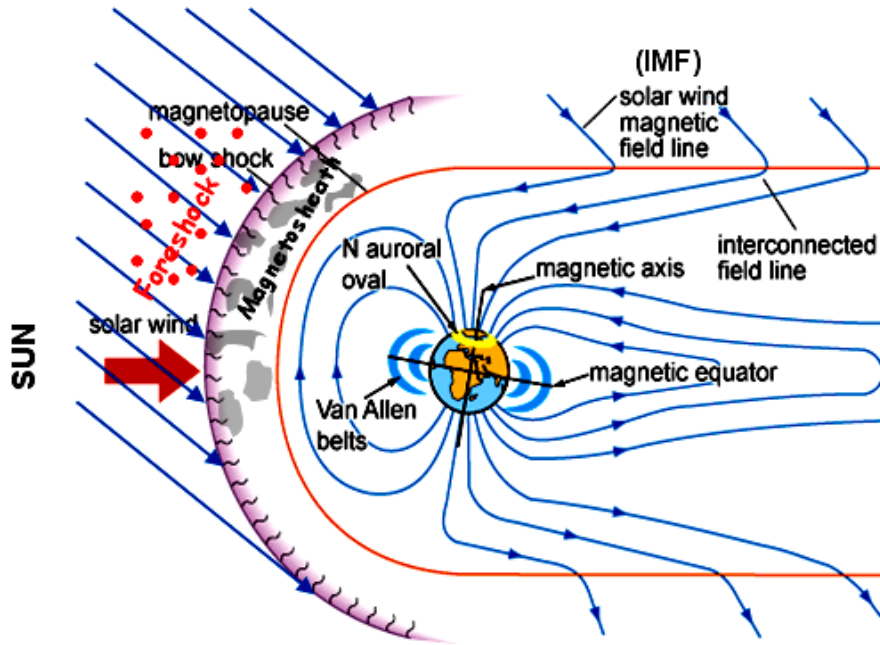


**Figure 1.3:** A schematic diagram of near-Earth space environment. The Sun is on left. The foreshock (red circles), the bow shock (purple), the magnetopause (red), all magnetic field lines (blue lines), and the magnetosheath cavities (grey areas with irregular shape) are presented here because of being major elements of the space environment between the Sun and the Earth.

### 1.3 The Bow Shock

The solar wind is very tenuous and light plasma. The mixture of the energetic electrons and protons in this plasma moves away from the Sun at supersonic speeds and sometimes can reach very high speeds like 800-1000 km/sec. With its average speed of, it will take 2-3 days to move through the distance between Sun and Earth. During its travel, the solar wind encounters with the Earth as an obstacle and its speed slow down from supersonic to subsonic at the shock in front of the Earth, and thus it can be deflected and flows smoothly around the Earth. This shock surface is known as the bow shock. Bow shocks occur around all magnetized planets. The Earth's bow shock is about 100-1000 km thick and located about 90,000 km from the Earth. The thickness, shape and location of the bow shock depend on the different factors. Two of the most important factors that determine the structure of the Earth's bow shock are the Mach number of the solar wind and the angle between the interplanetary magnetic field and the shock normal, which called  $\theta_{Bn}$  (theta Bn). Unlike the shocks that occur in front of the airplane flying at supersonic speeds, the

Earth's bow shock is not a propagating shock (Figure 1.4). Furthermore, it differs from the shocks in the atmosphere as being a collisionless shock. Because the solar wind is very tenuous and the energetic particles rarely collide to each other, these collisions have no significant effect on the formation of the shock (Kivelson and Russell, 1995).

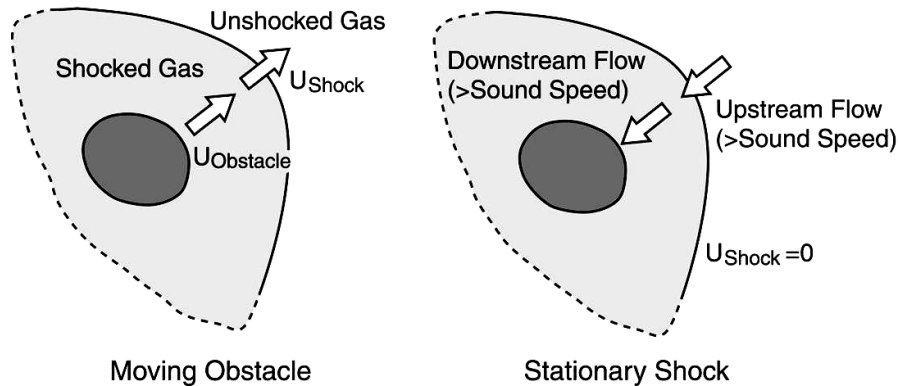


**Figure 1.4:** Propagating shock (left) because of moving obstacle. Stationary shock (right) in a flow with the sound speed. Earth's bow shock is a stationary shock with no speed of shock (Kivelson and Russell, 1995).

The Earth's bow shock in fact is a discontinuity surface where all kinds of magnetic waves interact. As being a discontinuity surface, mass, momentum and energy have to be conserved across bow shock. The Rankine Hugoniot conditions apply at the bow shock and describe the variations in these parameters across the bow shock. Owing to the compression at the bow shock, the density increases by fourth while the solar wind speed decreases to subsonic speeds being reduced to the one fourth of that in the upstream. The temperature and thermal pressure increase. The kinetic energy of the solar wind dissipates at the bow shock (Url-2). Thus the moving particles of solar wind are energized at the bow shock. The magnetic field also increases. Figure 1.5 gives an example of a bow shock observed by ISEE-1 spacecraft at 22:21:25 in 1977.

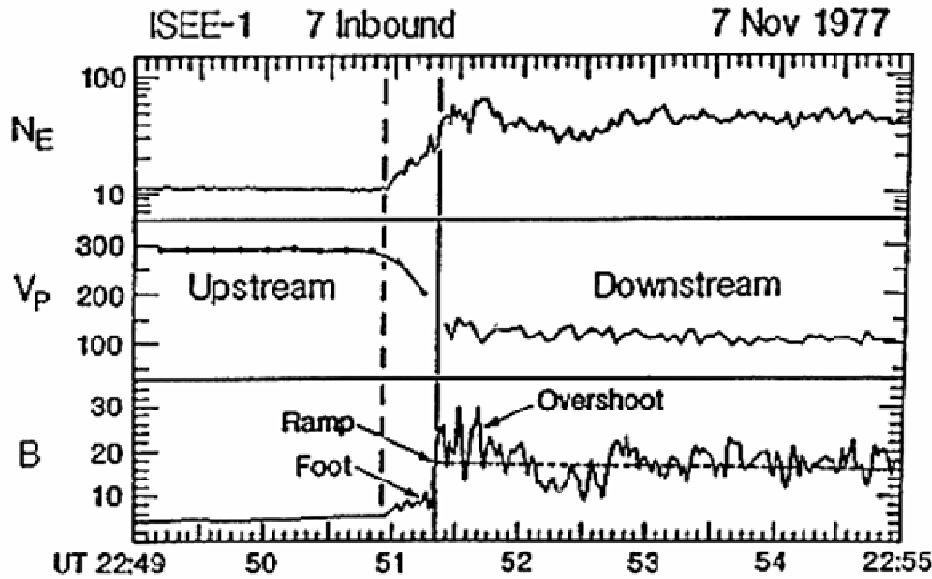


**Figure 1.5:** A bow shock crossing of ISEE-1 spacecraft on day November 7, 1977. Because of the compression at the bow shock, density and magnetic field magnitude increase. On the other hand, upstream solar wind slows down and its speed becomes subsonic at the bow shock (Kivelson and Russell, 1995).

#### 1.4 Upstream Bow Shock (The Foreshock)

The upstream region of the Earth's bow shock is known as foreshock region. This region is magnetically connected to the bow shock and contains some of inflowing solar wind and reflected charged particles from the bow shock. There are two foreshock regions depending on the velocity of reflected particles: the electron (faster) foreshock and the suprathermal ion (slower) foreshock (Figure 1.6).

The foreshock is characterized by an abundance of wave activity. Interaction between the backstreaming ions and the inflowing solar wind causes various instabilities. These instabilities result in ultra-low-frequency (ULF) MHD waves, acoustic waves, shocklets etc. Several waves are also generated at the bow shock and then propagate upstream (Figure 1.6). The waves in the foreshock region, coming from several sources, exist as a source of turbulence and waves in the magnetosheath (Url-2). An data example of a sinusoidal waves in the foreshock region, which is observed by ISEE on September 11, 1978, is given in Figure 1.7. The wave activity is clearly seen in magnetic field strength and its components.

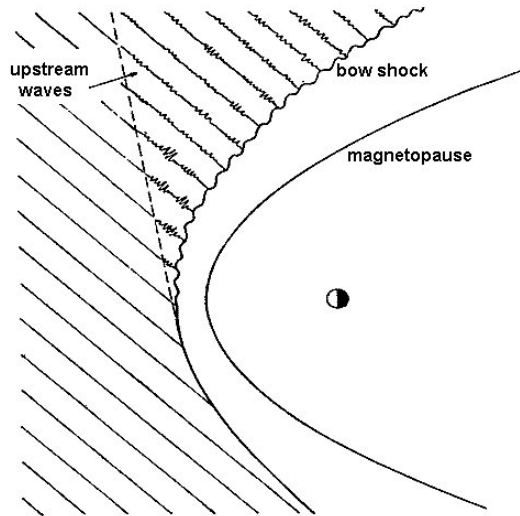


**Figure 1.6:** A schematic figure of foreshock region. Interaction between the backstreaming ions and the inflowing solar wind causes different waves in the upstream and also on the bow shock (Formizano, 1974).

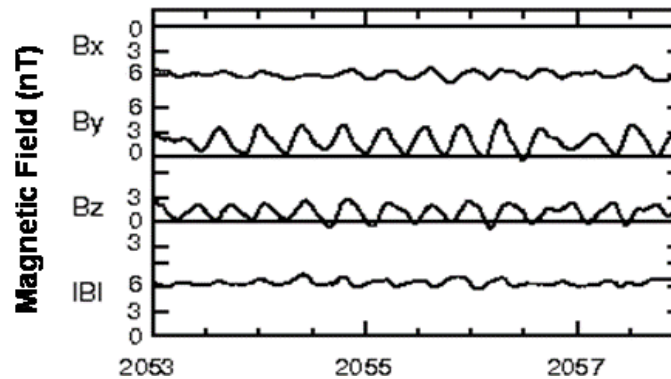


**Figure 1.7:** Upstream sinusoidal waves in foreshock region from an ISEE observation of September 11, 1978. Panels from top to bottom give the components of magnetic field and the magnetic field strength (Le and Russell, 1994).

The foreshock takes an important part in our study as it is one of the sources for the energized particles. The particles energized at the bow shock and streaming back into the solar wind can be carried by the incoming solar wind into the magnetosheath. These particles in turn can change the structure of the magnetosheath as they propagate.

## 1.5 The Magnetosheath

The region behind the bow shock is called magnetosheath. Because of the plasma and magnetic processes at the bow shock, all plasma and magnetic field parameters fluctuate within the magnetosheath. Therefore, turbulence is the main characterizing factor to describe the magnetosheath. In comparison to the solar wind and IMF, the magnetic field, ion density, and temperature are typically higher in the magnetosheath. From the bow shock to the magnetopause, the ion density decreases. However, it is still higher than the ion density of the magnetosphere. The magnetic field strength in the magnetosheath is weaker than the magnetospheric magnetic field.

While moving towards the Earth, the magnetic field lines of the shocked solar wind in the magnetosheath become deflected and draped over the magnetopause (Figure 1.8).

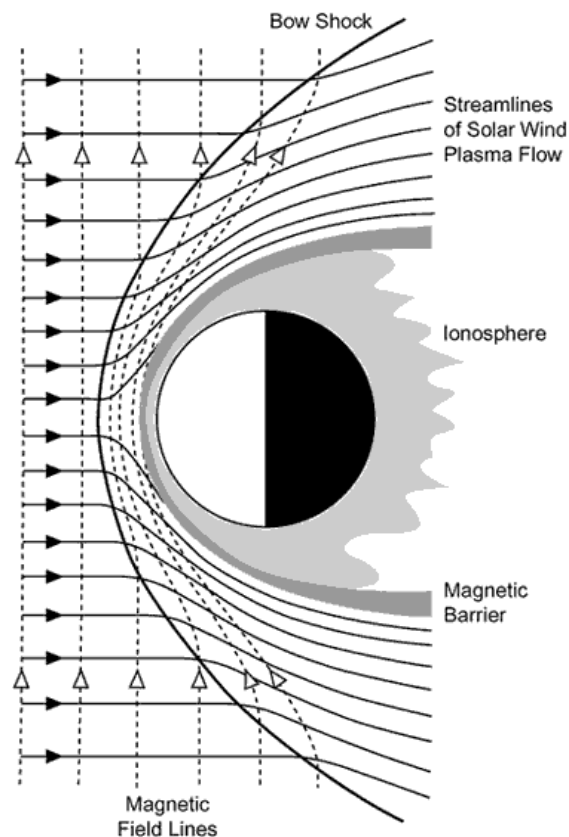


**Figure 1.8:** A sketch of principal currents and flows around the Earth's magnetosphere. Solar wind become shocked at the bow shock and it is draped over the magnetopause in the magnetosheath (Russell, 1999).



Not only the strength of magnetosheath magnetic field but also its direction is important for the reconnection process with the magnetospheric field lines. If the direction of the magnetic field is opposing to the magnetospheric field, then magnetic field reconnection may occur just inside the magnetopause. Especially, the north-south direction of the magnetosheath/solar wind magnetic field is very important in this connection between the Earth's magnetic field lines and solar wind magnetic field lines. Moreover, when the IMF is northward, generally, a different type of interaction is present between the magnetosheath/solar wind plasma/magnetic field and Earth. In this case, a plasma depletion layer occurs just outside the subsolar magnetopause, in which plasma density decreases but the magnetic field strength increases relative to the adjacent magnetosheath plasma and magnetic field.

The magnetosheath particles typically have energies 1keV/e for ions and 100 eV for electrons but sometimes the flux of more energetic particles ( $> 30$  keV) increases and it causes unpredicted variations in plasma and magnetic field parameters. Decreasing magnetic fields and densities in the presence of energetic particles is one of these and investigated in this thesis study in detail.

## **1.6 Magnetopause**

The magnetopause is the outermost boundary of the Earth's environment. It is a magnetic barrier, around which the shocked solar wind in the magnetosheath flows. The boundary is defined where the magnetic pressure of the geomagnetic field is counterbalanced by the dynamic pressure of the solar wind. Under the average solar wind conditions, the dayside subsolar magnetopause distance from the Earth's center stands at about  $10.5 R_E$ . It is wider on the sides being about  $15 R_E$  at the dawn and dusk flanks and is about  $25-30 R_E$  on the nightside. The location of the magnetopause changes depending on the solar wind conditions. It can move inward toward the Earth or outward away from the Earth in response to the varying solar wind speed and density.

Furthermore, the magnetopause can change its position locally. The hot flow anomalies transferred from the upstream solar wind, flux transfer events, Kelvin Helmholtz waves propagating along magnetopause etc. can change the position of

the magnetopause locally. In addition, the results of this study indicate that the magnetopause can move outward in the presence magnetosheath cavities resulting in response to the high flux of energetic particles. This variation on the location of the magnetopause has consequences on the magnetopause ionosphere coupling.

## **1.7 Terminology and Concepts**

At this part of our study, we briefly give definitions and explanations for some of the terms and concepts used throughout this dissertation.

### **1.7.1 Definitions**

#### **1.7.1.1 Plasma parameters**

Plasma parameters define various characteristics of a plasma, an electrically conductive collection of charged particles that responds collectively to electromagnetic forces. Some of these, especially the ones mostly used in this dissertation, are given below (Url-3).

#### **Gyrofrequency ( $\omega_g$ )**

Other names for gyrofrequency are cyclotron frequency or Larmor frequency. It is the frequency corresponding to the rotation of an electron or ion around a magnetic field line.

Gyrofrequency is derived using the motion of a single particle. Solving equation of motion for a single particle under the influence of homogenous magnetic field gives a circular motion in the plane perpendicular to the magnetic field with a radius called gyro radius and a linear motion along the magnetic field. Together, they result in a helix type motion along the magnetic field lines. The frequency of this motion around the magnetic field line or guiding center is defined by

$$\omega_g = q.B/m \tag{1.1}$$

where  $q$ ,  $B$ , and  $m$  are particle charge, magnetic field strength, and particle mass, respectively. As seen from the formula, the gyrofrequency depends on the charge ( $q$ ) of the particles, which indicate that electrons and ions gyrate in different directions, i.e. for electrons, counter-clockwise direction and for ions, clockwise direction. It is inversely proportional with the mass of the particle such that an electron gyrates

more than the ions owing to their mass. It also depends on the strength of the background homogenous magnetic field. The gyroradius that corresponds to gyrofrequency is:

$$r_g = V_{perp} / \omega_p \quad (1.2a)$$

$$r_g = m.V_{perp} / q.B \quad (1.2b)$$

where  $V_{perp}$  is particle's perpendicular velocity. As a result, electrons gyrate in smaller circle with a smaller gyroradius while ions move in a larger circle with larger gyroradius.

### **Plasma frequency ( $\omega_p$ )**

Plasma frequency is the frequency with which electrons oscillate when their charge density is not equal to the ion charge density (plasma oscillation). The plasma frequency for an electron is given as:

$$\omega_{pe} = (4.\pi.q^2 / m_e)^{1/2} \quad (1.3)$$

### **Ion skin dept (Plasma skin dept) ( $c/\omega_p$ )**

It is the distance in a plasma that an electromagnetic radiation can penetrate and is given as  $C_s/\omega_p$  ( $C_s$  is sound speed). Ion skin dept together with ion gyrofrequency is used in the modeling for expressing the model distances and model time respectively. These will be used in Chapter 6 in this study.

### **Thermal velocity ( $V_{th}$ )**

Thermal velocity is the velocity related to the kinetic average energy of the gas molecules. It is a function of temperature. From Maxwell Speed Distribution (described in part c below in detail), we can write the thermal velocity as  $V_{th} = (kT/m)^{1/2}$ . Since the temperature of electrons and ions differ, the thermal velocity of these particles differs in different plasmas.

### **Sound speed ( $C_s$ )**

The sound speed is the speed of the longitudinal waves resulting from the mass of the ions and the pressure of the electrons:

$$C_s = (\gamma.k.T/m)^{1/2} \quad (1.4)$$

where  $\gamma$ ,  $k$ ,  $T$ , and  $m$  are adiabatic index, Boltzmann constant, electron temperature, and mass, respectively.

#### **Alfvén velocity ( $V_A$ )**

The Alfvén velocity is the speed of the waves resulting from the mass of the ions ( $m_i$ ) and the restoring force of the magnetic field ( $B$ ):

$$V_A = B/(4.\pi.n_i.m_i)^{1/2} \quad (1.5)$$

#### **Mach number (M)**

It is the ratio of sound speed to the flow speed ( $C_s/V$ ). It measures the compressibility of the medium.

#### **Alfvén mach number ( $M_A$ )**

It is the ratio of Alfvén speed to the flow speed ( $V_A/V$ ).

#### **Suprathermal (or high energetic) ions**

It is the term used for the particles (ions or electrons) having energies, generally for instrumental values,  $> 20$  keV.

#### **Cone angle ( $\Phi$ )**

Cone angle measures the deviation of the solar magnetic field (IMF) away from the x-axis of the horizontal plane. It gives us how much the solar wind field is radial, namely near the horizontal plane. It is measured from the x-axis to west (+y). The zero clock angle means the field do not have any component in the y-direction and mostly in the x-direction assuming the z-component is most of the time is small except the solar activity times.

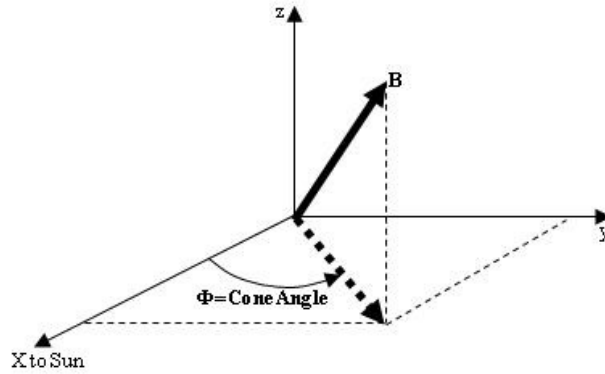


**Figure 1.9:** A schematic definition of cone angle ( $\Phi$ ) in xyz coordinate system.

### Clock angle ( $\Theta$ )

Clock angle measures the deviation of the solar magnetic field (IMF) from the horizontal plane in the cross-sectional plane. It is measured from the north and indicates how much the solar magnetic field is in the northward or southward direction.

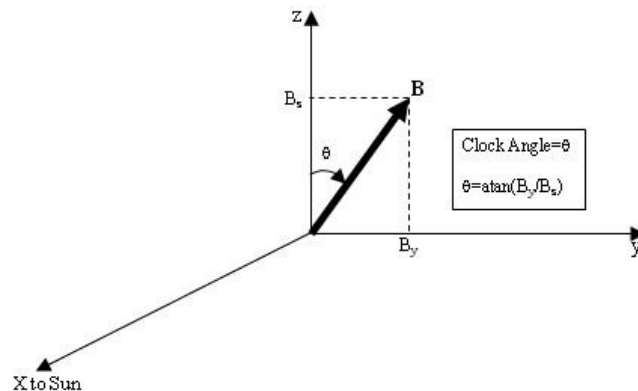


**Figure 1.10:** A schematic definition of clock angle ( $\Theta$ ) in xyz coordinate system.

### Flux

The term flux is commonly used in two ways in the various subfields of physics. In the study of transport phenomena (heat transfer, mass transfer and fluid dynamics), flux is defined as the amount that flows through a unit area per unit time. In the field of electromagnetism and mathematics, flux is usually the integral of **flux density** over a finite surface (Url-4). The result of the integration is a scalar quantity called **flux**. According to this definition, the magnetic flux is the integral of the magnetic vector field **B** (magnetic flux density) over a surface, and the electric flux is the integral of the electric vector field **E** (electric flux density) over a surface. Thus, we

can define the flux of the Poynting vector over a specified surface is the rate at which electromagnetic energy flows through that surface. It has units of watts per square metre ( $\text{W}/\text{m}^2$ ). In general integral form, the flux can be expressed mathematically as

$$\text{Flux} = \iint_S \vec{F} \cdot \hat{n} dS \quad (1.6)$$

In the case of electric field flux, this equation becomes,

$$\Phi_f = \int_s E \cdot dA \quad (1.7)$$

where:

- $E$  is a vector field of Electric Force,
- $dA$  is the vector area of the surface  $S$ , directed as the surface normal,
- $\Phi_f$  is the resulting flux.

Figure 1.11 illustrates the flux concept through an area perpendicular to the flow direction.

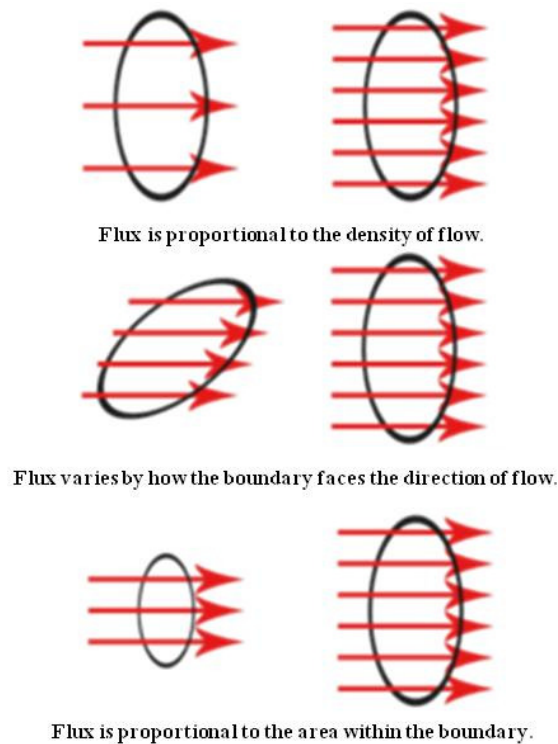


**Figure 1.11:** Schematic illustrating the flux concept. The rings show the surface boundaries. The red arrows stand for the flow of charges, fluid particles, subatomic particles, photons, etc. The number of arrows that pass through each ring is the flux (Url-4).

There are many fluxes. Each type of flux has its own distinct unit of measurement along with distinct physical constants. Nine of the most common forms of flux are given below:

1. Momentum flux, the rate of transfer of momentum across a unit area ( $\text{N}\cdot\text{s}\cdot\text{m}^{-2}\cdot\text{s}^{-1}$ ). (Newton's law of viscosity)
2. Heat flux, the rate of heat flow across a unit area ( $\text{J}\cdot\text{m}^{-2}\cdot\text{s}^{-1}$ ). This definition of heat flux fits Maxwell's original definition. (Fourier's law of conduction)
3. Diffusion flux, the rate of movement of molecules across a unit area ( $\text{mol}\cdot\text{m}^{-2}\cdot\text{s}^{-1}$ ). (Fick's law of diffusion)
4. Volumetric flux, the rate of volume flow across a unit area ( $\text{m}^3\cdot\text{m}^{-2}\cdot\text{s}^{-1}$ ). (Darcy's law of groundwater flow)
5. Mass flux, the rate of mass flow across a unit area ( $\text{kg}\cdot\text{m}^{-2}\cdot\text{s}^{-1}$ ). (Either an alternate form of Fick's law that includes the molecular mass, or an alternate form of Darcy's law that includes the density)
6. Radiative flux, the amount of energy moving in the form of photons at a certain distance from the source per steradian per second ( $\text{J}\cdot\text{m}^{-2}\cdot\text{s}^{-1}$ ). Used in astronomy to determine the magnitude and spectral class of a star. Also acts as a generalization of heat flux, which is equal to the radiative flux when restricted to the infrared spectrum.
7. Energy flux, the rate of transfer of energy through a unit area ( $\text{J}\cdot\text{m}^{-2}\cdot\text{s}^{-1}$ ). The radiative flux and heat flux are specific cases of energy flux.
8. Electric flux, the flux of electric field. It is the maximum number of electric field lines obtained due to a charged particle.
9. Magnetic flux, the flux of magnetic field. It is the maximum number of magnetic field lines passed through a unit area.

### **Electric flux**

The electric flux through a planar area is defined as the electric field times the component of the area perpendicular to the field. If the area is not planar, then the equation of the flux involves an area integral which takes the angle between the surface normal and the field vector, which is continually changing, into account.

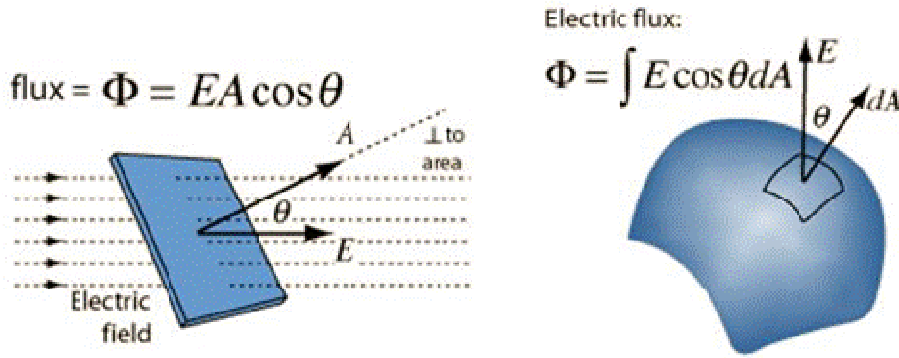


**Figure 1.12:** Illustrations of the electric flux on plane (left) and curved surface (right) (Url-4).

### Magnetic flux

Magnetic flux is the product of the average magnetic field times the perpendicular area that it penetrates ( $\Phi = B \cdot A$ ). The magnetic flux concept is illustrated in Figure 1.13 below.

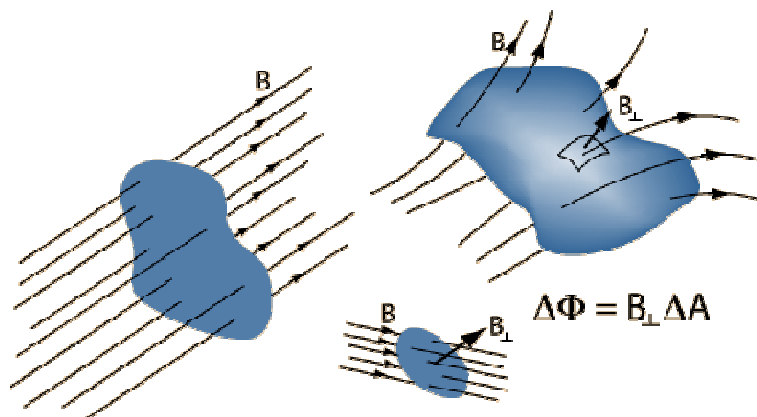


**Figure 1.13:** Illustration of the magnetic flux. The magnetic flux for a given area is equal to the area times the component of magnetic field perpendicular to the area (Url-4).

### Maxwellian speed distribution (MSD)

In the theory of an ideal gas, molecules bounce around at a variety of different velocities and do not interact with each other. It is a useful model for situations where the particle density is very low since in this case, the particles themselves are very small when compared to the space between them. The velocity distribution of these particles is given by the Maxwell Speed Distribution (MSD). It is a probability distribution describing the "spread" of these molecular speeds. The molecules are assumed to be in thermal equilibrium. It is derived, and therefore only valid, for an



ideal gas. In reality, although no gas is truly ideal, our atmosphere for example can be act like an ideal gas at standard temperature and pressure so that MSD can be used (Url-5).

The probability of a molecule having a given speed is related to the Boltzmann factor by:

$$(\text{probability of a molecule having speed } v) \propto e^{-mv_x^2/(2kT)}$$

Here,  $m$  is the mass of the molecule,  $k$  is Boltzmann's constant, and  $T$  is the temperature.

Above equation gives the probability that one component of particle's velocity  $v_x$ . In 3 dimension we need to count particles that has all possible combinations of  $v_x, v_y, v_z$  that results in  $v^2 = v_x^2 + v_y^2 + v_z^2$ . In other words, we need to sum all potential combinations of individual components in 3 dimensional velocity space. To get distribution in 3 dimension, we need to integrate above equations in  $dv_x, dv_y, dv_z$  over entire velocity space. If we picture the particles with speed  $v$  in a 3-dimensional velocity space, we can see that these particles lie on the surface of a sphere with radius  $v$ . The larger  $v$  is, the bigger the sphere, and thus the more possible velocity vectors there are. As a result, the number of possible velocity vectors for a given speed goes like the surface area of a sphere of radius  $v$ :

$$(\text{number of vectors corresponding to speed } v) \propto 4\pi v^2$$

Multiplying these two functions together gives the distribution, and normalizing it gives the MSD as shown below:

$$f(v)dv = \left(\frac{m}{2\pi kT}\right)^{3/2} \cdot 4\pi v^2 e^{-mv^2/(2kT)} dv \quad (1.8)$$

Since this formula is a normalized probability distribution, it gives the probability of a molecule having a speed between  $v$  and  $v + dv$ . The probability of a molecule having a speed between two different values  $v_0$  and  $v_1$  can be found by integrating this function with  $v_0$  and  $v_1$  as the bounds.

The average value of speed of MSD is calculated in three ways that are given below. These are the three different ways of defining the average velocity based on Maxwell

speed distribution and they are not numerically the same. Therefore, it is important to decide which of these quantities interest in our phenomena is.

- 1) By finding the maximum of the MSD (by differentiating, setting the derivative equal to zero and solving for the speed), the most probable speed ( $v_p$ ) can be found as:

$$v_p = \left( \frac{2kT}{m} \right)^{1/2} \quad (1.9)$$

- 2) The root mean square ( $v_{rms}$ ) of the speed is found by calculating the expected value of  $v^2$ :

$$v_{rms} = \left( \frac{3kT}{m} \right)^{1/2} \quad (1.10)$$

- 3) The mean value of  $v$   $\bar{v}$  from the MSD is found by:

$$\bar{v} = \left( \frac{8kT}{\pi m} \right)^{1/2} \quad (1.11)$$

Here,  $m$  is the mass of the molecule,  $k$  is Boltzmann's constant, and  $T$  is the temperature. In these relationships, it is obvious that  $v_p < \bar{v} < v_{rms}$ .

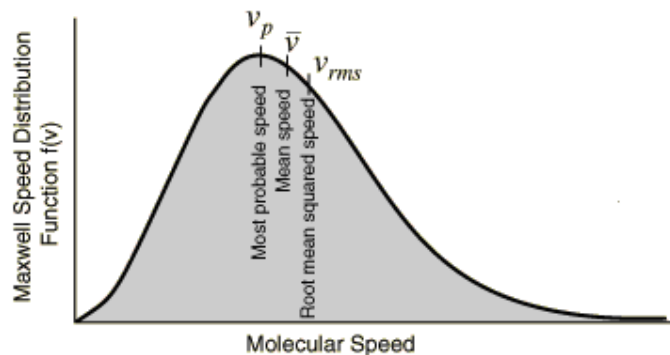


**Figure 1.14:** A diagram of MSD function versus Molecular speed. Most probable speed ( $v_p$ ), mean speed ( $\bar{v}$ ), and root mean squared speed ( $v_{rms}$ ) are given on the distribution graph (Url-5).

The important characteristics of MSD are:

- 1-) The fraction of molecules with very low or very high speeds is very small.

2-) The fraction of molecules possessing higher and higher speeds goes on increasing till it reaches a peak and then starts decreasing.

3-) The maximum fraction of molecules possess a speed, corresponding to the peak in the curve which is referred to as most probable speed.

The increase in temperature of the gas results in increase in the molecular motion. Consequently, the value of the most probable speed increases with increase in temperature. It may be noted that as long as the temperature of a gas is constant, the fraction having the speed equal to most probable speed remains the same but the molecules having this speed may not be the same. In fact, the molecules keep on changing their speed as a result of collisions.

### **Kinetic temperature**

The expression for gas pressure developed from kinetic theory relates pressure and volume to the average molecular kinetic energy. This leads to an expression for temperature known as the kinetic temperature (Url-6).

$$PV = nRT \Leftrightarrow PV = \frac{2}{3} N \left[ \frac{1}{2} mV^2 \right] \quad (1.12)$$

which leads Kinetic temperature as:

$$T = \frac{2}{3} \frac{N}{nR} \left[ \frac{1}{2} mV^2 \right] = \frac{2}{3} \frac{1}{k} \left[ \frac{1}{2} mV^2 \right] \quad (1.13)$$

The average molecular kinetic energy is expressed as:

$$KE_{avg} = \left[ \frac{1}{2} mV^2 \right] = \frac{3}{2} kT \quad (1.14)$$

## **1.7.2 Concepts**

### **1.7.2.1 Maxwell's equations**

Maxwell's equations are a set of four partial differential equations describing how the electric and magnetic fields relate to their sources. Individually, these four equations are known as Gauss's law, Gauss's law for magnetism, Faraday's law of induction,

and Ampère's law with Maxwell's correction. Together with the Lorentz force law, these equations form the foundation of classical electrodynamics, classical optics, and electric circuits. These in turn underlie the present radio-, television-, phone-, and information-technologies. Maxwell's equations are named after the Scottish physicist and mathematician James Clerk Maxwell, since they are all found in a four-part paper, *On Physical Lines of Force*, which he published between 1861 and 1862. The mathematical form of the Lorentz force law also appeared in this paper.

Conceptually, Maxwell's equations describe how electric charges and electric currents act as sources for the electric and magnetic fields. Further, it describes how a time varying electric field generates a time varying magnetic field and vice versa. (See below for a mathematical description of these laws.) Of the four equations, two of them, Gauss's law and Gauss's law for magnetism, describe how the fields emanate from charges. (For the magnetic field there is no magnetic charge and therefore magnetic fields lines neither begin nor end anywhere.) The other two equations describe how the fields 'circulate' around their respective sources; the magnetic field 'circulates' around electric currents and time varying electric field in Ampère's law with Maxwell's correction, while the electric field 'circulates' around time varying magnetic fields in Faraday's law (Url-7, Url-8).

**Table 1.1:** Maxwell's equations in microscopic form.

Name	Differential form	Integral form
Gauss's law	$\nabla \cdot \mathbf{E} = \frac{\rho}{\epsilon_0}$	$\oiint_{\partial V} \mathbf{E} \cdot d\mathbf{A} = \frac{Q(V)}{\epsilon_0}$
Gauss's law for magnetism	$\nabla \cdot \mathbf{B} = 0$	$\oiint_{\partial V} \mathbf{B} \cdot d\mathbf{A} = 0$
Maxwell–Faraday equation	$\nabla \times \mathbf{E} = -\frac{\partial \mathbf{B}}{\partial t}$	$\oint_{\partial S} \mathbf{E} \cdot d\mathbf{l} = -\frac{\partial \Phi_{B,S}}{\partial t}$
Ampère's circuital law (with Maxwell's correction)	$\nabla \times \mathbf{B} = \mu_0 \mathbf{J} + \mu_0 \epsilon_0 \frac{\partial \mathbf{E}}{\partial t}$	$\oint_{\partial S} \mathbf{B} \cdot d\mathbf{l} = \mu_0 I_S + \mu_0 \epsilon_0 \frac{\partial \Phi_{E,S}}{\partial t}$

### 1.7.2.2 Velocity moments and fluid approach

Fluid approach or Magnetohydrodynamics (MHD) approach is concerned with the collective behavior of the plasma particles. MHD is a mathematical model that describes the motion of a continuous, electrically conducting fluid in a magnetic field. In MHD, hydrodynamics and Maxwell equations coupled through Lorentz body force and Ohm's law. The velocity moments describe the macroscopic properties of the plasma like density, temperature etc.

The first 16 velocity moments of a particle distribution function give the density, velocity (3 components), the pressure (9 components), and heat flux of the distribution (Url-9). The moments themselves are given by,

$$n_i = \bar{n}_i \int f_i dv \quad \text{density} \quad (1.15)$$

$$V_i = \frac{1}{n_i} \bar{n}_i \int v f_i dv = \frac{\int v f_i dv}{\int f_i dv} \quad \text{velocity} \quad (1.16)$$

$$P_i = \bar{n}_i m_i \int (v - V_i)(v - V_i) f_i dv \quad \text{pressure} \quad (1.17)$$

$$H_i = \frac{1}{2} \bar{n}_i m_i \int v(v \cdot v) f_i dv \quad \text{heat flux} \quad (1.18)$$

The three integrals over velocity become,

$$\begin{aligned} \int dv &= \int_{\phi} d\phi \int_{\alpha} d\alpha \sin \alpha \int_{v} v^2 dv \\ &= \int_{\phi} d\phi \int_{\alpha} d\alpha \sin \alpha \int_{v} \frac{v}{m} dE \end{aligned} \quad (1.19)$$

If the distribution follows MSD, i.e. if it is Maxwellian, temperatures can be derived from the diagonal elements of the pressure tensor using the following equation,

$$p = n_i kT \quad (1.20)$$

### 1.7.2.3 Measurements of plasma macroscopic quantities

The instruments that measure the macroscopic quantities of plasma use the velocity distribution of the particles in space. For a typical energy-mass analyzer on a rotating spacecraft the calculation of the moments is done in the form of sums of instrument counts per sample ( $C_R$ ) over the three velocity -space coordinates- generally transformed into energy and two angles specifying the detector look direction (Url-9). Counts are converted to values of phase space density by,

$$\overline{n_i f_i} = \frac{C_R}{\Omega \delta t A_e v^3 \delta v} \quad (1.21)$$

where,

$\delta t$  = instrument accumulation period

$A_e$  = instrument effective area

$\Omega$  = instrument solid angle.

Defining an instrument geometric factor,  $G_F$ , as

$$G_F = \Omega A_e \left( \frac{\delta E}{E} \right)_{Inst} \quad (1.22)$$

(where,  $(\delta E/E)_{Inst}$  is the energy-dependent instrument bandpass at the energy corresponding to  $v$ , ) allows the distribution function to be expressed as,

$$\overline{n_i f_i} = \frac{m^2 C_R}{2 G_F E^2 \delta t} \quad (1.23)$$

In this expression E refers to the energy of the measured particle at the instrument aperture. In this case the moment equations become,

$$n = d\phi d\alpha \sum_E \sum_\phi \sum_\alpha C_R \frac{V_E dE}{G_F \Delta t V_{EP}^2 E} \sin \alpha \quad (1.24)$$

$$V_1 = \frac{d\phi d\alpha}{n} \sum_E \sum_\phi \sum_\alpha C_R \frac{V_E dE}{G_F \Delta t V_{EP}^2 E} \sin^2 \alpha \cos \phi \quad (1.25)$$

$$V_2 = \frac{d\phi d\alpha}{n} \sum_E \sum_\phi \sum_\alpha C_R \frac{V_E dE}{G_F \Delta t V_{EP}^2 E} \sin^2 \alpha \sin \phi \quad (1.26)$$

$$V_3 = \frac{d\phi d\alpha}{n} \sum_E \sum_\phi \sum_\alpha C_R \frac{V_E dE}{G_F \Delta t V_{EP}^2 E} \sin \alpha \cos \alpha \quad (1.27)$$

$$P_{11} = md\phi d\alpha \sum_E \sum_\phi \sum_\alpha C_R \frac{V_E dE}{G_F \Delta t V_{EP}^2 E} \sin \alpha (V_E \sin \alpha \cos \phi - V_1)^2 \quad (1.28)$$

or

$$P_{11} = -mV_1^2 + md\phi d\alpha \sum_E \sum_\phi \sum_\alpha C_R \frac{V_E dE}{G_F \Delta t V_{EP}^2 E} \sin \alpha (V_E \sin \alpha \cos \phi)^2 \quad (1.29)$$

$$P_{12} = md\phi d\alpha \sum_E \sum_\phi \sum_\alpha C_R \frac{V_E dE}{G_F \Delta t V_{EP}^2 E} \sin \alpha (V_E^2 \sin^2 \alpha \cos \phi \sin \phi - V_1 V_2) \quad (1.30)$$

or

$$P_{12} = -mV_1 V_2 + md\phi d\alpha \sum_E \sum_\phi \sum_\alpha C_R \frac{V_E dE}{G_F \Delta t V_{EP}^2 E} \sin \alpha (V_E^2 \sin^2 \alpha \cos \phi \sin \phi) \quad (1.31)$$

$$P_{13} = md\phi d\alpha \sum_E \sum_\phi \sum_\alpha C_R \frac{V_E dE}{G_F \Delta t V_{EP}^2 E} \sin \alpha (V_E^2 \cos^2 \alpha \cos \phi \sin \alpha - V_1 V_3) \quad (1.32)$$

or

$$P_{13} = -mV_1 V_3 + md\phi d\alpha \sum_E \sum_\phi \sum_\alpha C_R \frac{V_E dE}{G_F \Delta t V_{EP}^2 E} \sin \alpha (V_E^2 \cos^2 \alpha \cos \phi \sin \alpha) \quad (1.33)$$

$$P_{21} = P_{12}$$

$$p_{22} = md\phi d\alpha \sum_E \sum_\phi \sum_\alpha C_R \frac{V_E dE}{G_F \Delta t V_{EP}^2 E} \sin \alpha (V_E \sin \alpha \sin \phi - V_2)^2 \quad (1.34)$$

or

$$p_{22} = -mV_2^2 + md\phi d\alpha \sum_E \sum_\phi \sum_\alpha C_R \frac{V_E dE}{G_F \Delta t V_{EP}^2 E} \sin \alpha (V_E \sin \alpha \sin \phi)^2 \quad (1.35)$$

$$p_{23} = md\phi d\alpha \sum_E \sum_\phi \sum_\alpha C_R \frac{V_E dE}{G_F \Delta t V_{EP}^2 E} \sin \alpha (V_E^2 \cos^2 \alpha \sin \alpha \sin \phi - V_2 V_3) \quad (1.36)$$

or

$$p_{23} = -mV_2 V_3 + md\phi d\alpha \sum_E \sum_\phi \sum_\alpha C_R \frac{V_E dE}{G_F \Delta t V_{EP}^2 E} \sin \alpha (V_E^2 \cos^2 \alpha \sin \alpha \sin \phi) \quad (1.37)$$

$$P_{31} = P_{13}$$

$$P_{23} = P_{32}$$

$$p_{33} = md\phi d\alpha \sum_E \sum_\phi \sum_\alpha C_R \frac{V_E dE}{G_F \Delta t V_{EP}^2 E} \sin \alpha (V_E \cos^2 \alpha - V_3)^2 \quad (1.38)$$

or

$$p_{33} = -mV_3^2 + md\phi d\alpha \sum_E \sum_\phi \sum_\alpha C_R \frac{V_E dE}{G_F \Delta t V_{EP}^2 E} \sin \alpha (V_E \cos^2 \alpha)^2 \quad (1.39)$$

$$H_1 = \frac{1}{2} md\phi d\alpha \sum_E \sum_\phi \sum_\alpha C_R \frac{V_E^4 dE}{G_F \Delta t V_{EP}^2 E} \sin^4 \alpha \cos^3 \phi \quad (1.40)$$

$$H_2 = \frac{1}{2} md\phi d\alpha \sum_E \sum_\phi \sum_\alpha C_R \frac{V_E^4 dE}{G_F \Delta t V_{EP}^2 E} \sin^4 \alpha \sin^3 \phi \quad (1.41)$$

$$H_3 = \frac{1}{2} md\phi d\alpha \sum_E \sum_\phi \sum_\alpha C_R \frac{V_E^4 dE}{G_F \Delta t V_{EP}^2 E} \sin \alpha \cos^3 \alpha \quad (1.42)$$

where,



$$V_E = \left( \frac{2E}{m} + \frac{2e\Phi_{sc}}{m} \right)^{1/2} \quad (1.43)$$

$$V_{EP} = \left( \frac{2E}{m} \right)^{1/2} \quad (1.44)$$

and,

$V_E$  = velocity of the measured particle at the instrument aperture

$V_{EP}$  = velocity of the measured particle as it existed outside of the spacecraft sheath

$m$  = particle mass

$\Phi_{sc}$  = the spacecraft potential

$\alpha$  = polar angle with respect to the spacecraft spin axis

$\phi$  = azimuthal angle with respect to the spacecraft spin axis

$d\alpha$  = integration step size in polar angle

$d\phi$  = integration step size in azimuthal angle.

In these equations, we should note that, subject to the functional dependencies of the various instrument parameters, the order and placement of the summations can vary.

Finally, characteristic temperatures can be derived from the pressure tensor using the following equations,

$$\begin{cases} nkT_{11} = P_{11} \\ nkT_{22} = P_{22} \\ nkT_{33} = P_{33} \end{cases} \quad (1.45)$$

#### 1.7.2.4 Modeling of the plasmas

The modeling of the plasmas can be carried out in two ways:

- Analytical models
- Numerical models

### **Analytical models**

Analytical models are usually based on a higher number of assumptions. They are used mostly for one dimensional simulations and almost exclusively for the modeling of the plasma electrical properties. The most common approach in these models is to separate the discharges in three regions (two sheaths and the bulk plasma). It is the easiest and the fastest way to simulate electrical properties of discharges and in some cases have lead to excellent results (Lieberman, 1989; Kawamura et al., 1999; Haas and Braithwaite, 2000). However, the implementation of this kind of models to the rather complicated molecular gas discharges like the ones used for Plasma Enhanced Chemical Vapor Deposition (PECVD) is impractical and their use is limited to the simulation of noble gas discharges.

### **Numerical models**

Numerical models are generally more common in self - consistent plasma modeling. They can be further distinguished, according to the methodology used for the management of electron and ion transport in RF discharges, in the following categories:

- i. Kinetic Models
- ii. Fluid Models
- iii. Hybrid Kinetic/Fluid Models

#### ***i. Kinetic models:***

Kinetic models are time and spatially dependent solutions of the Boltzmann equation which produces electron and ion velocity distributions either by direct integration of the equation or by applying statistical techniques (Particle in Cell - Monte Carlo method) (Winske and Omidi, 1996). The kinetic approach although it is computationally intensive, is the least dependent on a-priori assumptions leading to more accurate results (Sommerer et al., 1991; Surendra and Graves, 1991; Yan and Goedheer, 1999).

#### ***ii. Fluid models:***

Fluid models solve moments of the Boltzmann equation in time and space, while the Electron Energy Distribution Function is calculated off-line and coupled to the fluid model providing the electron transport coefficients and the rate of electron molecule

reactions. The fluid approach, although it is not so accurate compared to kinetic methods, due to the shorter computational times, allows for higher dimensionality (2D, 3D) and for the introduction of more detailed physics to the models. However, these models are limited to gas pressures above 200 mTorr, as they assume a local equilibrium between electrons and the electric field (Bouef and Pitchford, 1995; Gogolides and Sawin, 1992; Young and Wu, 1993; Ogino, 1993; Raeder, 2003).

***iii. Hybrid models:***

Hybrid models use the kinetic approach in order to handle the non-local transport of electrons and ions in the discharges and to derive transport coefficients of charged species. The fluid approach is simultaneously applied in order to provide the density of the charged species and the electric field distribution. Hybrid models have been developed in order to simulate rather complex chemistries of gas discharges. The transport coefficients and the rate of reactions of electrons with molecules are derived kinetically, while the density of species and the time and space variation of the electric field are calculated using the fluid flow approach (Omidi et al., 2002). Nowadays, hybrid models are implemented very often especially in plasma-based applications that involve molecular gases since they combine the accuracy of kinetic models with the high dimensionality and short computational times of fluid models (Sommerer and Kushner, 1992a-b, Ventzek et al., 1995).

**1.7.2.5 Measurements in space**

The basic instruments to measure the plasma properties, i.e. density, velocity, temperature, magnetic field are magnetometers and plasma instruments. In addition to these, instruments to measure the flux of high energy particles, instruments to measure the low energy particles, electric field, spectral distribution of the particles etc. are also used on board spacecraft depending on the scientific purpose of the spacecraft. The instrumental characteristics vary according to the techniques by which they are built. In our study, spacecraft measurements from magnetometer, plasma instruments, and energetic particle flux instrument were used to study the underlying physics of the magnetosheath cavities. Some of the common, basic characteristics of the most commonly used on spacecraft are given below (Url-10).

### Spacecraft Magnetometers:

Magnetometers are one of the most widely used scientific instruments in exploratory and observation satellites. These instruments helped to discover the Van Allen radiation belts around Earth by Explorer 1; they have been used to detect the magnetic fields of the Earth, Moon, Sun, Mars, Venus and other planets. Current ongoing missions use magnetometers for the discovery of the magnetic fields of the outer planets like Saturn.

Spacecraft magnetometers basically fall into three categories: fluxgate, search-coil and ionized gas magnetometers. A main constraint on magnetometers used in space is the availability of energy and weight. The most accurate magnetometer set on spacecraft contain two separate instruments: one with a helium ionized gas magnetometer used to calibrate the second, the fluxgate instrument, for more accurate readings. Many later magnetometers contain small ring-coils oriented at  $90^\circ$  in two dimensions relative to each other forming a triaxial framework for indicating direction of magnetic field. The newest type of the magnetometer is the Obeurhauser type based on nuclear magnetic resonance technology. In Figure 1.14, a picture of fluxgate magnetometer, which is the most commonly used one on today's spacecraft, is given.

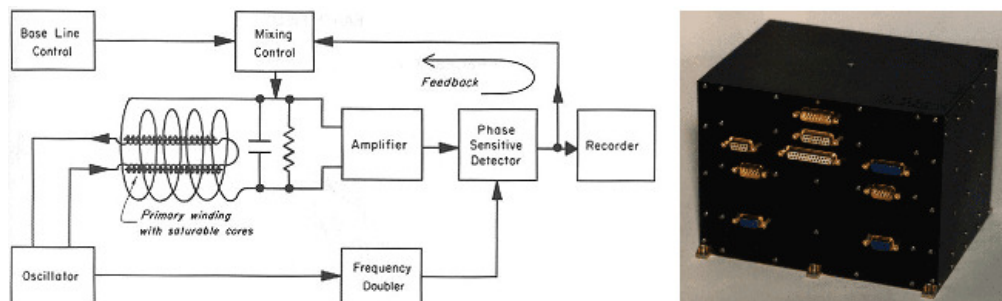


**Figure 1.15:** The electronic schematic and picture of the Mars Global Surveyor Magnetometer. The magnetometer is of type ring-coil of the 'vector' triaxial fluxgate magnetometers (Url-10).

### Plasma Instruments:

Plasma instruments are designed such that 3D distribution functions of particles in certain energy range are obtained along specific looking directions at each spin of spacecraft. From these distribution functions, velocity moments are determined, which will in turn give density, temperature and velocity components of the particles.

The characteristics of the instruments used on board Interball and Cluster spacecraft were described in their associated chapters, Chapter 3 and Chapter 4.

#### **1.7.2.6 Solar terrestrial effects**

The Sun is the energy source that powers whole heliosphere including the Earth and its atmosphere. Its effects vary from the technological aspects of our daily lives and the variations caused by the solar activity in climate of the Earth and structure of its atmosphere. Studying the Sun and Solar activity is crucial in order to understand its interaction with Earth and to maintain the life on Earth. Our magnetosphere protects us, and our atmosphere from the effects of solar activity. Our increasingly space technology dependent lives require to understand the sun and its activity and its effects on Earth in depth. The Sun sends many particles into space. When the conditions are right, some of these particles, which are highly energetic, they find their way into our atmosphere and thus change the atmospheric properties. Satellites and some of the sensitive instruments had to be turned off when such events occurred on the Sun. Otherwise, spacecraft failures, loss of attitude control of the spacecraft, instrumentals failures, malfunctioning of the sensitive instruments and communication errors with the ground stations are unavoidable. Especially, ionosphere of the Earth's atmosphere is a region where the charged particles allow long distance communication on the Earth and communication with satellites including e.g. geostationary, GPS, etc. These energetic particles from the Sun affect the ionization in the ionosphere and thus can cause unrecoverable errors in the communication and produce errors on radar systems, in navigational, defense and military systems, and result in electric grid bombardments caused by the excess of the geomagnetically induced currents (GIC) on the Earth's surface.

From these points of view, this dissertation study investigates the sources and causes of the high-energy particles in the near Earth space environment. It is the first study that emphasizes the effects of magnetosheath high-energy particles on the local motion of the magnetopause that, in turn, have consequences in the Earth's atmosphere.



## **2. ENERGETIC PARTICLES IN THE MAGNETOSHEATH**

### **2.1 Literature Survey**

High energy particles are important in the heliosphere and planetary systems as they play important role in the determination of mass, momentum, and energy transfer processes within the Sun-Earth system. The physical mechanisms behind their energization help us to understand the nature of the processes operating during the solar wind-planetary interaction in the dayside magnetosheath, elsewhere in the heliosphere, the substorms in the magnetotail, and radiation belts. While the controversy on the source of the energetic particles in the magnetosheath is still not resolved, two of the most commonly accepted views involve the bow shock accelerated energetic particles and their transmission into the magnetosheath with the solar wind flow (Gosling, J. T., 1983; Scholer, 1985; Crooker et al. 1981; Fuselier et al 1991; Chang et al., 2000; Hayosh et al., 2004) and the leakage of the energetic particles from the magnetosphere being energized through the substorms in the magnetotail (Scholer et al., 1981; Baker et al., 1988; Sibeck et al., 1987a, b; Sibeck and McEntire, 1988; Kudela et al., 1992). Many studies on the energetic particles in the magnetosheath have focus on determining their source and the nature of the energization processes.

One of the early studies on the energetic particles in the magnetosheath was carried out by Formizano et al. in 1973. Using 63 magnetosheath passes of HEOS-1 spacecraft, they tried to characterize the state of the magnetosheath under several solar wind conditions depending on the presence and absence of the upstream particles. It is the solar wind and IMF that determines most of the variability in the magnetosheath parameters. When the solar wind has low Mach number and low beta conditions, the magnetosheath is magnetically less turbulent, plasma is fluctuating and the magnetosheath velocity distribution is Maxwellian without the high energy tail. For high Mach number and beta solar wind under the absence of upstream wave conditions, the velocity distribution is seen to be none-Maxwellian with high energy tail. The magnetic field shows irregular fluctuations in both magnitude and direction

across the bow shock in this case. In the presence of the upstream waves for any Mach number and beta, the velocity distribution stays to be Maxwellian with high-energy tail. The upstream waves that are convected through and modified at the bow shock, cause the oscillations in the magnetic field.

Results of MHD and kinetic models (e.g. Thomas and Brecht, 1988) on the solar wind-magnetosphere-ionosphere interaction indicate that the suprathermal ions and waves create diamagnetic cavities in the foreshock region. These cavities are the regions where the magnetic field and density decrease from their ambient magnitudes. In the simulations, they are seen bounded by the enhanced densities and magnetic fields (Figure 2.1).

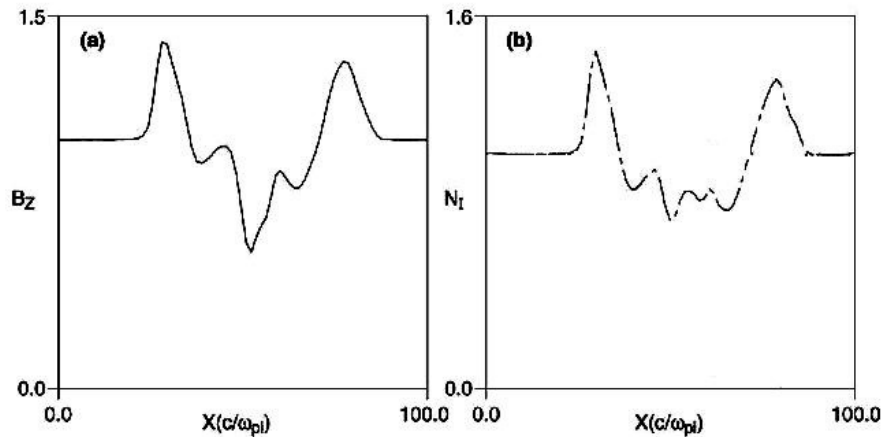


**Figure 2.1:** Results of kinetic simulation of cavities by Thomas and Brecht (1988). Diamagnetic depression regions which are the cavities and the shoulders surrounding them are seen.

Using IMP-8 observations in the upstream foreshock region, Sibeck et al. (2001) found that magnetic field and density in the cavities are inversely proportional to energetic particle counts. Figure 2.2 shows one of their events that presents the relationship between the energetic particles and density, and magnetic field from IMP-8. Enhanced energetic particle flux is clearly seen corresponding to a clear depression the magnetic field and density. Figure also shows that the cavities are surrounded by the increased density and magnetic fields. The compression owing to the energetic particles within the cavities results in these shoulder type structures. Sibeck et al. (2001) did not find any clear correlation between the velocity and the high energy particles while they see a decrease in temperature.



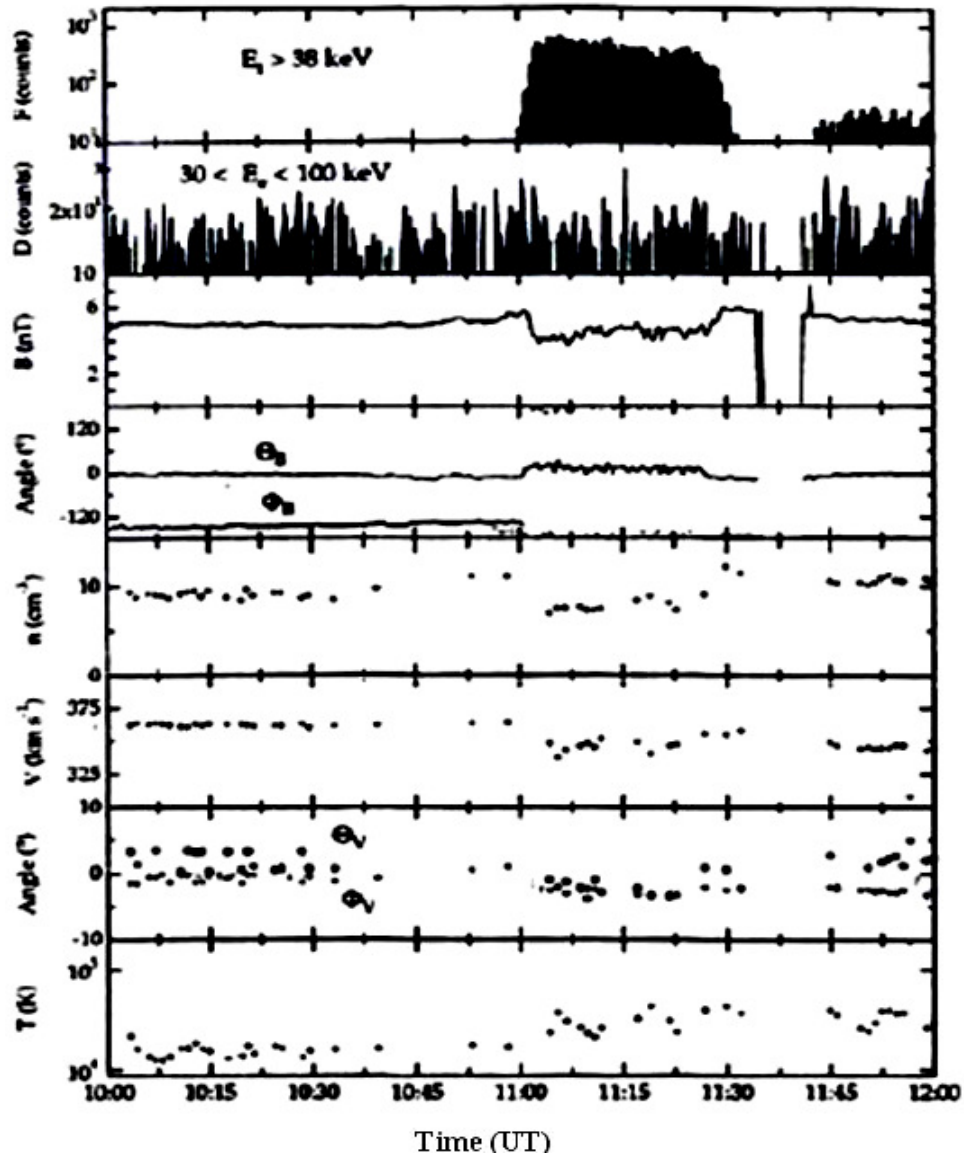


**Figure 2.2:** Example of an energetic particle event as seen by IMP-8 in the foreshock region. From top to bottom, energetic particle counts, magnetic field magnitude, magnetic field angles ( $\theta_B$ ,  $\Phi_B$ ), density, velocity magnitude, velocity angles, and temperature versus time (Sibeck, 2001).

The foreshock cavities observed by Sibeck et al. (2001) occur on bundles of interplanetary magnetic field (IMF) lines connected to the bow shock. They are seen most frequently upstream from the pre-noon bow shock during the high speed solar wind streams (Figure 2.3) and have durations that typically range from 1 to 10 min. The backstreaming suprathermal ions are thermalized and energized at the bow shock. They supply the pressure needed to inflate the cavities. As the cavities expand, the excavated densities and magnetic field strengths appear as enhancements

bounding the foreshock cavities. The study of Sibeck et al. (2001) suggests that these cavities are transferred into the magnetosheath along with the solar wind plasma. Thus the pressure variations caused by these diamagnetic cavities at the foreshock modify the solar wind-magnetosphere interaction at the magnetopause boundary layer through the magnetosheath. One of the implications of the foreshock cavities on the magnetopause boundary is illustrated in Figure 2.3 showing the magnetopause moving outward away from the Earth in response to the decreased pressure within the foreshock cavity. Another effect of the foreshock cavities suggested by Sibeck et al (2001) is on the field-aligned currents that connect the high latitude ionosphere to the magnetopause. The pressure variations at the magnetopause, thus, can modulate the field-aligned currents flowing into the high latitude ionosphere, which in turn modify the ionospheric currents and heat energy input.

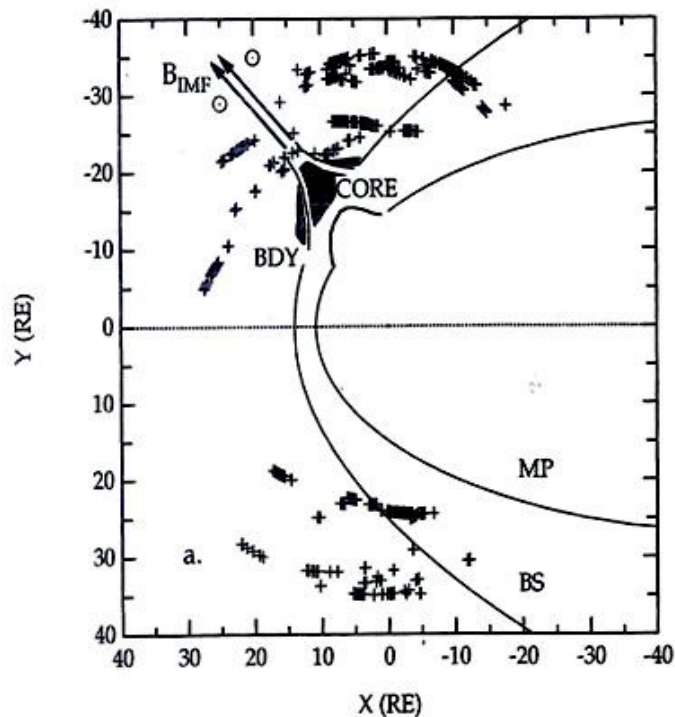


**Figure 2.3:** Average locations of diamagnetic cavities observed by IMP-8 in XY-plane. Figure also illustrates how the magnetopause boundary can move outward in response to the foreshock cavities occurring in the front of the bow shock (Sibeck et al., 2001).

These results from IMP-8 observations confirmed the predictions of kinetic simulations on the evolution of the diamagnetic cavities by Thomas and Brecht (1988). The simulations of the interaction between the solar wind and the

counterstreaming ion beams show that crater like structures like foreshock cavities and hot flow anomalies (HFAs) are created by depressed magnetic field and the solar wind density bounded by enhanced edges. These ion beams create Alfvén waves which have large amount of the energy that heats the plasma that are seen in within the foreshock cavities. Some of the signatures observed within the foreshock cavities are also found in the hot flow anomalies (HFAs) which are examined in detail by Sibeck et al. (1999) and in the depressed densities of the cavitons seen in the upstream solar wind (Blanco et al., 2009). HFAs are very similar to the foreshock cavities but they have great enhanced temperature (up to several ten million Kelvin). Contrary to the foreshock cavities, HFAs can be identified as regions of large deflection of solar wind flow transverse to the Sun-Earth line and decreasing speeds (Sibeck et al 2001; Omid and Sibeck, 2007).

In a later study employing Wind observations, Sibeck et al. (2002) compared characteristics of the foreshock cavities with those of hot flow anomalies and discussed the differences between the hot flow anomalies and foreshock cavities. Figure 2.4 from Sibeck et al. (2002) shows phase space density traces of Wind 3DP during 30 min period from 20:00 to 20:30 UT on April 19, 1996. Panel (a) and (b) give PESA-H observations from 1.9 to 27 keV and SST ion observations from 70 to 4440, respectively. Figure 2.5 presents the corresponding plasma and magnetic field observations for the same period. As seen in figures, Wind observes two crater-like structures in IMF strength and solar wind density: one between 20:11 and 20:17 UT and the other with a shorter duration between 20:26 and 20:28 UT. They found decreases in flow velocity within the foreshock cavities, large amplitude plasma and magnetic field variations with increased fluxes of suprathermal ions, no associations with abrupt IMF discontinuities and modest increases in ion temperature. These distinguish foreshock cavities from hot flow anomalies.

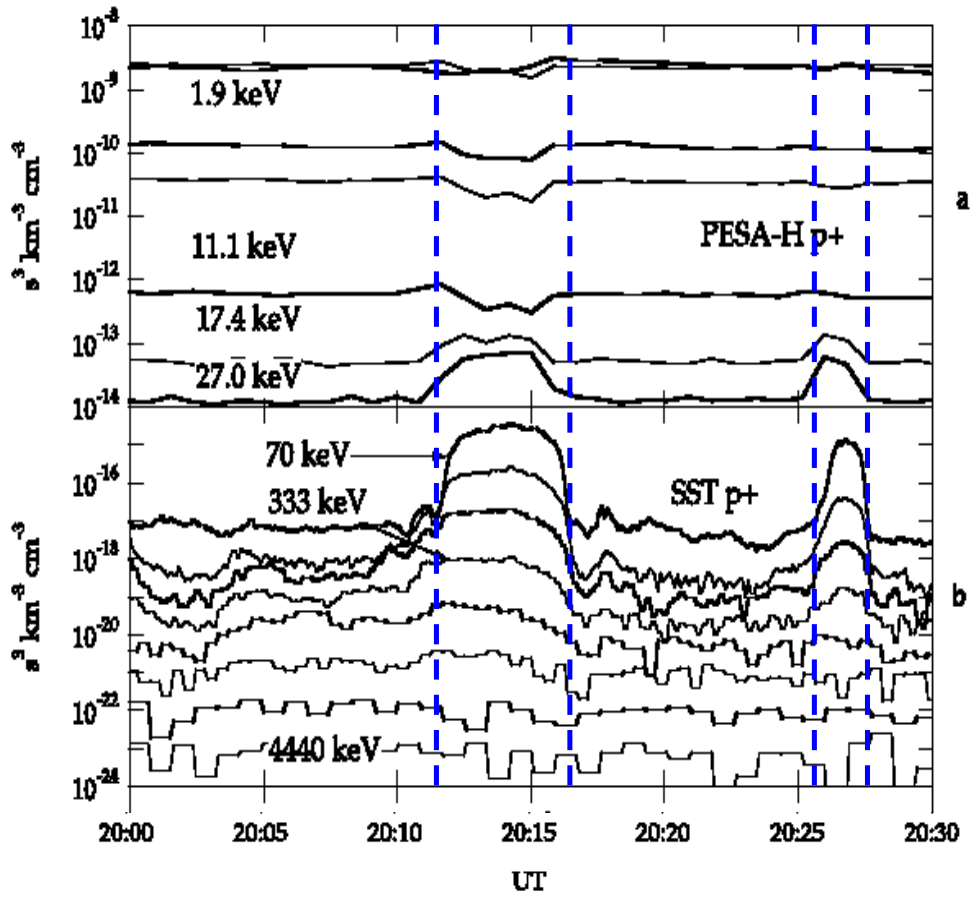


**Figure 2.4:** Wind 3DP phase space densities versus time from 20:00 to 20:30 UT in April 19, 1996. From top to bottom: (a) PESA-H observations from 1.9 to 27.0 keV, (b) SST ion observations from 70 to 4440 keV (Sibeck et al., 2002).

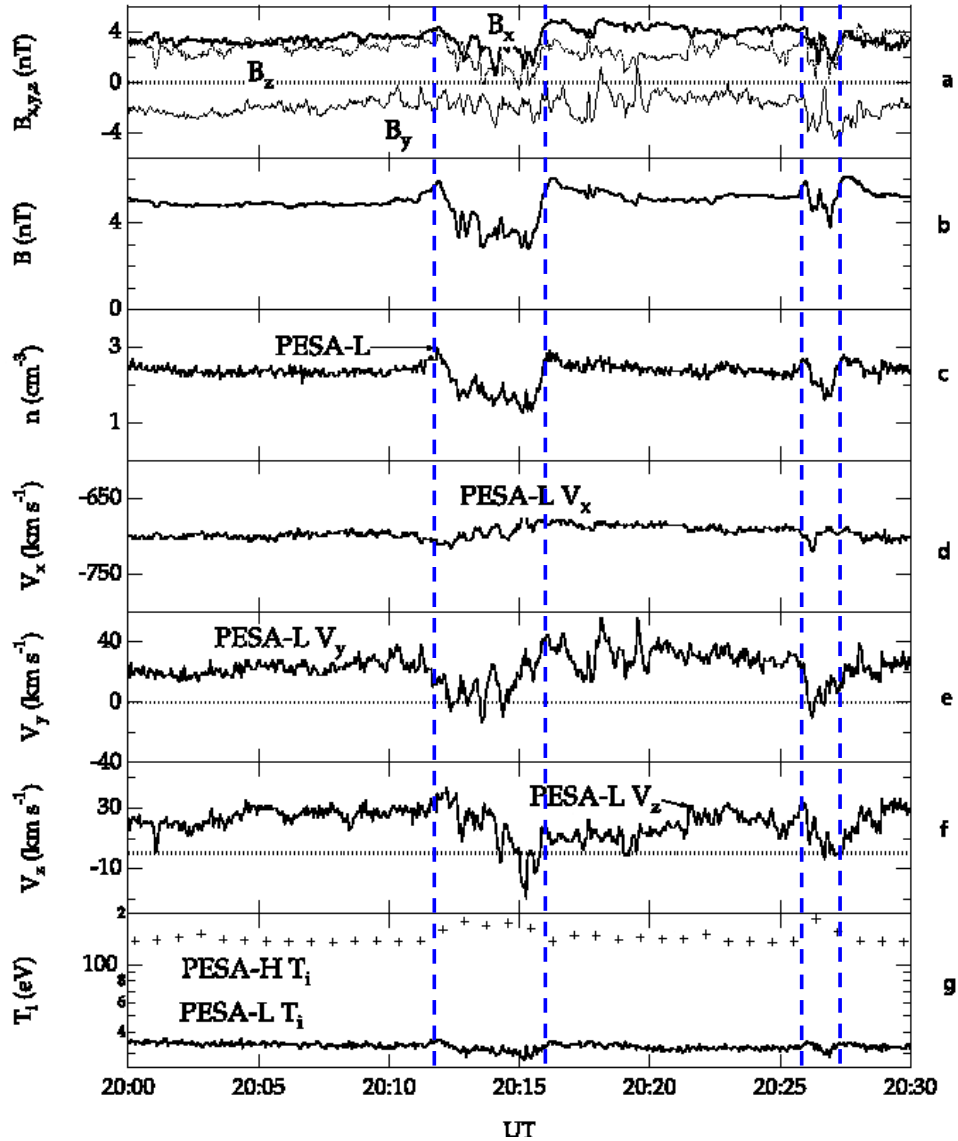


**Figure 2.5:** Wind 3DP plasma and magnetic field parameters versus time. From top to bottom, the panels show (a) three components of magnetic field, (b) total magnetic field strength, (c) core solar wind densities measured by PESA-L, (d-f) x, y, and z components of solar wind flow velocity, (g) core solar wind (measured by PESA-L) and suprathermal (measured by PESA-H) total temperatures. The magnetic field components are in GSE coordinates (Sibeck et al., 2002).

Although the ion temperature measured by the cold plasma portion of the plasma instrument decreases in the cavity, most likely as a result of the near-adiabatic expansion, the overall temperature calculated by incorporating the suprathermal ions actually increases. This helps to explain the previous IMP-8 findings indicating temperature decreases in foreshock cavities. The IMP-8 instrument MIT plasma detector only measures ions with energies below 7 keV and therefore misses the

suprathermal ions that can make a significant contribution to the temperature and pressure within the cavities.

Omidi (personal communication, 2009) and Sibeck et al. (2008) recently simulated the interaction of the energetic particles with the ambient solar wind in the foreshock region using 2.5-D global hybrid model and found events with foreshock cavity characteristics (Figure 2.6). Omidi (personal communication, 2009) inspected the response of the magnetosheath plasma and magnetic field to the presence of energetic particles. He predicted that the magnetic field decreases while the density increases in the presence of energetic particles, a prediction that has not yet been confirmed or denied previously by magnetosheath observations, one of the primary purposes of this study.

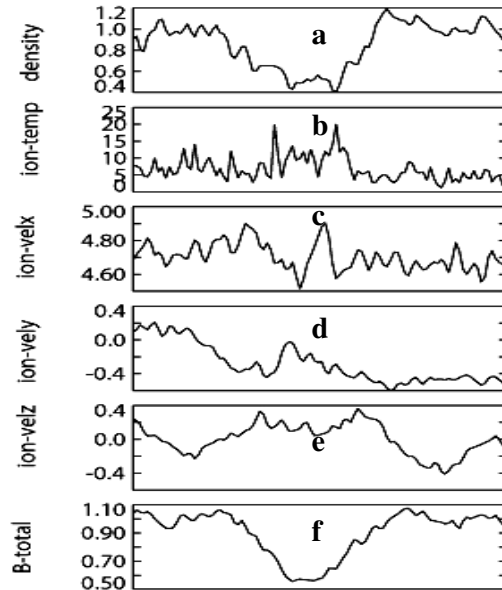


**Figure 2.6:** Simulations of foreshock region using 2.5-D global hybrid model. From top to bottom: (a) ion density, (b) ion temperature, (c), (d), (e) X, Y, Z components of ion velocity, and (f) total magnetic field (Omidi, 2009).

Sibeck et al.'s study (2001) raises questions concerning how foreshock cavities evolve and whether they are swept antisunward into the magnetosheath with the solar wind flow. Turk et al. (2003) used four years of Interball-1 observations at 2 minutes time resolution to address this question. They inspected magnetic field (MFI), plasma (CORALL), and proton energy flux (DOK-2) data in the energy range from 22 keV to 28 keV. Their search did not reveal a clear relationship between high energy particle fluxes and magnetosheath parameters. DOK-2 frequently recorded prolonged

particle flux enhancements but not isolated particle flux bursts. Nevertheless, they identified three types of magnetosheath behavior in response to high energy particles. Depressed magnetic field strengths and densities accompanied enhanced high energy particle fluxes in one type, similar to foreshock cavities. However, a second type exhibited enhanced densities and depressed magnetic fields. They concluded that a clear, definite relationship between energetic particles and magnetosheath parameters is hard to detect in Interball-1 data. Low interaction potential between the magnetosheath parameters and the energetic particles might depend on the low energy ranges of energetic particle fluxes that instrument observes and the long time criterion for the selection of energetic particle events..

## **2.2 Purpose of the Dissertation**

The main purpose of our study is to investigate the effects of energetic particles on the natural state of the magnetosheath plasma and magnetic field, and their possible consequences on the magnetosphere by taking the advantage of the latest available spacecraft data measured using the on-board high-tech instruments. Another important purpose of our study is to compare the results from the global hybrid simulations with those of observations. The differences or the similarities with the simulation results will help us to understand the physical mechanisms on the occurrence of the magnetosheath cavities, on their variations, and on the factors/conditions that they depend on. Thus, both the results of the observational analysis and the simulations will refine the proposed implications of the previous studies given above, e.g. whether the foreshock cavities are carried into the magnetosheath, and whether the proposed effects of the cavities on the magnetopause are observed, and, if so, how much etc. are some of those.

This study is the first to demonstrate that there is a clear, distinct identifiable effect between the high energy particles and the magnetosheath parameters. It is shown that magnetosheath cavities are seen as a result of the interaction between the energetic particles and the magnetosheath field and the plasma. The 2.5-D kinetic hybrid model results, which we used in our study, to simulate the formation and effects of the cavities have shown that they occur under the especially radial IMF conditions in the magnetosheath. In the simulations, clear indications that the cavities are propagated from the solar wind into the magnetosheath have been demonstrated. In

our study, we further show that the magnetosheath cavities affect the local magnetopause position.

In this thesis, Chapter 3, 4 and Chapter 5 present the results from the search using INTERBALL and CLUSTER spacecraft observations in the magnetosheath respectively. A systematic search on the existence of the magnetosheath cavities and a thorough analysis of both case examples and statistical events obtained in approximately two years time interval from each spacecraft were carried out in these chapters. Chapter 6 describes the simulation results from the global hybrid model run for different IMF conditions and compares the results with those obtained from the spacecraft observations. The final chapter, Chapter 7 summarizes our findings and concludes the thesis study.



### **3. RESULTS FROM INTERBALL SPACECRAFT DATA**

#### **3.1 Interball Spacecraft, Instruments, and Data**

Interball-1 is the major part of multi-national project of INTERBALL and one of two pairs (satellite-subsatellite) of satellites orbiting in the Earth's magnetosphere. The multi-national project consists of four spacecraft: two main spacecraft (Prognoz), made in Russia, and two small subsatellites (Magion) of main spacecraft made in Czechoslovakia. Interball-1 (Tail probe) comprises a main Prognoz satellite and a subsatellite called Magion-4. The main objective of Tail Probe of Interball-1 is to study how the solar wind energy is carried into the Earth's magnetosphere, ionosphere, and atmosphere during magnetic substorms. This probe has an elongated elliptical orbit with inclination  $63^\circ$  scanning high altitude cusp, subsolar magnetopause, and the neutral sheet in the nightside. Its perigee and apogee are about 800 km and 193 000 km. One orbit takes about a period of 92 hours and inclination of  $62.8^\circ$  (Zelenyi et al., 1997). As we do not use data from the subsatellite Magion-4, we drop the label "1" from the name of the Interball-1 and call it plainly as Interball throughout this study.

Interball spacecraft provides the magnetic field, plasma (velocity, density, and temperature) energetic particle spectrum to study the physical mechanisms for the transmission of solar wind energy to the Earth's magnetosphere. Although the spacecraft stays in the magnetotail for long time periods (about half of a year), the data that the spacecraft provides from the bow shock and dayside magnetosheath enables scientist to study. Figure 3.1 illustrates the different phases of the spacecraft in different magnetospheric regions.

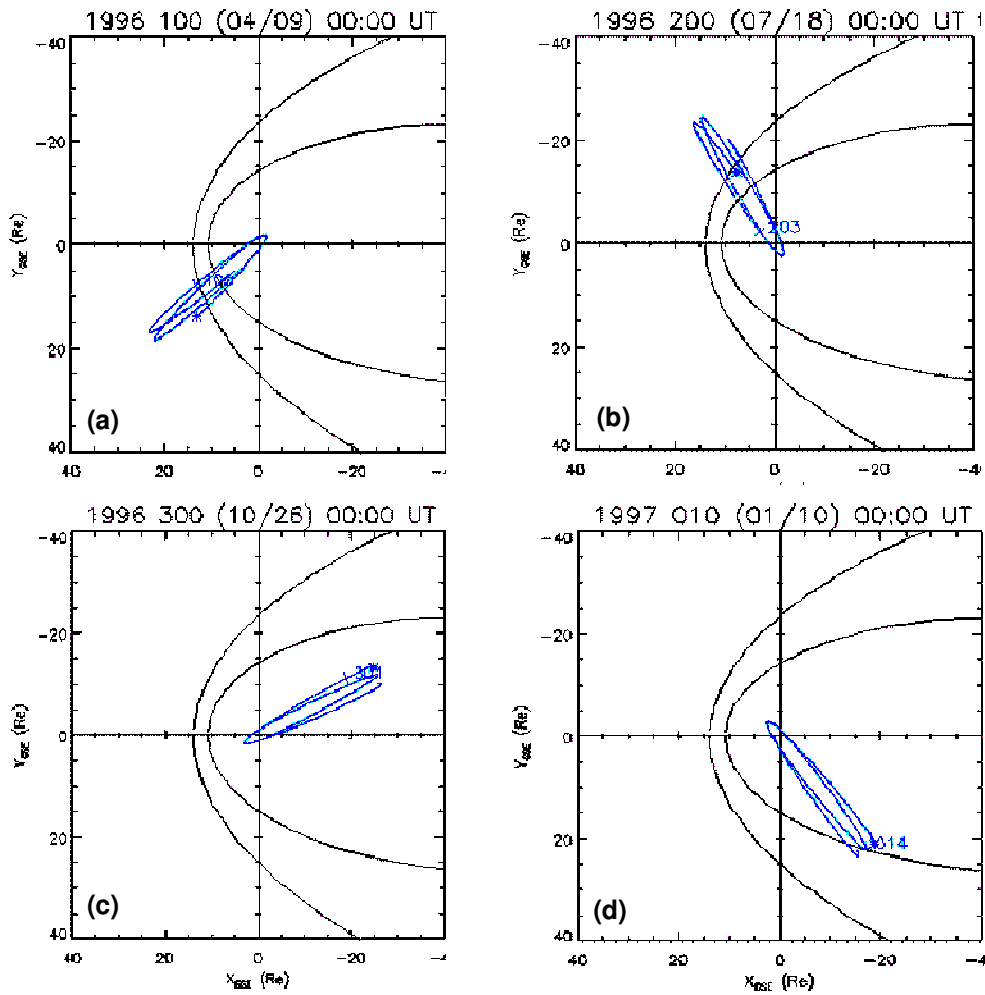


**Figure 3.1:** 7-day examples (approximately two orbital periods) of Interball spacecraft trajectory in different months of 1996 scanning different regions of the magnetosphere, magnetosheath and solar wind. Plots from SSCWeb are given in the XY-plane for (a) April 1996, (b) July 1996, (c) October 1996, and (d) January 1997. The Sun and the Earth are located at the left of each plot.

The instruments carried on board Interball spacecraft and their characteristic features are given in Table 3.1.

**Table 3.1:** Instruments carried on Interball spacecraft and their characteristics.

<b>Instrument Name</b>	<b>Measured Quantity</b>	<b>Characteristics/Limits etc.</b>
<b>MIF-M/PRAM</b>	GSE and GSM Magnetic Field Vector	2 min Resolution
<b>CORALL</b>	Ion Density, GSE and GSM velocity vector, temperature 0.025-25 keV. Particles with energy range 30-24200 eV per charge (30-2420 eV/q) at 32 energy steps	Works only when spacecraft enters the magnetosheath 1 Spin resolution
<b>AKR</b>	Radiointensity flux in the ranges 100, 252, 500 kHz	2 min resolution
<b>ELECTRON</b>	Electron density, mean energy in the range 0.01-30 keV	2 min resolution
<b>DOK-2 and SKA-2</b>	Electron Fluxes in 21- 26, 76-95, 150-500 keV Proton Fluxes in 22-28, 1000-3000 keV	2 min resolution
<b>PROMICS</b>	Counts of H <sup>+</sup> and O <sup>+</sup> ions, 1.0-30 keV	Three directions 1 Spin
<b>VDP</b>	Antisunward Ion Flux	2 min resolution Measurements are stop at the magnetopause.

The instruments highlighted with blue in Table 3.1 were used in this study. The key instrument in our analysis is DOK-2 energetic particle spectrometer that measures the energetic particle flux data in the magnetosheath. On this instrument, the first proton and electron sensors are offset at an angle 180° with respect to the spacecraft X axis (look antisunward). Second sensors are not operational since November 1, 1995 and this sensor is permanently offset at an angle 62°. The instrument provides

energetic ion fluxes in the range of 21–28 keV, 22-27 keV and above 1 keV. In our study, we use the energy range of 21-28 keV.

The raw data, we used in this study, from MIF\_M/PRAM and DOK-2 instruments on board are collected in a higher resolution (3 sec) by Prof. Kudela and his group in Slovak Academy of Science, but all the parameters are computed on the ground and shared with the public as 2 min averages. UT time scale with the 2 min step is used for all key parameters except PROMICS and CORALL instruments. Parameters are averaged in the 2 minutes intervals centered on the round odd minutes. Ion key parameters (PROMICS and CORALL data) are given once per spacecraft spin period (approximately 117-118 s).

Antisunward ion flux is measured by the sunward-looking Faraday cup of the VDP experiment. Only positive values of the measured charged flux (ion flux in the solar wind and magnetosheath) are included in this dataset. Effects caused by the spacecraft-plasma interaction (influence of floating potential, interferences in the wave data, etc) are not corrected (URL-11).

Using DOK-2 data, we visually scanned proton flux data for two years from 1996 to 1998 on the NASA's CDAWeb web page. We used particle flux that falls in the energy channel of 22-28 keV from DOK-2 instrument and searched for the intervals when the flux of the protons within this energy range exceeds a certain threshold. Based on 3-year search, we established the following criteria to identify the high flux events. These criteria are:

- The flux of energetic protons in 22-28 keV range exceeds 100 #/ (cm<sup>2</sup>.s.keV.st).
- Each high flux event lasts at least 10 minutes.

The flux is measured in #/ (cm<sup>2</sup>.s.keV.st). For simplicity, throughout this study, we will use PFU as proton flux unit corresponding #/ (cm<sup>2</sup>.s.keV.st).

For plasma measurements, i.e. density, velocity and temperature, we used Wide Range 3-D Ion spectrometer (CORALL). The CORALL instrument is designed to measure the magnetospheric plasma. It gives 3D ion spectra with azimuthal step 11° in 5 directions (Yermolaev, 1997). The moments, then, are calculated to obtain density, velocity and temperature for protons and electrons.

The magnetic field on INTERBALL spacecraft is measured by Multicomponent Investigations of Fluctuations of Magnetic Fields (MIF-M/PRAM) instrument magnetic field and its components. The time resolution of all parameters available on the CDAWeb is 2 minutes.

In order to investigate the dependence on the solar wind plasma and IMF, WIND spacecraft at L1 point was used together with Interball. From WIND spacecraft we used Magnetic Field Investigation (MFI) instrument for the magnetic field strength and its components, and the Solar Wind Experiment (SWE) instrument for solar wind plasma. Interball data in the magnetosheath have been delayed to account for the solar wind time from WIND at L1 to Interball in the magnetosheath, using the concurrent solar wind speed measurements from WIND.

In this part of the study with Interball spacecraft, we searched for the times of the high flux of energetic particles within the 22-28 keV energy range measured by DOK-2 instrument during a magnetosheath passage of Interball spacecraft. In 3 years, we found 51 magnetosheath passes (Cases) that satisfy both criteria mentioned above. The flux in the magnetosheath varies. One magnetosheath pass (or one case) can comprise several flux events, i.e. events with flux higher than 100 PFU. The intervals that do not satisfy both threshold conditions were excluded from the analysis. This gave us 51 cases. Figure 3.2 illustrates the orbits belong to our cases in the magnetosheath. An example of high flux of energetic particle case is also presented in Figure 3.3.

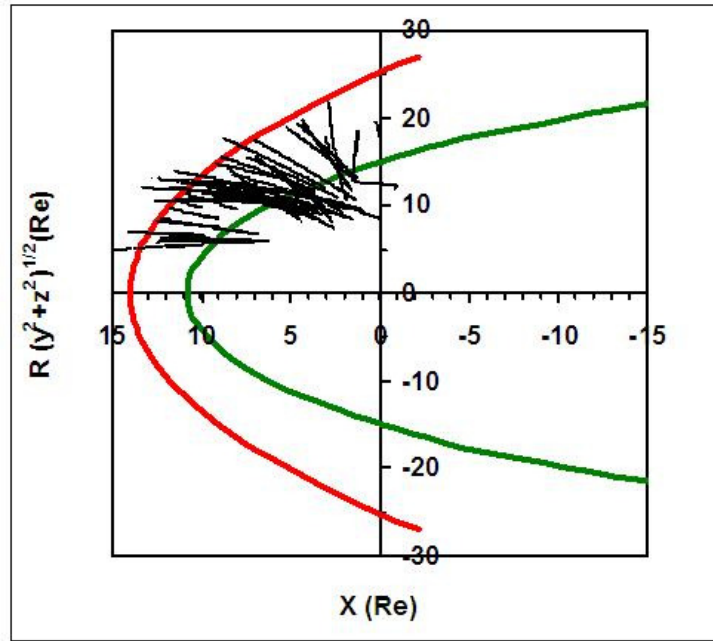


**Figure 3.2:** An illustration for the orbits for 51 magnetosheath cases in XR-plane.

Figure 3.3 is an example out of 51 magnetosheath crossings that satisfy the flux criteria. From top to bottom, it gives the magnetic field from MIF-M/PRAM, density from CORALL, and energetic proton flux (EPI) from DOK-2 for May 12, 1998. The data resolution is 2 minutes. The red line at 05:30 UT and green line at 10:12 UT show the bow shock and the magnetopause respectively. The black dashed line in lowermost panel indicates the threshold level for proton flux at 100 PFU. The trajectory of Interball for this crossing is given in the XZ- (left) and XR- (right) planes in the Figure 3.4. We can see several intervals in which the energetic particle flux exceeds the threshold, 100 PFU. These magnetosheath intervals are indicated in purple boxes on the bottom panel of Figure 3.3. In this example, there are four events starting at 05:45 UT, 07:15 UT, 09:00 UT, and at 09:45 UT used in this study as events and satisfied both criteria. The fourth event seen near the magnetopause extends well into the Earth's magnetosphere and represents the one excluded from our analysis.

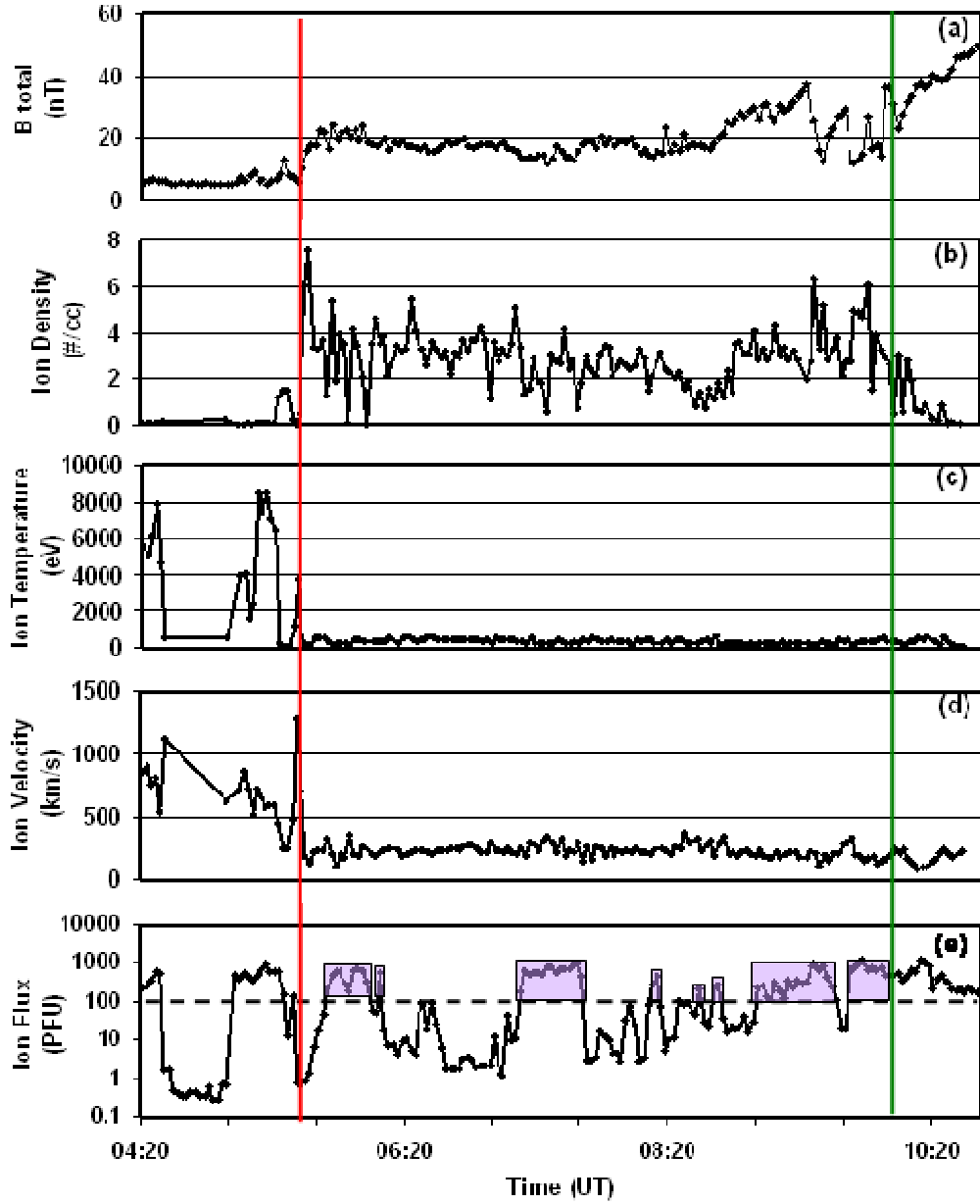


**Figure 3.3:** An example of a magnetosheath crossing of Interball spacecraft on May 12, 1998. The panels from top to bottom give (a) total magnetic field, (b) ion density, (c) ion temperature, (d) ion velocity, and (e) ion flux observed 2 minutes resolution.

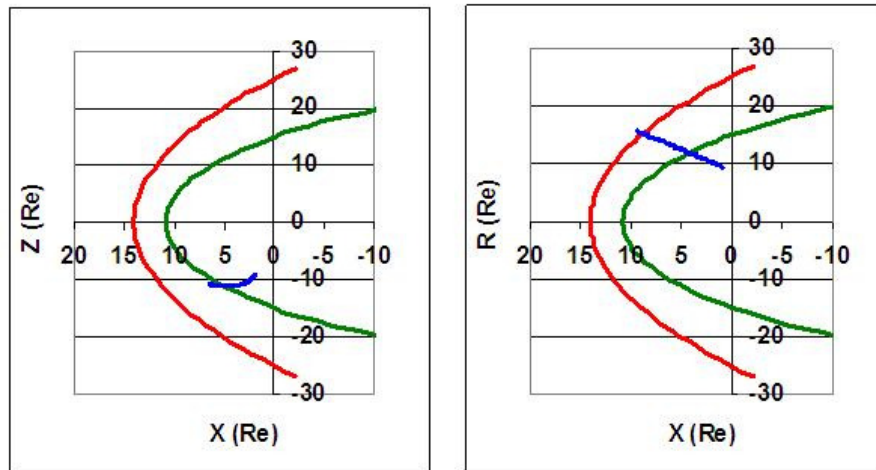


**Figure 3.4:** The trajectory of Interball spacecraft for the magnetosheath crossing in XZ- (left) and XR- (right) planes in May 12, 1998.

After determining the high flux events, we then determined the signatures in the magnetosheath magnetic field and density that correspond to the increases in the high energy particle flux levels. In Figure 3.3, for example, we notice that in three events (except first event), there is a clear decrease in total magnetic field and increase in ion density corresponding to the increased high flux levels. The classification of these signatures seen in the magnetic field and density results in 4 types of distinct structures in the magnetosheath in the presence of high energy particles; Type-1, Type-2, Type-3 and Type-4. In Type-1, the magnetic field increases and density decreases simultaneously as response to the high energy particles while both magnetic field and density show decreases in Type-2. Type-3 consists of the cases with decreased magnetic field and increased densities and the last group, Type-4 represents the cases with increased magnetic field and density. Among these types, Type-2 is seen only in 19 cases out of 51 cases and thus occurs only 16% of the time. The occurrence rates of the other types, Type-1, Type-3 and Type-4, are 37%, 22%, and 25% respectively. Table 3.2 presents the characteristics of these different types found in Interball data.

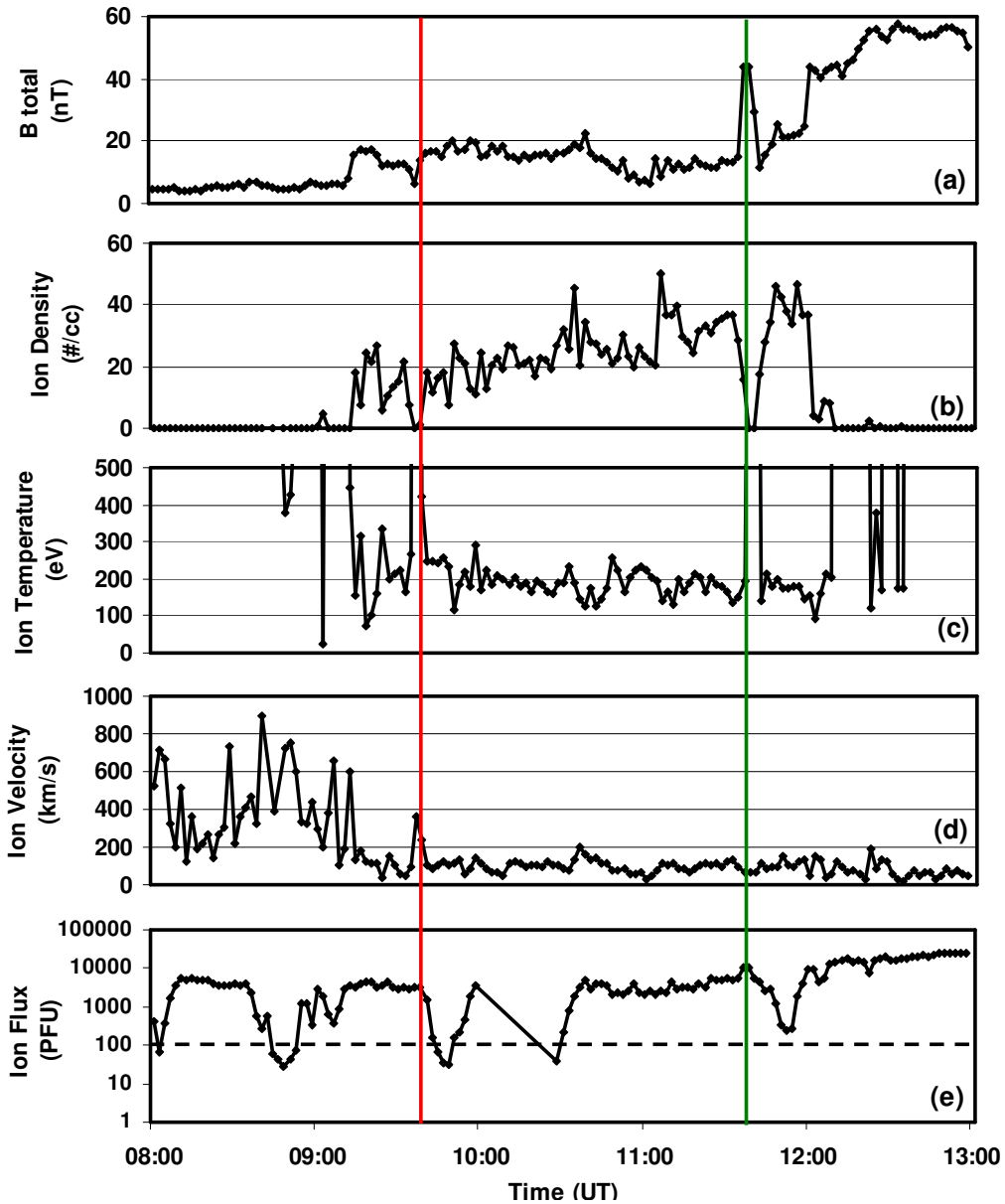


**Table 3.2:** Types of the structures seen in Interball magnetosheath data accompanying the high energy particles.

<b>Type</b>	<b>Bt (nT)</b>	<b>Ni (#/cc)</b>	<b>Number (#)</b>
<b>Type-1</b>	↑	↓	<b>19</b>
<b>Type-2</b>	↓	↓	<b>8</b>
<b>Type-3</b>	↓	↑	<b>11</b>
<b>Type-4</b>	↑	↑	<b>13</b>

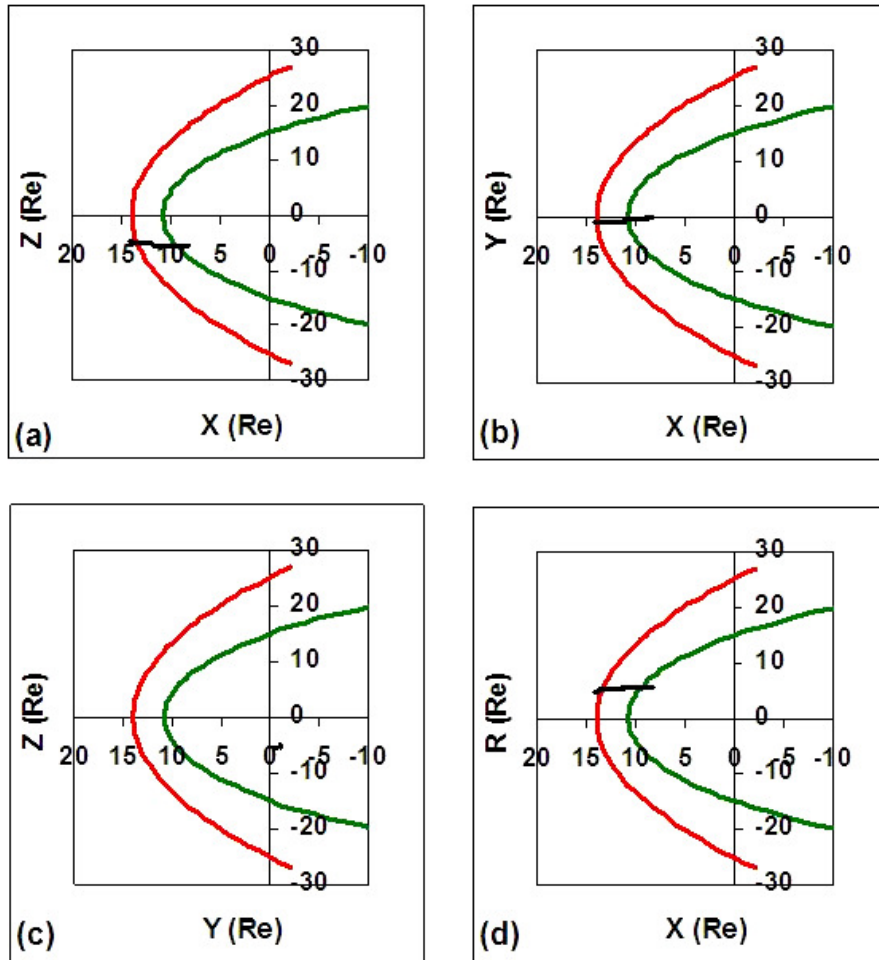
These statistics obtained using Interball data indicate that the foreshock alike cavities, Type-2, in which both the magnetic field and density decreases when the flux of the high energy particles increases, are very rare in the magnetosheath. The most commonly seen structures as response to the presence of energetic particles in the magnetosheath appears to be Type-1.

Figure 3.5 is an example of Type-1 that shows the increasing magnetosheath magnetic field and decreasing density as the flux of energetic particles increase in the magnetosheath.



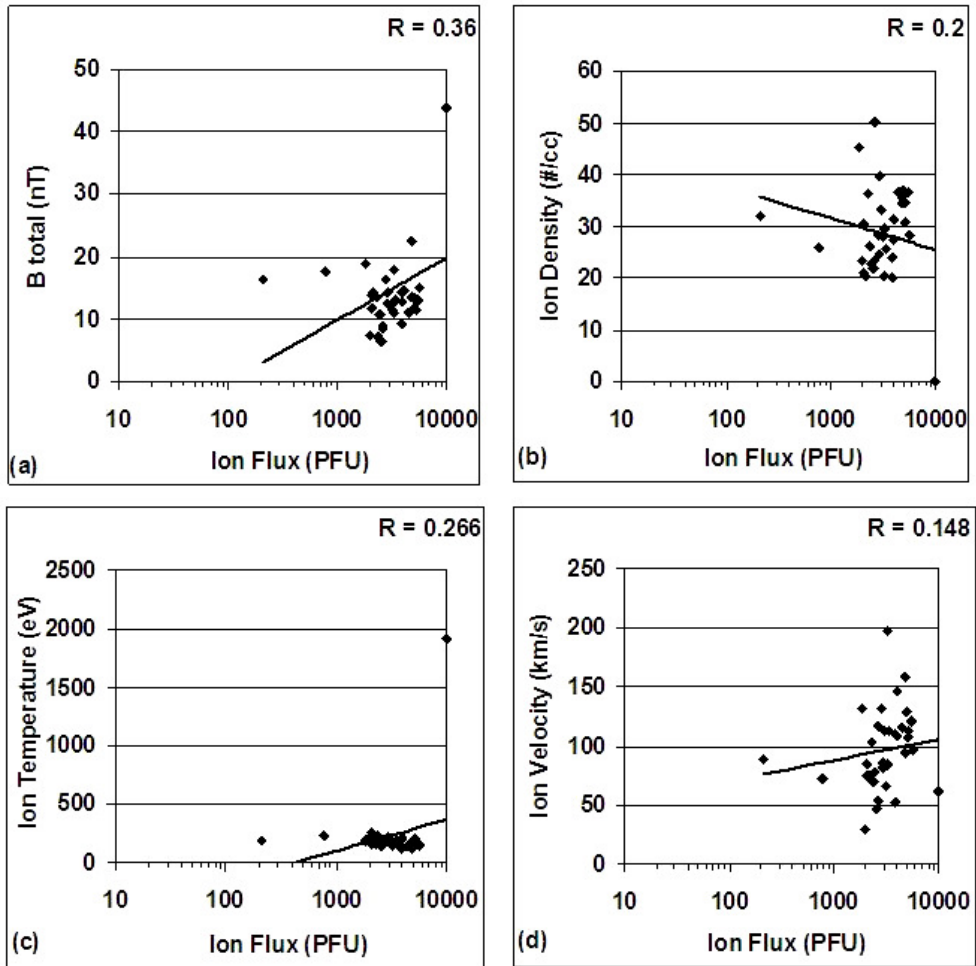
**Figure 3.5:** Type-1 example of Interball in June 1, 1996. The panels from top to bottom are (a) total magnetic field, (b) ion density, (c) ion temperature, (d) ion velocity, and (e) ion flux.

The trajectory of Interball for this magnetosheath crossing in June 1, 1996 is given in Figure 3.6. The red line at 09:37 UT and the green line at 11:39 UT indicate the bow shock and the magnetopause respectively. In this magnetosheath crossing, there is only one event starting at 10:30 UT and satisfying both time duration and flux level criteria.



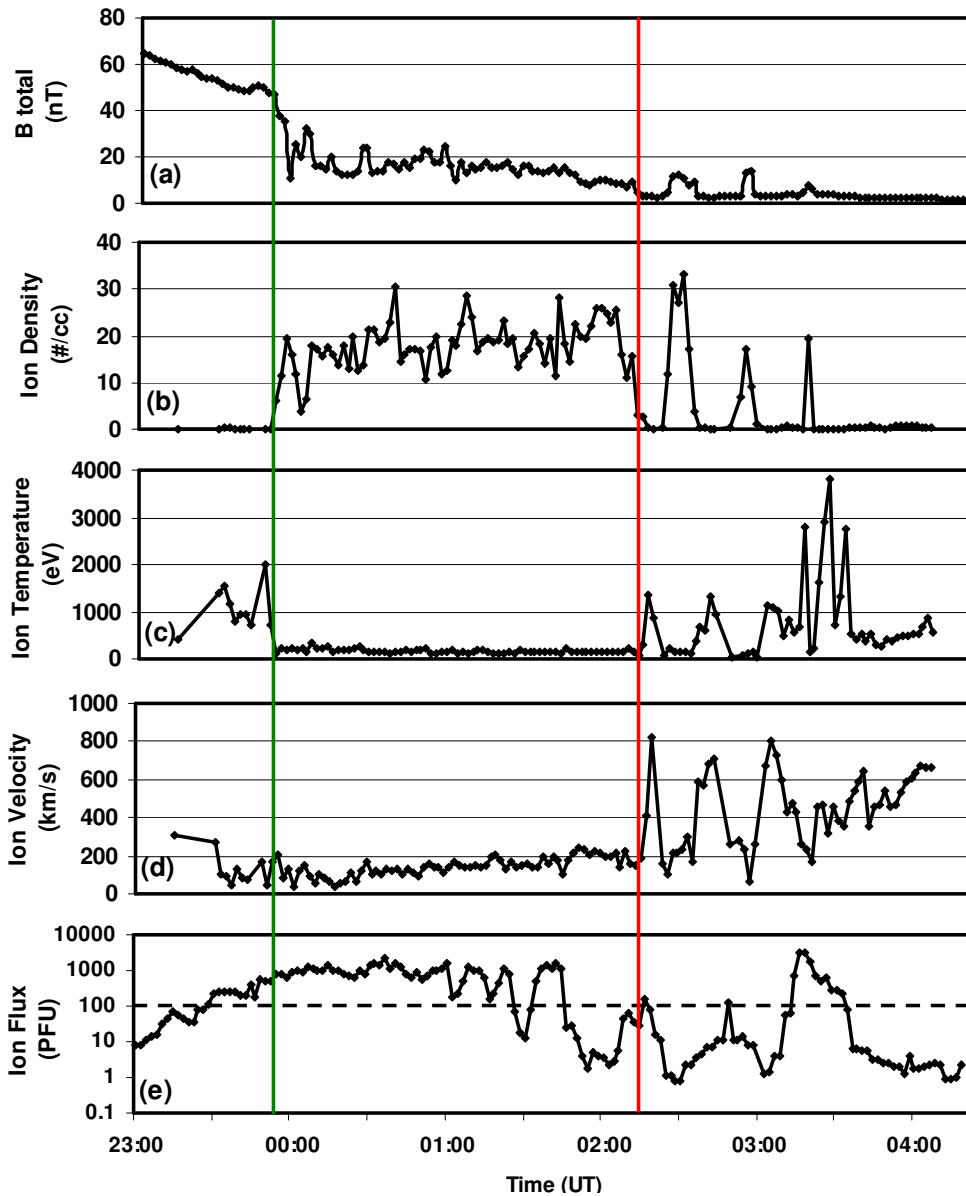
**Figure 3.6:** Trajectory of Interball spacecraft in (a) XZ-, (b) XY-, (c) YZ-, and (d) XR- planes for June 1, 1996 corresponding to the case in Figure 3.5.

Figure 3.7 gives the scatter plots of total magnetic field (a), ion density (b), ion temperature (c), and ion velocity (d) for this event. The correlation coefficients are shown on the right corner of each panel. Although the scatter is high, a line is fitted to the data in all panels. Fitted line roughly indicates a possible linear relationship between the increasing energetic particle flux and magnetic field, density, velocity and temperature. An increase in magnetic field and a decrease in density corresponding to high energetic particle flux can be noticed. Ion temperature seems decreasing while velocity increases. The times series plots and the scatter plot do not seem to agree with each other in the sense that scatter plot gives one to one variations in both parameters while the time series plot is good to detect a general variation within the “event” time. Point to point correlation causes the scatter. Correlation coefficients are low being the highest for the magnetic field panel with  $R=0.36$  and lowest for the velocity with  $R=0.148$ .



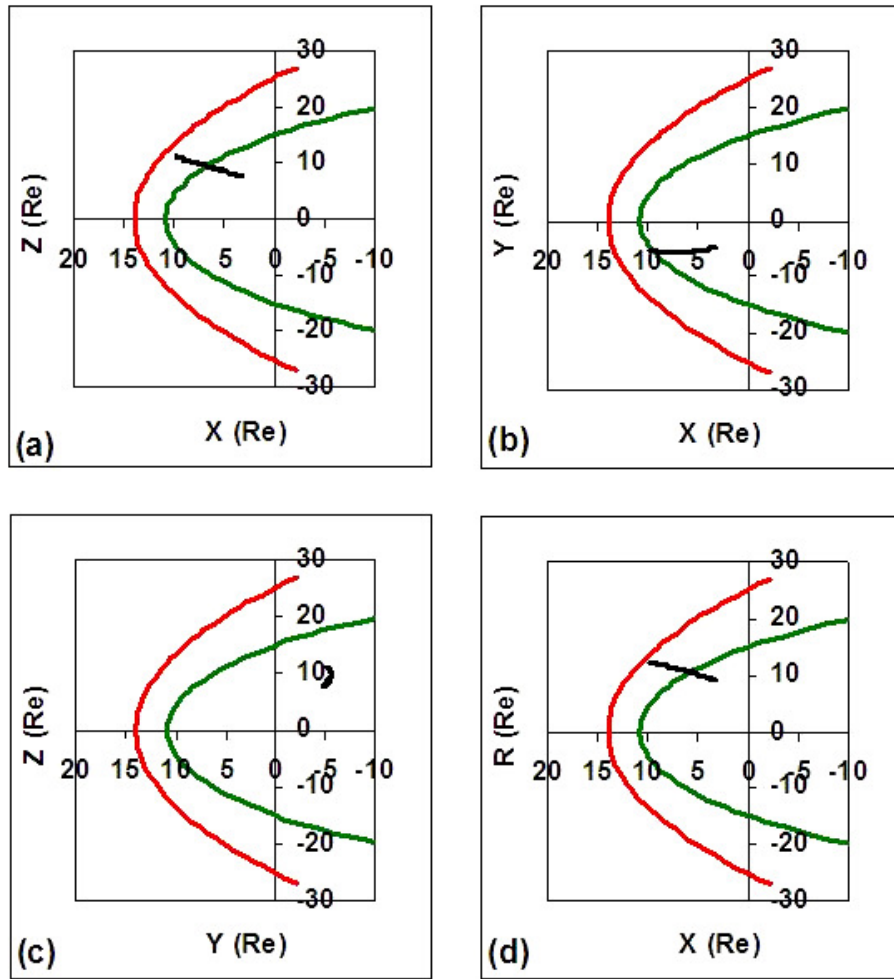
**Figure 3.7:** The scatter plots of (a) total magnetic field, (b) ion density, (c) ion temperature, and (d) ion velocity of the magnetosheath versus ion flux for June 1, 1996 case.

Figure 3.8 is an example of Type-2 that represents both magnetosheath magnetic field and ion density decreases in response to the presence of the energetic particles in the magnetosheath.



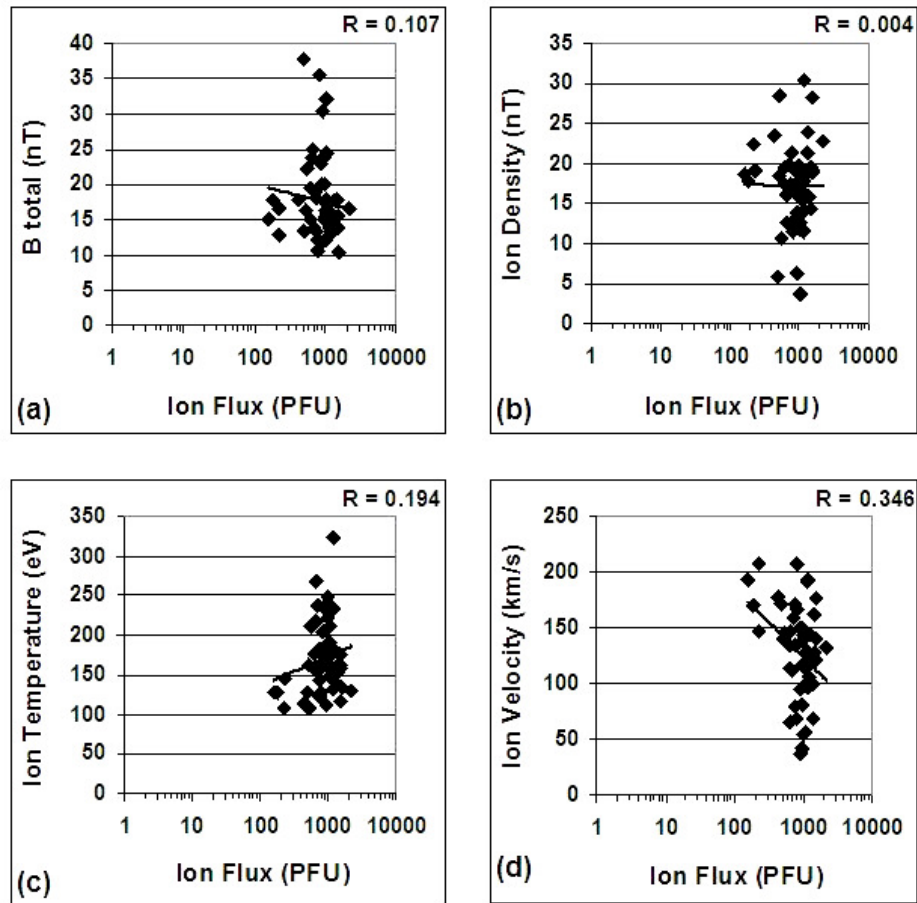
**Figure 3.8:** Type-2 example of Interball observed in June 1-2, 1996. The panels from top to bottom give (a) total magnetic field, (b) ion density, (c) ion temperature, (d) ion velocity, and (e) ion.

The trajectory of Interball for this magnetosheath crossing is given in Figure 3.9. As in Figure 3.6, the green line at 23:53 UT and the red line at 02:12 UT show the magnetopause and the bow shock respectively. In this example, the first event is a long lasting event starting at 23:55 ends at 01:25 UT. The second one is the rise starting at 01:35 UT. These both events satisfy the criteria.



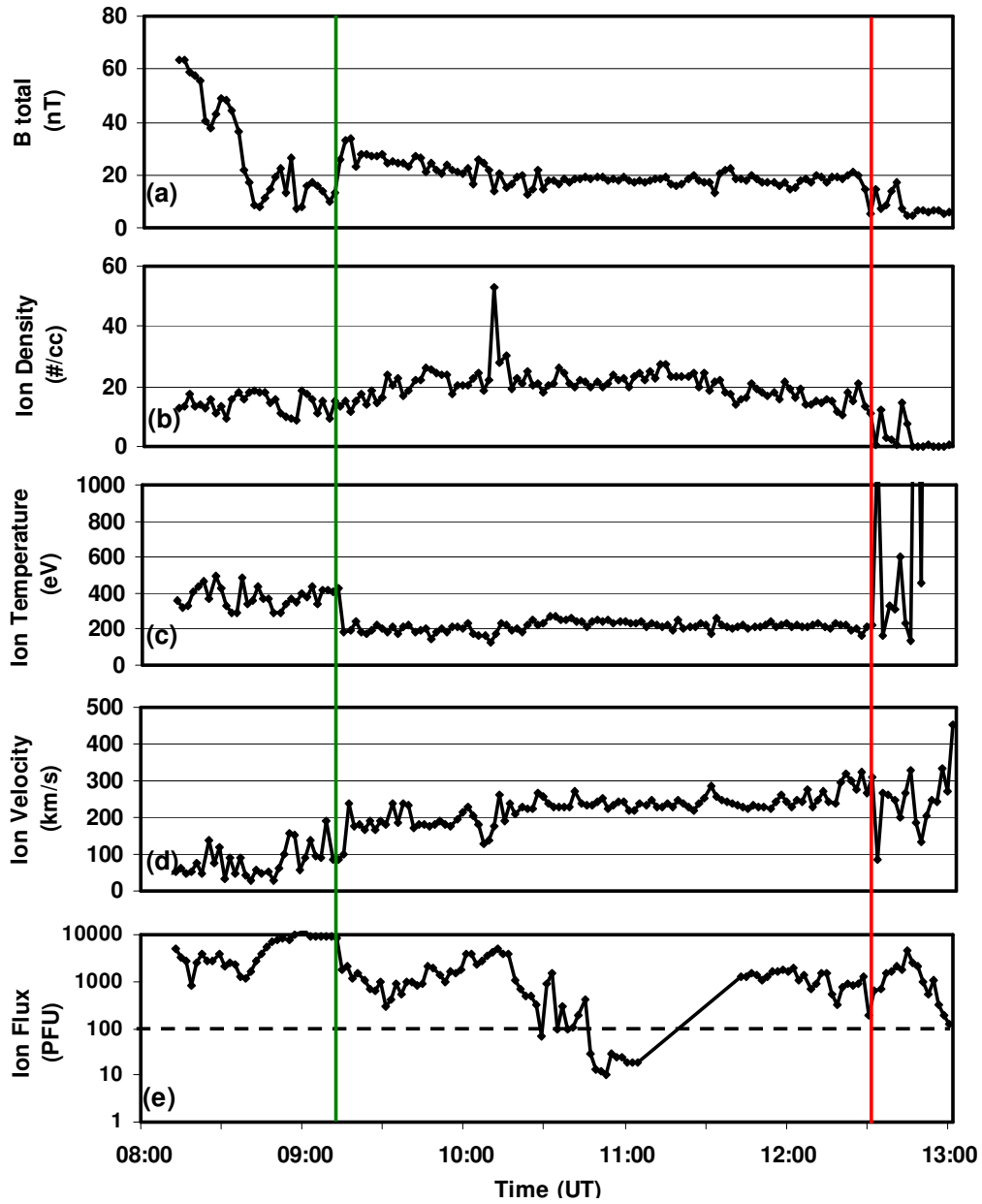
**Figure 3.9:** Trajectory of Interball spacecraft in (a) XZ-, (b) XY-, (c) YZ-, and (d) XR- planes for June 1-2, 1996 corresponding to the case in Figure 3.8.

Figure 3.10 presents the scatter plots corresponding to total magnetic field (a), ion density (b), ion temperature (c), and ion velocity (d) for the combined data of these two events. The fitted lines and the correlation coefficients are indicated on the right corner of each panel as in the previous scatter diagram. Panels in Figure 3.9 give very low correlation coefficients for all parameters. Fitted lines suggest slight decreases in total magnetic field, ion density, and ion velocity corresponding to increasing energetic particle flux. The temperature, on the other hand, appears to increase slightly in Type-2. These features resemble the characteristics of foreshock cavity. The lowest correlation is seen for ion density with  $R=0.004$  while the highest correlation coefficient with  $R=0.346$  is obtained for velocity magnitude.



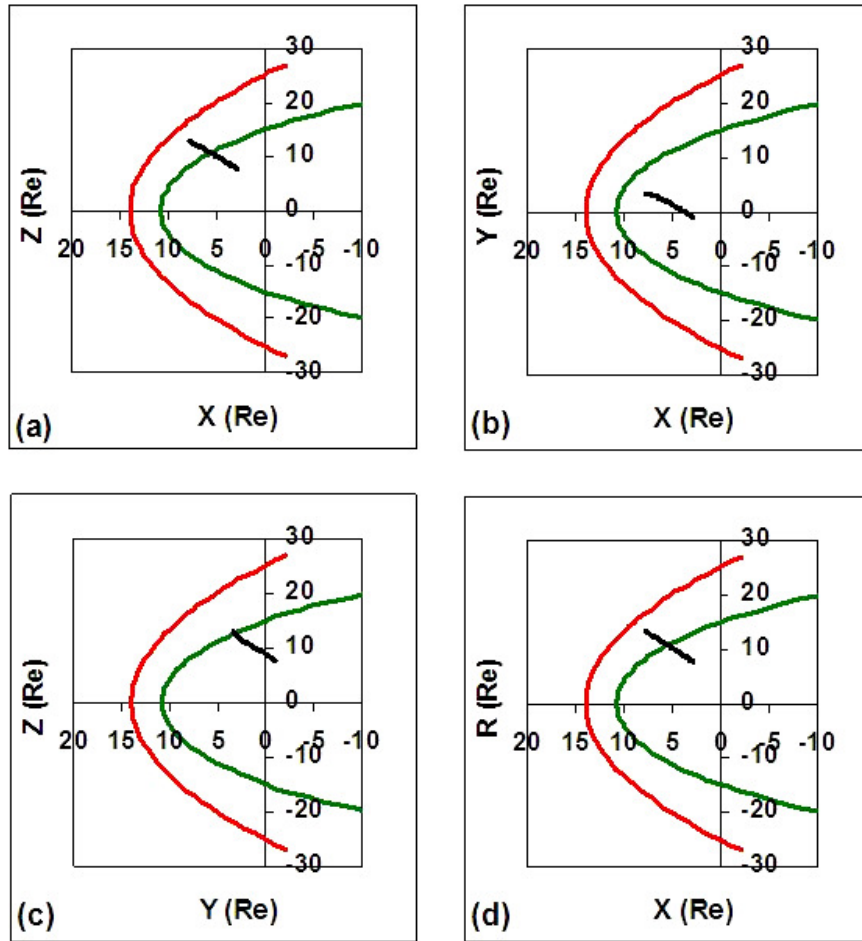
**Figure 3.10:** The scatter plots of (a) total magnetic field, (b) ion density, (c) ion temperature, and (d) ion velocity of the magnetosheath versus ion flux for June 1-2, 1996.

Figure 3.11 is an example of Type-3 displaying decreasing magnetosheath magnetic field and increasing density as the flux of energetic particles increases in the magnetosheath. The trajectory of Interball for this magnetosheath crossing in March 29, 1996 is given in Figure 3.12. The magnetopause and bow shock for this event are seen at 9:15 and 12:32 UT respectively and shown in green and red lines. In this example, there are two events, one from 09:15 UT to 10:45 UT and the other is from 11:40 UT to bow shock.



**Figure 3.11:** Type-3 example of Interball observed in March 29, 1996. The panels from top to bottom give (a) total magnetic field, (b) ion density, (c) ion temperature, (d) ion velocity, and (e) ion flux.





**Figure 3.12:** Trajectory of Interball spacecraft in March 29, 1996 in (a) XZ, (b) XY, (c) YZ, (d) XR planes.

In Figure 3.11, corresponding to these two events, magnetic field decreases and density increases as the energetic particle levels rise. Figure 3.13 exhibits the scatter plots for total magnetic field (a), ion density (b), ion temperature (c), and ion velocity (d) corresponding to these two events. The correlation coefficients are shown on the right corner of each panel. The fitted line indicates a slight increase in magnetic field, an increase in density, decreases in both velocity and temperature for Type-3 events. The lowest correlation is seen in magnetic field with  $R=0.156$  while the highest correlation coefficient with  $R=0.394$  is obtained for density.

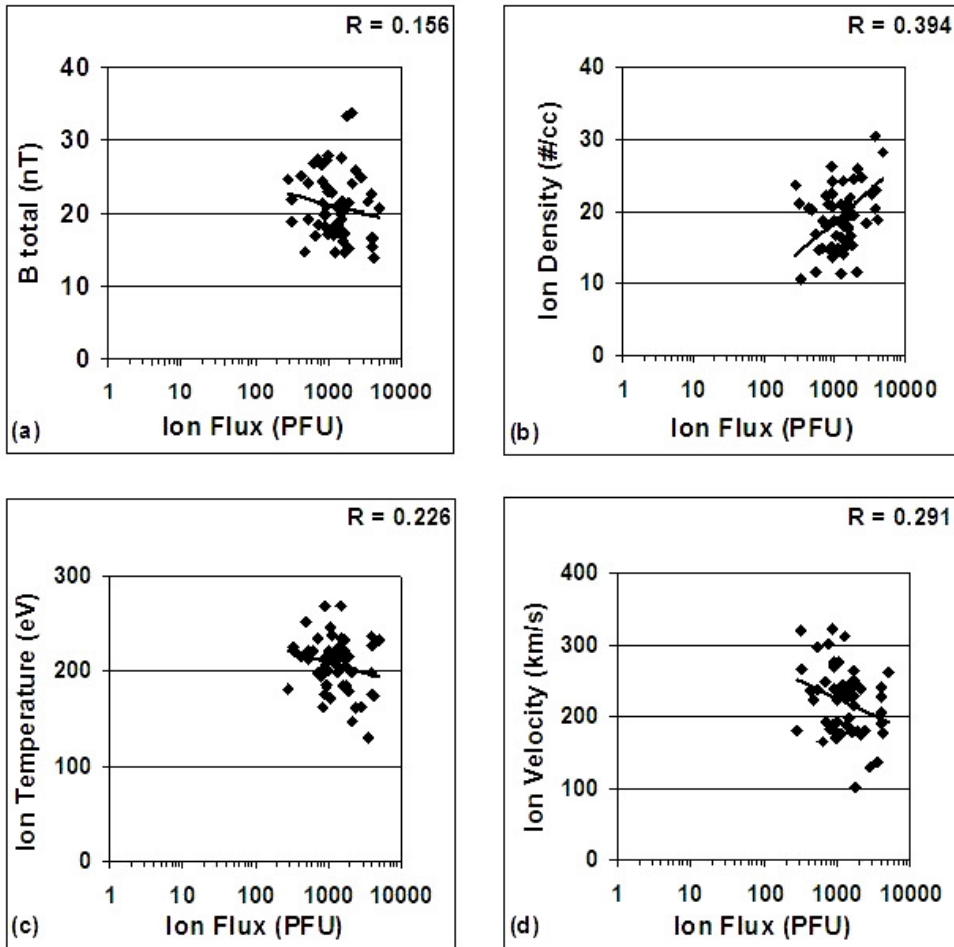


**Figure 3.13:** Scatter plots of (a) total magnetic field, (b) ion density, (c) ion temperature, and (d) ion velocity versus ion flux for March 29, 1996.

Figure 3.14 is an example for Type-4 representing increased magnetosheath magnetic field and ion density as response to the increased high energy particle flux. The trajectory of Interball for this magnetosheath crossing in March 17, 1998 is given in Figure 3.15. The green line at 00:47 UT indicates the magnetopause. Bow shock is observed at 4:40 UT. In this example, the flux is not very high but several intervals exceed 100 PFU. The first event is between 00:47 UT and 01:19 UT. The other two events start at 01:43 UT and 04:20 UT.

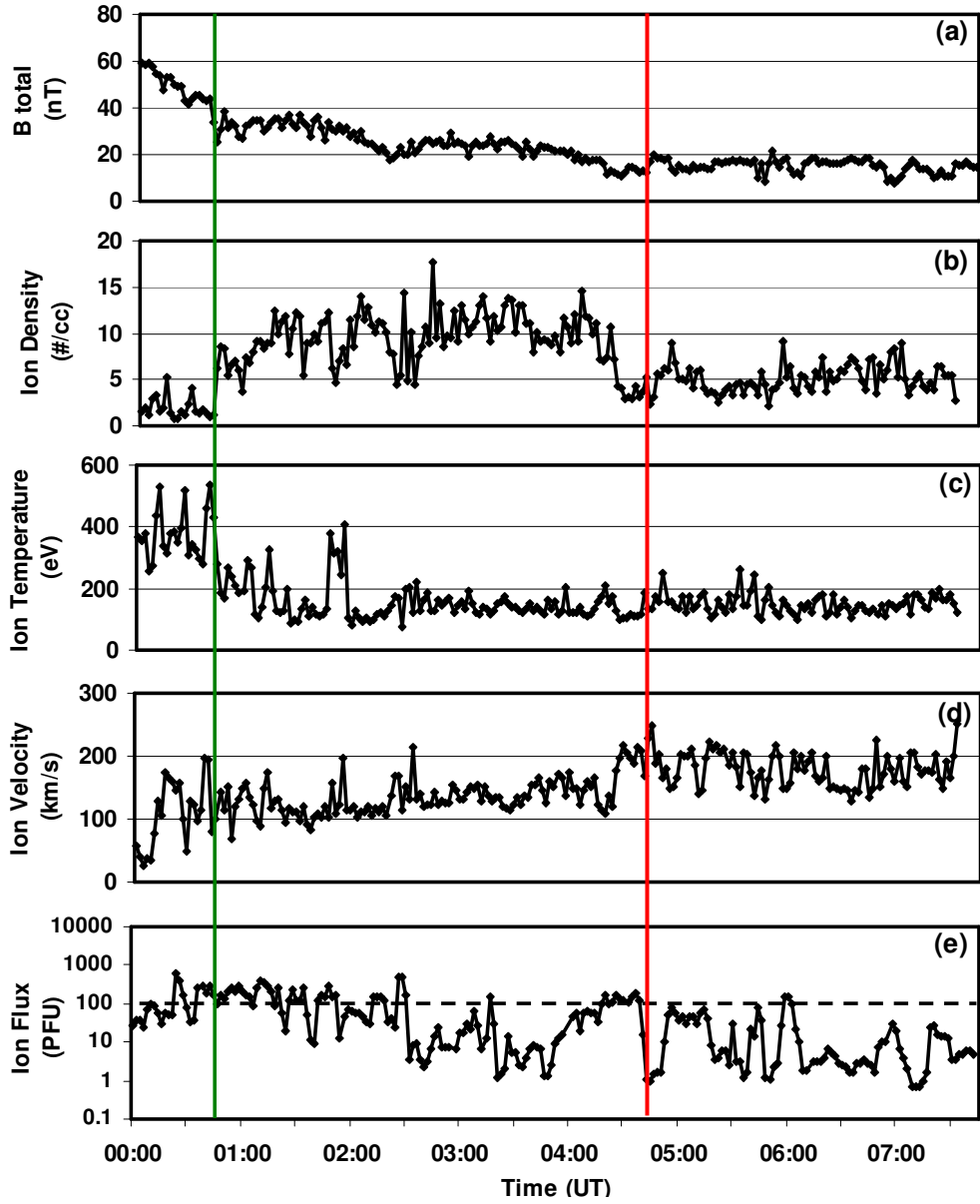


**Figure 3.14:** Type-4 example of Interball in March 17, 1998. The panels from top to bottom give (a) total magnetic field, (b) ion density, (c) ion temperature, (d) ion velocity, and (e) ion flux.

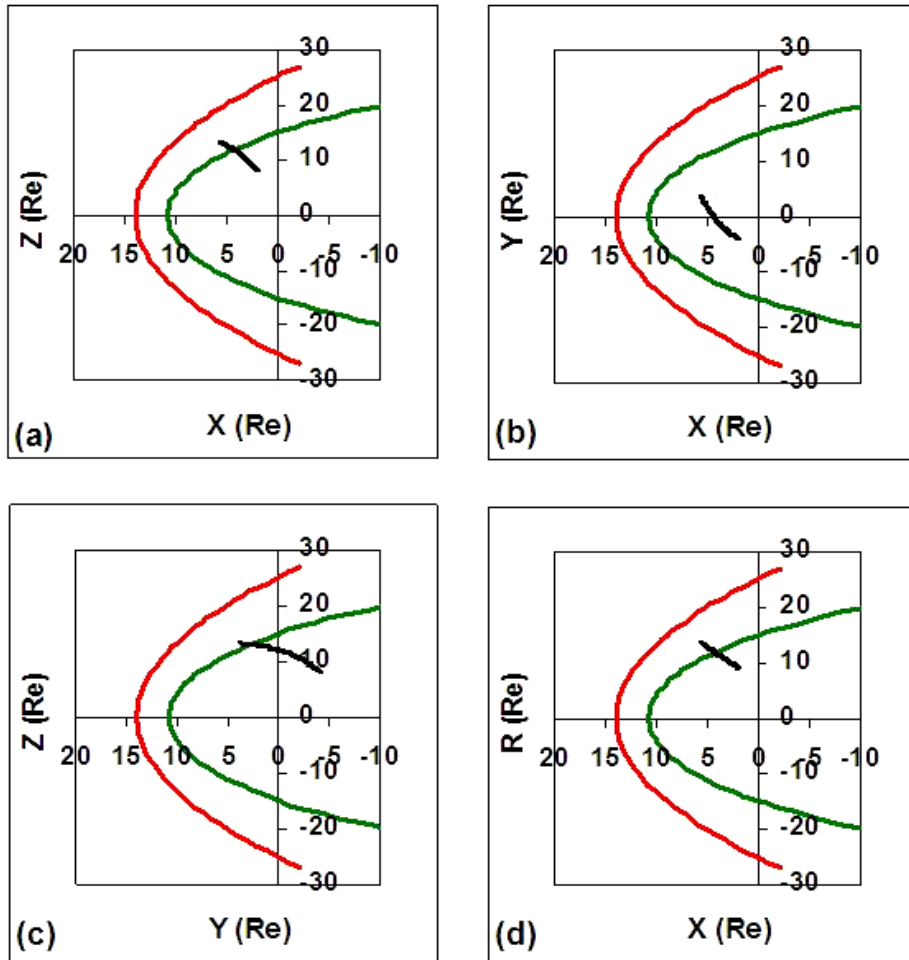


**Figure 3.15:** Trajectory of Interball spacecraft for the magnetosheath crossing in March 17, 1998 in (a) XZ-, (b) XY-, (c) YZ-, (d) XR- planes.

Figure 3.16 illustrates the scatter plots of total magnetic field (a), ion density (b), ion temperature (c), and ion velocity (d) for these three events. The fitted lines and the correlation coefficients indicate slight increases in total magnetic field, ion density, and ion temperature corresponding to increasing energetic particle flux. On the other hand, we see that ion velocity decreases. The lowest correlation is seen for ion velocity with  $R=0.187$  while the highest correlation coefficient is obtained for ion density as  $R=0.264$ .

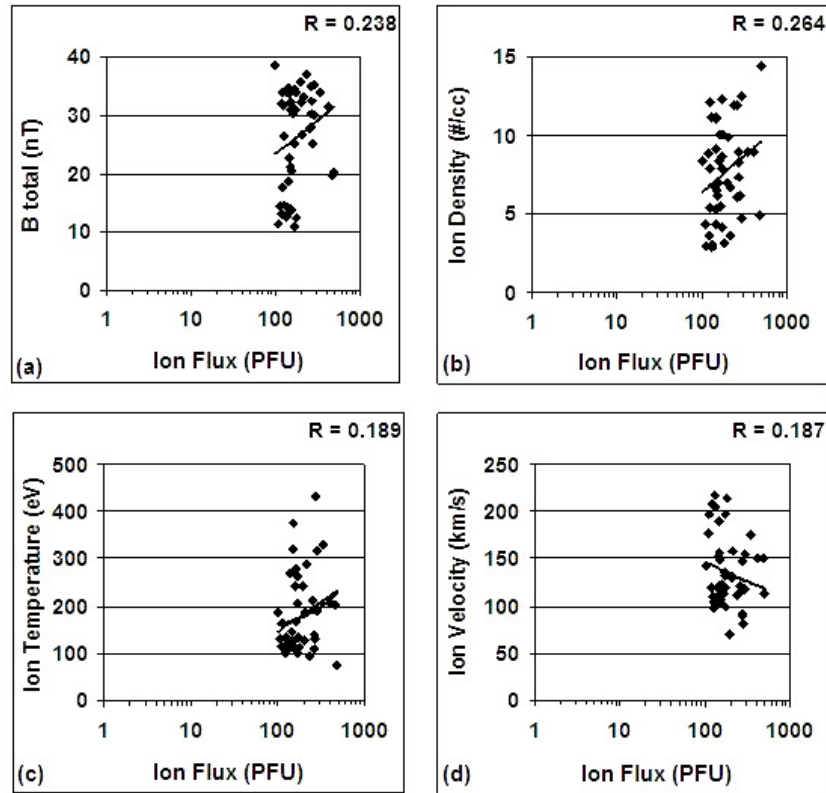


**Figure 3.16:** Scatter plots of (a) total magnetic field, (b) ion density, (c) ion temperature, and (d) ion velocity of the magnetosheath versus ion flux for March 17, 1998.

As a summary of these four types of responses in magnetic field, density, velocity and velocity in response to the high energetic particle flux, correlations are not high enough to determine clear and definite statistical conclusions. The turbulent character of the magnetosheath causes scattered values in magnetic field and plasma parameters. In comparison with the data of 1997 and 1998, less gap is seen in the magnetosheath data of 1996. To decrease the scattering and improve the correlation coefficients, several methods were applied to the 22 crossings detected in 1996. The methods applied to the values are:

- Normalization of magnetosheath values with solar wind data.
- Median analysis of ion flux data using 100, 200, and 500 PFU flux steps (PFU = Proton Flux Unit =  $\#/(cm^2 \cdot s \cdot keV \cdot st)$ ).
- Z-Score analysis of magnetosheath values.

In the next section, we test these methods using a new magnetosheath crossing from Interball corresponding to Type-2. The case is observed in March 10, 1996.

### 3.2 March 10, 1996

Figure 3.17 presents the time series for March 10, 1996 to illustrate the results of different tests that are used to improve the correlations in the previous examples. Panels from top to bottom show total magnetic field, density, temperature, and proton flux. Multiple bow shock crossings are observed. The vertical dashed red line marks innermost bow shock at 14:12 UT. The magnetopause shown with green line is observed at 08:51. The black dashed line marks the flux threshold level on the lowest panel. Blue colored intervals indicate our events that satisfy the criteria for this case.

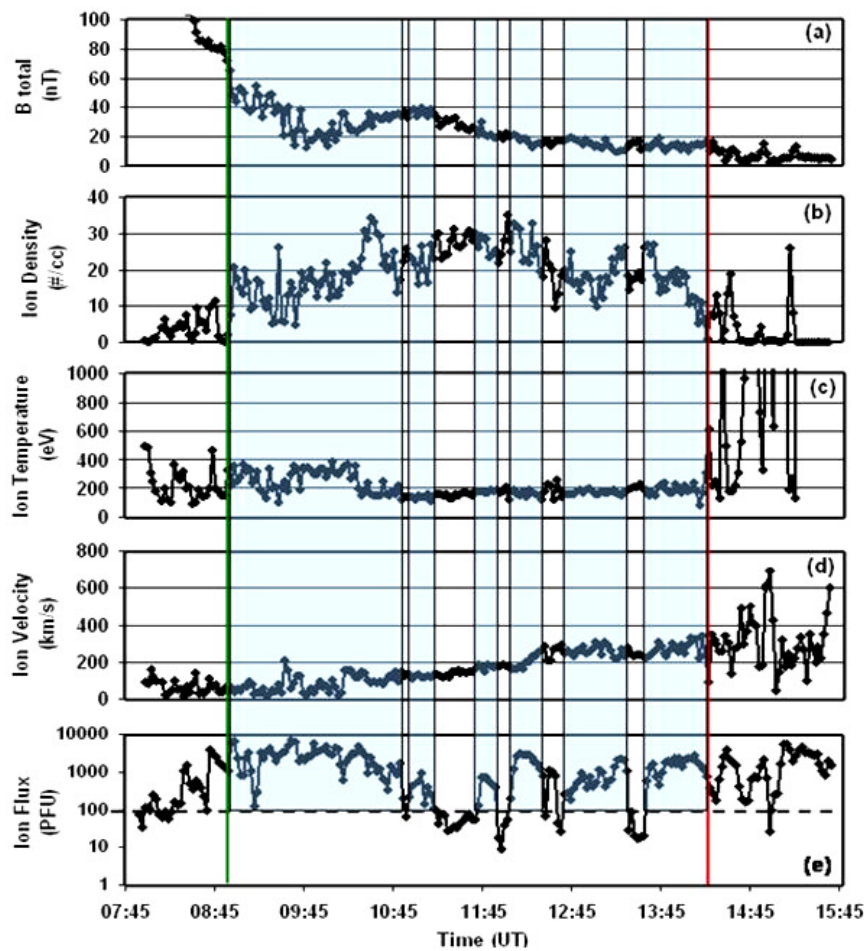


**Figure 3.17:** From top to bottom, time series of total magnetic field, ion density, ion temperature, ion velocity, and ion flux for March 10, 1996. Green and red lines mark the magnetopause and the bow respectively. Flux threshold is indicated by a black dashed line in the flux panel.

Among six high energy flux events seen in the figure, only the first interval presents a clear, detectable signature in the magnetic field and density panels. In other events, we do not see a clear response corresponding to the increased energetic particle flux levels. Within the first interval, by visual inspection of Figure 3.17, we can state that as the particle flux increases up to 8000, total magnetic field and density both show a general decrease while temperature increases slightly. Therefore, this event observed in March 10, 1996 presents another example of Type-2 that resembles to foreshock type cavity.

Figure 3.18 gives the scatter plots of total magnetic field (a), ion density (b), ion velocity (c), and ion temperature (d) for this event from 08:51 UT to 10:51 UT in March 10, 1996. Figure 3.18 represents a lot of scatter especially in panels (b), (c), and (d) as in previous figures.

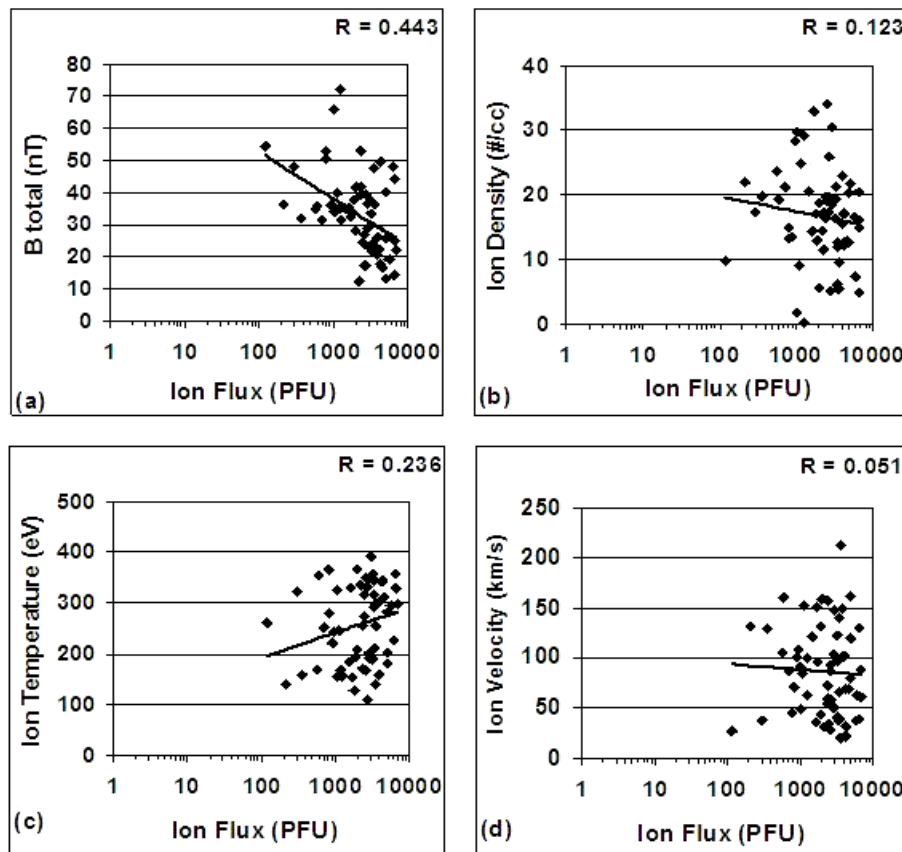


**Figure 3.18:** Scatter plots of total magnetic field (a), ion density (b), ion temperature (c), and ion velocity (d) of the magnetosheath versus energetic particle flux for March 10, 1996. Linear fit lines with black solid line are added to each panel. Correlation coefficients for each parameter are given on the top right corners of the each panel.

The magnetosheath by nature is a very turbulent region and the presence of the high energetic particles adds more complicity on the structure of the magnetosheath that makes any clear, meaningful relation harder to detect. Despite the scatter, we applied a linear fit to the data obtained the correlation coefficients shown on the right corner of each panel. The fitted line indicates a possible linear relationship between the increasing energetic particle flux and magnetic field, density, velocity and temperature. A moderate decrease in magnetic field, a slight decrease in density and velocity, and a slight increase in temperature panels emerge. The lowest correlation is seen in ion velocity panel with  $R=0.051$  while the highest correlation coefficient with  $R=0.443$  is obtained for total magnetic field panel. These correlation coefficients are small. To determine the goodness of the correlation, a two-sided significance test is performed at a decided significance level of 0.05. For total magnetic field (Bt), ion density (Ni), temperature (Ti), and velocity (Vi), t-values (test values) are calculated by using:

$$t_{value} = \frac{r\sqrt{n-2}}{\sqrt{1-r^2}} \quad (3.1)$$

Here,  $r$  is the correlation coefficient and  $n$  is the number of data.

**Table 3.3:** Calculated correlation coefficients, t-values, and significance of relationship for March 10, 1996 case (Type-2).

$\alpha=0.05$	$r$	$t\text{-value}$	<b>Significance</b>
<b><i>Bi</i></b>	-0.445	-5.60	significant
<b><i>Ni</i></b>	-0.123	-1.40	Not significant
<b><i>Ti</i></b>	0.236	2.74	significant
<b><i>Vi</i></b>	-0.051	-0.59	Not significant



The critical value is 1.9599 for  $\alpha=0.05$  significance level. To achieve a significance level of 0.05 for a two-sided test, the absolute t-value must be greater than or equal to the critical value 1.9599. The t-values of total magnetic field and ion temperature fall into the significant correlation regions of normal distribution as shown in Figure 3.19. Their correlation coefficients are significant. On the other hand, the t-values of ion density and velocity are not sufficient for a reasonable linear regression since they fall out of the significance regions. Their correlation coefficients are not sufficient enough to be statistically significant for this Type-2 event.

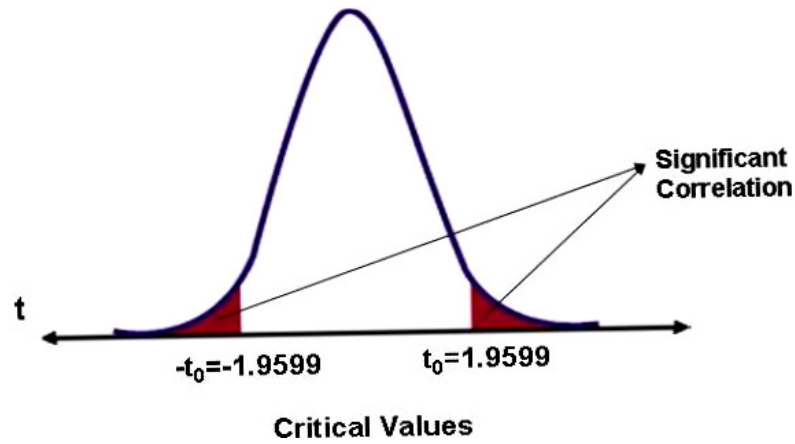


**Figure 3.19:** Normal distribution with significant correlation regions (red regions on left and right) specified by critical values for significance level of 0.05.

For most of the 51 cases without any applied methods, the correlation coefficients are generally not high enough to find a clear relationship between the high energy particles and the magnetosheath parameters. The correlation coefficient between high energy particles and total magnetic field is less than 0.5 for 38 cases. Likewise the correlation coefficient between high energetic particles and ion density is less than 0.5 for 49 cases.

Next we apply normalization method for March 19, 1996 event to see if this improves the significance test and increase the correlation coefficients.

### 3.2.1 Normalization with solar wind data

One way to reduce the scatter in the magnetosheath data is to normalize it to the concurrent solar wind plasma and magnetic field data measured by WIND. The magnetosheath consists of shocked solar wind plasma and magnetic field, and is therefore highly dependent on the changes in the solar wind. To reveal the changes inherent to the magnetosheath, or the changes that are caused by other sources, other than the solar wind, we normalize the magnetosheath data to the solar wind plasma and magnetic field. This process will eliminate the IMF or solar wind plasma related features from the magnetosheath data.

This is applied for the case of March 10, 1996. The magnetic field, density, speed and temperature data measured by Interball in the magnetosheath are normalized to the IMF, solar wind density, solar wind speed, and solar wind temperature data measured by WIND spacecraft at L1 distance. The panels in Figure 3.20 present the scatter plots using normalized quantities for magnetic field, density, speed, and temperature versus energetic particle flux. Comparisons with Figure 3.28 indicate that the normalized density and temperature have, though small, an improvement over the unnormalized cases. Correlation coefficients of magnetic field and velocity for normalized cases are less than the unnormalized cases. They are 0.144 and 0.02 for magnetic field and velocity of unnormalized cases respectively. Visually we can see that there is no improvement with the scatter in the magnetic field panel. On the contrary, normalization of Interball magnetic field data by WIND magnetic field data results in lesser correlation coefficient and more scatter. Improvement for ion density is better than the temperature for which the correlation coefficient changes from 0.123 in panel (b) of Figure 3.18 to 0.195 in panel (b) of Figure 3.20.

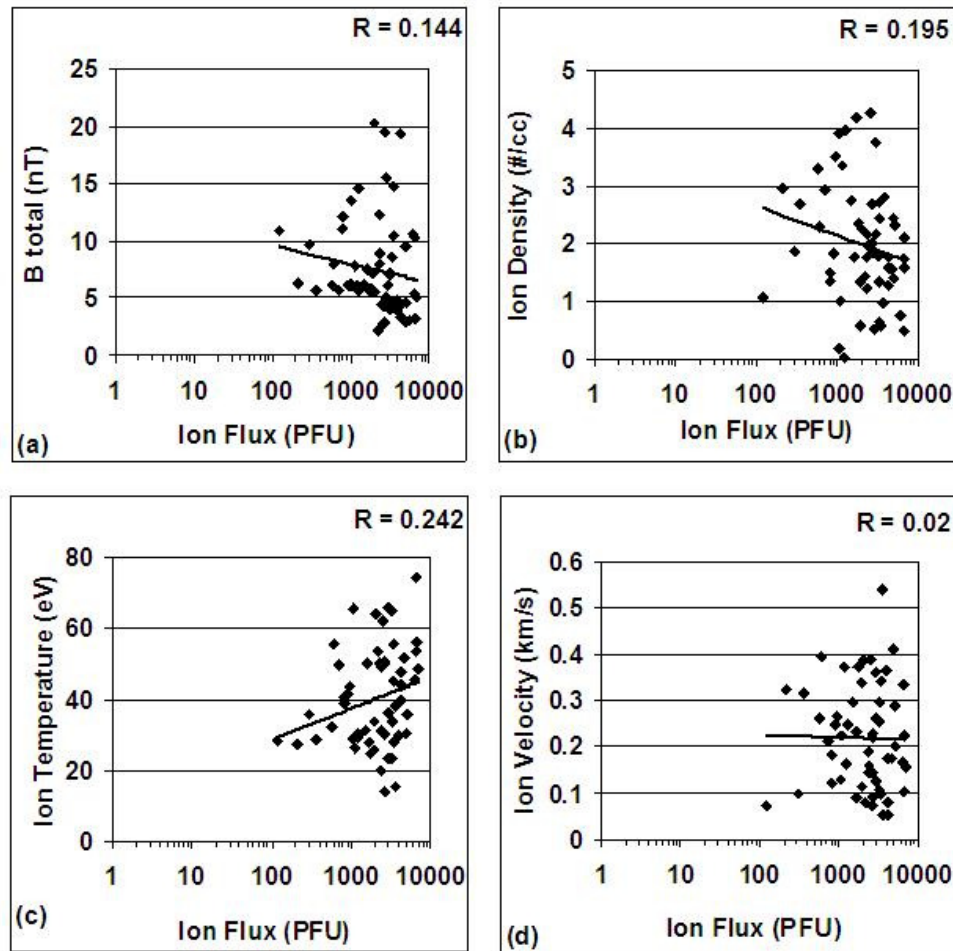


**Figure 3.20:** The scatter plots of normalized (a) total magnetic field, (b) ion density, (c) ion temperature, and (d) ion velocity of the magnetosheath versus energetic particle flux for March 10, 1996. Linear fit lines with black solid line are added to each panel. Correlation coefficients for each parameter are given on the top right corners of the each panel.

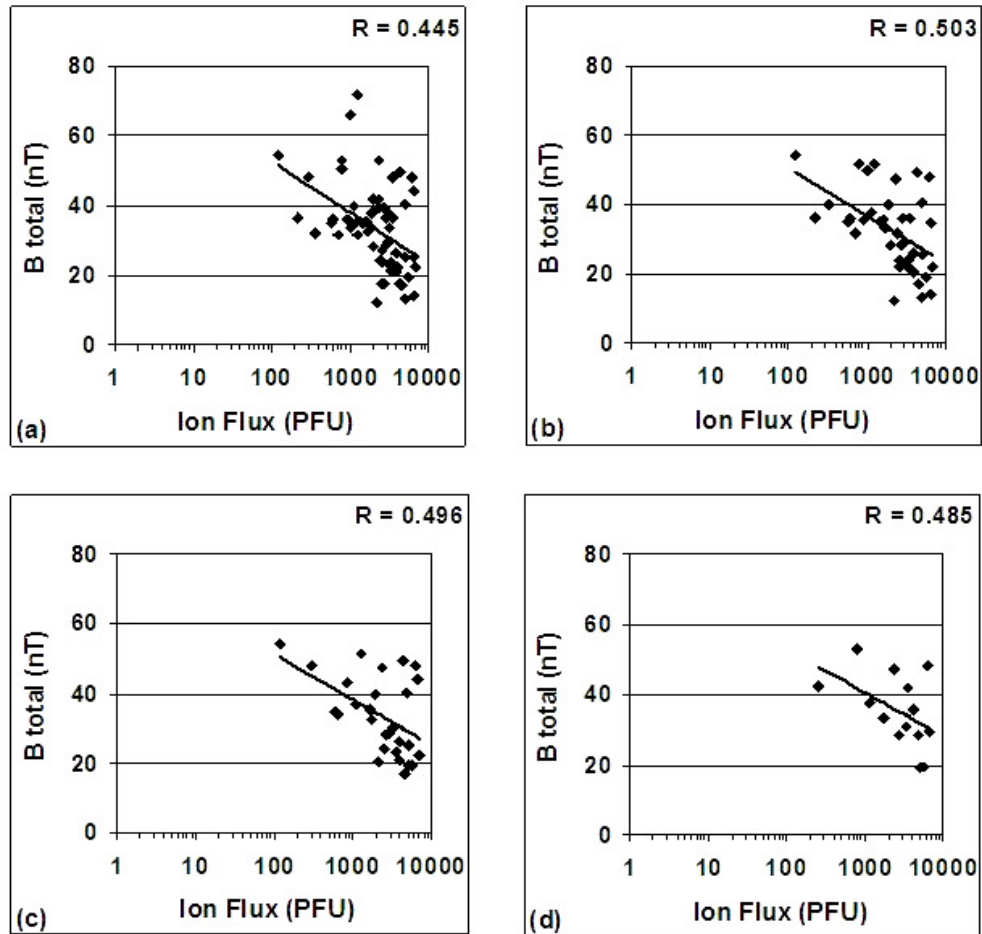
A two-sided significance test is again performed at a significance level of 0.05. The comparison of t-values for each parameter with the critical value of 1.9599 gives that the correlation coefficients of normalized ion density and temperature are significant. On the contrary, the absolute t-values of normalized total magnetic field and ion velocity are less than critical value, so that there are no significant correlation between ion flux and normalized magnetic field and ion temperature as seen in the Table 3.4.

**Table 3.4:** Calculated correlation coefficients, t-values, and significance of relationship for March 10, 1996 case (Type-2). Normalized values are used to determine the correlation and significance.

$\alpha=0.05$	$r$	$t$ -value	Significance
<b>Bi</b>	-0.145	-1.65	Not significant
<b>Ni</b>	-0.195	-2.25	significant
<b>Ti</b>	0.243	2.82	significant
<b>Vi</b>	-0.020	-0.23	Not significant

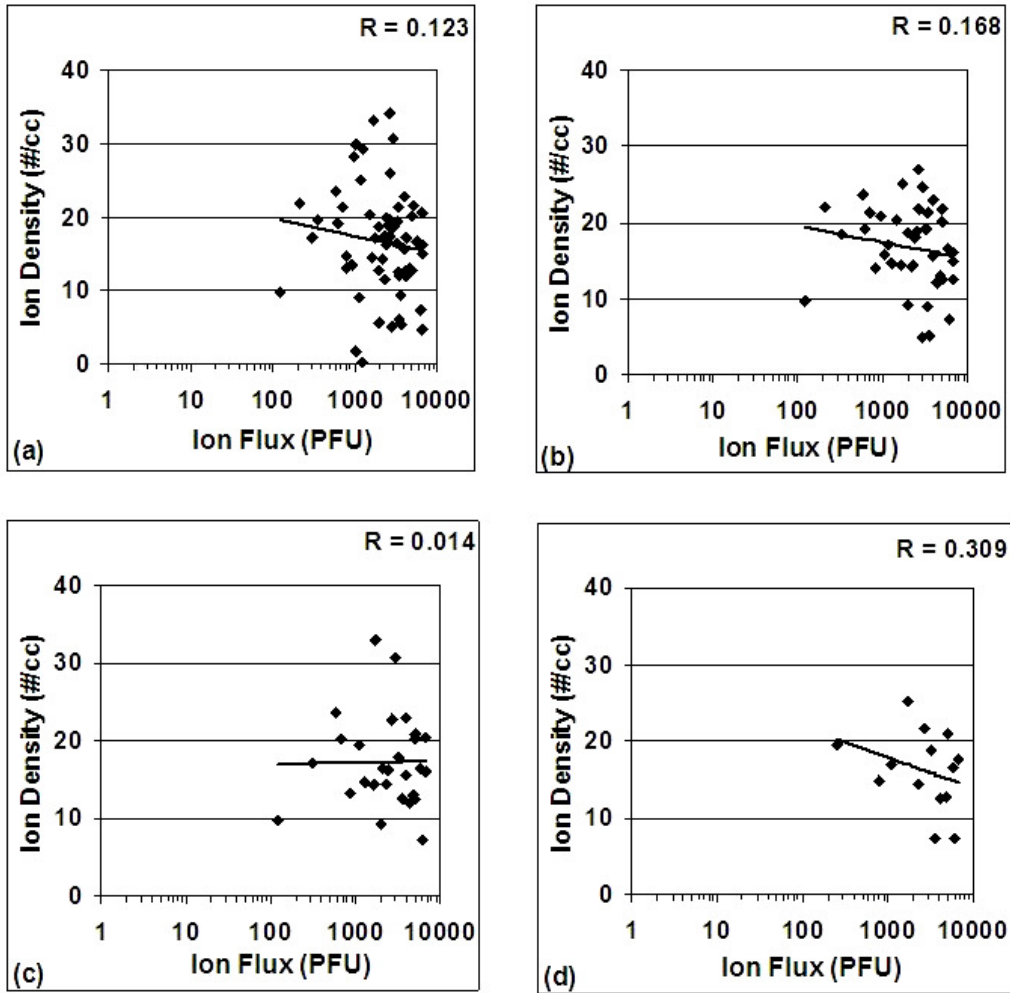
### 3.2.2 Median analysis of ion flux using 100, 200, and 500 PFU flux steps

The second method we tried to improve the correlation coefficients and reduce the scatter is to use the median analysis for ion flux data. For this procedure, we first find the median value of the magnetic field, density, speed, temperature data in the magnetosheath corresponding to the median values of particle flux in each 100 PFU flux increment. We used unnormalized magnetosheath data in this part. We tried other flux increment levels, 200 PFU, and 500 PFU until we obtain a desired, acceptable level of scatter in the plots. Figure 3.20 shows the results of this procedure and plots the median values of magnetosheath magnetic field versus median values of particle flux in each 100 PFU, 200 PFU and 500 PFU flux increment. Panel (a) in Figure 3.21 gives the unnormalized magnetic field versus flux while other panels give the median test for 100 PFU (b), 200 PFU (c) and 500 PFU (d). Correlation coefficients were calculated for each panel and shown on the right top corner as in previous figures. The median method with 100 PFU gives the highest correlation coefficient for magnetic field. We can see that the correlation coefficient changed from 0.445 to 0.503.



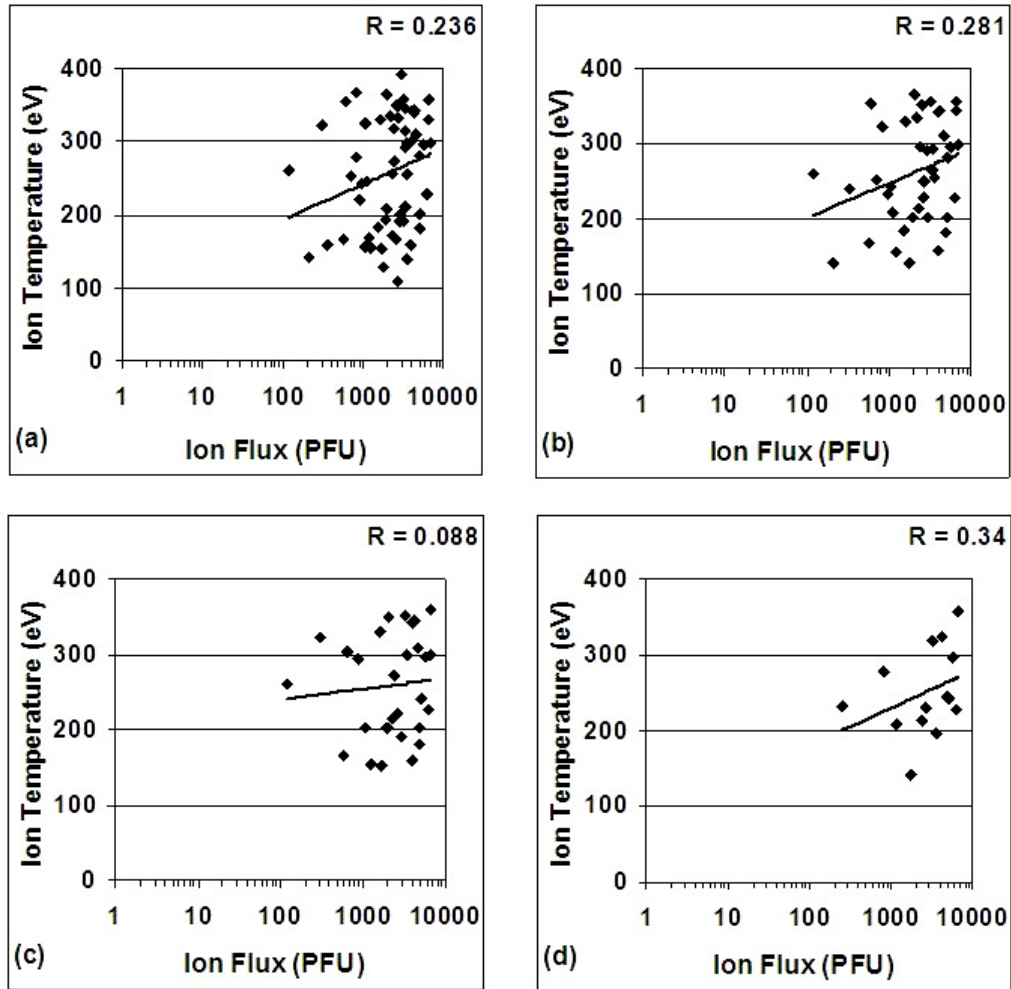
**Figure 3.21:** Scatter plots of magnetosheath magnetic field (unnormalized) versus ion flux (a). The median plots are given in panels of (b), (c) and (d) for flux increment levels of 100, 200, and 500 PFU respectively. The correlation coefficient for each case is given at the top right corner of the each panel.

The median analysis is also applied to density. This is illustrated in Figure 3.22. The correlation coefficients for 100 PFU, 200 PFU and 500 PFU flux increment are shown on the right top corner of each panel. The highest correlation coefficient is found as 0.309 for 500 PFU median analysis which is very good improvement over the original correlation of 0.123.



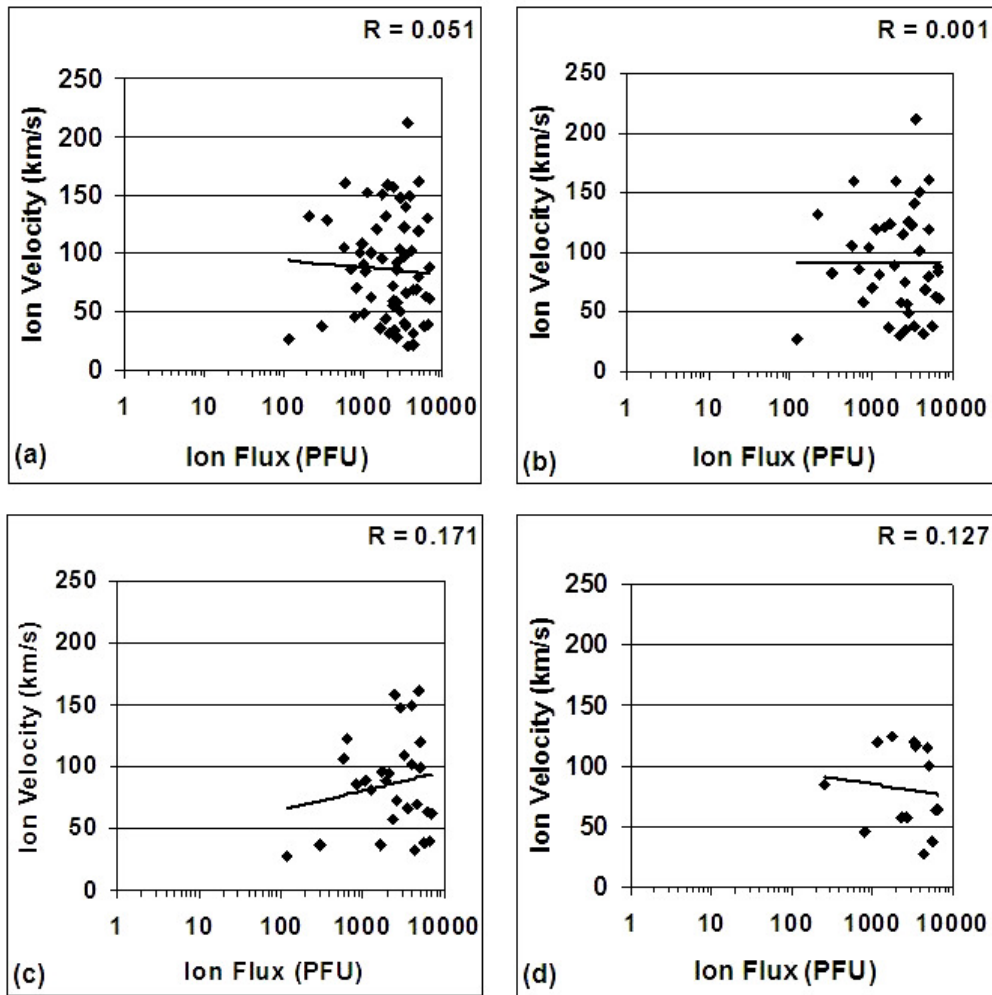
**Figure 3.22:** Scatter plots of magnetosheath density (unnormalized) versus ion flux (a). The median plots are given in panels of (b), (c) and (d) for flux increment levels of 100, 200, and 500 PFU respectively. The correlation coefficient for each case is given at the top right corner of the each panel.

Figure 3.23 shows the plots of, 100, 200, and 500 PFU median analysis for magnetosheath ion temperature. Panel (a) in Figure 3.23 gives the unnormalized ion temperature versus. Correlation coefficients were calculated for each panel and shown on the right top corner. The median method with 500 PFU gives the highest correlation coefficient for ion temperature. We can see that the correlation coefficient changed from 0.236 to 0.34. 200 PFU median analysis results in lowest correlation coefficient in comparison with others.



**Figure 3.23:** Scatter plots of magnetosheath ion temperature (unnormalized) versus ion flux (a). The median plots are given in panels of (b), (c) and (d) for flux increment levels of 100, 200, and 500 PFU respectively. The correlation coefficient for each case is given at the top right corner of the each panel.

The median analysis is also applied to ion velocity. Panel (a) in Figure 3.24 gives the unnormalized ion velocity versus flux while other panels gives the median test for 100 PFU (b), 200 PFU (c) and 500 PFU (d). The correlation coefficients for 100 PFU, 200 PFU, and 500 PFU flux increment are shown on the right top corner of each panel. The highest correlation coefficient is found as 0.171 for 200 PFU median analysis. It is seen that the correlation coefficient changed from 0.051 to 0.171. The lowest correlation coefficient is found as 0.001 for 100 PFU median analysis.



**Figure 3.24:** Scatter plots of magnetosheath ion velocity (unnormalized) versus ion flux (a). The median plots are given in panels of (b), (c) and (d) for flux increment levels of 100, 200, and 500 PFU respectively. The correlation coefficient for each case is given at the top right corner of the each panel.

To test the significance of correlation coefficients calculated by 100, 200, and 500 PFU median analysis, two-sided significance test is applied to data. Different critical numbers are determined for each median analysis because of the difference in the number of data used in each median analysis. Correlation coefficient of total magnetic field is already significant for all median analysis of 100 PFU, 200 PFU, and 500 PFU flux increments. To consider the relationships between ion flux and the magnetic and plasma parameters, correlation coefficients of 500 PFU median analysis seem most significant as seen in Table 3.5.



**Table 3.5:** Calculated correlation coefficients, t-values, and significance for March 10, 1996 case for the median tests with bandwidths of 100, 200, and 500 PFU corresponding to different critical values (left most panel). Each critical value corresponds to a median analysis with different bandwidth.

<b>Critical Value</b>	<b>Parameter</b>	<b><i>r</i></b>	<b><i>t</i>-value</b>	<b>Significance</b>
<b>1.9599</b>	Bt-100	-0.503	-6.56	significant
	Ni-100	-0.168	-1.92	not significant
	Ti-100	0.281	3.31	significant
	Vi-100	-0.001	-0.01	not significant
<b>2.0484</b>	Bt-200	-0.496	-6.44	significant
	Ni-200	-0.014	-0.16	not significant
	Ti-200	0.088	1.01	not significant
	Vi-200	0.171	1.96	not significant
<b>2.1447</b>	Bt-500	-0.485	-6.26	significant
	Ni-500	-0.309	-3.67	significant
	Ti-500	0.34	4.08	significant
	Vi-500	-0.127	-1.45	not significant

### 3.2.3 Z-Score analysis

Another method we applied to reduce the scatter in our plots is the Z-Score analysis. Z-Score (standard score) describes how much a point deviates from the mean of data. The formula to calculate the standard score is given as:

$$z = \frac{x - \mu}{\sigma} \quad (3.2)$$

where  $x$  is a raw data point to be standardized,  $\mu$  is the mean of data, and  $\sigma$  is the standard deviation of data.

In Figure 3.25, panels show the scatter plots of standardized magnetic field (a), ion density (b), temperature (c), and velocity (d) versus standardized ion flux of magnetosheath in March 10, 1996. In general, we see that the method did not improve the correlation much over the correlation we obtained with raw data as seen on the left panels. There is as much scatter on the Z-score panels as on the raw data panels in Figure 3.18.

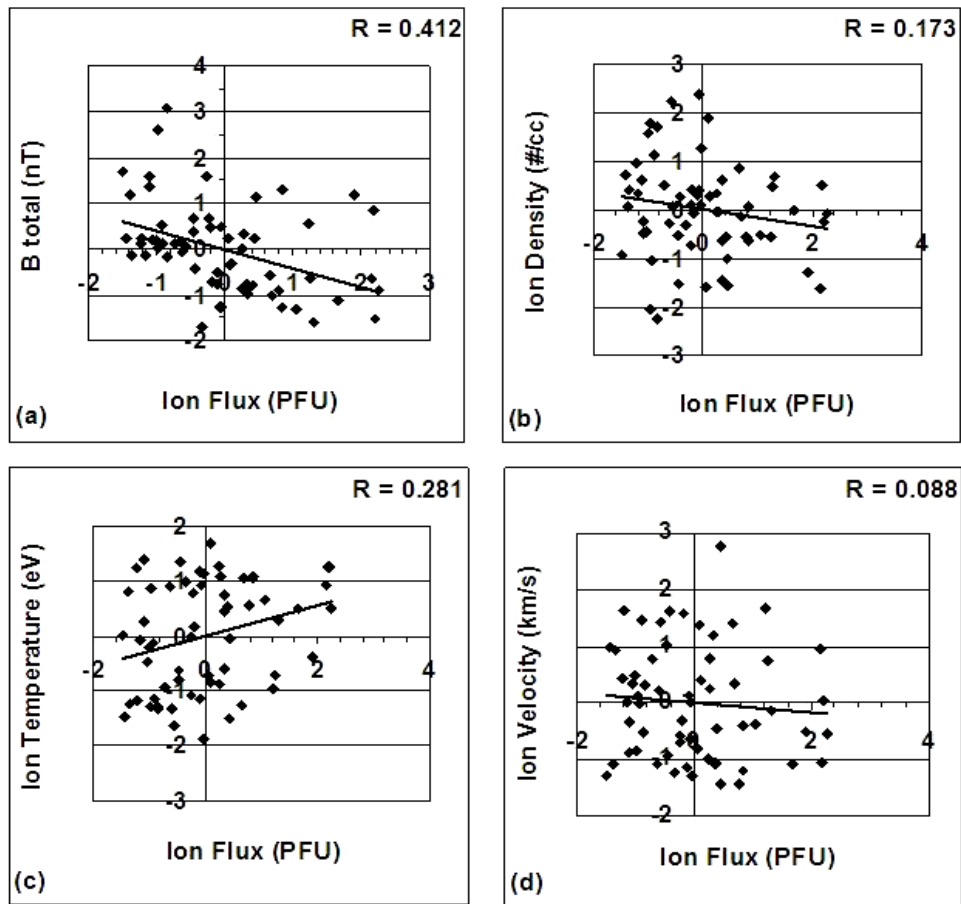


**Figure 3.25:** Scatter plots of magnetosheath standardized magnetic field (a), density (b), ion temperature (c), and ion velocity (d) versus ion flux for the crossing on March 10, 1996 . All panels give scatter plots of standardized magnetic and plasma parameters versus standardized ion fluxes. Recalculated correlation coefficients using standard scores are given at right top corner of each panel.

A two-sided significance test is applied to standardized data. The comparison of t-values for each parameter with the critical value of 1.9599 gives that the correlation coefficients of standardized total magnetic field, ion density and temperature are significant while normalized ion velocity is not significant as well (Table 3.6).

**Table 3.6:** Calculated correlation coefficients, t-values, and significance of relationship between the ion flux and standardized magnetic field and plasma parameters for March 10, 1996.

$\alpha=0.05$	$r$	$t$ -value	Significance
$Bi$	-0.413	-5.11	significant
$Ni$	-0.173	-1.98	significant
$Ti$	0.281	3.30	significant
$Vi$	-0.088	-1.00	Not significant

### 3.3 IMF and Solar Wind Plasma Connection

Table 3.7 gives the corresponding averaged IMF and solar wind parameters for these four types seen in Interball data. The first column indicates types of structures found in the magnetosheath in the presence of high energy particles. Other columns are averaged values of IMF strength, IMF Bz, solar wind ion density, temperature, speed and dynamic pressure respectively. Among all types, Type 2 presents the lowest density, lowest magnetic field strength, lowest temperature and relatively high solar wind speed. Northward IMF Bz seems to be dominant in all types except Type-3.

**Table 3.7:** Average IMF and solar wind parameters for each magnetosheath cavity type.

	IMF Bt (nT)	IMF Bz (nT)	SW Ion Density (#/cc)	SW Ion Temp (eV)	SW Speed (km/s)	Dynamic Pressure (nPa)
<b>TYPE-1</b>	6.59	0.03	6.45	8.82	433.65	1.95
<b>TYPE-2</b>	5.64	0.04	6.19	16.19	430.80	1.98
<b>TYPE-3</b>	6.69	-0.13	9.70	15.60	420.20	3.31
<b>TYPE-4</b>	7.47	0.45	9.15	10.61	419.61	2.30

### 3.4 Discussion and Summary on Interball Search

In this part of our study, we investigated the effects of energetic particles on the magnetosheath plasma and magnetic field. In addition to this general purpose, we searched whether foreshock cavity signatures are seen in the magnetosheath. For this purpose, we used Interball spacecraft measurements from CORALL for density, velocity, and temperature, from DOK-2 for energetic particle fluxes, and from MIF for magnetic field when the spacecraft travels in the magnetosheath. Our search covered three years of time span from 1996 to 1998. In terms of solar activity level this time period corresponds to the quiet phase of the Sun and the level of activity is expected to be at low levels. Figure 3.26 gives the sunspot activity period and our search period with respect to that corresponds to the time period of Cluster spacecraft used in Chapters 4 and 5. It shows that our search period starts when the sunspot number is minimum in 1996 and slightly increasing toward 1998. We do not anticipate high solar activity during this period. Thus, our search with Interball is representative of the quiet time magnetosheath conditions.

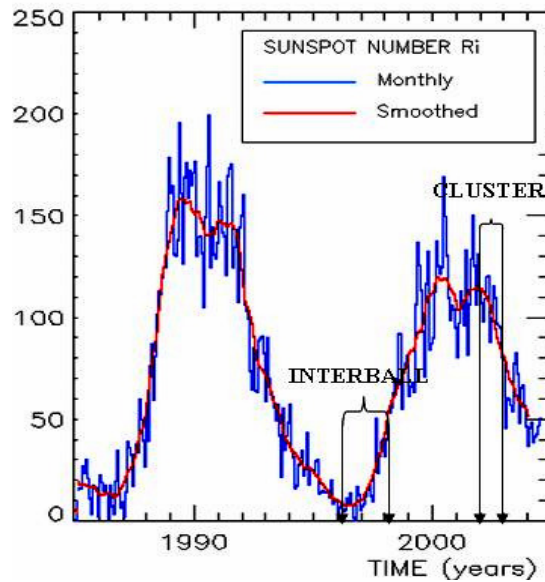


**Figure 3.26:** Solar activity cycle from 1985 to 2005. The data coverage years from Interball and Cluster spacecraft are indicated by the intervals between the arrows on the figure.

We searched visually on NASA CDAWeb for the time intervals when high energy particles are observed in the magnetosheath. We determined 51 cases in three years and examined the variations for these cases qualitatively. The variations in magnetic field, density, velocity and temperature of the magnetosheath in the presence of the high flux of energetic particles are expected to help us to understand the physical and dynamical changes in the magnetosheath.

By its nature, magnetosheath is a highly turbulent region. Due to the high wave activity and the effects of the bow shock, all quantities show high fluctuations within the magnetosheath. The foreshock cavities observed in IMP-8 and WIND data studied by Sibeck et al (2001) and Sibeck et al. (2008) imply that the foreshock cavities are transported into the magnetosheath where they can cause changes in the magnetic field and density structure of the magnetosheath. These cavities have also consequences at the magnetopause, when they reach, by changing the boundary locally.

Our search results using Interball spacecraft data in the magnetosheath suggest that there exist four types of structures that visually exhibit detectable variations in the magnetic field and density in the magnetosheath. Among these types, foreshock type signature, Type-2 that designates decreasing magnetic field and density, is found to occur less frequently. Over time intervals of about one hour or so, the general visual inspection of the magnetic field and density variations indicates that Type-1 occurs most commonly when the energetic particles are present in the magnetosheath. These types of variations, increasing magnetic fields and decreasing densities, are commonly seen near the subsolar magnetopause especially during the northward IMF. The magnetosheath region where this is seen is called depletion layer owing to the depleted densities as a result of increasing magnetic effects against magnetopause. Strong draping of the northward magnetic field of the magnetosheath creates a region where the magnetosheath particles are accelerated away from the region and thus depleting the region. Subsolar depletion layers may last half an hour or more depending on the solar wind and IMF conditions.

The average values of IMF and solar wind parameters have been calculated for all high flux events of Type-1. All types represent northward IMF Bz and relatively normal solar wind plasma conditions. In fact, the magnitude of IMF Bz that these types correspond is very small indicating that the IMF is in the radial plane when the high energy flux events, thus the cavities in the magnetosheath, are seen. The highest average solar wind speed and lowest temperature are observed for Type-1. Figure 3.27 gives the spatial distribution of these types. We can see that Type-1 events occur closer to the equatorial plane in this figure.

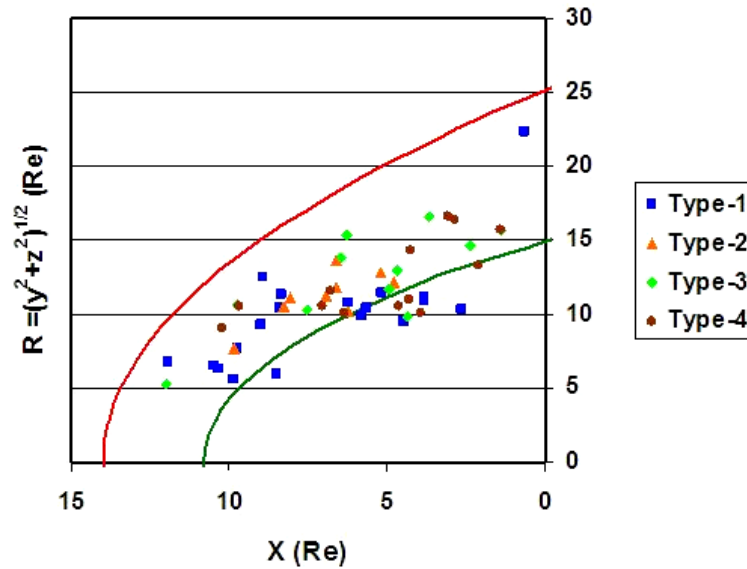


**Figure 3.27:** Average locations of all 51 magnetosheath cases observed by Interball spacecraft in XR- plane.

Another reason for the presence of Type-1 variations is the slow mode waves. The slow mode waves are also determined in the subsolar depletion layer. The wave analysis for these events requires a further broad research, beyond our proposal in this thesis.

Type-4 events found in Interball data could be the results of the foreshock cavities modified at the bow shock. Owing to the compressional waves and heating at the bow shock, this type of increased magnetic field and density regions are observed within the magnetosheath. With an occurrence rate of 26%, Interball data indicate that it is the second class of structures observed frequently within the magnetosheath.

Within the resolution of Interball data, our search indicates that it is possible to categorize the effects of the energetic particles in the magnetosheath in 4-types. The correlations we obtained are low due to the high scatter in the data. Several methods were applied to the data to reduce the scatter. Normalizing to solar wind and IMF gives improved correlation coefficients. The improvement is seen better in the density than in the magnetic field. As the magnetosheath is a highly fluctuating region owing to both variations in the solar wind, at the bow shock, and locally within the magnetosheath, a higher resolution data, shorter than 2 min, could reveal higher variations in the magnetic field and density. This can help us to relate the magnetosheath variations detected in the presence of the energetic particles to the various wave activities that are observed in the magnetosheath.

This part of our study establishes the large scale, on the order of half an hour or so, characteristics of the magnetosheath in the presence of high energy particles. The absence of the strong correlations is of concern and these may be ascribed to several factors. One is the energy level of the particles measured by DOK-2 instrument on Interball spacecraft. The energy range of the particles measured by DOK-2 is 22-28 keV. The weak correlations we obtained could suggest an energy threshold for the particles to cause clear signatures in the magnetosheath parameters. The particles in the energy range of 22-28 keV may not be energetic enough to cause strong variations on yet highly variable magnetic field and density structure of the magnetosheath. This point will be checked in Chapter 4 where we used Cluster spacecraft measurements with 3 sec resolution data. One last concern is if it is due the solar cycle effect. The Cluster spacecraft search looks into this too as the available data from Cluster cover the years of 2000-2003 that corresponds to high solar activity period (see Figure 3.26).





## **4. CLUSTER SEARCH AND MAGNETOSHEATH CAVITIES**

### **4.1 Cluster Spacecraft, Instruments and Data**

The Cluster spacecraft is a tetragonal multi spacecraft system to study especially the micro-scale structures in the Earth's magnetic environment. The spacecraft has a highly elliptical orbit with a perigee of  $\sim 4$  RE and an apogee of  $\sim 19.7$  RE. RAPID (RAP) measures energetic electron and proton fluxes from 28 to 1500 keV (Wilken et al., 1997). We use RAPID observations of protons with energies  $>30$  keV and  $> 100$  keV to search for particle flux bursts. In addition, we use Cluster Ion Spectrometer (CIS) (Rème et al., 2001) and Flux Gate Magnetometer (FGM) (Balogh et al., 1997) observations to study the magnetosheath plasma (density, velocity and temperature) and magnetic field structure. Figure 4.1 gives a picture of the spacecraft for May 10-11, 2002, an example of one of the high latitude trajectory through magnetopause, magnetosheath and bow shock and back, and the instruments from which we used data in our search. In order to investigate the solar wind plasma and IMF dependence, the data from ACE satellite is used. ACE position with respect to Cluster position given in Figure 4.1 is illustrated in Figure 4.2. The magnetosheath intervals corresponding to the selected high flux intervals of energetic particles from Cluster were delayed concurrently by the solar wind arrival time to Cluster for each event. In the case of ACE, for the magnetic field strength and its components, data from MFI (Smith et al., 1998) instrument and for solar wind plasma, data from SWEPAM (McComas et al., 1998) instrument on board of ACE were used.

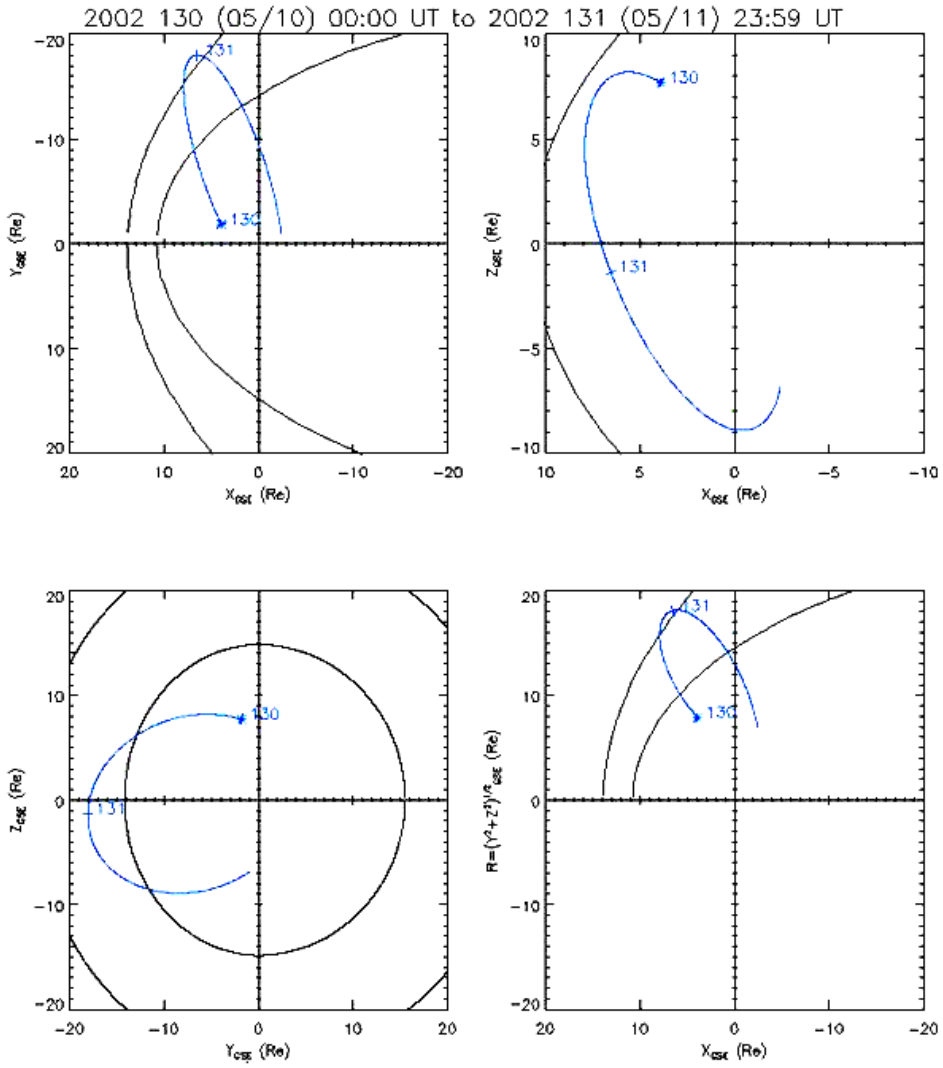


**Figure 4.1:** An example of a high latitude trajectory of Cluster spacecraft from SSCWeb in (a) XY-, (b) XZ-, (c) YZ-, and (d) XR- planes for May 10-11, 2002. The model magnetopause and bow shock are given in black lines.

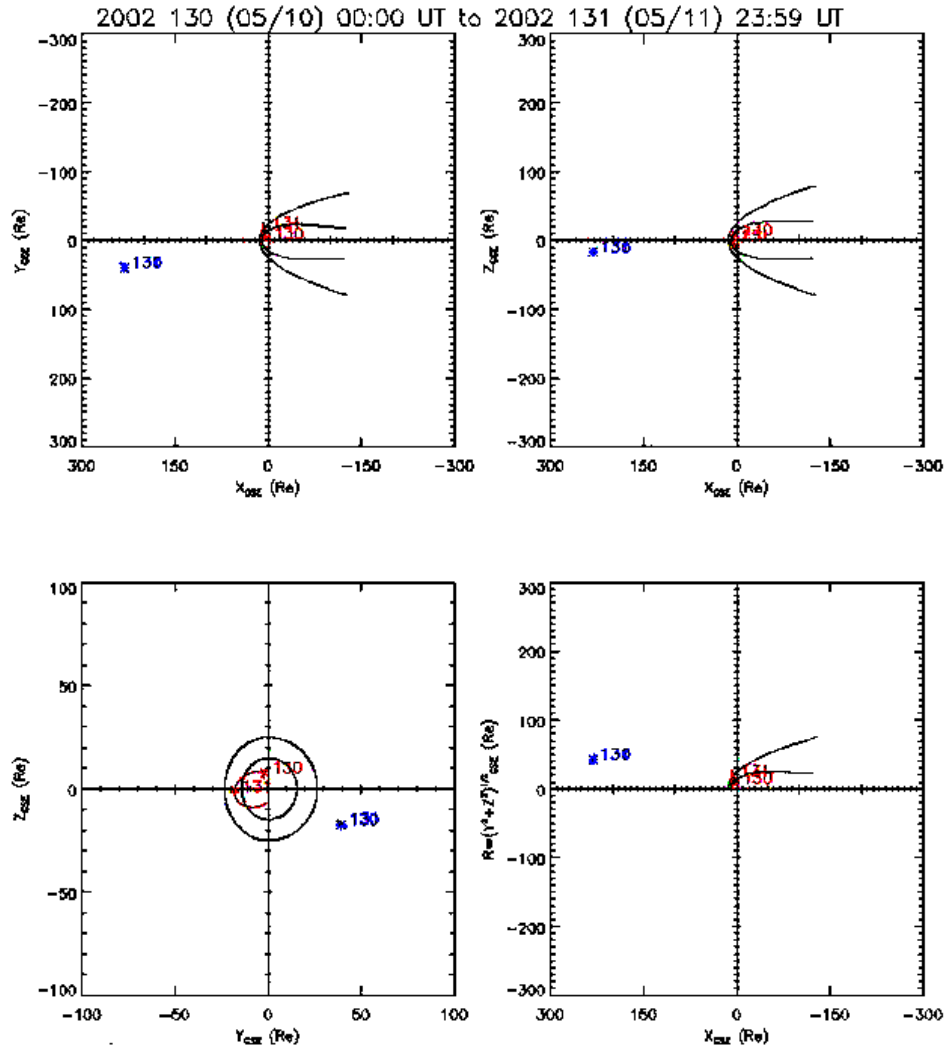


**Figure 4.2:** The trajectories of Cluster (red) and ACE (blue) spacecraft from SSCWeb in (a) XY-, (b) XZ-, (c) YZ-, and (d) XR- planes for May 10-11, 2002.

In this part of our study, as in Interball case, we first visually scanned Cluster energetic particle fluxes from 2002 to 2003, for two years. Then, we examine and describe the variations in the magnetosheath magnetic field and density in the presence of high energy particles. We are especially interested in detecting the signatures of decreasing magnetic field and densities during these intervals, i.e. in the presence of the foreshock cavities, described in Chapters 2 and 3, in the magnetosheath.

In this chapter, we present selected cases that best describe the response of the magnetosheath to the presence of high energetic particles. Figure 4.3 represents a case on 11 March 2002. Panels in (a) and (b) in Figure 4.3 explains how we select

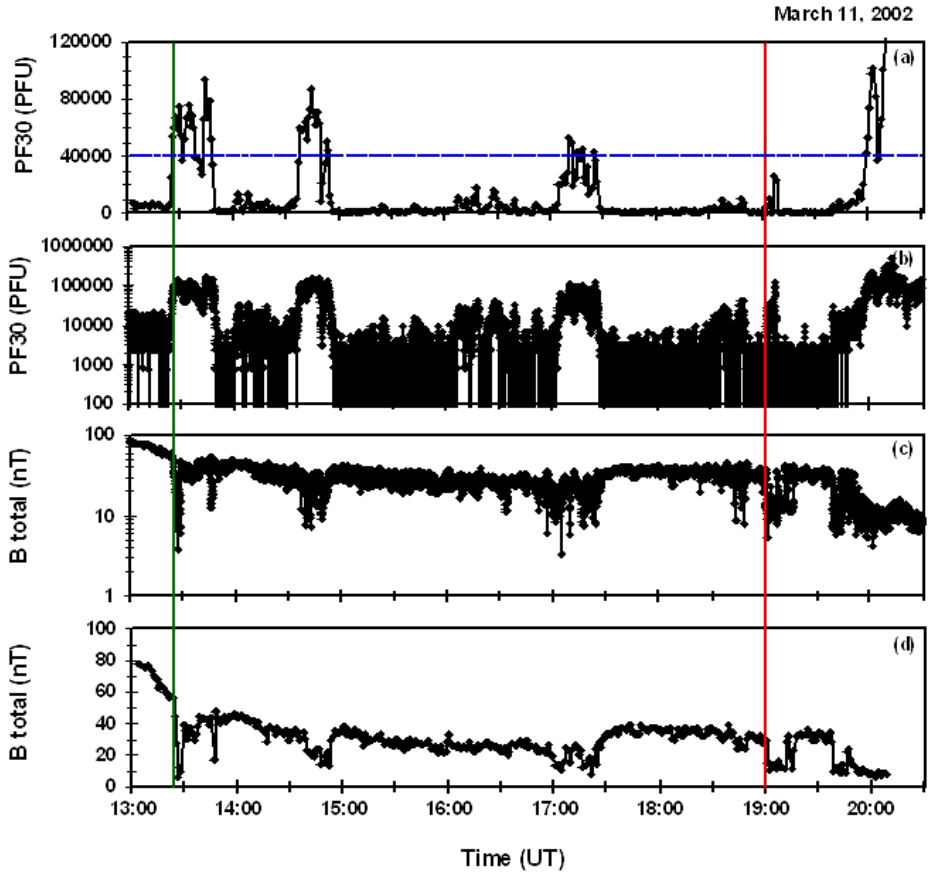
our cases. We searched for intervals of high energy particles as seen in panels (a) and (b) and examine the behavior of the magnetosheath parameters during these intervals. The bottom two panels in Figure 4.3 illustrate the state of the magnetic field in the magnetosheath and characterize its variations in the presence of the energetic particles seen in the top two panels. From top to bottom, the panels in Figure 4.3 show 1-min particle flux data for particles with energies above 30 keV (Particle flux above 30 keV=PF30 hereafter), which is used throughout this thesis study, 4-sec PF30 in units of Particle Flux Unit (PFU=  $\#/cm^2$  str), 4-sec and 1-min magnetosheath magnetic field. The green and red lines mark the magnetopause (13:25 UT) and the bow shock (19:00 UT) as Cluster moves out of the magnetosphere through the magnetosheath and into the solar wind. In many of our events, the flux also increases at energies above 100 keV (PF100). Since PF100 fluxes are usually much lower, we used PF30 at 1-min time resolution as our energetic particle flux indicator throughout this study.

Figure 4.3 shows flux bursts with different flux levels. Some of the flux occur very close to or at the bow shock and magnetopause, and some are well within the magnetosheath. Based on our two year search, we established several criteria to identify flux burst events. We select an event as a flux burst event (FBE) if the flux increase within a time interval greater than 10-min is above 40 000 PFU. This is shown in the first panel of Figure 4.3 in blue color. We constrain our analysis to flux bursts which are situated away from the bow shock and magnetopause boundary. Whether a flux burst event is near the bow shock or/and magnetopause was determined visually by scanning and examining the magnetosheath crossings. The first in a series of flux bursts often occurs at the bow shock or magnetopause, and is therefore excluded. In Panel (a), a dashed, black line at 40,000 PFU indicates the threshold and we excluded the flux burst event observed just at the magnetopause around 13:30 UT in this example. We describe a “Case” as one of our magnetosheath crossings that includes at least one flux burst event exhibiting corresponding signatures in the magnetic field and/or plasma as seen in the bottom two panels of Figure 4.3. Table 4.1 summarizes statistics from our event search. We investigated a total of 369 magnetosheath crossings in two years (2002 and 2003). Out of these 369 magnetosheath crossings, we found 182 (49%) cases that fit our criteria. There were data gaps in 22% of the magnetosheath crossings, i.e. either the flux (mostly) and/or

the corresponding magnetosheath plasma and magnetic field data were missing. In 97 (26%) of the magnetosheath crossings, we saw neither a flux increase nor field or plasma signatures, i.e. mainly depressions in the magnetic field. The absence of flux bursts in Table 4.1 refers to the absence of flux burst events well within the magnetosheath, excluding those at the bow shock and/or magnetopause. Thus, this group also includes crossings in which flux burst events occurred at the bow shock and/or magnetopause if there was no flux burst event well within the magnetosheath. Take note that we did not find any flux burst event corresponding to group 2 in Table 4.1. In two years of data search, we always see either a depression and/or an increase in variability (especially in the magnetosheath magnetic field) corresponding to the high energy particle bursts. One or the other, or both, of these signatures was present during each of 182 magnetosheath flux burst events.

**Table 4.1:** Statistics for Flux Burst Events (FBE) determined in two years of Cluster data. Expected Signal refers to either variability and/or depressed regions corresponding to the times of high energy particle flux. The absence of FBE” refers to the times when FBE were not observed well within the magnetosheath, excluding those at the bow shock and magnetopause.

<b>Group</b>	<b>Description (on a Case Basis) Magnetosheath Crossings</b>	<b>N total 369</b>	
<b>1(“Case”)</b>	<b>FBE Present and Expected Signal Present</b>	<b>182</b>	<b>49.32%</b>
<b>2</b>	<b>FBE Present and Expected Signal Absent</b>	<b>0</b>	<b>0%</b>
<b>3</b>	<b>FBE Absent and Expected Signal Absent</b>	<b>97</b>	<b>26.29%</b>
<b>4</b>	<b>Cases which do not fall 1, 2 and 3</b>	<b>7</b>	<b>1.89%</b>
<b>5</b>	<b>Data Gaps</b>	<b>83</b>	<b>22.49%</b>



**Figure 4.3:** Particle Flux (PF) and corresponding magnetic field variations in the magnetosheath for March 11, 2002 at different time resolutions. The panels give (a) 1 min PF30 (particle flux for particles with energies  $\geq 30$  keV), (b) 4 sec PF30 in logarithmic scale, (c) 4 sec magnetosheath magnetic field in logarithmic scale, and (d) 1 min magnetosheath magnetic field. Particle flux unit PFU stands for the Particle Flux Unit in  $\#/cm^2 \cdot sec \cdot str$ . Red and green lines show the bow shock and the magnetopause boundaries as Cluster travels the magnetosheath from the magnetosphere into the solar wind. The dashed blue line is the flux threshold level used in selecting flux burst events.

Figure 4.4 illustrates the variability of the magnetic field is illustrated in detail. This figure shows an expanded view of the interval from 14:20 UT to 15:10 UT shown in Figure 4.3. Figure 4.4 represents a typical case. Panels in the figure show 4 sec particle flux, 4 sec and 1 min magnetic field data, Panels b and c show highly variable magnetic field within a region in which the magnetic field strength was greatly depressed. Panel a shows that this region corresponds to enhanced energetic particle fluxes. This example will be analyzed extensively in Section III along with two other cases but is briefly presented here as part of the data selection procedure. To summarize, we identify two characteristic features in the magnetosheath when

high energy particles are present: (1) depressed magnetic field strengths and (2) the large amplitude variations. We call the regions of depressed magnetosheath magnetic field strength magnetosheath cavities.

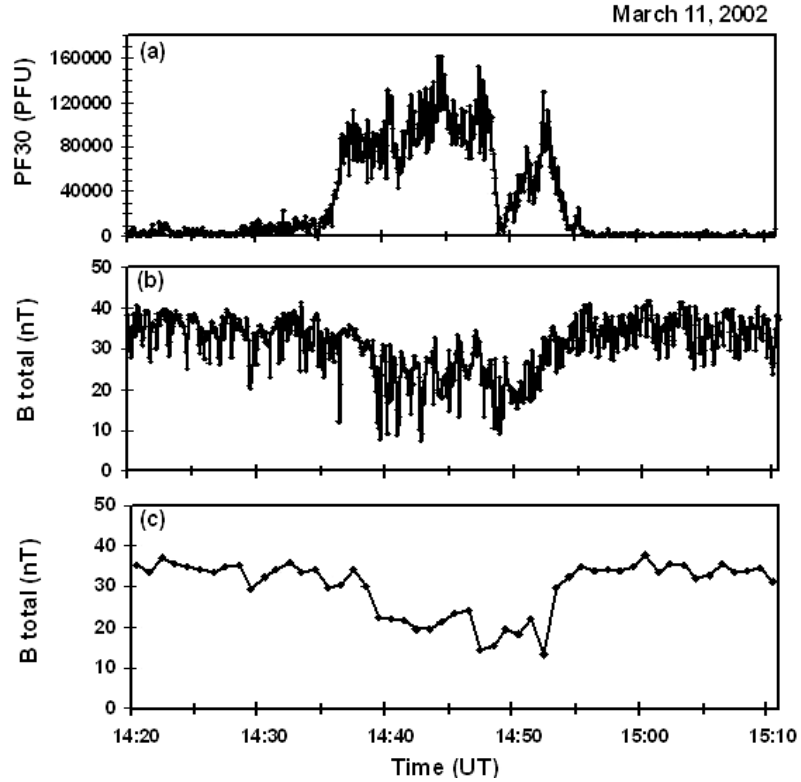


**Figure 4.4:** The expanded time interval from 14:20 UT to 15:12 UT in Figure 4.1 for March 11, 2002 to illustrate large variations within the depressed magnetic field region. Panels show (a) 4 sec PF30, and (b, c) 4 sec and 1 min magnetosheath magnetic field.

## 4.2 Event Selection

In this section, we present three cases selected out of 182 magnetosheath crossings with flux bursts. These are Jan 02, 2002, March 11, 2002, and February 04, 2003. Figure 4.5 shows the trajectory of the Cluster spacecraft in the (a) XY-, (b) XZ-, (c) YZ and (d) XR-planes for these three cases. The predicted magnetopause and bow shock for average solar wind conditions were added for reference (Roelof and Sibeck, 1993).

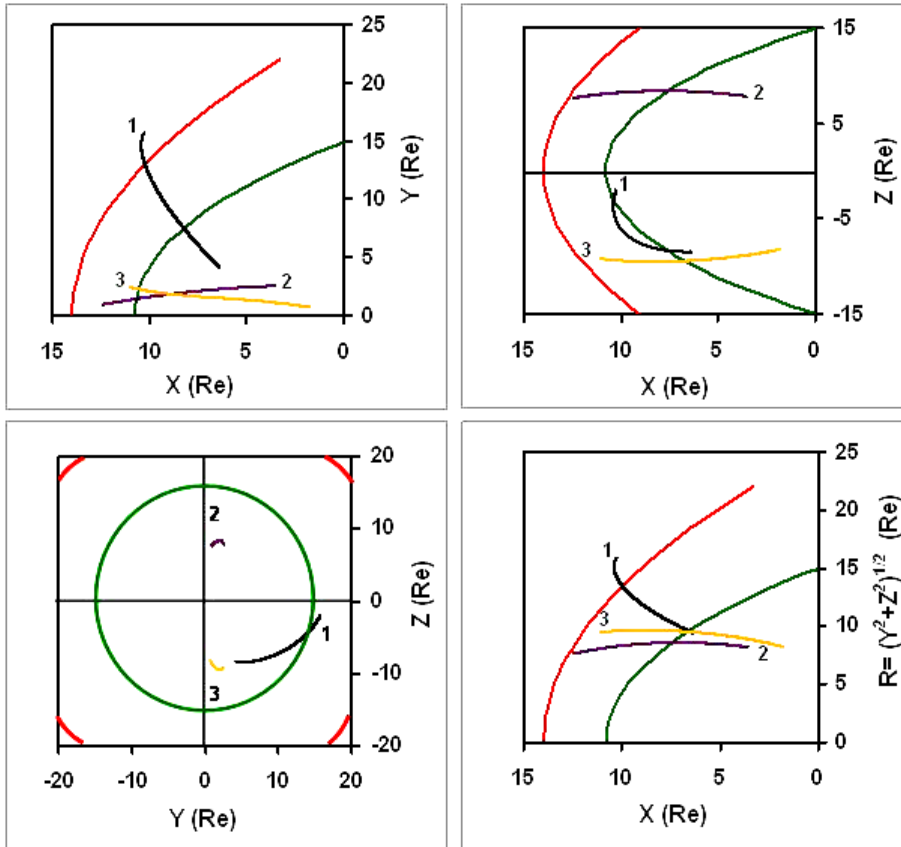


**Figure 4.5:** Trajectories of Cluster spacecraft in (a) XY-, (b) XZ-, (c) YZ-, and (d) XR- planes for (1) January 2, 2002, (2) March 11, 2002, and (3) February 4, 2003. The magnetopause and bow shock was drawn for average solar wind conditions.

#### 4.2.1 Case 1: January 2, 2002

Figure 4.6 presents observations for Case 1 on January 2, 2002. Panels from top to bottom show the particle flux (PF30), magnetic field, density, speed and temperature. For this case, the spacecraft was located at  $x = 9.3$  Re,  $y = 13$  Re and  $z = -6.8$  Re. Multiple bow shock crossings and brief magnetosheath intervals are observed. Two vertical lines at 21:00 and 08:45 UT mark the magnetosheath boundaries between the last bow shock (red) and first magnetopause (green). One can easily identify 8 high energy flux events lasting from a few minutes (spikes) to several hours and with flux levels above  $2 \times 10^4$  PFU within the magnetosheath. Although it varies from case to case, the background flux level in this case is seen to be  $1 \times 10^4$  PFU. In Figure 4.6, we selected with flux levels above  $4 \times 10^4$  PFU starting at 00:20 UT, 01:48 UT and 04:00 UT as flux burst events. Dashed blue vertical lines indicate the time intervals for these flux burst events.



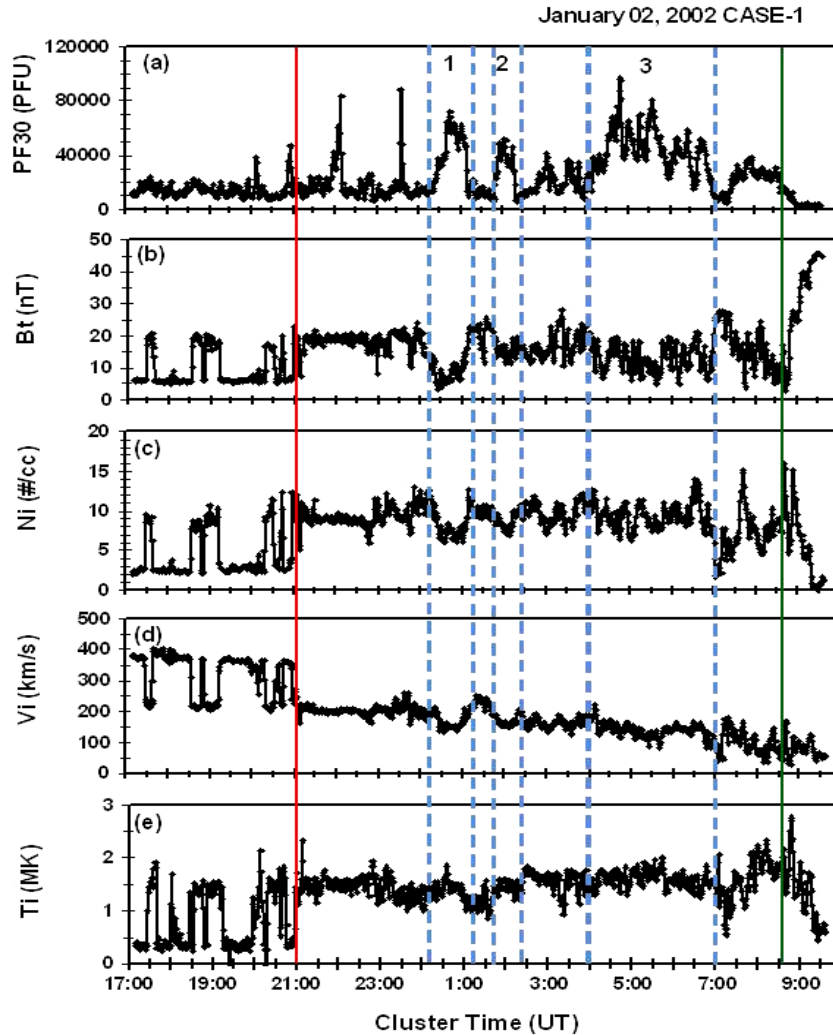


**Figure 4.6:** Plot of particle flux (PF30), magnetic field strength, density, speed, and temperature data in the magnetosheath (from top to bottom) versus time for January 2, 2002. Red and green lines mark the bow shock, magnetopause and blue lines for the flux burst events studied.

The first burst event from 00:20 UT to 01:10 UT is associated with a well defined depression in magnetic field strength, density, and velocity and a slight increase in temperature. In this event, the magnetic field strength decreases by 70 % from its pre-event value. The density decreases by 50 % and the speed decreases by 30 %. The temperature rises by about 40 %.

Fluctuation levels within the depressed magnetic field region are another typical characteristic of magnetosheath cavities. We detected variations with relatively large amplitudes within all flux burst events. Figure 4.7 presents an expanded view of the time interval corresponding to Burst 1. Large amplitude fluctuations within the region of depressed magnetic field strengths correspond to enhanced particle flux

intervals. In this example, the magnetic field within the depressed region in Panel c fluctuates with periods shorter than 10 secs in Panel (c). Although the fluctuations are smoothed in Panel (d), the region of depressed magnetic field strengths and varying magnetic fields is still clear when compared with the pre- and post event magnetosheath fields.

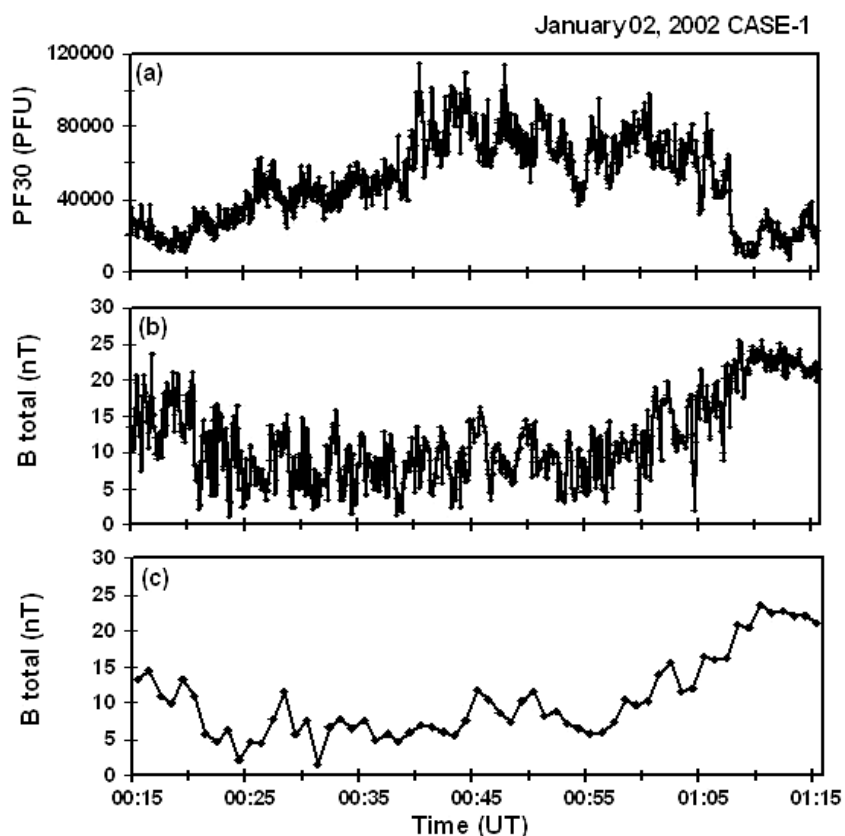


**Figure 4.7:** Plot of the expanded time interval for Burst 1 in Case 1. Panels give (a) 4 sec PF30, and (b, c) 4 sec and 1 min magnetosheath magnetic field.

The region of depressed magnetic field strengths can be weak sometimes. The duration and level of the PF30 enhancement and the presence of a PF100 enhancement influence the strength and duration of the magnetic field depression. Depressions in the density are also common, but less pronounced than magnetic field strength depressions. We have cases when we see the magnetic field depression without any significant decrease in density. In most cases, the density varies substantially within the event even if the density depression is not very pronounced. These signatures are similar to those of foreshock cavity events reported by Sibeck et al. (2001). We can therefore consider them to be the magnetosheath counterparts of foreshock cavities. Because of their similarities, we define regions of depressed

magnetic field strength accompanied by high energetic particle flux levels as magnetosheath cavities.

The second and third burst events in Case 1 occurred from 01:48-02:17 04:00-07:00 UT, respectively. We found magnetic field and plasma signatures corresponding to these events too. Burst 3 differs from the first two bursts in that it lasts longer and contains several increases that can be considered collectively as one flux burst event. The corresponding magnetic field depression is clear but not as sharp and pronounced as those for Bursts 1 and 2. High fluctuation levels again occur within the region of depressed magnetic field strengths. The magnetic field varies between 3nT and 15 nT compared to the 20 nT pre-event magnetic field in the magnetosheath. The density varies between 6 and 10  $\text{cm}^{-3}$  within the magnetosheath cavity, which is lower than the pre-event density of about 10  $\text{cm}^{-3}$ . The speed declines while temperature does not show an obvious increase

Figure 4.8 presents a scatter plot for the magnetic field, density, speed, temperature versus PF30 ion flow over the time interval from 00:00 UT to 07:00 UT. The horizontal axis is the energetic particle flux in PFU on a logarithmic scale while the vertical axis is the magnetic field strength (a), density (b), speed (c), and temperature (d). The correlation coefficients for these panels are found 0.56, 0.45, 0.56, and 0.38 for (a), (b), (c), and (d). The large scatter results from the highly fluctuating fields within the cavities. These scatter plots indicate that the magnetic field, density and speed decrease while the temperature increases as the energetic particle flux increases.

January02, 2002 CASE-1

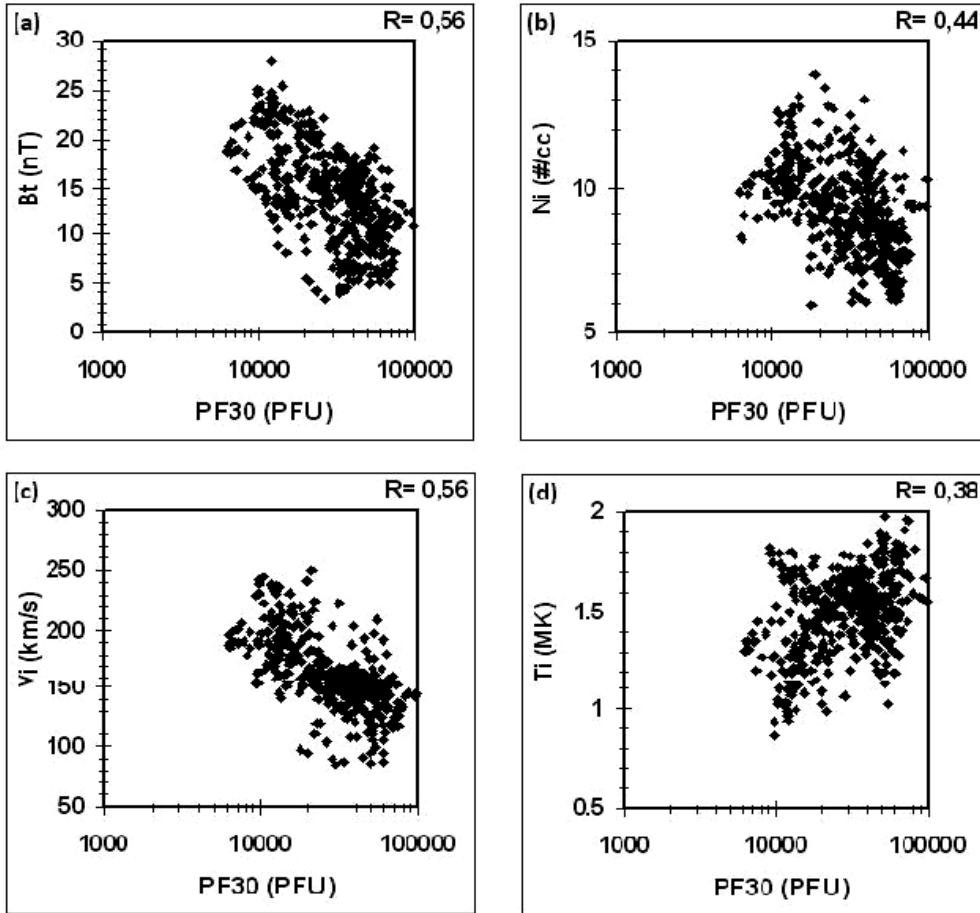


**Figure 4.8:** Scatter plots of magnetosheath parameters from 00:00 UT to 07:00 UT covering only the intervals for Bursts 1, 2, and 3. Horizontal axis is the energetic particle flux in PFU in logarithmic scale while vertical axis is (a) magnetic field strength, (b) density, (c) speed, and (d) temperature.

Figure 4.9 presents the magnetic field components and the magnetic latitude in the magnetosheath to see if there is any specific feature corresponding to the depressed regions. PF30 is shown at the top of the figure for reference. Strong  $B_x$  and  $B_y$  components downstream from the bow shock indicate magnetosheath magnetic field draping. On average, all three components change considerably either by decreasing or switching signs compared to their pre- or/and post- event values. The magnetic latitude represents the inclination of the magnetic field out of the xy-plane. When the angle lies between  $0^\circ$  and  $90^\circ$ , the field has a northward component and when it lies between  $0^\circ$  and  $-90^\circ$ , the field has a southward component. It is hard to derive a meaningful clear pattern from these plots. Nevertheless, an examination of all burst events in all cases shows that the  $B_z$  component of the magnetosheath field is

predominantly northward within the depressed regions with lesser  $B_y$  and  $B_x$  components on average. This is also clear in the magnetic latitude panel.

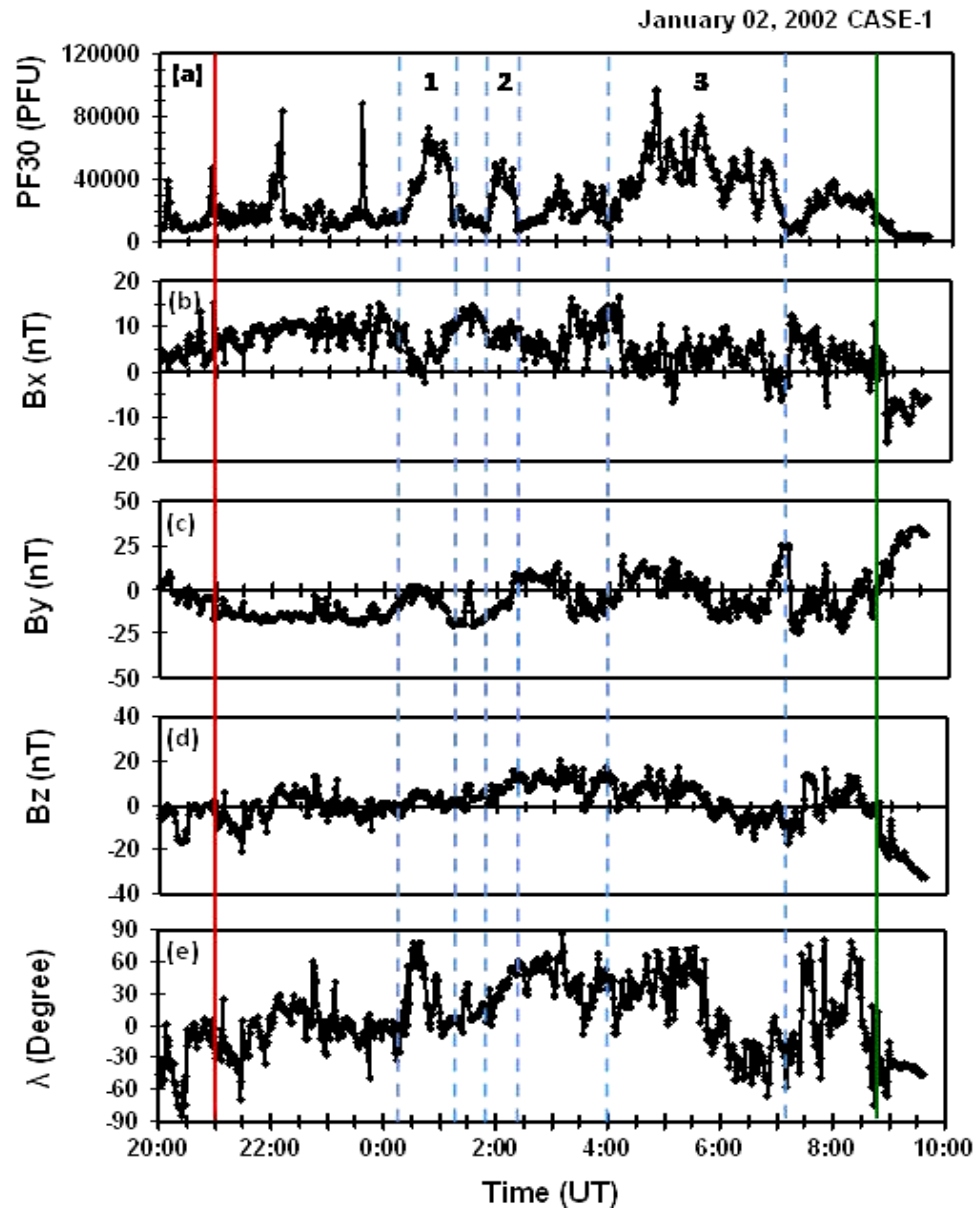


**Figure 4.9:** Plot of particle flux (PF30) and magnetosheath magnetic field components,  $B_x$ ,  $B_y$ , and  $B_z$  and magnetic latitude ( $B_\theta$ ) from top to bottom versus time for January 2, 2002. The vertical lines mark the bow shock (red) and magnetopause (green).

Figure 4.10 is a scatter plot of magnetic longitude versus magnetic latitude for (a) the burst intervals and (b) the background magnetosheath. Burst intervals include Bursts 1 and 2 while the magnetosheath intervals are the regions immediate neighboring them. The plot shows that the magnetosheath field within the cavities is highly

scattered while the background magnetosheath appears to be more focused on specific directions.

**January 02, 2002 CASE-1**

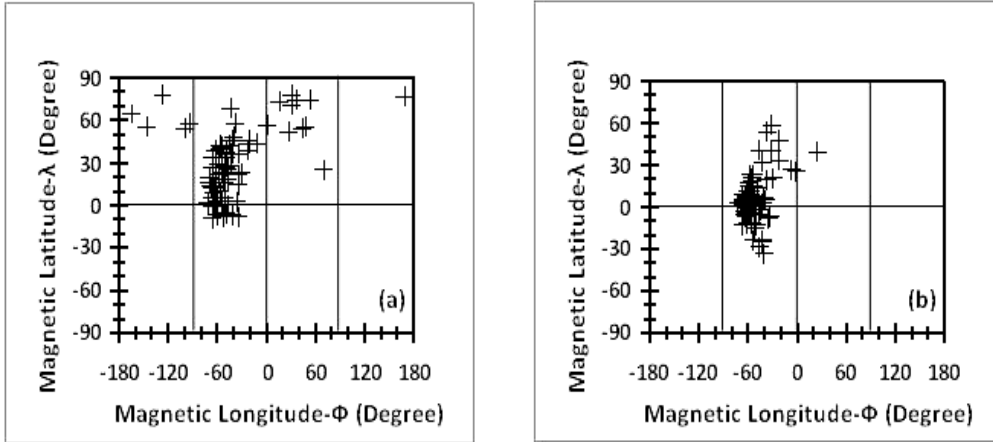


**Figure 4.10:** Scatter plots of magnetic latitude versus magnetic longitude (a) within Bursts 1 and 2, and (b) in the ambient magnetosheath surrounding Burst 1 and Burst 2 for January 2, 2002.

Figure 4.11 presents ACE IMF and solar wind plasma observations for the interval from 23:30 UT to 07:30 UT corresponding to Figure 4.6. Cluster data have been shifted to ACE times on a point-to-point basis using the ACE solar wind speed to account for convections time. ACE was located at  $(x, y, z) = (241, 5, 19.5)$  Re and the time delay between ACE and Cluster in this example varies between 40 and 70 minutes. A plot of Cluster energetic particle flux data (PF30) was added to the top of each figure to guide inspection of features corresponding to Cluster events. Times on the horizontal axis are those at ACE. From top to bottom, the panels in Figure 4.11a shows PF30, IMF Btot, IMF Bx, IMF By, IMF Bz, and IMF clock angle while those panels in Figure 4.11b give PF30, IMF Btot, solar wind density, speed, and radial temperature for ions. The IMF clock angle in Figure 4.11a was calculated using  $\Theta = \tan^{-1}(B_y/B_z)$  and  $0^\circ$  to  $+180^\circ$  indicates northward while  $0^\circ$  to  $-180^\circ$  southward IMF.

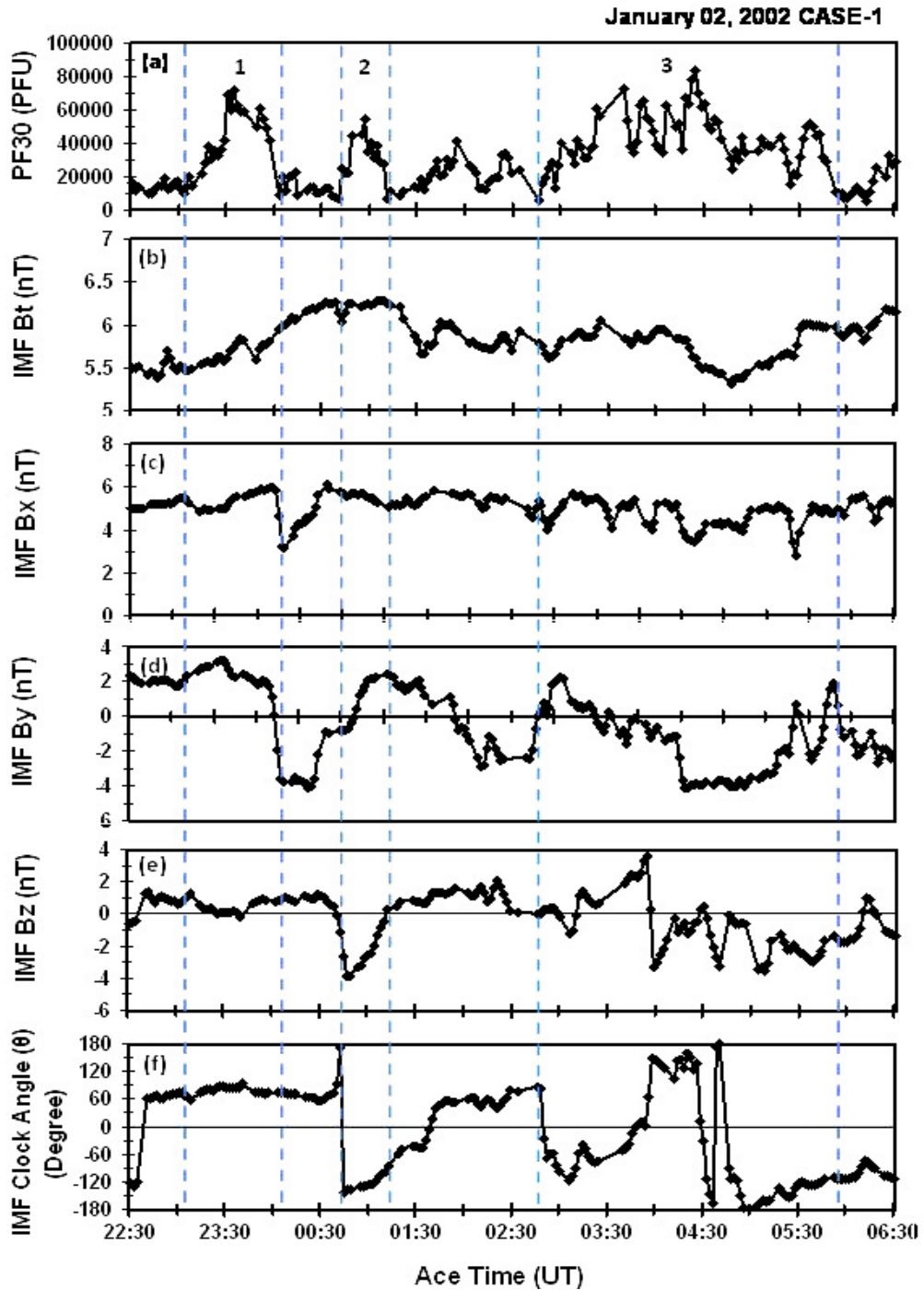


**Figure 4.11a:** ACE magnetic field data for Jan. 2, 2002. From top to bottom, panels give PF30, IMF strength, IMF Bx, IMF By, IMF Bz, and IMF clock angle versus time. PF30 was added to guide the features in Cluster data. Cluster data were shifted to the ACE times concurrently to account for the solar wind convection time from ACE to Cluster. Horizontal axis indicates the time at ACE spacecraft.

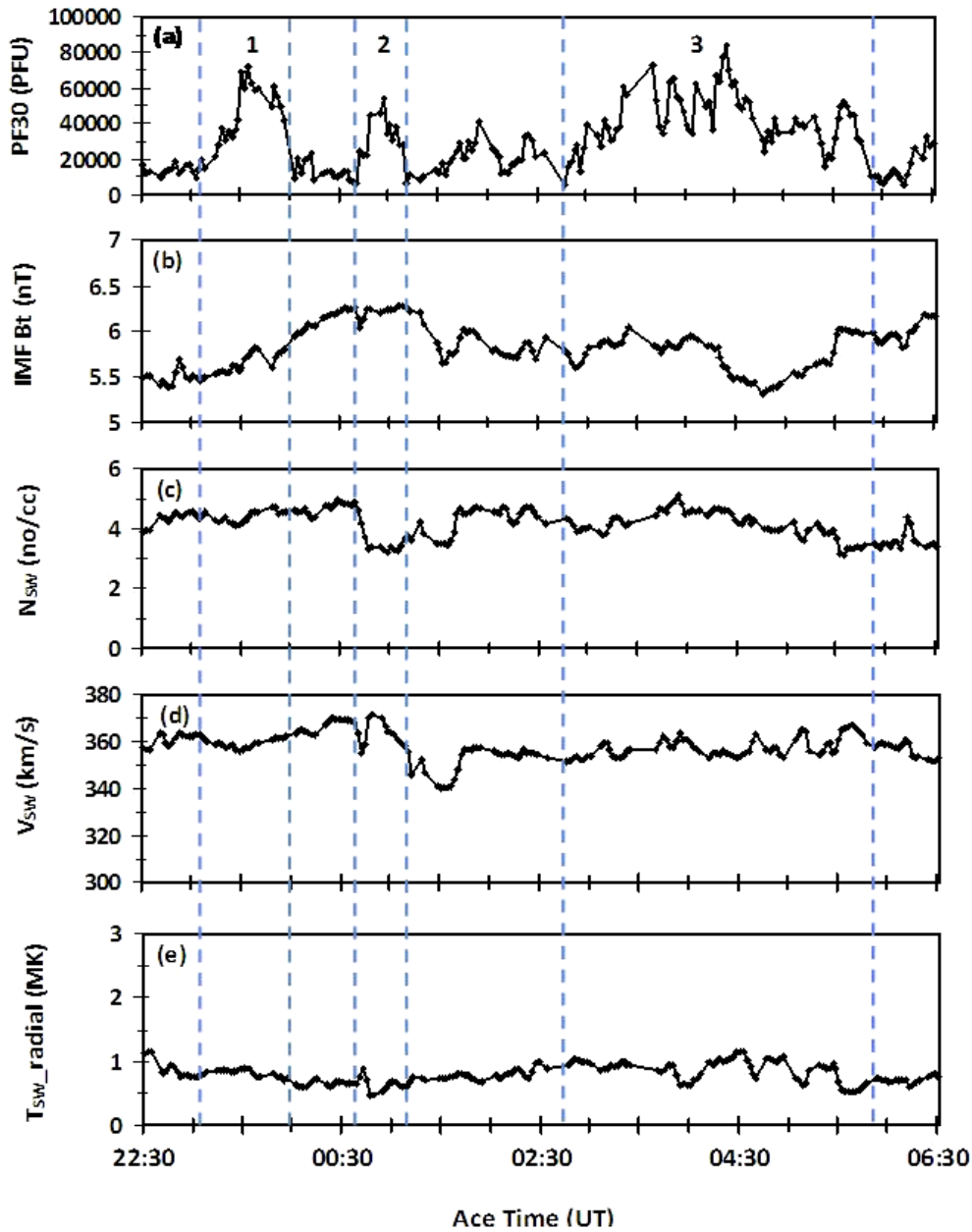
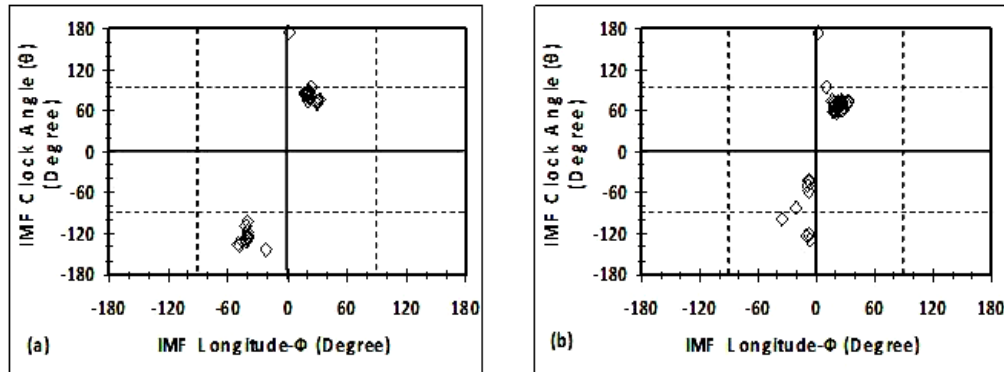


**Figure 4.11b:** ACE solar wind plasma data for Jan. 2, 2002. From top to bottom, panels give (a) PF30, (b) IMF strength, (c) density, (d) solar wind speed, and (e) proton temperature (radial) versus time. PF30 was added to guide the features in Cluster data. IMF strength was included for easy comparison. Cluster data were shifted to the ACE times concurrently to account for the solar wind convection time from ACE to Cluster. Horizontal axis indicates the time at ACE spacecraft.

In the panels of Figure 4.11, IMF does not show any particular feature that corresponds to the high energy particle flux increases in the magnetosheath. Within Burst 1, the solar wind speed, and density show a slight decrease. IMF Bx and IMF



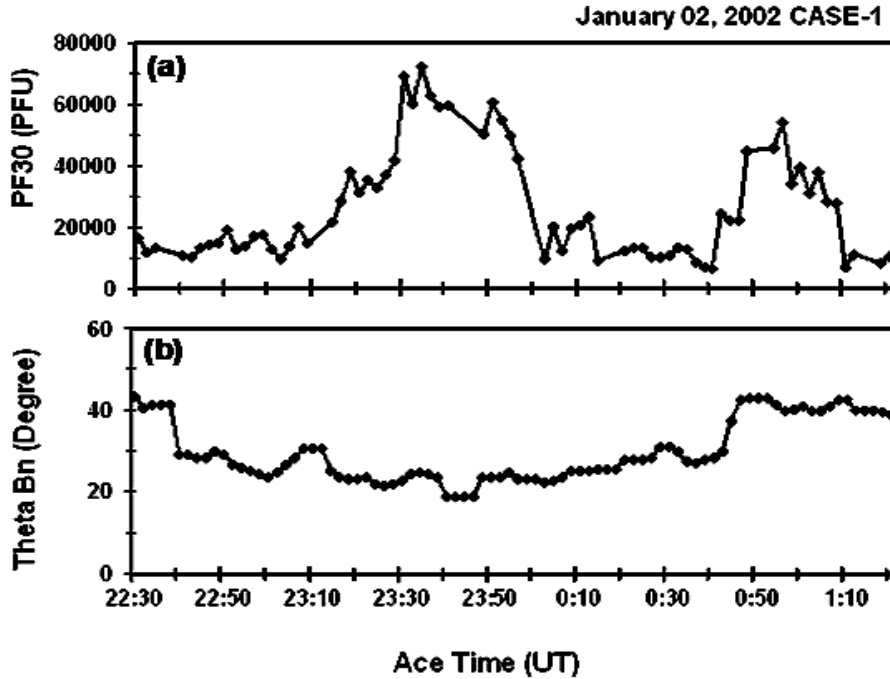
By do not change much at times corresponding to the cavity intervals. IMF Bz is either very close to zero or switches to southward orientations. The IMF Bx and By components corresponding to Burst 1 are about +5 nT and +2 nT respectively while IMF Bz decreases to zero. The solar wind density and speed are  $\sim 5 \text{ cm}^{-3}$  and  $360 \text{ km s}^{-1}$ . The solar wind temperature is  $\sim 80 \text{ MK}$ . Within Burst 2, IMF Bx is  $\sim 6 \text{ nT}$  and IMF By changes from  $-2 \text{ nT}$  to  $+4 \text{ nT}$  while IMF Bz is southward with a maximum of  $4 \text{ nT}$ . Solar wind density, speed and temperature do not change much. The clock angle variation shows that the IMF Bz is predominantly northward within Burst 1 and southward in Burst 2. Within Burst 3, IMF Bz switches from north to south, staying southward on average. The solar wind density, speed and temperature change little at times corresponding to Burst 3. Considering that magnetosheath phenomena are controlled by the IMF and solar wind plasma, Figure 4.11 does not reveal any particular feature or change in the IMF or solar wind plasma corresponding to the depressed regions in the magnetosheath. In Figure 4.12, we have examined scatter plots of IMF clock angle versus IMF longitude for (a) Bursts 1 and 2 excluding the magnetosheath intervals and (b) the magnetosheath intervals just around them but find that there is no specific field orientation for this event. The field orientation when particles are present in (a) resembles that when they were absent.



**Figure 4.12:** Scatter plots of IMF clock angle versus IMF longitude (a) within Flux Bursts 1 and 2, and (b) in the ambient magnetosheath surrounding Burst 1 and Burst 2 for January 2, 2002.

To investigate the IMF dependence further, we calculated the angle between the IMF and the bow shock normal ( $\Theta_{Bn}$ ) at the bow shock. To do this, we used the Kobel and Flückiger (1994) model to trace magnetosheath magnetic field lines from the spacecraft position back to the parabolic bow shock location given by Cooling et al.

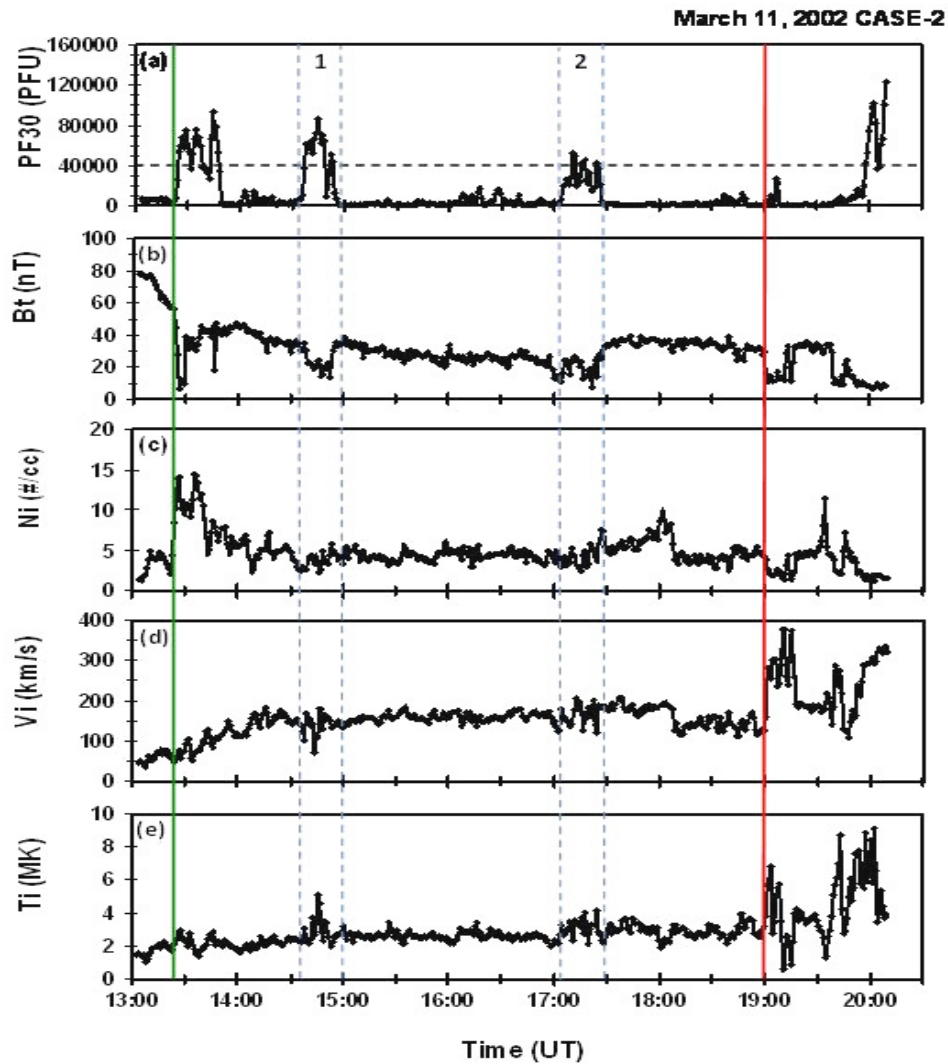
(2001). We then calculated  $\Theta_{Bn}$  at this location. Figure 4.13 compares (a) Cluster high energy particle flux observations with (b)  $\Theta_{Bn}$  versus time.  $\Theta_{Bn}$  varies between  $20^\circ$  and  $45^\circ$ , suggesting a quasi parallel shock for Case 1.



**Figure 4.13:** Theta Bn angle ( $\Theta_{Bn}$ ) for Case 1 (Jan. 2, 2002) including time intervals for Bursts 1 and 2.

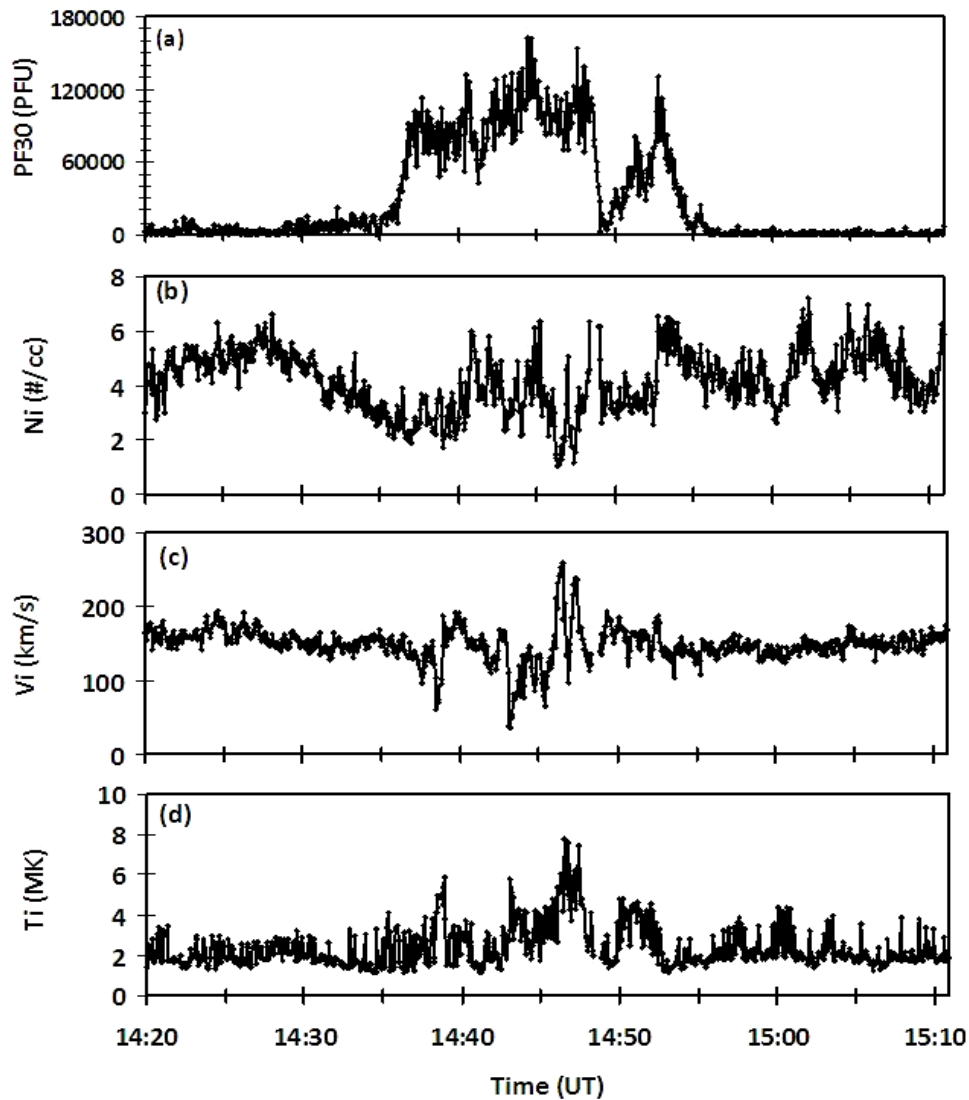
#### 4.2.2 Case 2: March 11, 2002

Figure 4.14 presents Case 2, which occurred on March 11, 2002. The spacecraft crossed the magnetopause (green) at 13:25 UT and the bow shock (red) at 19:00 UT. As in Figure 4.6, from top to bottom, the panels show 1 min energetic particle flux for  $PFU \geq 30$  keV, the magnetic field, density, speed, and temperature. High flux levels around 90,000 PFU in PF30 are noticeable in this case. We selected the events lasting 30 minutes from 14:30 UT to 15:00 and from about 17:00 UT to 17:30 UT as our flux burst events, and excluded the burst event at 13:00 UT. This case was shown earlier in our discussion of data selection.



**Figure 4.14:** From top to bottom, panels give particle flux (PF30), magnetosheath magnetic field strength, density, speed, and temperature data versus time for March 11, 2002. Red and green lines denote the bow shock and magnetopause while blue lines show intervals of the burst events studied.

When energetic particles occur, magnetic field strengths are depressed and variable. The magnetic field decreases from about 38 nT in the magnetosheath to 10 nT within Burst 1 and from 30 nT in the magnetosheath to 10 nT within Burst 2. Densities decrease from 5.5 to 2 cm<sup>-3</sup> within Burst 1 and from 5 to 2 cm<sup>-3</sup> in Burst 2. The speed decreased from 150 to 70 km s<sup>-1</sup> in Burst 1 and from about 150 to 100 km s<sup>-1</sup> in Burst 2. The temperature increased from 2.2 to 5.5 MK in Burst 1 and from 2.8 to 5.1 MK in Burst 2. The magnetic field fluctuated greatly within the cavities (Figure 4.4). High fluctuation levels are also seen in high resolution density, speed and temperature data (Figure 4.15).



**Figure 4.15:** The expanded time interval, including first flux burst of Case 1, from 14:20 UT to 15:10 UT for March 11, 2002 (Case 2) to illustrate high fluctuations in 4 sec (a) PF30, ion density (b), velocity (c), and temperature (d) data.

Figure 4.16 presents 1 min time resolution observations that also exhibit considerable variability. This is one of the clearest cases showing decreases in the magnetic field strength, density, and speed, but increases in the temperature. The temperature increases within the cavities are particularly noticeable in Case 2.

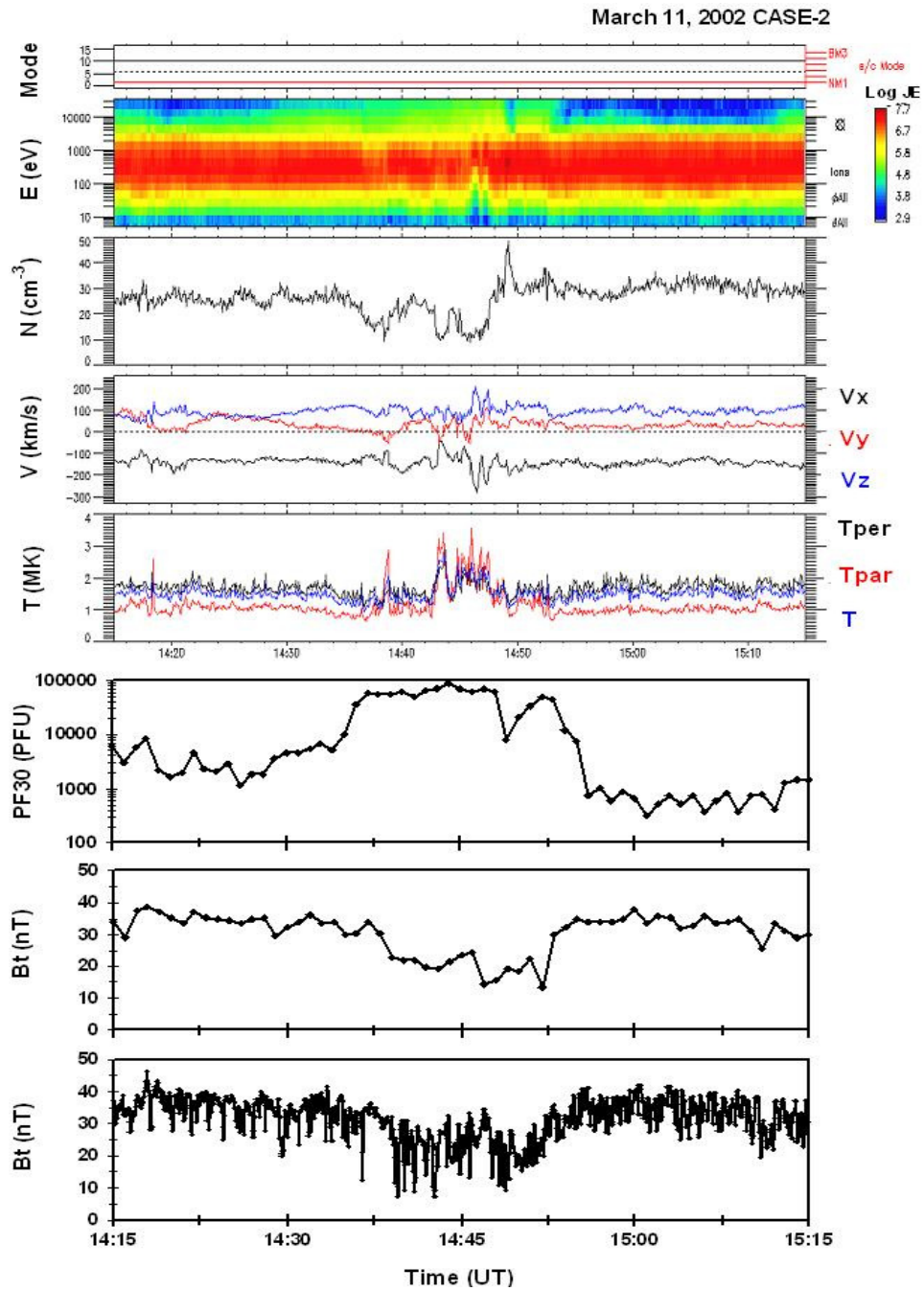


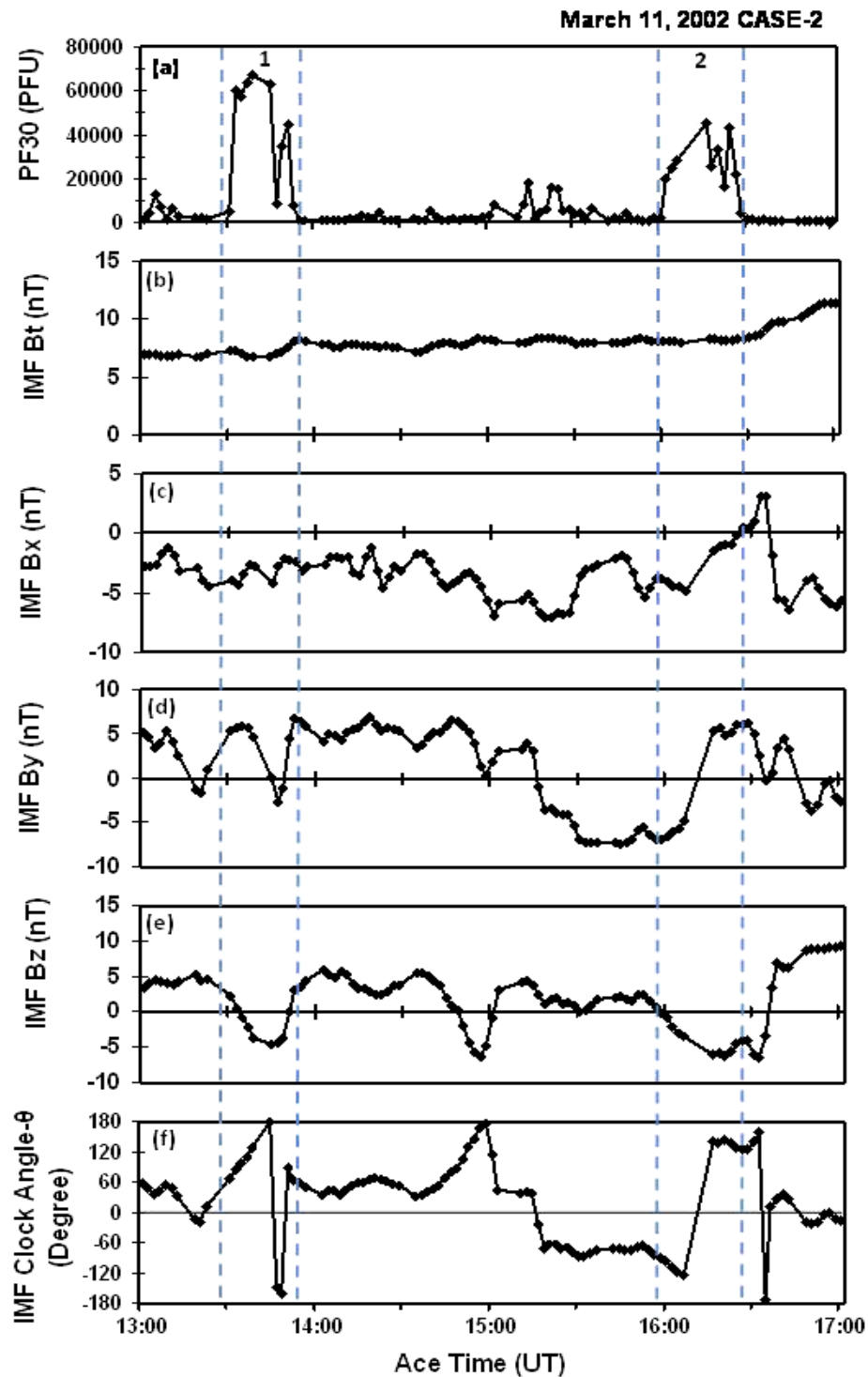
**Figure 4.16:** Spectral plot for Flux Burst 1 from 14:15 to 15:15 UT in March 11, 2002. Panels from top to bottom are mode of the instrument, energy in eV (left) and particle flux (right), density, velocity (left) and velocity components (right), and temperature (blue) for hot ions versus time. For comparison, we added 1 min PF30, 1 min magnetic field and 4 sec magnetic field in the figure.

The temperature increase seen in Case 2 corresponds to the presence of high energy particles within the magnetosheath cavities. CIS data (HIA instrument) ion distribution functions provide evidence for heating. Figure 4.16 presents CIS energy

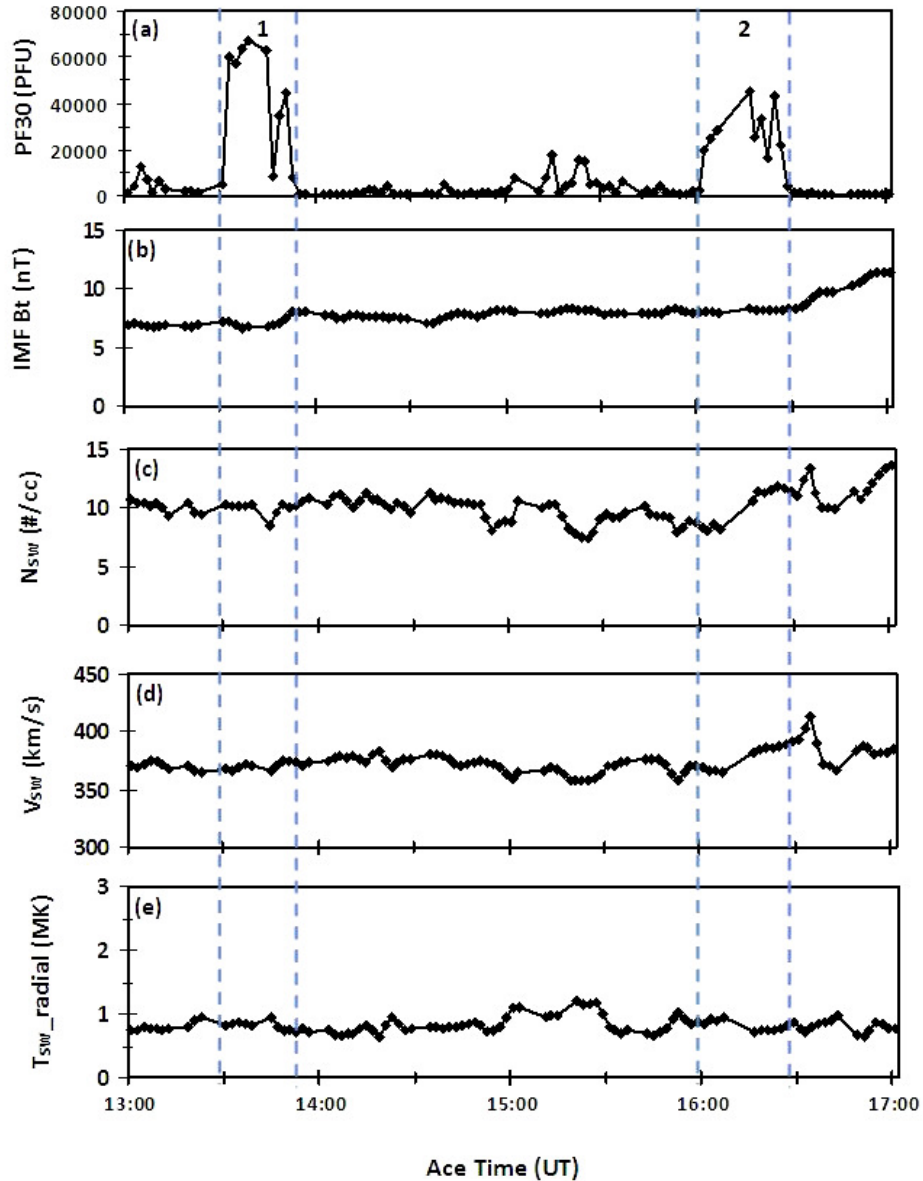
spectra for the interval from 14:15 UT to 15:15 UT covering Burst 1 in Figure 4.3. From top to bottom, the panels show the instrument mode, energy (eV) (scale on left) - particle flux (scale on right)-time ion spectrogram, density ( $\text{cm}^{-3}$ ), speed ( $\text{km s}^{-1}$ , left) and velocity components (right), and temperature (MK, in blue) versus time. At the bottom of this plot, we added our 1 min RAPID energetic particle, and 1 min and 4 sec magnetic field data. The spectra indicate that most particles in the distribution have energies from 40 to 2000 eV. Within the cavity from 14:38 to 14:52 UT, fluxes of suprathermal ions with energies above 10 keV are enhanced. We interpret this as the heating and the formation of a broader distribution. In three Cases presented in this study, we see temperature increases within the magnetosheath cavities. Examination of spectral plots and distribution functions for all our flux burst events shows some level of heating. Based on these spectral plots, we associate the slight temperature increases that occur within the cavities with the presence of high energy particles.

Plots for the magnetic field components and magnetic longitude versus magnetic latitude angle provide no further enlightening results on the structure of the magnetosheath cavities and are therefore not shown here. As in the previous case, we can only note that  $B_x$  and  $B_z$  decrease while  $B_y$  exhibits a substantial magnitude within the flux burst events, especially in Burst 2. Once again magnetic field directions are more variable during flux burst events than outside them.

Figure 4.17 presents IMF and solar wind plasma variations for Case 2. The IMF  $B_x$  and  $B_z$  components corresponding to both bursts are negative while IMF  $B_y$  varies between +5 nT and -5 nT. IMF  $B_z$  changes from +5 nT in the magnetosheath to -5 nT within Burst 1 and from +3 nT in the magnetosheath to -5 nT in Burst 2. The solar wind density decreases from 11 to  $8 \text{ cm}^{-3}$  during Burst 1, the speed from 375 to  $300 \text{ km s}^{-1}$ , and the temperature rises from  $\sim 2$  to  $\sim 4$  MK. A plot of the IMF clock angle versus the IMF magnetic longitude (not shown) does not show any particular direction favored for the burst intervals. Calculations of  $\Theta_{Bn}$  for Case 2 (not shown) give values between  $40^\circ$  and  $60^\circ$  for the event but  $\sim 20^\circ$  outside the event intervals in the magnetosheath.



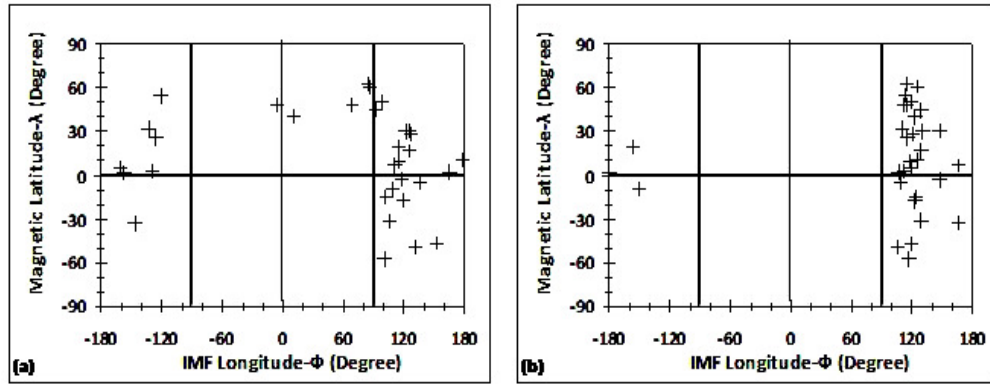
**Figure 4.17a:** ACE magnetic field data for Case 2, March 11, 2002. From top to bottom PF30, IMF strength, IMF Bx, IMF By, IMF Bz, and IMF clock angle versus time. PF30 was added to guide the features in Cluster data. Cluster data were shifted to the ACE times concurrently to account for the solar wind convection time from ACE to Cluster. Horizontal axis indicates the time at ACE spacecraft.



**Figure 4.17b:** ACE solar wind plasma data for Case 2, March 11, 2002. From top to bottom, panels give (a) PF30, (b) IMF strength, (c) density, (d) speed, and (e) proton temperature (radial) versus time. PF30 was added to guide the features in Cluster data. IMF strength was included for easy comparison. Cluster data were shifted to the ACE times concurrently to account for the solar wind convection time from ACE to Cluster. Horizontal axis indicates the time at ACE spacecraft.

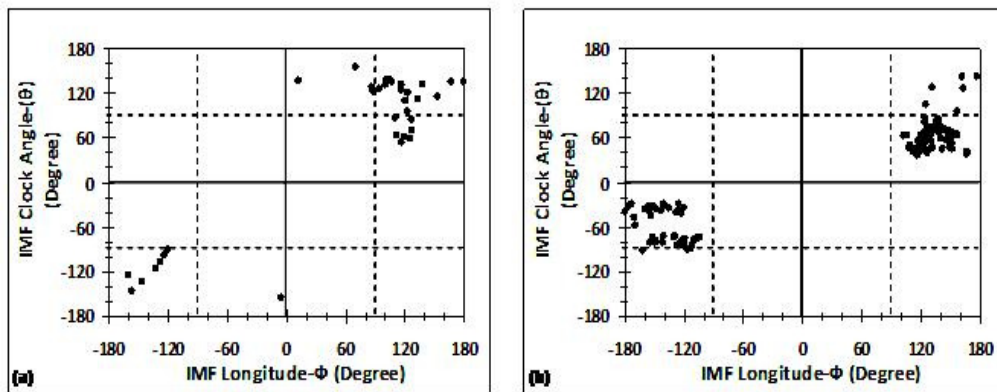
In Figure 4.18, we have examined scatter plots of IMF clock angle versus IMF longitude for (a) Bursts 1 and 2 excluding the magnetosheath intervals and (b) the magnetosheath intervals just around them seen in March 11, 2002. As in Figure 4.12, plots do not reveal any clear, close relationship between the field orientation and presence of the energetic particles.





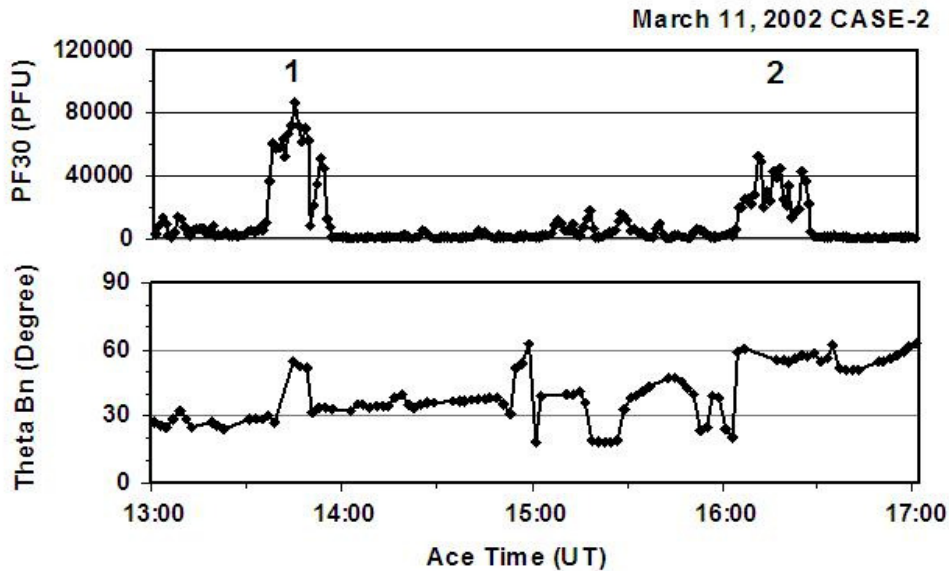
**Figure 4.18:** Scatter plots of magnetic latitude versus magnetic longitude (a) within Bursts 1 and 2, and (b) in the ambient magnetosheath surrounding Burst 1 and Burst 2 for March 11, 2002.

Figure 4.19 gives the plot of the IMF clock angle versus the IMF magnetic longitude seen. This figure does not show any noticeable direction favored for the flux burst intervals.



**Figure 4.19:** Scatter plots of IMF clock angle versus IMF longitude for (a) within Flux Bursts 1 and 2 and (b) magnetosheath intervals around Flux Bursts 1 and 2 for March 11, 2002.

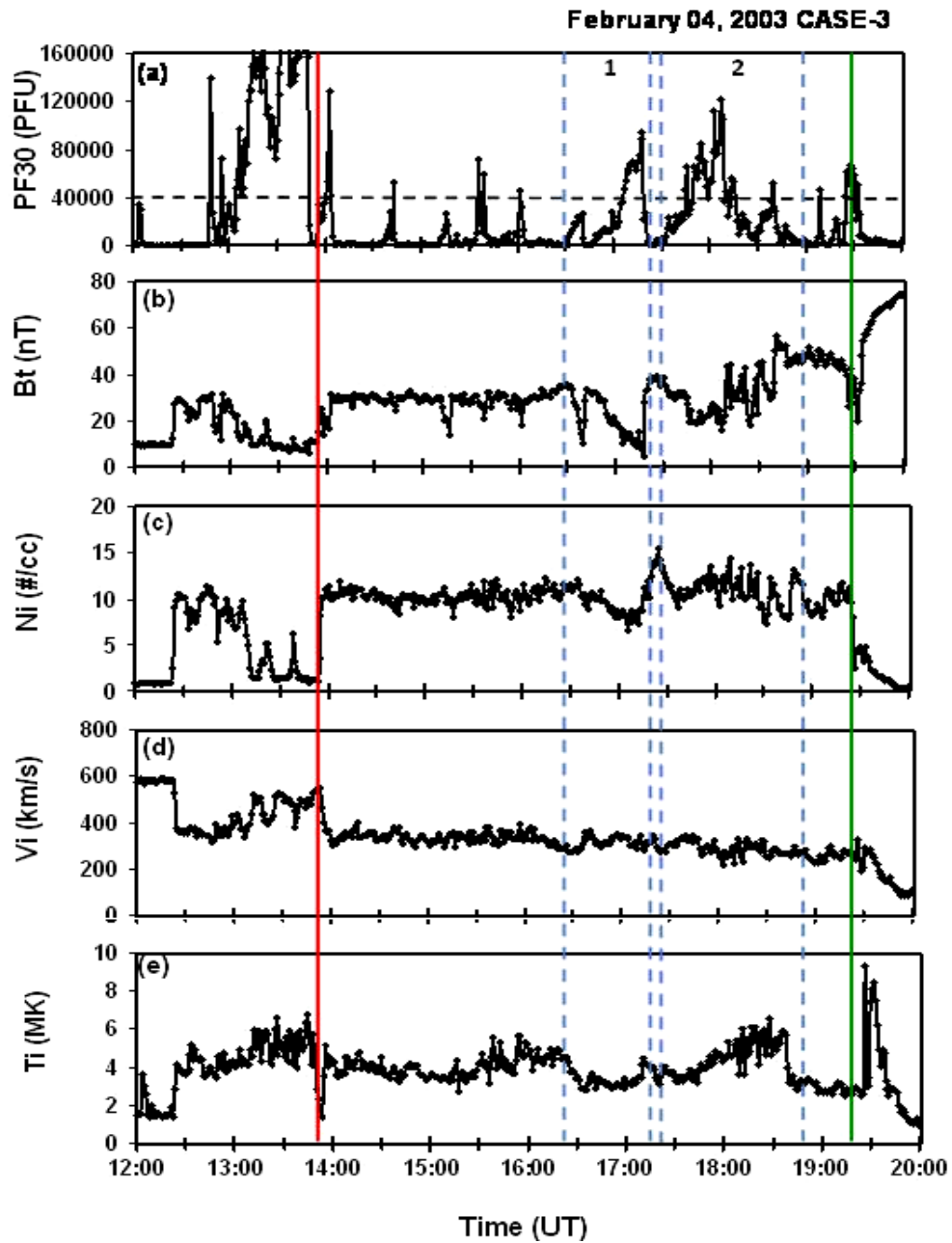
Calculations of  $\Theta_{Bn}$  for Case 2 (Figure 4.20) give values between  $40^\circ$  and  $60^\circ$  for Flux Burst 1 and Flux Burst 2 but  $\Theta_{Bn}$  is  $\sim 20^\circ$  outside intervals of flux burst events in the magnetosheath.



**Figure 4.20:** Theta Bn angle ( $\Theta_{Bn}$ ) for Case 2 (March 2, 2002) including time intervals for Flux Bursts 1 and 2.

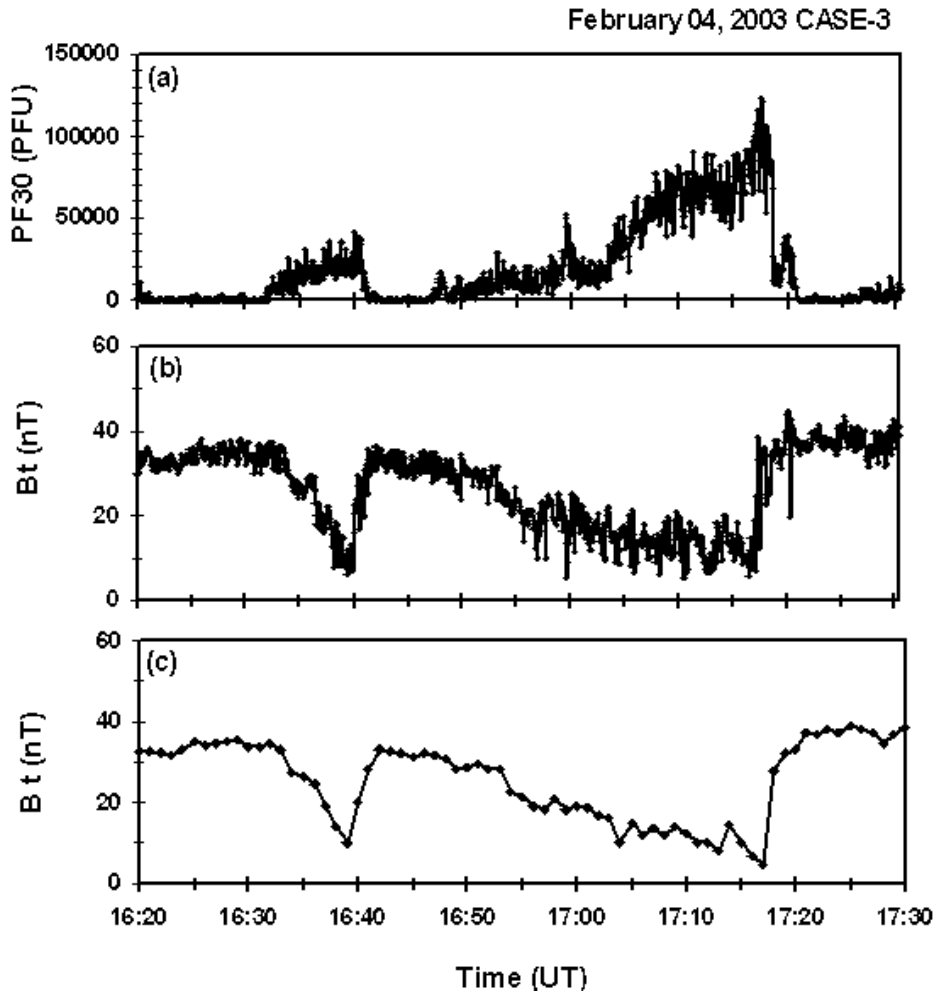
#### 4.2.3 Case 3: February 4, 2003

Figure 4.21 presents our third example, observed in February 4, 2003. This is a clear case in which each sharp, spiky increase in the high energy ion flux elicits a corresponding variation in the magnetic field strength and density. The bow shock (red) and magnetopause (green) were observed 13:50 UT and 19:20 UT, respectively. Two bursts delimited by vertical dashed blue lines were selected as flux burst events. Burst 1 lasted 45 min from 16:30 UT to 17:15 UT and Burst 2 lasted 85 min from 17:23 UT to 18:48 UT. Peak flux levels varied between 90,000 PFU and 110,000 PFU. The corresponding magnetic field and density data show large depressions and enhanced variations within the cavity regions corresponding to these burst events. The background level of the magnetosheath variations outside the events was low compared to that within the depressed regions. The magnetic field decreased from 35 nT in the ambient magnetosheath to 5 nT in Burst 1 and 22 nT in Burst 2. The density decreased from  $11 \text{ cm}^{-3}$  in the ambient magnetosheath to  $7.5 \text{ cm}^{-3}$  within Burst 1 and  $8.5 \text{ cm}^{-3}$  within Burst 2. Despite depression signature evident in Burst 2, the large amplitude fluctuations mark the boundaries of this event best. The temperature shows a great and distinct increase and enhanced variability within Burst 2. The intervals of high energy protons correspond to slight decreases in the velocity and enhanced fluctuations.



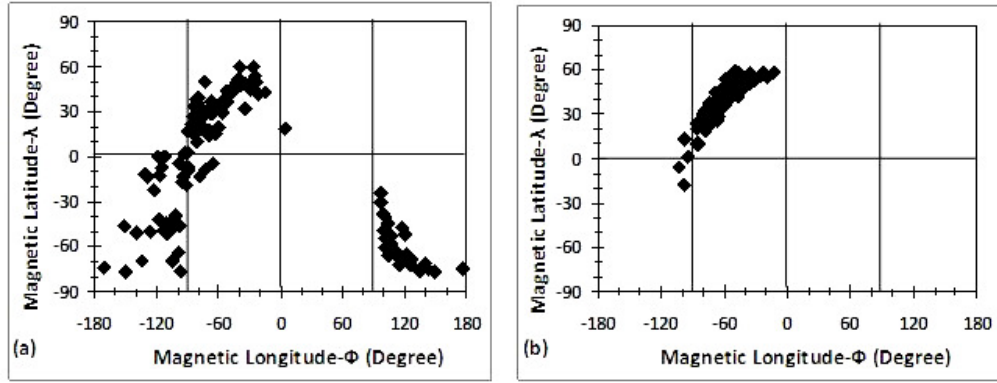
**Figure 4.21:** Plots of particle flux (PF30), magnetosheath magnetic field strength, density, speed, and temperature data versus time for February 4, 2003 (from top to bottom). Red and green lines show bow shock and magnetopause while blue lines indicate the burst events studied.

Figure 4.22 presents observations of Burst 1 in the same format as that of Figures 4.4 and 4.7. The figure reveals the highly variable magnetic field within the depressed region.



**Figure 4.22:** Plot of the expanded time interval for Burst 1 in Case 3 (Feb. 4, 2003). As in Figure 2 and Figure 5, panels give (a) 4 sec PF30, and (b, c) 4 sec and 1 min magnetosheath magnetic field.

While plots of the magnetic field components provide no further details about the depressed regions, the plot of magnetic longitude versus latitude again indicates greater magnetic field variability in the depressed regions than in the surrounding magnetosheath magnetic fields (Figure 4.23).



**Figure 4.23:** Scatter plots of magnetic latitude versus magnetic longitude (a) within Bursts 1 and 2, and (b) in the ambient magnetosheath surrounding Burst 1 and 2 for February 4, 2003.

Figure 4.24 presents IMF dependence for Case 3. As in previous Cases, the panels in Figure 4.24a gives IMF components and IMF Clock Angle, and Figure 4.24b shows solar wind plasma data for the time interval of 16:10 UT to 19:10 UT in Figure 14. IMF  $B_x$  is strong within both flux burst events, but IMF  $B_y$  decreases. IMF  $B_z$  decreased from 5-8 nT during intervals corresponding to the magnetosheath proper to a slightly southward average value in Burst 1 and 5 nT southward in Burst 2. The solar wind density stays almost constant near  $3 \text{ cm}^{-3}$  while the speed decreases within the bursts. The temperature varies around 0.25 and 0.3 MK within Bursts 1 and 2, respectively.

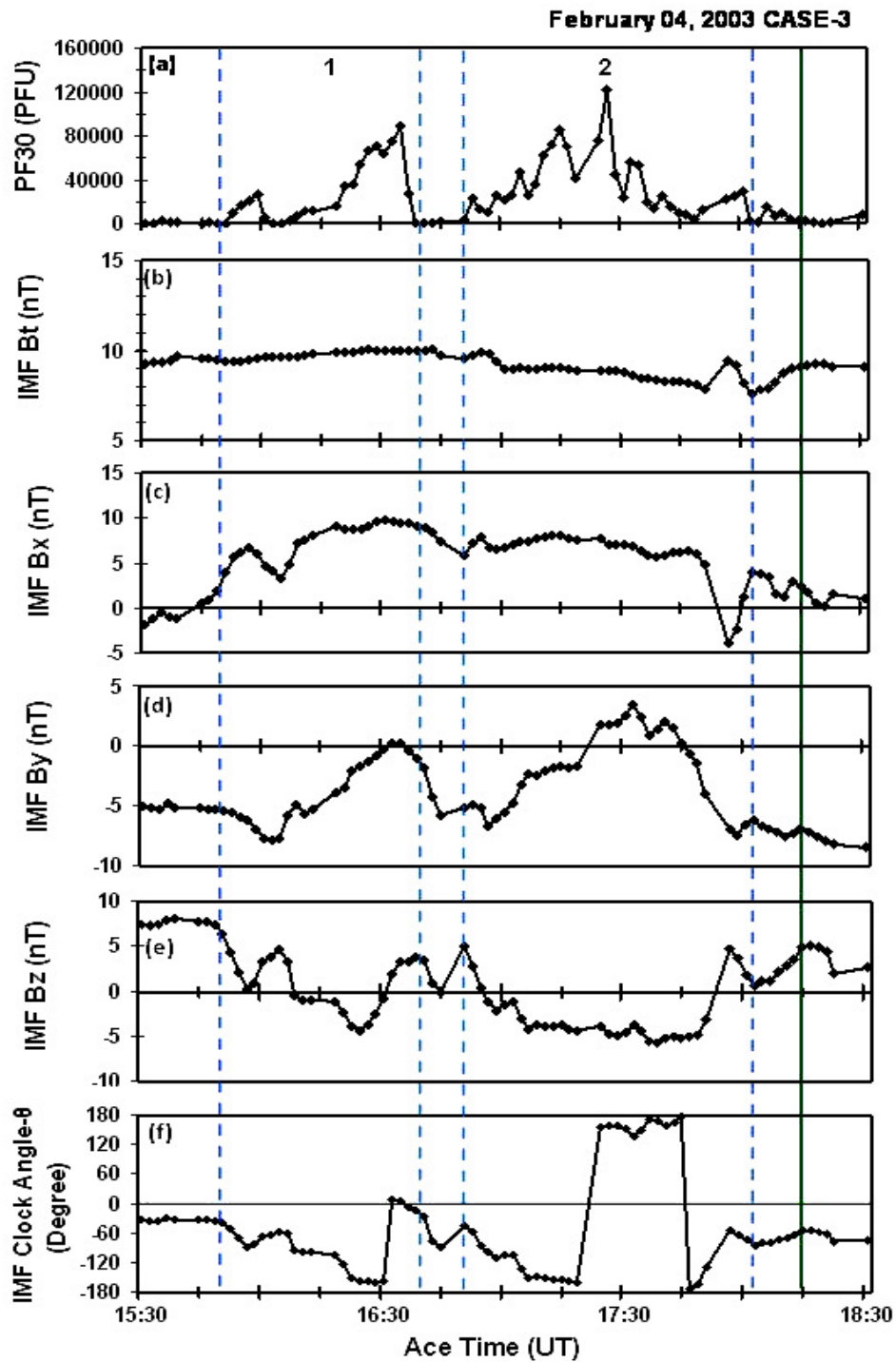


**Figure 4.24a:** ACE magnetic field data for Case 3, Feb. 4, 2003. From top to bottom PF30, IMF strength, IMF Bx, IMF By, IMF Bz, and IMF clock angle. PF30 was added to guide the features in Cluster data. Cluster data were shifted to the ACE times concurrently to account for the solar wind convection time from ACE to Cluster. Horizontal axis indicates the time at ACE spacecraft.

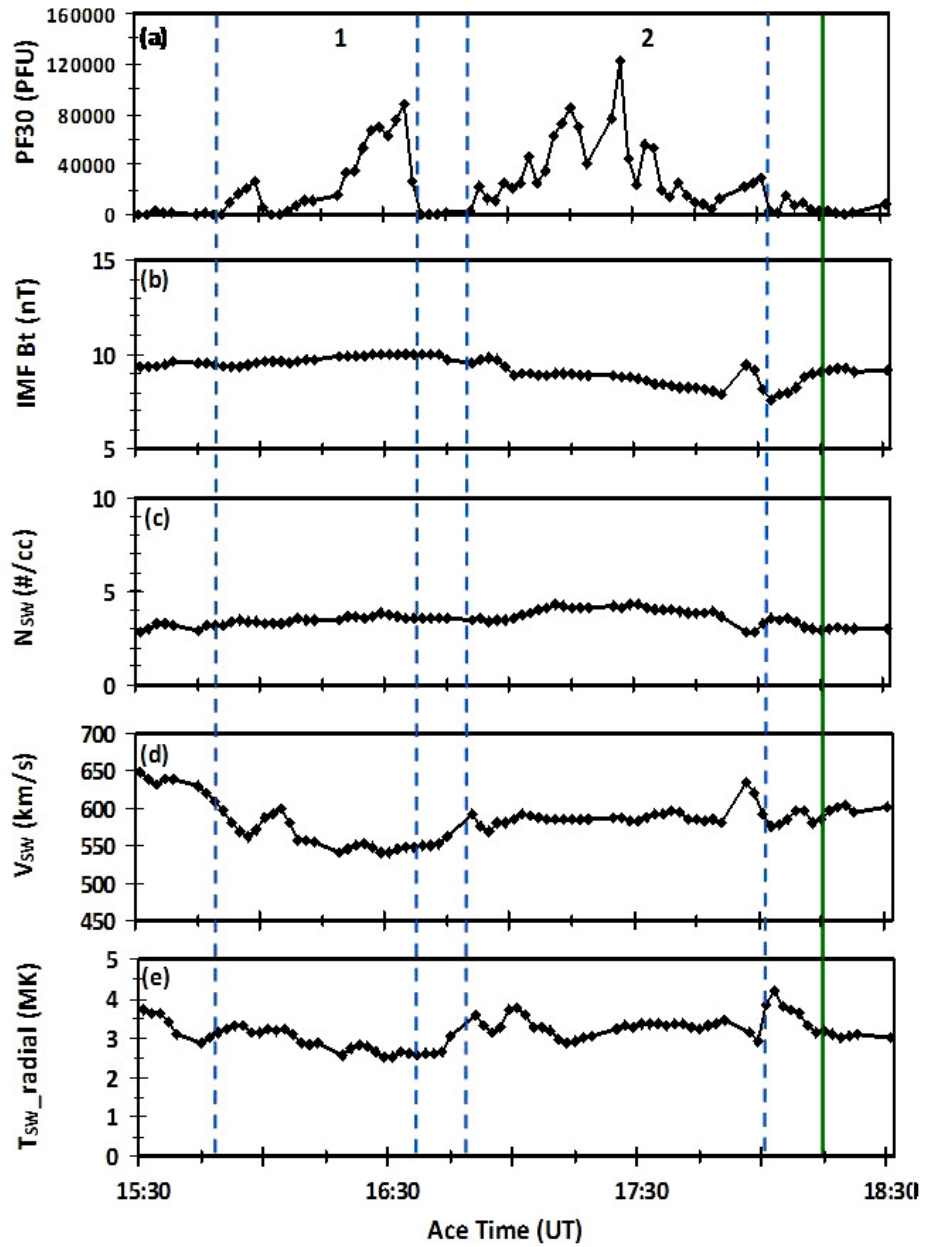


**Figure 4.24b:** ACE solar wind plasma data for Case 3, Feb. 4, 2003. From top to bottom, panels give (a) PF30, (b) IMF strength, (c) density, (d) speed, and (e) proton temperature (radial) versus time. PF30 was added to guide the features in Cluster data. IMF strength was included for easy comparison. Cluster data were shifted to the ACE times concurrently to account for the solar wind convection time from ACE to Cluster. Horizontal axis indicates the time at ACE spacecraft.

### 4.3 Comparison with the Foreshock Cavities

The examples presented above demonstrate the existence of magnetosheath cavities characterized by depressed magnetic field strengths, densities and speeds, but enhanced temperatures. They occur in conjunction with bursts of  $\geq 30$  keV ions. We attribute the presence of the magnetosheath cavities to pressure effects associated with the energetic particles.

The depressions in the magnetosheath magnetic field strength and density within the magnetosheath cavities can reach as much as 70% and 50% with respect to values in the ambient magnetosheath. The speed decreases by about 40% and the temperature increases by about 60% within the magnetosheath cavities. As a result, the total pressure calculated by summing the gas, ram (dynamic) and magnetic pressures within the magnetosheath can drop by as much as 80% within the cavities. Figure 4.25 presents the time variation of the total pressure within Bursts 1 and 2 of Case 1. The anticorrelation between the high energy particle flux (a) and the total pressure (b) within the magnetosheath cavities is evident. Variations in the dynamic pressure (not shown) exceed those of the gas and magnetic pressures. Figure 18a presents a scatter plot of energetic particle fluxes versus total pressure. The best chi-square linear fit to the data in Figure 18a gives a correlation coefficient around 0.8.

The magnetopause moves in response to solar wind/foreshock pressure pulses (Sibeck et al., 1989a, b; 1990, 1995; 2001; Russell et al., 1997), the Kelvin-Helmholtz instability (Ogilvie and Fitzenreiter, 1989; Safrankova et al., 1997), and flux transfer events (Sibeck, 1995; Russell, 1997), but lies at rest where magnetosheath and magnetospheric pressures balance. Since the magnetosheath pressure is proportional to the solar wind dynamic pressure, observations from solar wind monitors far upstream from the bow shock are frequently used to predict the location of the magnetopause. However, our results indicate that the densities and pressures within magnetosheath cavities are far less than those in the ambient magnetosheath and therefore less than those that would be predicted on the basis of solar wind observations. Depressed pressures should permit the magnetopause to expand outward. We used the model of Shue et al. (1997) to calculate the distances to the magnetopause as a function of the north/south IMF orientation and the



dynamic pressure. Shue et al. (1997) give the relationship between the subsolar magnetopause, dynamic pressure and IMF B<sub>z</sub> as follows:

$$r_0 = (11.4 + 0.013B_z) \cdot (D_p)^{-1/6.6} \quad \text{for } B_z \geq 0$$

$$r_0 = (11.4 + 0.14B_z) \cdot (D_p)^{-1/6.6} \quad \text{for } B_z < 0$$
(4.1)

$$\alpha = (0.58 - 0.0010B_z) \cdot (1 + 0.010D_p)$$
(4.2)

$$r = r_0 \left( \frac{2}{1 + \cos \theta} \right)^\alpha$$
(4.3)

where  $r_0$ ,  $D_p$ , and  $\alpha$  are the standoff distance, dynamic pressure and the level of tail flaring, respectively. Standoff distance ( $r_0$ ) is the distance at which the solar wind dynamic pressure and Earth's dipole magnetic field at subsolar region counterbalances each other.  $\theta$  is the angle between the Earth-Sun line and the direction of  $r$ . We calculated the magnetopause distance using Cluster observations and Ace observations in Shue et al.'s (1997) magnetopause model. Figure 4.25 presents the ratio of the distance to the magnetopause determined from Cluster observations to the distance determined from lagged ACE measurements for Case 1. Values for  $(Rmp)_{\text{Ratio}}$  exceed 1 throughout the interval shown but reach 1.3 within the cavities. The scatter plots in Figure 4.26 show the relationship between the magnetopause ratio and the high energy particle flux. The ratio is greater when the flux of energetic particles is large. The correlation coefficient is found to be about 0.8 in both cases.

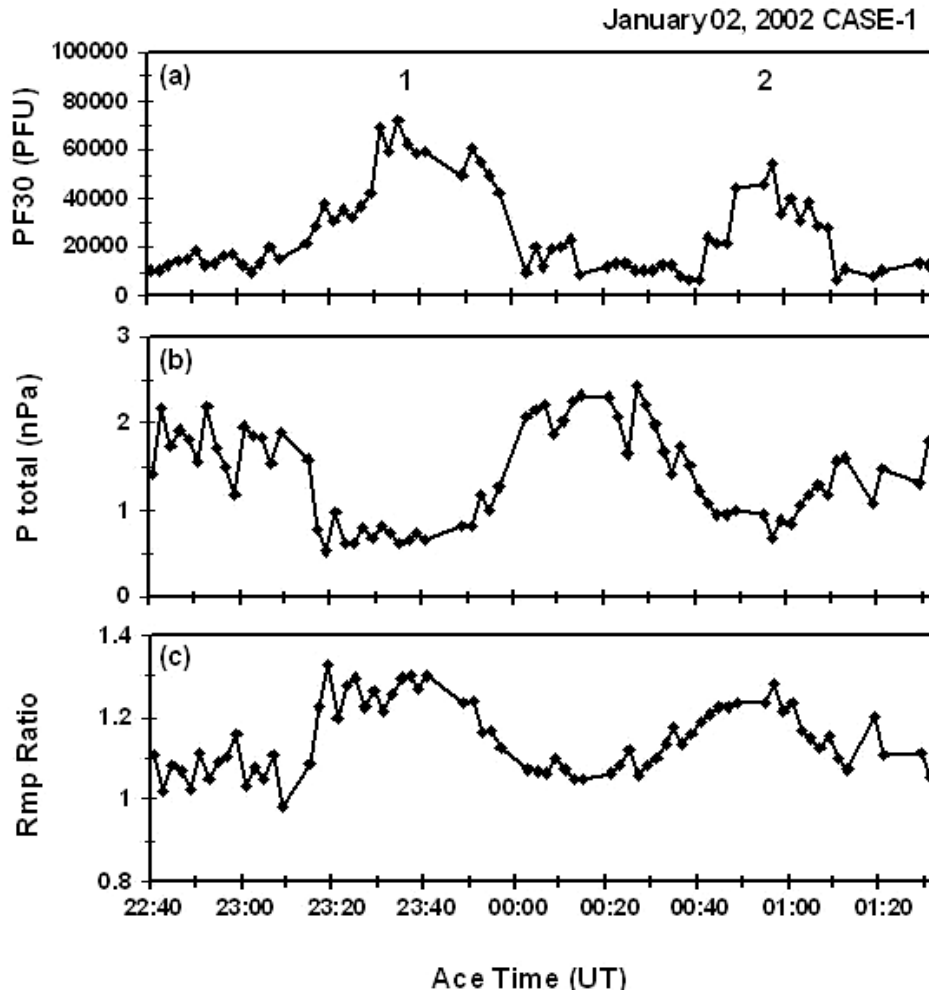


**Figure 4.25:** Time variation of total pressure and the magnetopause ratio for Case 1 (Jan. 2, 2002). Panels from top to bottom give (a) particle flux (PF30), (b) total pressure in the magnetosheath, and (c) the ratio of the magnetopause distances calculated using Cluster magnetosheath and Ace solar wind observations. Shue's magnetopause (1997) was used to calculate the magnetopause boundary. Time interval covers Bursts 1 and 2 in Case 1 and horizontal axis shows the time at ACE.

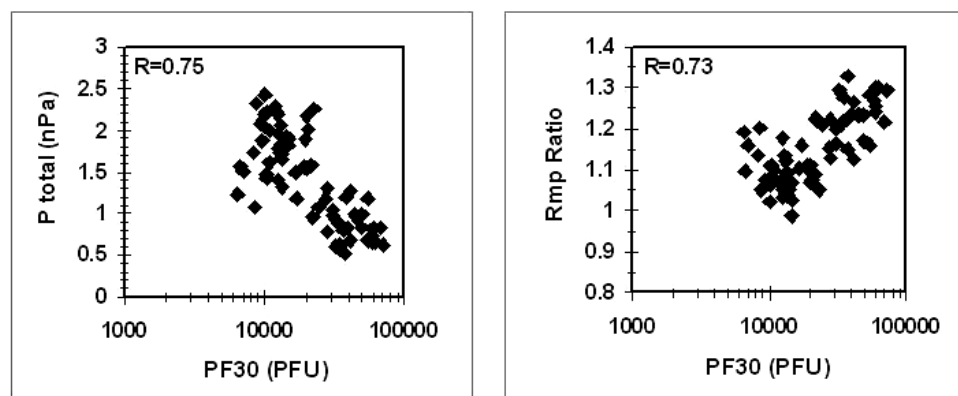


**Figure 4.26:** Scatter plots of total pressure in the magnetosheath (left) and magnetopause ratio (right) versus particle flux (PF30) for January 2, 2003. The panels show how total magnetosheath pressure and the magnetopause ratio vary with increasing energetic particle flux.

Some aspects of magnetosheath cavities resemble those of foreshock cavities, while others do not. Both types of cavities are associated with energetic particles. They both exhibit depressed magnetic field strengths and densities and large variations in these parameters. Although thermal plasma temperatures decrease within foreshock cavities, suggesting an expansion in response to the enhanced pressures associated with the presence of suprathermal ions, inclusion of these ions in moment calculations actually results in enhanced temperatures within the cavities. Expanding cavities compress neighboring plasmas, creating shoulders of enhanced density and magnetic field strength on their edges. Magnetosheath cavities do not exhibit these shoulders, indicating that they are not expanding. Whereas foreshock cavity durations typically vary from 1 to 10 min, average durations for magnetosheath cavities range from 15 to 30 min (Sibeck et al., 2001).

In addition to depressions in the magnetic field strength and density, magnetosheath cavities can be identified on the basis of enhanced fluctuations in all parameters. The magnetic latitude versus longitude plots for all three cases (e.g. Figure 4.10) exhibit this scatter. Hayosh et al. (2004) sought evidence for a relationship between high energy particle fluxes and the total ion flux in 5 years of Interball nightside flank observations. They found only a weak relationship. On the other hand, they found a stronger relationship between the flux levels of high energy particles and fluctuations in the magnetosheath, particularly when either streamlines or field lines connected the point of observation to the quasiparallel shock. They concluded that most of the

energetic particles originated from the foreshock and were swept into the nightside magnetosheath. Thus both the upstream solar wind and foreshock regions contributed to the ion flux fluctuations of the nightside magnetosheath. Our study also found a close association between large amplitude fluctuations in the magnetosheath parameters and the presence of the energetic particles. In fact, we frequently used the fluctuations to identify the magnetosheath cavities.

Sibeck et al. (2001) reported that the foreshock cavities occur on magnetic field lines connected to the bow shock. Sibeck et al. (2002) found that the cavities were not associated with sharp IMF discontinuities. We have found no particular dependence on the IMF orientation or solar wind plasma conditions. Within the majority of our flux burst events, the corresponding IMF is predominantly southward. Within long lasting flux burst events, IMF Bz usually switches its direction from north to south or vice versa. The ambient magnetosheath intervals appear to correspond to an IMF with substantial equatorial components.  $\Theta_{Bn}$  varied between  $20^\circ$  and  $45^\circ$  within our events, suggesting they are also associated with the quasi-parallel shock.

Recent results from global hybrid code simulations (N. Omidi, personal communication, 2009) indicate that foreshock cavities can be convected through bow shock and into the magnetosheath. Within the magnetosheath structures, magnetic field strengths and temperatures were correlated, magnetic field strengths and densities anticorrelated, and fluctuation levels high. By contrast, our case studies from Cluster presented in this section show that magnetic field strengths and densities diminish in response to increasing temperatures. The comparative study of the Cluster findings with the results from the hybrid simulations were investigated in Chapter V.

#### **4.4 Summary from the Cluster Search**

In this part of our study, we presented three case studies of Cluster observations to study the effects of energetic particles on the magnetosheath plasma and magnetic field. We summarize our findings below:

1. When enhanced fluxes of energetic particles are present in the magnetosheath, magnetic field strengths, densities and velocities decrease, but

temperatures increase. We call these intervals magnetosheath cavities by analogy to foreshock cavities.

2. All magnetosheath parameters exhibit enhanced fluctuations within magnetosheath cavities.

3. Spectral plots indicate ion heating within the cavity regions.

4. Decreases in the total pressure applied to the magnetosphere by the cavities should permit the magnetopause to lie 30% further outward from the position that would be predicted on the basis of solar wind observations made far upstream.

5. We find no dependence of magnetosheath cavities on IMF or solar wind plasma conditions, with the exception that preliminary  $\Theta_{Bn}$  calculations show that the events correspond to quasiparallel shock conditions.

6. Simultaneous multipoint observations are needed to determine whether magnetosheath cavities result from foreshock cavities transmitted into the magnetosheath.

7. Further studies are also needed to determine how magnetosheath cavities may affect magnetosheath/magnetosphere coupling, including boundary motion and reconnection.



## **5. STATISTICAL RESULTS BASED ON CLUSTER CASES**

### **5.1 Plasma and Magnetic Field Structure of the Magnetosheath in the Presence of Energetic Particles**

Chapter 4 described the magnetosheath cavities, their characteristics and IMF and solar wind dependence on case basis. In this section, we present the statistical results for approximately 267 flux burst events detected in 182 magnetosheath crossings (cases) of two years of Cluster data coverage from 2002 to 2003. The selection criteria (increase in flux within a time interval greater than 10-min and above 40 000 PFU) were applied to each case. Figure 5.1 gives the average positions of the trajectory for each magnetosheath crossing of 267 events in (a) XY-, (b) XZ-, (c) YZ-, and (d) XR- planes. The magnetopause and bow shock positions for average solar wind conditions were shown in green and red respectively.

Similar to Case studies presented in the previous chapters, we carefully examined each of the 267 burst events and categorized the variations that we see in magnetic field, density, temperature and speed parameters in the magnetosheath. Table 4.1 in the next page summarizes the result of this search.

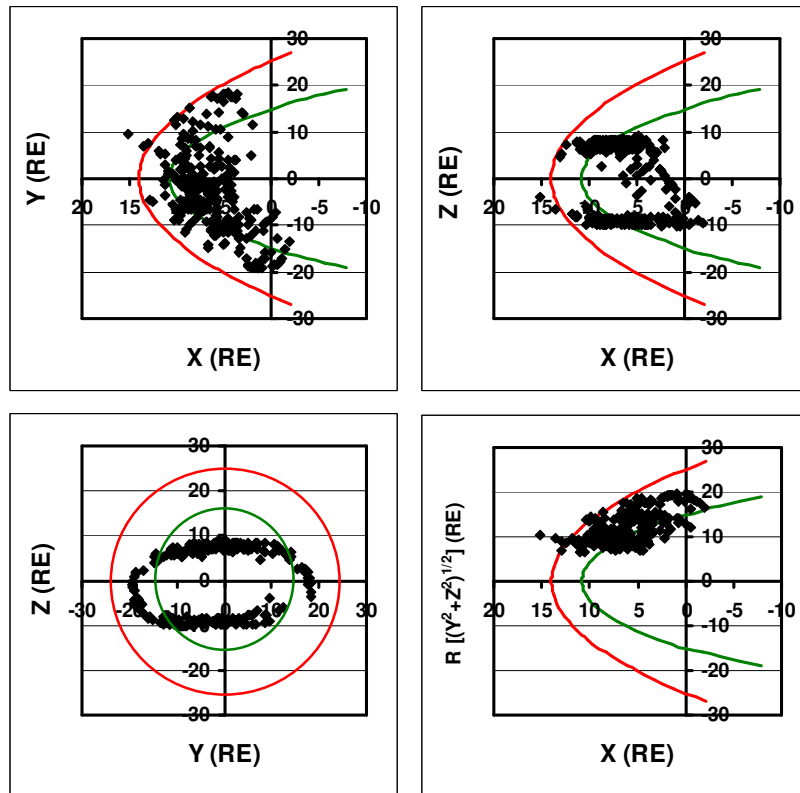


**Figure 5.1:** Average positions of the Cluster trajectories in the magnetosheath for all events (267 flux burst events) in (a) XY-, (b) XZ-, (c) YZ-, and (d) XR-planes. The magnetopause and bow shock for average solar wind conditions were indicated in green and red respectively.

**Table 5.1:** Average characteristics of the magnetosheath plasma and magnetic field seen in 267 events in the presence of the high energy particles.

Magnetosheath Parameter	Variation
Total Magnetic Field	Decreasing + Fluctuating
Ion Density	Decreasing + Fluctuating
Ion Temperature	Increasing + Fluctuating
Ion Velocity	Variable Sometimes Decreasing + Sometimes Fluctuating



Histograms in Figure 5.2 present the distributions of the normalized magnetic field for the cavities corresponding to flux burst events (a) and for the ambient magnetosheath of each cavity (b). The second case is named as non-cavity (Non-FBE). The magnetic field in these histograms was normalized to the total IMF to depict the energetic particles effects by removing the IMF related variations.

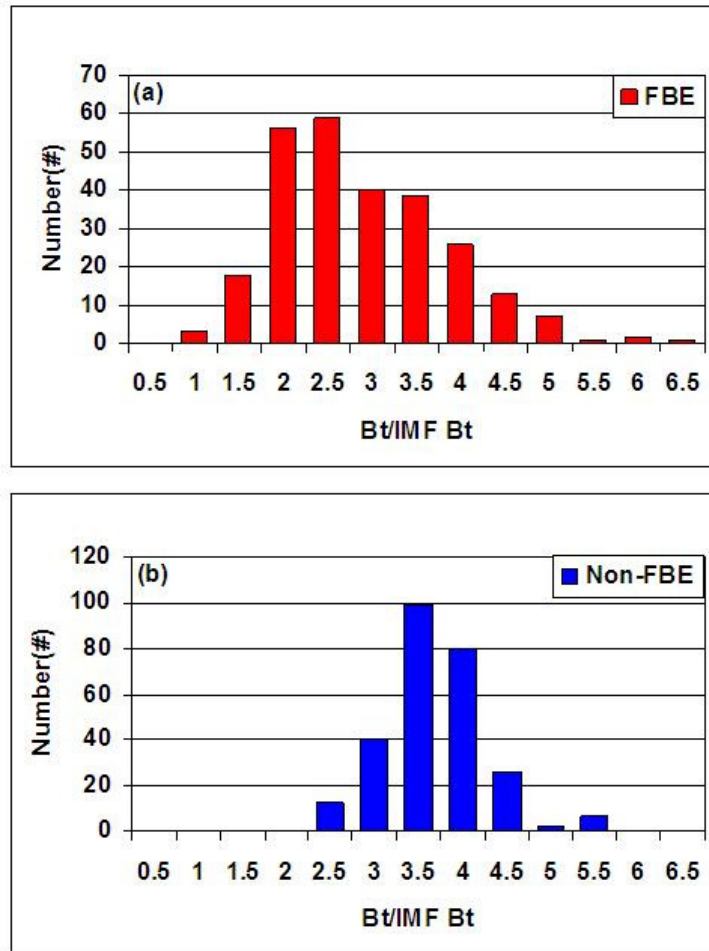


**Figure 5.2:** Histograms of total magnetic field within the cavities (a) and for ambient magnetosheath of the cavities (b) of 267 Burst Events. The magnetic field given on the horizontal axis is normalized to total concurrent IMF. A clear shift toward higher magnetic fields is seen in the non-cavity case given in (b).

It is clear that the histograms are left sided in the case of FBE panel while it is right sided in the non-FBE panel. In the histograms, we see that the magnetic field within the cavities peaks at 2.5 while non-cavity events have a peak at 3.5. Out of 267 flux burst events, 58 % have magnetic fields ranging from 2 to 3 within the cavities (histogram (a) in Figure 5.2). On the other hand, in the non-cavity histogram, 37 %

of the non-FBEs have magnetic fields 3.5. These histograms clearly verify the depression of the magnetic field within the cavities seen in the presence of the high energy particles in the magnetosheath.

Figure 5.3 gives the similar histograms for density (a), temperature (b), and speed (c). In the histograms, the red represents the in-cavity events while the blue represents the out-cavity which is the ambient magnetosheath.

Within the cavity events, density peaks at 1 while speed and temperature peak at 0.5 and 30 respectively. Out of the cavities, density and temperature and speed peak at the same number of the cavity events.

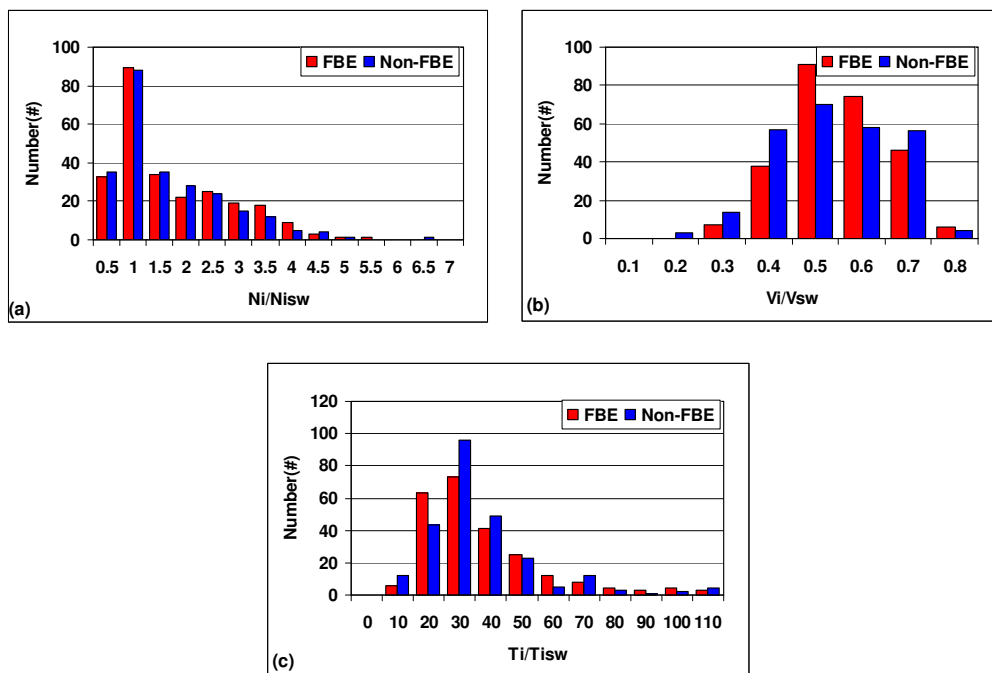


**Figure 5.3:** Histograms of ion density (a) ion density, speed (b), and temperature (c) for cavities (red) and ambient magnetosheath (blue) for 267 Burst Events. Parameters given on the horizontal axis were normalized to solar wind parameters.

## 5.2 Fluctuation Levels in the Presence of Energetic Particles

In Chapter 3 and especially in Chapter 4 we have emphasized that the energetic particles increases the level of fluctuations within the cavities. All magnetosheath parameters exhibit enhanced fluctuations within magnetosheath cavities. The large amplitude variations are one of the distinguishing features of the magnetosheath cavities in the presence of high energy particles. Figure 5.4 illustrates this point and

presents the scatter plots of the magnetosheath field versus the IMF within the cavities (a) and outside the cavities (b). As seen in the right panel of Figure 5.4, IMF is carried the magnetosheath and remains mostly same while there are no high energy particles in the magnetosheath. Therefore, the correlation coefficient is very close to 1 (0.9) as indicated on the top right corner of the panel (b). However, the correlation coefficient is lower as 0.5 owing to the scattering and enhanced fluctuations within the magnetosheath cavities (Figure 5.4a).

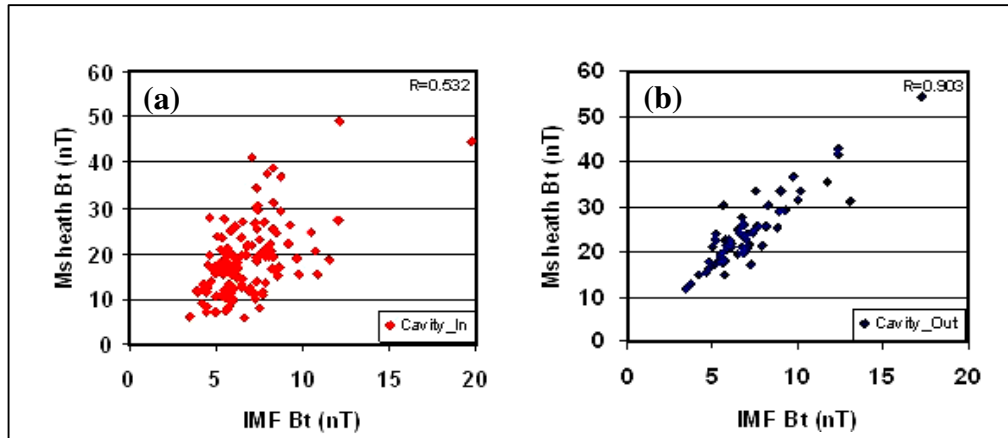


**Figure 5.4:** The scatter plots of IMF strength versus total magnetic field for (a) cavities and (b) ambient magnetosheath. Correlation coefficients are given in top right corner of each panel

### 5.3 Dependence on IMF and Solar Wind Plasma

Interball and Cluster survey based on the case studies in the previous chapters suggested that there is no clear relationship between the magnetosheath cavities and IMF and solar wind plasma. Case studies of Cluster spacecraft indicated that the cavities occur during the low Theta Bn ( $\Theta_{Bn}$ ), less than  $45^\circ$ , which corresponds to quasiparallel shock conditions. However, we did not find any clear dependence on the IMF magnetic latitude, the IMF magnetic longitude and the IMF clock angle which imply the absence of any particular direction that favors the occurrence of the magnetosheath cavities. As a result of their IMP-8 search, Sibeck et al. (2001) found that the foreshock cavities occur during the low solar wind velocities and they were not able to find any dependence on IMF direction. They showed that their foreshock events occurred outside the dawn (prenoon) and dusk (postnoon) regions of the bow shock, being seen more on the prenoon bow shock, owing to the orbital restriction of the IMP 8 spacecraft and the spiral configuration of the IMF. Although they have not

explicitly shown, both of these factors lead them to suggest that their events occurred during more common orientations of the IMF near ecliptic plane on the prenoon bow shock. Here we look at the IMF cone angle dependence of the magnetosheath cavities. The cone angle is the angle between IMF direction and the Sun-Earth line. It shows that how much the IMF deviates in XY-plane. Thus, a zero cone angle means that the IMF lies on the ecliptic plane and the IMF orientation is radial, being dominantly in the x-direction. To show this, we calculated the IMF cone angles for the cavity region and the ambient magnetosheath around the cavities by using corresponding ACE data. Figure 5.5 presents the IMF clock angles (a) and cone angles (b) for 267 flux burst events. In panel (a), we do not see a particular clock angle orientation that all flux burst events are concentrated. The data were scattered between  $120^\circ$  and  $-120^\circ$ . On the other hand, IMF cone angle panel gives a clear pattern towards low cone angles (less than typical  $45^\circ$ ) which correspond to radial IMF, namely IMF on the ecliptic plane. This dependence is used to test the global hybrid simulations of the magnetosheath cavities which is presented in Chapter 5.

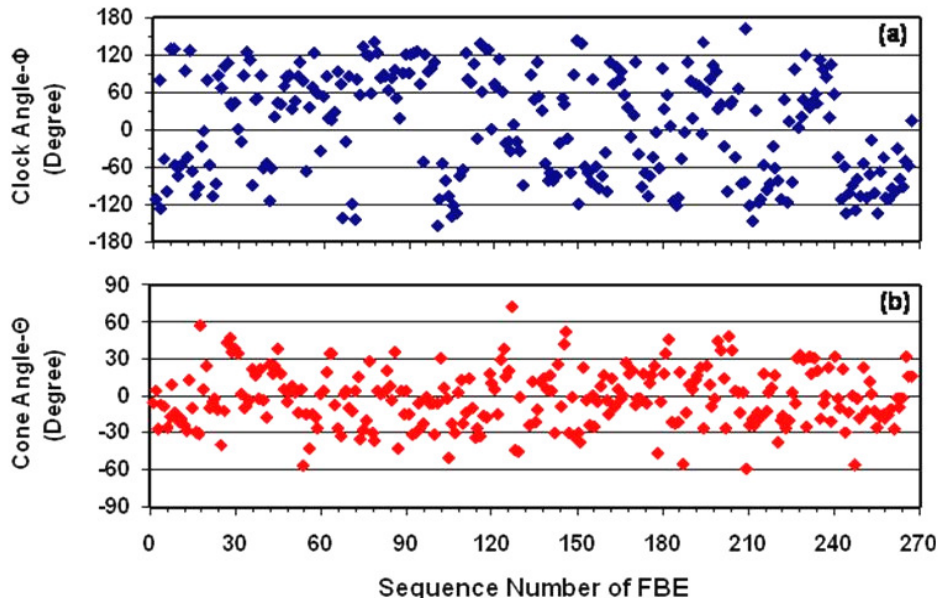


**Figure 5.5:** IMF clock angle- $\Phi$  (a) and cone angle- $\theta$  (b) dependence of the magnetosheath cavities.

The dependence of the magnetosheath on the IMF cone angle is suggestive of these cavities may be carried by the solar wind into the magnetosheath across the shock when the IMF has low cone angles.

#### 5.4 Effects on Magnetopause Location

Similar to the case studies presented in Chapter 4, the ratio of the magnetopause distance is calculated for all cavity events (267 flux burst events). In Chapter 4, we found that the magnetopause calculated by using magnetosheath parameters are found to be larger by about 25-30% with respect to the solar wind driven magnetopause with reference to the Shue's et al (1997) magnetopause. Figure 5.6 gives  $(R_{mp})_{Ratio}$  calculated as described in the previous chapter for all flux burst events. The fact that  $(R_{mp})_{Ratio}$  is greater than 1 within most of the cavities indicate that the magnetopause is larger when the effects of energetic particle are taken into account in the magnetosheath. The magnetopause can be as large as 2 factor when the energetic particles are present in the magnetosheath than that driven by the upstream solar wind. Our events shows that the decreased total pressure within the magnetosheath cavities in the presence of energetic particles are the cause of these local motions on the magnetopause location. .

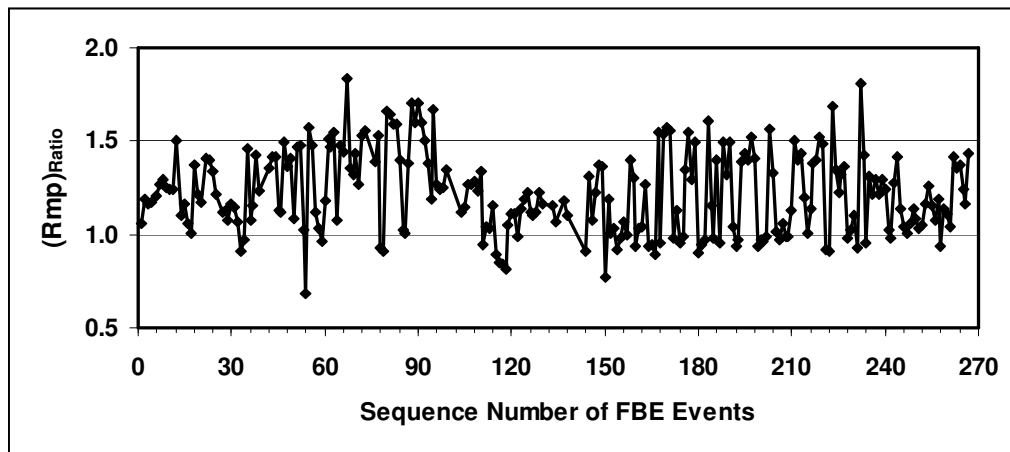


**Figure 5.6:** Comparison of magnetopause size calculated using the magnetosheath and upstream solar wind parameters. The ratio of the magnetopause distances is presented. In the figure, the ratio “1” indicates that there is no difference between the magnetopause distances calculated from the magnetosheath parameters and upstream solar wind parameters.

#### 5.5 Duration of the Magnetosheath Cavities

To determine the lifetime of the magnetosheath cavities, we determined how long each cavity (267 flux burst events) lasts in the magnetosheath. This is taken as the time interval between the start and end times of the cavities. Figure 5.7 presents the

results of this survey. The majority of cavities (175 events, 65%) last less than or equal to 30 minutes. About 151 events (57 %) persist about 15-30 minutes. Only 3 events have 5 min duration. Maximum duration is seen as 158 min. On the average, we can state that the magnetosheath cavities last typically between 15 and 30 minutes.

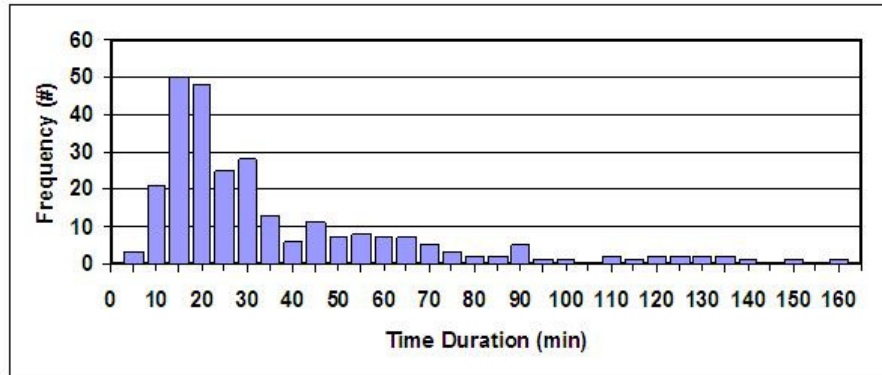


**Figure 5.7:** Time durations of 267 flux burst events. Maximum and minimum durations are 158 min and 5 min respectively. Maximum occurrence frequencies point that the typical lifetime of magnetosheath cavities as 15-30 minutes.

Figure 5.8 is taken from Sibeck et al. (2001) showing the duration times of foreshock cavities seen in the upstream bow shock region. They found that typical durations of their foreshock cavities last 1-10 min. Maximum duration that they detected is around 100 min (about 1.5 hours). We have seen a magnetosheath cavities which can last more than 1.5 hours. 14 events (5.6 %) last more than 1.5 hours.

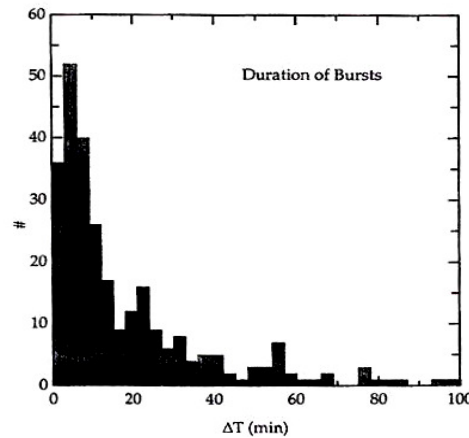


**Figure 5.8:** Time durations of foreshock cavities seen in the upstream bow shock region (Sibeck et al., 2001).

## 5.6 Summary of the Statistical Results

In this Chapter, we have presented the statistical analysis of 267 magnetosheath cavities corresponding to the high energy particle flux burst events detected as a result of the two year search of Cluster data from 2002 to 2003. The results of the statistical analysis confirm the results from the Cluster case studies, in that the depressed magnetic field and density regions are commonly seen in the magnetosheath (90%) when the high energy particles exist in the magnetosheath. Thus the term magnetosheath cavities, introduced for the first time for these depressed magnetic field and density regions, were confirmed with the large number of the events. These results are important as they define the general characteristics of the magnetosheath cavities based on large number of events and thus determine the inputs which should be included in the models that study and simulate the energetic particle effects on the magnetosheath structure. We summarize the results in this section as follows:

1. Magnetosheath cavities are the depressed regions of the magnetic field and density in the magnetosheath seen in the presence of the high energy particles. The magnitude of these depressions for magnetic field and density within the cavities are found to be about 27 % and 8 % respectively.
2. The temperature within the magnetosheath cavities increases while the speed tends to decrease although it does not always give a clear distinct signature.
3. All magnetosheath parameters show high fluctuations within the magnetosheath cavities compared to their surrounding magnetosheath.
4. Magnetosheath cavities occur mostly when the IMF is in the radial direction.
5. Magnetosheath cavities typically last 15-30 min.
6. Magnetosheath cavities can move the magnetopause by about 25-30 % from its expected position under the normal magnetosheath conditions. This, in turn, has implications on the magnetosheath-magnetopause-ionosphere coupling.

We incorporate these findings in the next chapter to further investigate especially on the sources of the magnetosheath cavities using the global hybrid simulations.





## **6. MODELING THE MAGNETOSHEATH CAVITIES**

### **6.1 Introducing Kinetic Hybrid Model**

A kinetic hybrid simulation model comprises of hybrid algorithms which are used for low frequency electromagnetic phenomena. Particle In Cell (PIC) methods are used for simulating the particles in this study. It is possible to find different kind of hybrid codes (Winske, 1985 and Quest, 1989), but hybrid codes with particle ions and massless fluid electrons have become the most common simulation way for space plasma physics in the last decades. One or more than one ion species as macro particles with differing mass, charge etc. are modeled kinetically via standard PIC methods used in particle codes. The electrons are treated passively, as a charge neutralizing massless fluid because the observations show that they do not have important effects like acceleration, heating etc. Therefore, they do not play significant role especially in ion foreshock and the effects of electrons are ignored (Winske and Omid, 1993).

### **6.2 Kinetic-Hybrid Model for Magnetosheath Cavities**

Recent results from global kinetic hybrid simulations (N. Omid, personal communication, 2009) indicate that foreshock cavities can be carried by the solar wind and convected through bow shock into the magnetosheath. These cavity structures in the foreshock are caused by the nonlinear evolution of two types of ULF waves generated by the backstreaming ions in the foreshock. First type is 30-second parallel propagating, sinusoidal waves with right or left hand polarization. The second one is highly oblique, linearly polarized, fast magnetosonic waves (shocklet waves).

Results from the electromagnetic hybrid simulations of the magnetosphere show that there is a significant difference in the foreshock structure during different IMF orientations due to the changes in wave generation. A major difference from the intermediate cone angle case is that during radial IMF there is a lack of spatial separation

between 30-sec sinusoidal and fast linearly polarized oblique (FLO) waves. As a result of radial IMF, these waves become tightly coupled and exhibit formation of unique features associated with large ( $\sim 50\%$ ) drops in density and magnetic field strength which is referred to as foreshock cavities. Formation of cavities also is the result of the replacement of shocklets with fast linearly polarized oblique (FLO) waves which lead to spatially localized regions of density and magnetic field depletion surrounded by higher densities and fields. Kinetic hybrid simulations for radial IMF show that foreshock cavities are convected by the solar wind back into the shock and carried into the magnetosheath (Omidi and Sibeck, 2007).

In this study, to understand the macrostructures of the bow shock, ion foreshock, as well as the structure of and structures in the magnetosheath, Omidi's 2.5-Dimensional (2.5-D) kinetic hybrid model is used (Omidi et al., 2005). In this chapter, we present the results from the 2.5-D global kinetic hybrid model for magnetosheath cavities during the periods of radial and inclined IMF orientations and we compare our findings with those presented in the previous chapter obtained from Cluster spacecraft. In addition to supporting the observational results on the magnetic field strength and plasma parameters in the magnetosheath, the simulation results also suggest a casual relationship between IMF orientation and the presence of the magnetosheath cavities, and confirm the larger magnetopause as response to the magnetosheath interaction at the magnetopause boundary. The model results presented here suggest that the magnetosheath cavities exist in the magnetosheath during the radial IMF orientations. Thus, they shed light on the source of the magnetosheath cavities, their occurrence, characteristics and wave structure, and their implications on the magnetopause. In this respect, results of this study on the comparisons of the hybrid model and the Cluster observations are highly significant to the community who are working in the magnetosheath.

### **6.2.1 Model definition**

The model box used in the kinetic hybrid simulation model used in this study is illustrated in Figure 6.1. The model is described in detail in Omidi et al. (2004, 2005). As mentioned above, electrons are treated as a neutralizing massless fluid and ions are treated kinetically via standard PIC methods used in particle codes. X-axis is along Sun-Earth line pointing toward Earth, Y-axis is along dipole axis (northward),

and Z completes a right handed coordinate. The model is symmetric in the cross-sectional plane.

The model is 2-D in space, with  $\partial/\partial z = 0$ , however the electromagnetic fields and plasma velocities are treated in 3-D. Therefore, it is called 2,5-D hybrid model. System domain size in X- and Y- directions is 1000 X 1600 ion skin depth ( $c/\omega_{pi}$ ). In the model, the distances are measured in terms of ion skin depth  $c/\omega_{pi}$ , where c is the speed of light, and  $\omega_{pi}$  is the ion plasma frequency. Ion skin depth is the distance which electromagnetic radiation can penetrate in a plasma.

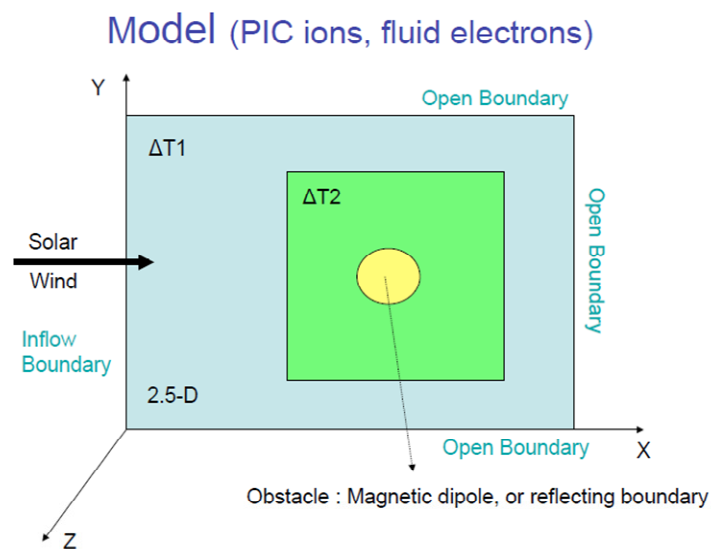


**Figure 6.1:** A model box in the kinetic hybrid model created for this study by Dr. Nick Omidi.  $\Delta T1$  and  $\Delta T2$  show that model has 2 different zones with different time steps. The obstacle with magnetic dipole refers to the Earth.

Total number of particles that are present in the domain is 39.500.100 and number of particles per cell may vary while keeping the charge to mass ratio constant. In the regions where we need to do better statistics on ion population, local number of particles per cell may be increased by using particle splitting schemes. (Lapenta, 2002). The splitting is performed in two steps:

1. A single ion is split into more particles with keeping the velocity same as the original ion has.
2. Each of newly formed ions is split again into more particles in the same way.

A line dipole described by Ogino (1993) is placed within the simulation box at an arbitrary location as  $700 \times 1050 c/\omega_{pi}$  with its axis along y- direction. There is a non-rotating planet with a radius of 30 ion skin depth centered at this dipole point. Proton and electron betas (ratio of kinetic pressure to magnetic pressure) are assumed to be  $\beta_p = \beta_e = 1$ . In order to reach quasi-steady state, the electrical resistivity in the simulations is considered spatially uniform with a resistive scale length of about  $0.03 c/x_p$  in the solar wind. The electric field is set to zero, which corresponds to a perfectly conducting ionosphere. The ratio of ion plasma to gyrofrequency (the same as the ratio of speed of light to Alfvén velocity) is taken to be 4000.

The results presented in this chapter are obtained from the simulations with uniform spatial grids but non-uniform temporal grid. As seen in Figure 6.2, system domain has two zones with different time steps. For optimization of the computation time, the simulation box is divided into two different zones to solve the evaluation of plasma and electromagnetic fields in different time steps. Time steps, which are used in the model, are measured in terms of the ion gyrofrequency. An ion gyrofrequency is the angular frequency of the circular motion of an ion or electron in the plane perpendicular to the magnetic field and is a function of the magnetic field strength and the mass of the particle. In our simulations, Zone-1 has time steps of  $\Delta T_1 = 0.0025 \Omega^{-1}$  (inverse of ion gyrofrequency) and Zone-2 has smaller time steps of  $\Delta T_2 = 0.00125 \Omega^{-1}$ .

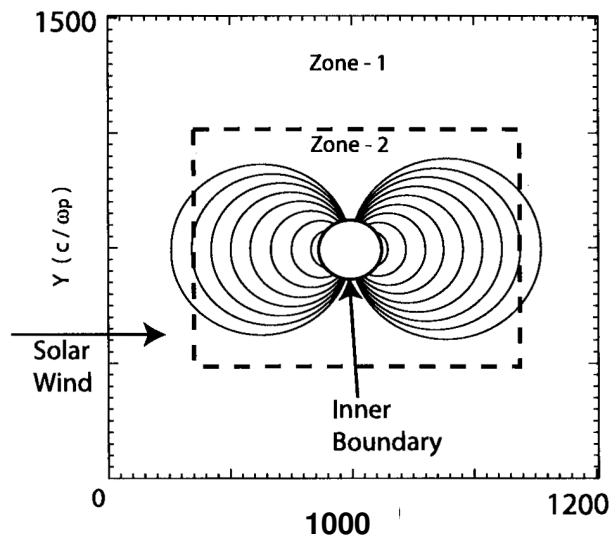


**Figure 6.2:** Illustration of the domain used in the global hybrid model for this study.

Solar wind is continuously injected along x- direction with Alfvénic Mach number of 12 (Alfvén speed=75 km/s). The plasma leaves the simulation box from other three simulation walls. Except for velocity, which is normalized to Alfvén speed, all other plasma and magnetic field parameters are normalized to their corresponding solar wind velocity. Normalized values of the parameters used in this study are:

- $B_{t_{msheath}}/IMF B_t=6$
- $N_{ion}/N_{sw}=1$
- $T_{ion}/T_{sw}=1$

To create a normal dipole field with bow shock and magnetopause in the simulations, the distance of the nose of magnetopause from dipole center ( $D_p$ ) could be greater than 20.  $D_p$  is normalized to solar wind skin depth and taken to be 100 to ensure a terrestrial-like magnetosphere in our kinetic hybrid model.

### 6.2.2 Model results for magnetosheath cavities

Figure 6.3 gives an example of the normalized magnetic field for inclined IMF orientation throughout the simulation box in color scale. The panel on the right illustrates expanded region seen on the left in dashed rectangular area. X- and Y- scales are given in ion skin depth ( $c/\omega_{pi}$ ). The black solid circle shows the Earth as a magnetized obstacle with  $D_p=100$ . The boundaries are easily noticeable in the expanded view where the yellowish outer boundary of the white region on the dayside magnetosphere indicates the magnetopause and the boundary between the region in darker blue color of the solar wind and the region with mixed red and lighter blue color of magnetosheath denotes the bow shock.

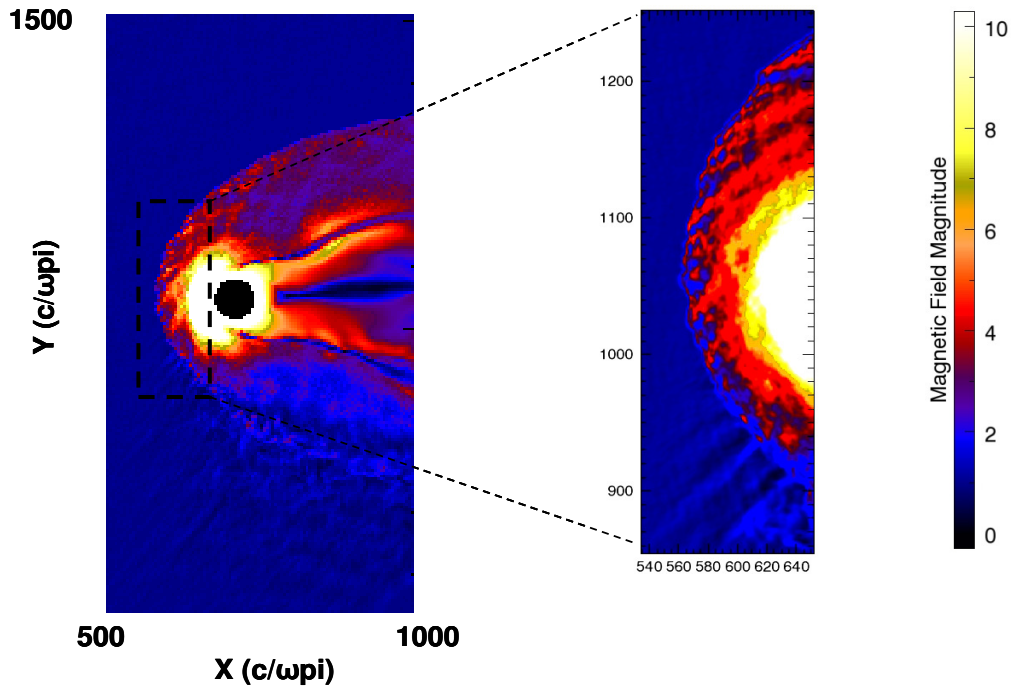


**Figure 6.3:** On the left, simulation box seen after running the model including the boundaries and the area that we simulate. The Earth as a magnetized obstacle is presented in black solid circle. The bow shock and the magnetopause boundaries can be visibly seen in the expanded view on right.

As an initial condition for this run, at the start of the run, the cone angle (the angle between IMF direction and x axis) is selected  $45^\circ$  which indicates  $45^\circ$  inclined IMF orientation with respect to the x-axis. At time step 300, IMF direction is switched from the inclined to radial by defining the cone angle as  $0^\circ$ . At time step 900, IMF is switched again to be inclined by  $45^\circ$ . In Figure 6.3, the inclined IMF orientation is evident from the wavy structure of the solar wind upstream to the bow shock. Figure 6.4 illustrates the differences at different IMF configurations as IMF switches from inclined (a) to radial (b), and to inclined again (c). In the magnetosheath, simulation results show that the magnetic field strength varies around 5 for inclined IMF while it is much lower, around 2 to 3, for radial IMF. In panel (b), we can see that the magnetic field decreases to even lower values close to zero. The lowest magnetic fields are found near the magnetopause boundary but also from place to place in the central magnetosheath as well. These lower magnetic fields, especially in the central regions of the magnetosheath downstream of the bow shock, during the radial IMF resemble those within magnetosheath cavities where the magnetic fields decrease. As

Figure 6.4 gives only a few instantaneous views at three different IMF cone angles, to see how the magnetic field structure of the magnetosheath changes in more detail as the IMF cone angle varies, please check the movie “Btot” on DVD that is supplied with the thesis.

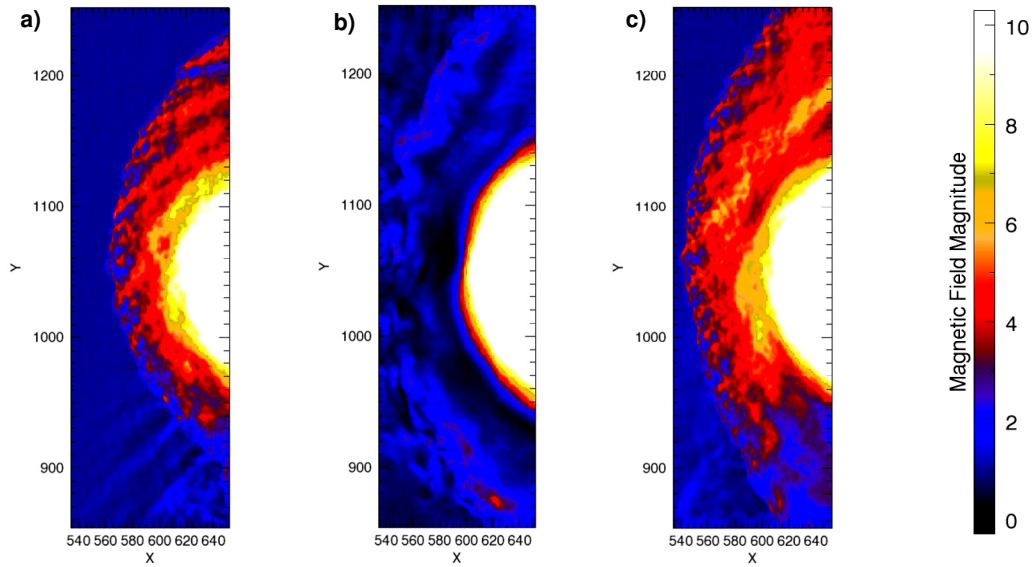


**Figure 6.4:** Simulated total magnetic field views at different times as IMF switches from inclined (a), to radial (b), and to inclined again (c).

Figure 6.5 presents the simulation results for ion densities for different IMF cone angle orientations in the same format as given in Figure 6.4. In the panels, we can see that the density presents rather homogenous structure when the IMF has a inclined direction. The magnitudes range from 3 to 5 for the inclined IMF cases. In panel (b), on the other hand, we can see that this homogeneous structure is lost and become more fractured. In between the high density regions seen in panels (a) and (c) lower density regions were scattered. This difference is a result of the radial IMF. In panel (b) we see that the magnitudes of the density vary between 1 and 3. Low density regions seen during the radial IMFs are larger, more extended in nature in the afternoon sector while they look more focused in the prenoon sector. They are not symmetrically distributed. Lower density regions are present more in the subsolar region. Another important point that needs to be emphasized in panel (b) is that the density structure becomes highly turbulent indicating that the fluctuations increase as the IMF turns to radial. Panels (a) and (c) represent rather smooth, less structured views indicating less turbulent and fluctuating density fields when compared to those

in panel (b). As in the magnetic field case, details of the density variations as the IMF cone angle changes are found in DVD as movie “Den”. The evolution of the fluctuations and turbulence as the IMF varies to radial IMF orientation are clearly seen in the magnetosheath during radial IMF.

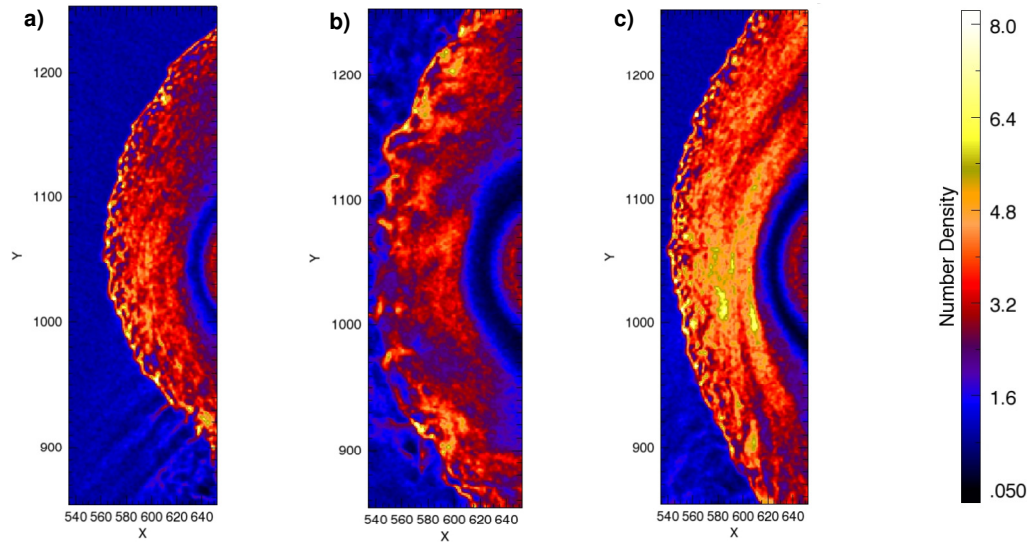


**Figure 6.5:** Simulated ion densities at different times for inclined IMF (a), radial IMF (b), and inclined IMF again (c).

Figure 6.6 presents the simulated ion temperatures for the 3 different IMF orientations in the format as in Figures 6.4 and 6.5. All panels indicate the heating at the bow shock. However, comparing three panels shows that the temperatures increase throughout the magnetosheath from the subsolar region toward the dawn and dusk flanks when the IMF is radial and becomes more homogeneous while heating in the other two panels of inclined IMF is seen to be fractured and concentrated on the subsolar region of the downstream bow shock. Panel (a), as in panel (a) of Figure 6.5, shows the solar wind particles in the upstream dusk side of the bow shock which are energized and reflected back into the solar wind along the magnetic field lines which are connected to the bow shock. These backstreaming ions are the reasons of the high temperatures of the southern foreshock region during inclined IMF. Even if IMF changes its orientation from inclined to radial, we can still see some of these energized backstreaming ions farther dusk flank in the upstream bow shock. Ion temperature varies between 20-80 during the inclined IMF but it exceeds 70s throughout the magnetosheath from the bow shock to the magnetopause



and even more, higher than 80s, in and around the subsolar region when IMF becomes radial. Temperature fields become more turbulent near the downstream dawn and dusk bow shock in the magnetosheath, further near the high latitudes. (For more details, again movie “Temp” is available on DVD)

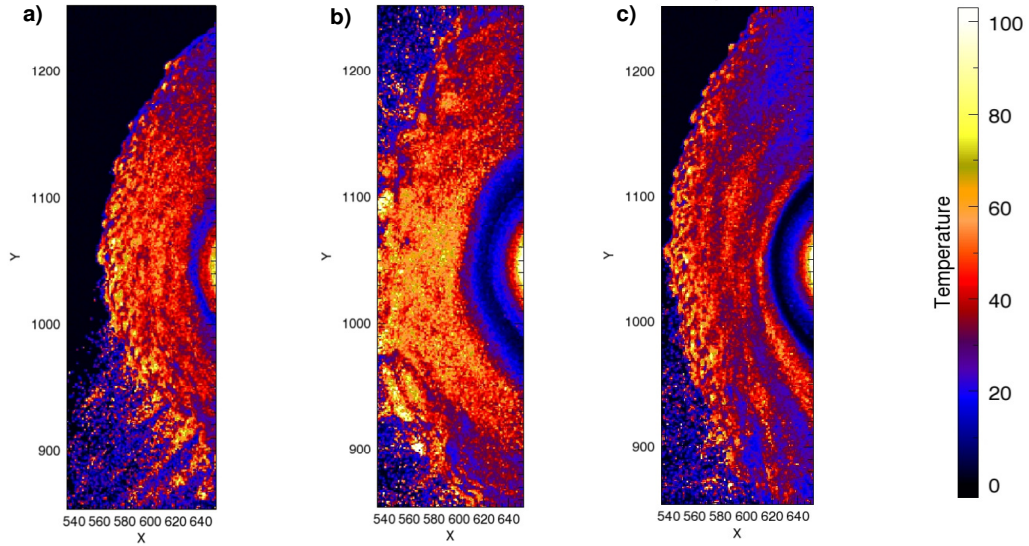


**Figure 6.6:** Simulated ion temperature views for inclined IMF (a), radial IMF (b), and inclined IMF again (c). The backstreaming ions in the dusk foreshock region for inclined IMF are clearly visible (a).

Examining the simulated views given above closely, as we will further describe and quantify, depicts also that the magnetopause size becomes larger as the IMF changes from inclined orientation towards radial orientation, a result which confirms the larger magnetopause when the magnetosheath cavities are present.

To study the variations in more detail, we present the profiles of magnetic field magnitude, ion density and temperature along the path shown in white in Figure 6.7 at a plane of ( $X=395.66 - 612.01$ ,  $Y=1067.95 - 1068.67$ ). Next three figures, Figures 6.7, 6.8 and 6.9, give the profiles at different model time steps corresponding to different phases of the IMF orientation in which the first and third phases correspond inclined IMF orientation while the second phase refers to the radial IMF.

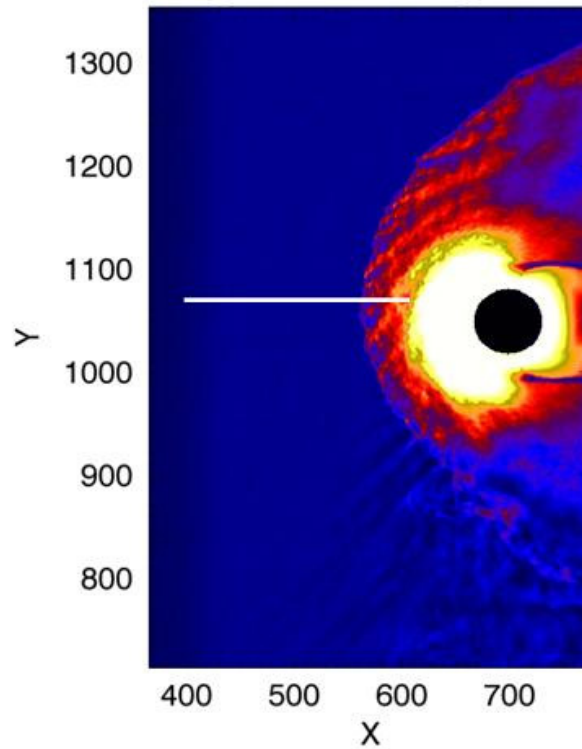


**Figure 6.7:** Model magnetic field in the plane of ( $X= 395.66 - 612.01$ ,  $Y=1067.95 - 1068$ ) for inclined IMF conditions.

In Figure 6.8, the model time step is 480, and the panels from top to bottom are magnetic field magnitude, ion density, and ion temperature along the white line at the plane of  $x$  and  $y$  as defined above. The bow shock (red vertical line) is determined at about  $x=550$ . The dotted area shows the magnetosheath. Magnetopause is not seen in the figure at this time frame but it is known that magnetopause is located at the distances higher than  $X=612.01$ . The magnetic field magnitude is 2.5 at the bow shock and increases toward higher values, up to 8, while moving towards the magnetopause. The ion density increases to 7 at the bow shock and fluctuates around 4 in the magnetosheath to the magnetopause. Temperature increases at the bow shock and stays around 40, and it displays high fluctuations throughout the magnetosheath.

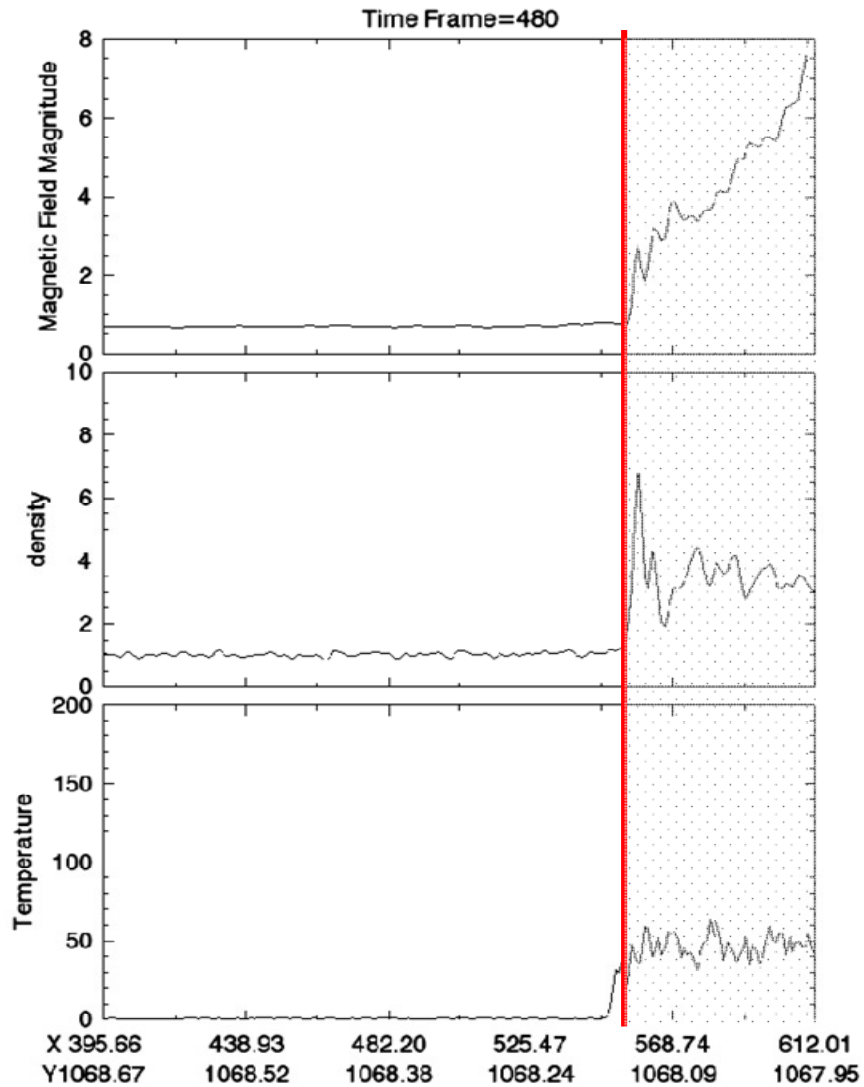


**Figure 6.8:** Profiles of magnetic field magnitude, density, and temperature of along the white line indicated in Figure 5.7 on the cut plane of (X, Y) as defined in the text for inclined IMF conditions. Bow shock is indicated in red.

Previous figure illustrated the variations in magnetic field magnitude, density and temperature for inclined IMF. Figure 6.9 gives the similar profiles in the same format for radial IMF orientation. In this case, the bow shock is not sharply defined as in the inclined IMF case while the magnetopause is clearly seen at  $X=590,37$  owing to the fact that it moves outward. The magnetic field magnitude is seen to be decreased in the magnetosheath from 3 to 1 at  $X=568,74$ . Correspondingly, density slightly increases from 2.9 to 3.2 while temperature increases steadily from 40 to 90 and fluctuates.

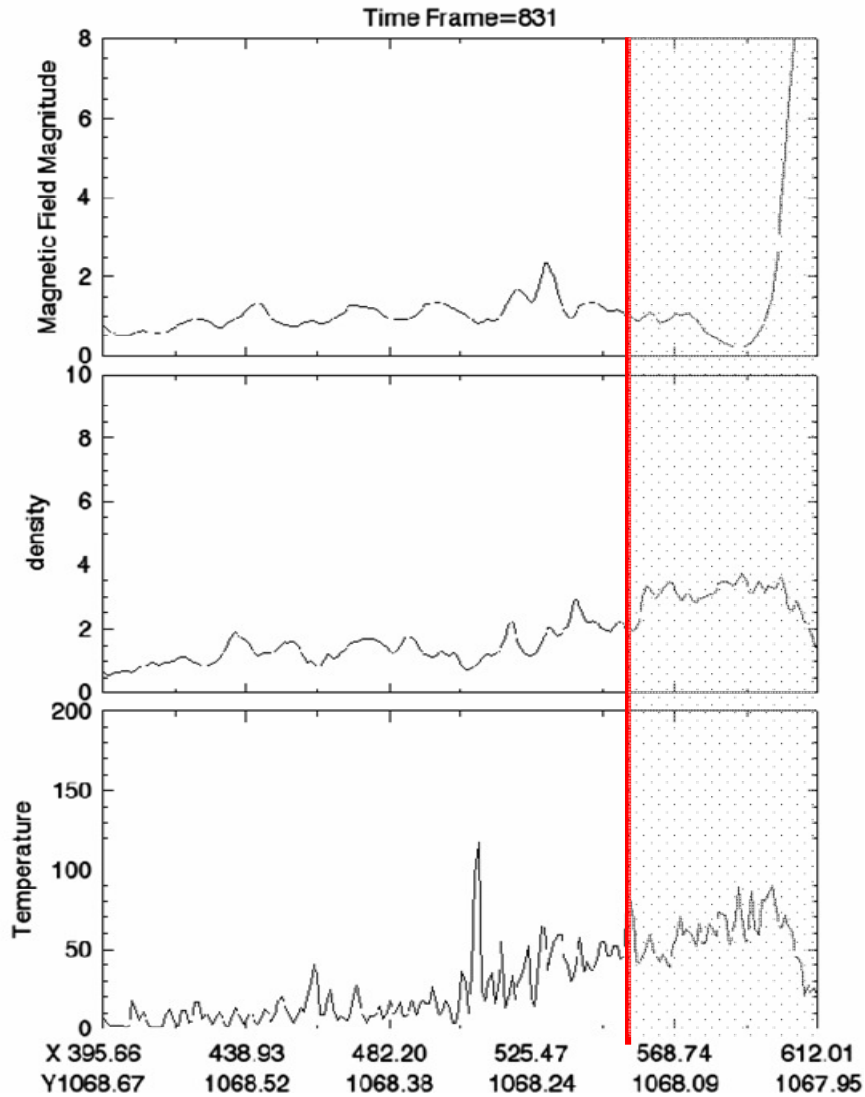


**Figure 6.9:** Profiles of magnetic field magnitude, density, and temperature of along the white line indicated in Figure 5.7 on the cut plane of (X, Y) as defined in the text for radial IMF conditions. Bow shock is indicated in red.

Figure 6.10 demonstrates the profiles at time step 1272 for inclined IMF again, Now the IMF turned to inclined again. A big difference from Figure 6.9 is the character of the bow shock which is very well defined in this inclined IMF case of the model results. We see the similar variations in the magnetic field magnitude, ion density and temperature as in Figure 6.8.

Evaluating these three profiles puts down the differences on the fluctuation levels and the magnitudes of the magnetosheath parameters for radial and inclined IMF conditions. However, it is clear of the Figures 6.4, 6.5, and 6.6 that the degree of the

differences depends on the selection of the cut plane and the path along which the profile has been taken.

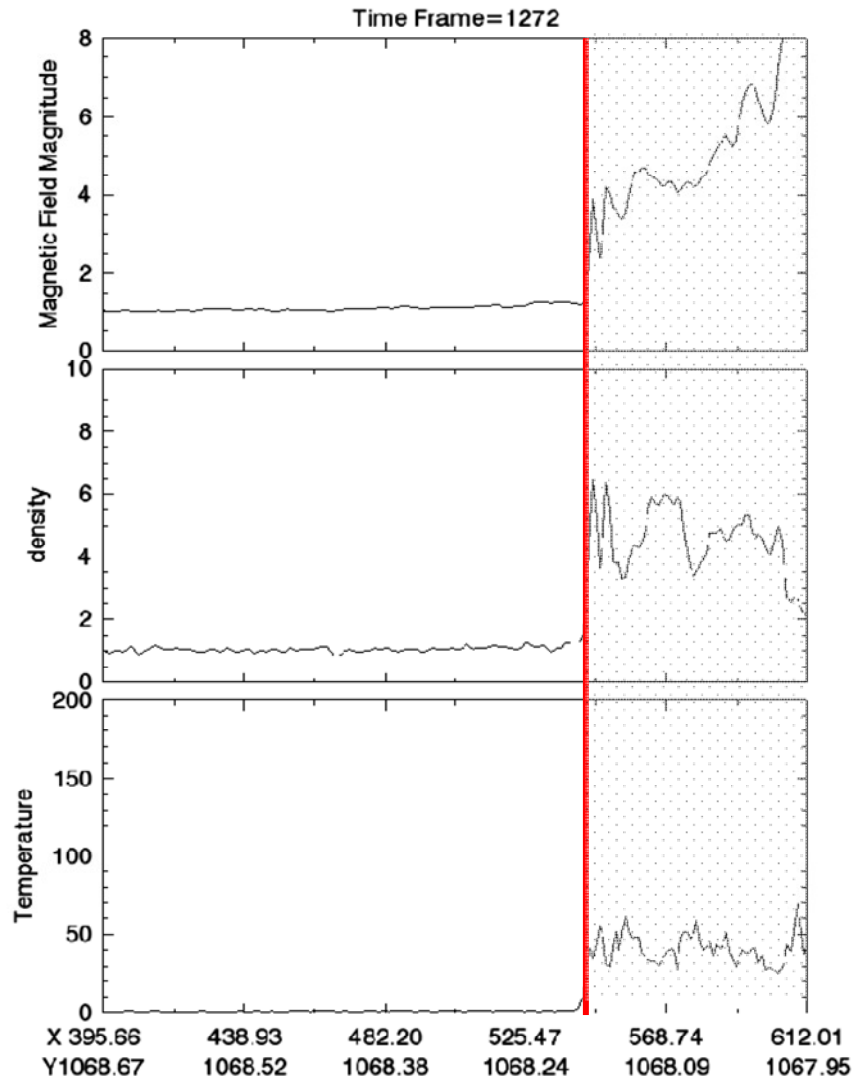


**Figure 6.10:** Profiles of magnetic field magnitude, density, and temperature of along the white line indicated in Figure 5.7 on the cut plane of (X, Y) as defined in the text for inclined IMF conditions. Bow shock is indicated in red.

To see the time evolution of the structures at a particular location in the magnetosheath for different IMF cone angles, we selected four points as indicated in Figure 6.11. This survey thus will help us to identify both the temporal and spatial variations of the magnetosheath parameters at a particular location for a specific IMF orientation.

Points selected is illustrated in Figure 6.11 as point 1, which is closer to the bow shock and subsolar line, points 2 and 3 are selected at the high latitudes/or farther dawn and dusk due to the symmetry in YZ-plane in the model, point 4 is selected close to the bow shock in the mid-latitudes.

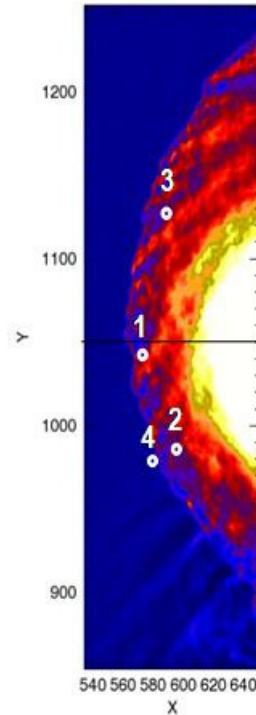


**Figure 6.11:** Locations of the four points at which the time variations will be studied.

In panels (a), (b), (c), and (d) in Figure 6.12, the time series plots of density, temperature and magnetic field at the selected locations (a=1, b=2, c=3, d=4) are given for model time steps between 300 and 1400. During the model time from 0 to 300, model creates a magnetized Earth with the boundaries of bow shock and the magnetopause and a conducting ionosphere. After creating a dipole magnetic field, boundaries and ionosphere, model first simulates inclined IMF case (cone angle  $45^\circ$ ) until about time step 600. Then, IMF cone angle is changed to  $0^\circ$  between time steps of 600 and 1150. The next phase of inclined IMF starts at time step 1150 and continues until the end of run.

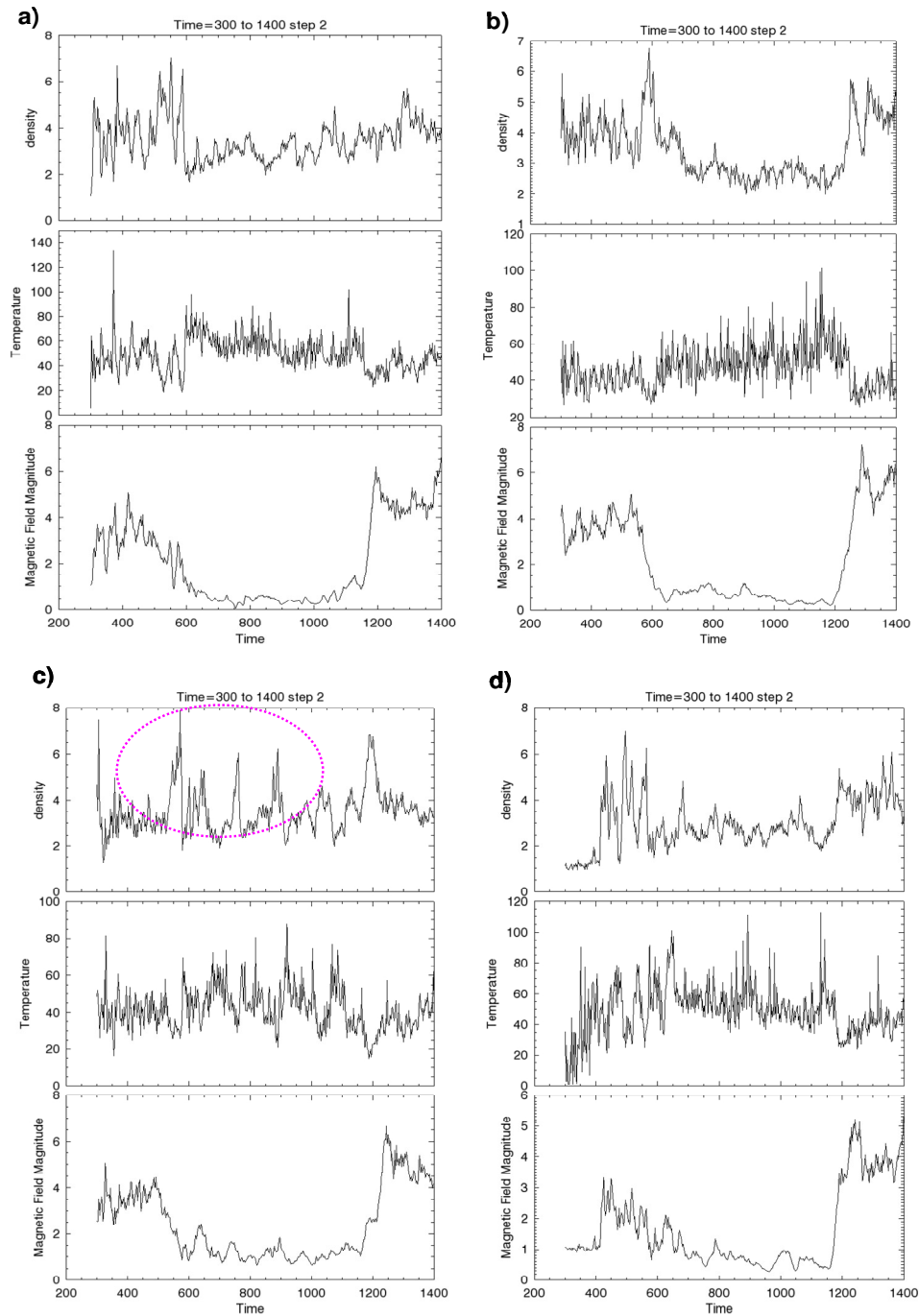


**Figure 6.12:** Time series plots of density, temperature, and magnetic field magnitude at the selected points of (a) Point 1, (b) Point 2, (c) Point 3, and (d) Point 4 shown in Figure 5.11. Time steps here are the model time steps. The plots run for model time steps from 300 to 1400 on the horizontal axis. Time from 300 to 600 is when the inclined IMF case (cone angle is  $45^\circ$ ) is simulated; time from 600 to 1150 is the time when the cone angle is  $0^\circ$  corresponding to radial IMF, and time from 1150 to 1400 corresponds to the inclined IMF again.

Simulation results on the magnetosheath cavities reveal several interesting details. While supporting most of the features that we see in both Interball and especially Cluster data presented in previous chapters, new features were also revealed. All panels show a clear difference between the variations seen for the time interval from 300 to 600 or 1150 to 1400 corresponding to the inclined IMFs and those seen from time step 600 to 1150 that corresponds to the radial IMF. The first thing one can see in all panels, the all parameters become much more turbulent when the IMF lies in the ecliptic plane and cone angles is zero. The magnetic field shows less fluctuations compared to the density and temperature but still a clear wavy structure is evident in the magnetic field panels at all selected points. The cavity like structure during the radial IMF is also very clear in all panels. The magnetic field and density are seen to decrease and temperature rises during the radial IMF. Both density and temperature becomes highly fluctuating as well. Table 6.1 gives the characteristics of these parameters for the radial and inclined IMF cases at all four points selected.

**Table 6.1:** The characteristics of the magnetic field and plasma parameters for radial (R) and inclined (I) IMF cases at all four points selected.

AVERAGE NORMALIZED PARAMETER	POINT 1			POINT 2			POINT 3			POINT 4		
	I	R	I	I	R	I	I	R	I	I	R	I
<b>Magnetic field magnitude</b>	4	0.5	4	4	0.5	4	3.5	1	5	1.5	0.5	4
<b>Density</b>	4	3	4	4	2.5	4	3	4	4.5	4	3	4
<b>Temperature</b>	40	60	40	40	60	40	40	55	40	60	55	40

The simulation results confirm the occurrence of magnetosheath cavities. Moreover, they indicate that the source of the decreased magnetic fields and densities and increased temperatures in the magnetosheath can be the radial IMF as these signatures typify the radial IMF features seen in Figure 6.12 and Table 6.1.

If the solar wind carries the foreshock features, like cavities, into the magnetosheath, we expect to see signatures of these diamagnetic cavities filled with hot, tenuous plasma. At all selected points, magnetic field magnitude decreases 75-80 % during the radial IMF conditions corresponding to model time steps from 600 to 1150.



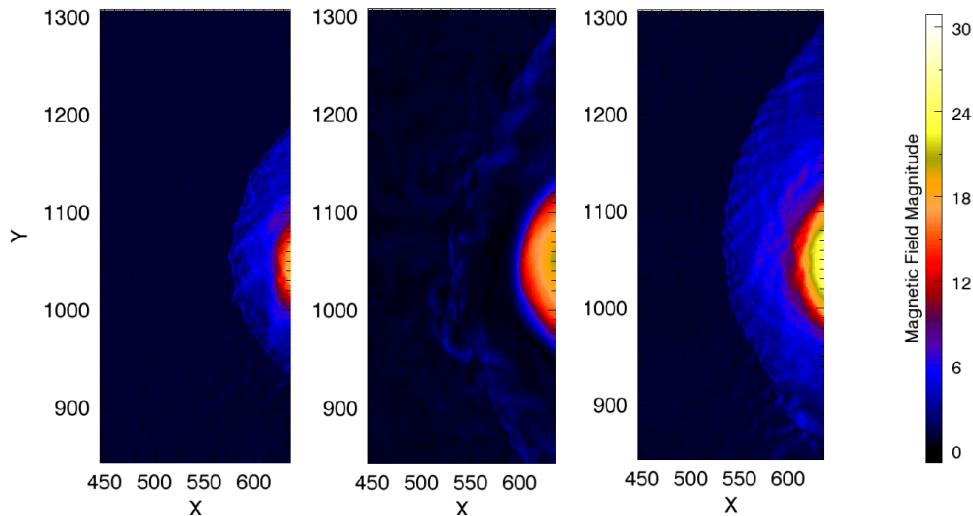
These indicate that the magnetosheath cavities are seen at all locations and they are similar to foreshock diamagnetic cavities. Thus we can conclude that they are carried by the solar into the magnetosheath by the radial IMF and they can be seen anywhere in the magnetosheath independent of the location during the radial IMFs.

Figure 6.12 also indicates that the model magnetosheath cavities are bounded by the shoulder like high magnetic field regions. This is consistent with the findings of Sibeck et al. (2000) about the characteristics of the foreshock cavities. Similar foreshock cavities with shoulders have been reported by Paschmann et al. (1988), Schwartz et al. (1988), and Safrankova et al. (2000).

We note on the variations of density at point 3 specifically as the density exhibits a different character than those in other locations. On the average, there is not much difference in density values between the inclined and radial IMF. However, it shows a high amplitude periodic fluctuating wave structure during the radial IMF. This is indicated by a purple ellipse on the density panel. Corresponding to these periodic pulsations of ion density, the temperature decreases and magnetic field magnitude decreases. These waves could be created locally by some kinetic processes in the middle regions of the magnetosheath or they may be fast mode compressional waves with higher magnetic field values. There is an abundance of MHD discontinuities and shock waves in the solar wind, which one or some of them could be the cause of the disturbances and turbulence seen in the parameters presented in panel (c). Wave structure with high fluctuations within the magnetosheath cavities is also obvious in Cluster data but their periodic character is not clear as in the model simulations.

During the model simulation, we also notice that the magnetopause size varies for different IMF cone angles as we have mentioned before. This point is explored in Figure 6.13 in detail. Figure 6.13 shows the magnetopause for three different IMF cone angles. In panel (a) for inclined IMF on left, the magnetopause is located at about  $640 c/\omega_{pi}$  on the Sun-Earth line. The magnetopause moves outward when IMF changes to radial direction (middle panel). The magnetopause from the earth in this case is seen to be at 600 indicating that it moved by about  $40 c/\omega_{pi}$ . Lower values of density during the radial IMFs, thus decreasing the total pressure applied on the magnetopause boundary, cause the expansion of the magnetopause into the magnetosheath as seen in this panel. When the IMF is switched back to inclined orientation as illustrated in panel (c), we notice that the magnetopause retrieves back

toward the Earth and the size of the magnetopause becomes smaller. This leads into a result that the size of the magnetopause increases by 30-40 % during the radial IMFs as indicated in panels (a) and (b).



**Figure 6.13:** From left to right, the figures give the simulations of magnetic field magnitude during inclined, radial, and again inclined IMF orientations. Different color scale is used to notice locations of the bow shock and the magnetopause very well.

### 6.3 Summary and Conclusions

In this chapter, we presented the results from the kinetic hybrid model simulations. In order to understand the characteristics of the magnetosheath cavities, we run the model for different IMF cone angles. IMF cone angle is used because the Cluster observations indicate that the magnetosheath cavities occur in the presence of the high energy particles during the low IMF cone angles within  $45^\circ$ . The comparisons suggest several important features regarding the characteristics of the magnetosheath cavities. The model results verify the Cluster observations. In addition, they present new features regarding the magnetosheath cavities. We summarize the model results as follows:

1. Model results verify the decreasing magnetic fields and densities and increasing temperatures within the magnetosheath cavities.
2. Model results verify highly fluctuating structures observed within the magnetosheath cavities. These fluctuations are seen in all model magnetosheath parameters but less in magnetic field strength.

3. Model results show that the magnetosheath cavities occur during the radial IMFs when cone angle is zero. Magnetic fields and densities decrease in the magnetosheath while the temperature increases during the radial IMF. This further suggests that the foreshock cavities are carried into the magnetosheath by the radial IMF.
4. Model results indicate that the occurrence of magnetosheath cavities are generally independent of the location in the magnetosheath, but their characteristics may slightly change. We see more wavy structure within the model cavities towards the high latitudes of the magnetosheath.
5. Model results show that there are periodic wave structures within the cavities. Quantifying wave features requires wave analysis which is the subject of our further study.
6. During the radial IMF, the model magnetopause becomes larger by about 40% when compared to that corresponding to non-radial IMF.



## **7. CONCLUSION AND FUTURE WORKS**

### **7.1 Thesis Summary and Conclusions**

This thesis study investigates the effects of energetic particles on the magnetosheath magnetic field and plasma structure. The motive for this research comes from the foreshock cavities which are generated in the upstream bow shock as a result of the interaction between the incoming solar wind particles and the particles energized and reflected from the shock. The questions arise on whether these reflected energetic particles and their consequence foreshock cavities are transferred into the magnetosheath which can, in turn, modify the interaction between the solar wind, magnetosphere and ionosphere, especially at the boundary of magnetopause. The magnetosheath of the Earth's magnetosphere is a transition region between the Earth's atmosphere and the solar wind. The region is important in that the energized and heated solar wind impacts upon the magnetopause, which is the plasma boundary of the Earth's atmosphere and prevents direct penetration of the shocked solar wind into the lower levels of the atmosphere. The interaction between the magnetopause and the magnetosheath flow (shocked solar wind) produces variations in the size, location, and structure of the magnetopause which are eventually transmitted to the ionosphere and neutral atmosphere. Thus, it is very crucial to understand the magnetosheath's structure, its variations, and the physical and dynamical processes occurring in the magnetosheath through which the solar wind couples into the magnetosphere-ionosphere-atmosphere system.

The magnetosheath region is one of the most difficult regions to study in space environment since it is such a turbulent place involving many wave activities and their interactions. It is very hard to isolate the specific effects by removing the disturbances caused by these wave activities. High energy particles into the magnetosheath may come from different sources. The energies that we are studying in this thesis are above 20-30 keV range. One of the most plausible sources is the bow shock and the foreshock regions. The particles can either be energized and carried antisunward into the magnetosheath with the shocked solar wind or they can

be energized and reflected back to sunward into the solar wind and then dragged with the incoming solar wind into the magnetosheath or both can be operating. The questions we addressed in this study may be summarized as follows:

How do the energetic particles modify the magnetic field and plasma structure of the magnetosheath? That is, how do the magnetic field and plasma in the magnetosheath change in the presence of the high energy particles. Can we identify the sources of these energetic particles or the structures that we identify as magnetosheath cavities based on the observations? What are the factors that affect the characteristics of these cavities? How are they distributed spatially within the magnetosheath? Is there a particular location or region that they present different features? Is there any connection to IMF and solar wind plasma? If so, what is the connection? What are the consequences of the magnetosheath cavities on the magnetopause? Can any of the models predict them? How do the results of the models on the magnetosheath cavities compare with the observations? Can we learn from models about the source of the magnetosheath cavities? Can we learn from models about the formation and evolution of the magnetosheath cavities?

This thesis investigates these questions comprehensively using large number of data sets that we obtained from the recent spacecraft that were available when we start in our search. In the organization of the thesis, Chapter 1 and Chapter 2 introduce the problem, concepts, terminology, presents the literature survey, and lays the outline for proceeding chapters; Chapters 3 and Chapter 4 present the observational results of the case studies from Interball and Cluster spacecraft; Chapter 4 gives and discusses the statistical results based on the observations from the Cluster spacecraft; Chapter 6 explores the modeling attempts and presents the results from the kinetic hybrid model simulations and compares them with those obtained from the observations in Chapters 3, 4 and 5. The kinetic hybrid model, that we used in our study to simulate the effects of the energetic particles in the magnetosheath, is especially run for us by Prof. Nick Omidi, who is our collaborator at Solana Beach Company of Space Research in California, using the inputs we obtained in Chapter 5. Finally, Chapter 7 summarizes and concludes our search. We present future work in Chapter 8.

In Chapters 3 and 4, a through and careful search of Interball and Cluster data is carried out by visually scanning the data over on NASA's CDAWeb page. In these

chapters, we have presented the case study results that determine the magnetosheath magnetic field and plasma variations in the presence of the high energy particles in the magnetosheath. Within the data resolution of DOK-2 instrument, Interball spacecraft search brings out four types of variations seen in the magnetosheath in response to the high energetic particles. Among these, the majority shows a signature of increasing magnetic fields and decreasing densities (Type 1). Foreshock type cavity signatures (Type 2) are found rarely in Interball data. In this section we did not see any IMF connection of the cavities although low solar wind conditions were dominant for our cases. We detected cases that show increasing magnetic field and decreasing densities which are the signatures of the plasma depletion layer near the magnetopause. The investigation of these structures is left for future study as given in Chapter 8. Due to the high scatter in all cases, the correlation coefficients obtained were very low. Scatter within the magnetosheath is common owing to the high turbulence. However, several factors can contribute to the absence of any high level correlation between the energetic particles in the magnetosheath and coherent variations of the magnetosheath magnetic field and density. One of these factors is the resolution of the Interball data which was 2 min. This restricts us to detect the variations longer than 2 min, if any present. Considering the duration of the foreshock cavities which majority last about 5 min, it will be hard to detect them in the magnetosheath in Interball data. Especially if they were transferred through the bow shock into the magnetosheath, they were subjected to the kinetic processes at the bow shock and thus their characteristics were most likely modified including their durations. All four types of variations we detected in Interball data usually last on the order of half to an hour. Finer variations within this time period do not show any coherency between magnetic field, density and energetic particles to result in a good correlation. A second factor on the low correlation obtained with Interball data is related to the DOK-2 instrument that was used to measure the high energy particles. Instrument measures energetic particles with energies between 22 and 28 keV. This energy range may not be high enough to create any detectable coherent effect on already turbulent and fluctuating magnetic field and density of the magnetosheath. The flux of the particles at these energies reaches, for example, to 20 000 PFU very rarely. Although they satisfy the high flux limits, still the amount of flux may not be enough for any coherent, detectable signature in the magnetic field and density. As compared to this, Cluster spacecraft energetic particle flux can very

often reaches and exceeds 20 000 PFU limit. One last factor that is worth to mention is solar activity level. Interball spacecraft was launched and send data during the low, or slightly increasing phase of the solar activity period. The Sun is less active which may have an affect on the amount of flux of energetic particles. Despite of these, Interball data stimulated us for a further, deeper search on the topic which we carried out using Cluster measurements.

Cluster spacecraft carries RAPID instrument for measuring the energetic particles with energy ranges over 30 keV ( $> 30$  keV) and the flux of these energetic particles very often reaches and exceeds 20 000 PFU and at times even reaches to 100 000 PFU. The time period that Cluster was launched and sends data corresponds to the high solar activity time. The correlations that we obtained between the energetic particle flux and the variations in the magnetic field and density are higher than the acceptable level and these results are presented in Chapters 4 and 5. The case studies of the Cluster search showed that the magnetic field and density decreases in the magnetosheath as response to the high flux of energetic particles. These signatures are similar to those of foreshock cavities which, as an analogy, led us to call them as magnetosheath cavities. They are the depressed regions of magnetic field and density. In addition, the velocity usually decreases and the temperature increases. The spectrograms of the cases presented in Chapter 4 showed that increasing temperatures are related to the heating within the cavities as a result of the high flux of energetic particles within them. Thus the magnetosheath cavities, as in foreshock cavities, are filled with hot, tenuous plasma. As contrary to foreshock cavities, these magnetosheath cavities do not show any shoulder like structures at the borders of the ambient magnetosheath. How the magnetosheath cavities survive throughout the magnetosheath is related to the pressure balance at the border of the cavity between the cavity and surrounding magnetosheath. Ambient magnetosheath pressure is balanced with the gas pressure of the plasma and the high energy particles within the cavity. All cases we examined showed that the magnetic field, density, velocity and temperature become highly turbulent within the magnetosheath cavities in the presence of the energetic particles as compared to those in ambient magnetosheath. The amplitude of the fluctuations was also seen to be much larger than those in the ambient magnetosheath. As in Interball case, we did not find any IMF relation of the magnetosheath cavities. Only, the cases we presented in Chapter 4 showed a



correlation with the Theta Bn angle of bow shock. They imply a quasi-parallel bow shock structure for their presence. We did not also see any clear dependence on the solar wind plasma, i.e. solar wind density, speed and temperature.

The statistical study of 267 magnetosheath cavities verified the results from the case studies presented in Chapter 4 regarding the changes in the structure of the magnetic field and density of the magnetosheath, the variations in temperature, and the fluctuating structure of these parameters within the magnetosheath cavities. In addition, they indicated that magnetosheath cavities occur during the radial IMF which corresponds to the low IMF cone angle orientations, cone angles less than  $45^\circ$ . This is a very significant finding which has important implications on the source of the magnetosheath cavities. Statistical study also showed us that the magnetopause in the presence of high energy particles expands into the magnetosheath away from the Earth. The magnetopause becomes larger by about 15-20 % when the magnetosheath cavities exist. This result, too, is a very important result which has consequences on the solar wind, ionosphere and atmosphere interaction. As the magnetic field lines connected to the magnetopause moves outward and inward, it changes the electrodynamics of the ionosphere and thus can affect the atmospheric dynamics at those high levels of the atmosphere. Additionally, the electrical currents flowing along the field lines from the magnetopause to the upper atmosphere can influence the heat structure at those heights. In this chapter, we have also seen that the magnetosheath cavities can last typically 15-30 min before they disappear. This duration is longer when we compare it with the durations of the foreshock cavities which last between 1 to 10 min. This shows us that the magnetosheath cavities are more robust structures that they can stay longer in the magnetosheath.

Global kinetic hybrid simulations of the magnetosheath cavities presented in Chapter 6 brought new insights on their formation in addition to confirming of the observational results presented in Chapters 4 and 5. In addition to the standard model parameters, as IMF orientation, finding in Chapter 4, radial IMF, is introduced in the model. By varying the IMF cone angle, a dependence found in Chapter 5, from inclined which corresponds to  $45^\circ$  to  $0^\circ$  and then back to  $45^\circ$  again, we identified the features in the model simulations. The model is designed by Dr. Nick Omidia in order to study the kinetic interaction between the solar wind particles with the magnetosphere. The model clearly demonstrated that the structure of the

magnetosheath during the radial IMFs changes into a state with very low magnetic field and densities. It becomes more turbulent and presents a less homogenous structure under the low cone angle directions of IMF. When the IMF inclined and the cone angle is  $45^\circ$ , then the structure of the magnetosheath becomes less turbulent, more homogenous with higher magnetic field and densities. Time profiles at several selected locations in the magnetosheath show that the fluctuations within the cavities are periodic, indicating high wave activity within them. These are especially clear on the high latitudes of the magnetosheath. Spatial profiles also verify the low magnetic field and density structure of the magnetosheath cavities.

The model simulations give signatures on the source of these magnetosheath cavities. Model results imply that the probability of their appearance in the magnetosheath is much higher during the low IMF cone angles than that at times of large IMF cone angles. The fact that they are seen during the radial IMFs indicates that they are carried from the upstream region by the solar wind into the magnetosheath when the IMF is radial. Kinetic hybrid model results support the observational results on this issue.

This thesis study comprehensively investigated the magnetosheath cavities using large set of data from Cluster and Interball spacecraft and comparing the findings with those from kinetic hybrid simulations. Our findings are crucial for, and help the experimentalists and modelers who work on the magnetosheath to understand its physical and dynamical variations, consequences on the terrestrial environment, and the mechanisms that govern the interaction between the magnetosheath flow and the magnetosphere, ionosphere, atmosphere system. Our findings presented here are new and presented for the first time in this thesis. Many of the concepts and terms are introduced to the literature in this thesis. The name, magnetosheath cavities, is for the first time used and introduced in this study. Chapter 4 of this study is published in *Annales Geophysicae*. Two more papers based on the statistical and modeling results are under preparation.

## **7.2 Future Research**

Especially model results suggest many points that need to be studied with the spacecraft data and further with the model runs as well. Some of these are:

- 1) The simulations indicated that the magnetosheath cavities were carried by the solar wind into the magnetosheath. Observationally to demonstrate this requires simultaneous multipoint spacecraft data.
- 2) The structure of the magnetosheath cavities seems to differ according to the location within the magnetosheath. That is, the character of the magnetosheath cavities in the subsolar region is different than that in the high latitudes or dawn/dusk flanks of the magnetosheath. Using multipoint observations in the magnetosheath, we can improve this dependence.
- 3) Periodic, highly fluctuating wavy structures were seen within the model magnetosheath cavities. Identifying the characteristics of these wave structures requires further spectral tests.
- 4) Spectral tests should also be applied to the observations to detect the characteristics of the fluctuations seen within the magnetosheath cavities and compare them with those obtained from the model simulations.
- 5) Location dependence of the magnetosheath cavities can also be investigated via the models. Periodic wavy structures were detected in density, temperature, and magnetic field at the higher latitudes. It is possible to improve this study in the direction to investigate the source of these waves. By selecting more cuts in the simulations and examining their features closely can give us information about their sources.
- 6) Further studies are also needed to advance the magnetopause, ionosphere coupling in the presence of the magnetosheath cavities.
- 7) Interball search suggests that the plasma and magnetic field structure near the magnetopause can be modified by the energetic particles. Type-1 signatures detected in the presence of energetic particles using Interball data indicated that the magnetic fields increase while densities decrease. This is the expected signature for the presence of plasma depletion layer (PDL) near the magnetopause. Therefore, the causal relationship between the PDL and energetic particles and their effects on the magnetopause need to be clarified. This proposed study on PDL was already started and the preliminary results, presented in RAST 2007 by Katircioglu et al., show that the flux of high energy particles tends to increase in PDL. In many of Cluster magnetosheath

crossings, increasing flux of high energy particles is determined near the bow shock and the magnetopause. Understanding the PDL structure in the presence of high energy particles can help us to enhance our perception on the magnetosheath-magnetopause-magnetosphere interaction and to improve the modeling efforts involving the magnetopause boundary.

## REFERENCES

- Asbridge, J. R., Bame, S. J., Gosling, J. T., Paschmann, G., and Scopke, N.,** 1978: Energetic ions within Earth's magnetosheath, *Geophys. Res. Lett.*, **5**, 953-955.
- Balogh, A., Dunlop, M. V., Cowley, S. W. H., Southwood, D. J., Thomlinson, J.G., et al.,** 1997: The Cluster magnetic field investigation, *Space Sci. Rev.*, **79**, 65-92.
- Baker, D., Belian, R. D., Fritz, T. A., Higbie, P.R., Krimigis, S. M., Sibeck, D. G., and Zwickl, R. D.,** 1988: Simultaneous energetic particle observations at geostationary orbit and in the upstream solar wind: evidence for leakage during the magnetospheric compression event of November 1, 2984, *J. Geophys. Res.*, **93**, 14317-14327.
- Blanco-Cano, X., Omidi, N., and Russell, C. T.,** 2009: Global hybrid simulations: Foreshock waves and cavitons under radial interplanetary magnetic field geometry, *J. Geophys. Res.*, **114**, A01216, doi:10.1029/2008JA013406.
- Boeuf, J. P., and Pitchford, L. C.,** 1995: Two-dimensional model of a capacitively coupled rf discharges and comparisons with experiments in the Gaseous Electronics Conference reference reactor, *Phys. Rev., E*, **51**, 1376.
- Chang, S.W., Scudder, J. D., Fennell, J.F., Friedel, R., Lepping, R. P., Russell, C. T., Trattner, K. J., Fuselier, S. A., Peterson, W. K., and Spence, H. E.,** 2000: Energetic magnetosheath ions connected to the Earth's bow shock: Possible sources of cusp energetic ions, *J. Geophys. Res.*, **105**, A3, 5471-5488.
- Chen, J., Fritz, T.A., Sheldon, R.B., Spence, H.E., Spjeldvik, W.N., Fennell, J. F., Livi, S., Russell, C. T., Pickett, J. S., and Gurnett, D. A.,** 1998: Cusp energetic particle events: implications for a major acceleration region of the magnetosphere, *J. Geophys. Res.*, **103**, A1, 69-78.
- Cooling, B.M.A., Owen, C. J., and Schwartz, S. J.,** 2001: Role of the magnetosheath flow in determining the motion of open flux tubes, *J. Geophys. Res.*, **106**, A9, 18 763-18 775.
- Crooker, N. R., Eastman, T.E., Frank, L.A., Smith, E.J., and Russell, C.T.,** 1981: Energetic magnetosheath ions and interplanetary magnetic field orientation, *J. Geophys. Res.*, **86**, 4455-4460.
- Formisano, V., Moreno, G., Palmiotto, F., and Hedgecock, P.C.,** 1973: Solar wind interaction with the Earth's magnetic field: 1. Magnetosheath, *J. Geophys. Res.*, **78**, 3714-3730.

- Formisano, V.**, 1974: The earth's bow shock fine structure in "Correlated interplanetary and magnetospheric observations", 187-223, D. Reidel Publishing Co., Germany.
- Fuselier, S.A., Klumpar, M. D., and Shelley, E.G.**, 1991: On the origins of energetic ions in the Earth's dayside magnetosheath, *J. Geophys. Res.*, **96**, 47-56.
- Gogolides, E., and Sawin, H. H.**, 1992: Continuum Modeling of Radio-Frequency Glow Discharges I: Theory and Results for Electropositive and Electronegative Gases, *J. Appl. Phys.* **72**, 3971.
- Gosling, J.T.**, 1983: Ion acceleration at shocks in interplanetary space: a brief review of recent observations, *Space Sci. Rev.* **34**, 113-126.
- Haas, F. A., and Braithwaite, N. St. J.**, 2000: Simple analysis of a capacitive discharge with a bi-Maxwellian electron distribution, *Plasma Sources Sci Technol.*, **9**, 1, 77-81.
- Katircioglu, F. T., Kaymaz, Z., and Sibeck, D. G.**, 2007: Plasma depletion layer and energetic particles, 3<sup>th</sup> *International Conference on Recent Advances in Space Technologies (RAST)*, Istanbul, Turkey, June 14-16.
- Kawamura, E., Vahedi, V., Lieberman, M. A., and Birdsall, C. K.**, 1999: Ion energy distributions in rf sheaths; review, analysis and simulation, *Plasma Sources Sci Technol.*, **8**, 3, R45.
- Kivelson, M. G., and Russell, C. T.**, 1995: *Introduction to space physics*, Cambridge University Press, United Kingdom, 133-134.
- Kobel, E., and Flückiger, E. O.**, 1994: A model of the steady state magnetic field in the magnetosheath, *J. Geophys. Res.*, **99**, A12, 23 617-23 622.
- Kudela, K., Sibeck, D. G., Slivka, M., Fischer, S., Lutsenko, V. N., and Venkatesan, D.**, 1992: Energetic electrons and ions in the magnetosheath at low and medium latitudes: prognoz 10 data, *J. Geophys. Res.*, **97**, 14849-14857.
- Lapenta, G.**, 2002: Particle rezoning for multidimensional kinetic particle-in-cell simulations, *J. Comput. Phys.*, **181**, 317.
- Le, G., and Russell, C. T.**, 1994: Solar wind source of magnetospheric Ultra-Low-Frequency waves, *Geophys. Monograph*, **81**, 81-98, AGU, Washington, DC.
- Lieberman, M. A.**, 1989: Spherical shell model of an asymmetric RF discharge, *J. Appl. Phys.*, **65**, 4186.
- McComas, D.J., Blame, S. J., Parker, P., Felman, W.C., Phillips, J. L., Riley, P., and Griffee, J. W.**, 1998: Solar Wind Electron Proton Alpha Monitor (SWEPAM) for the Advanced Composition Explorer, *Space Sci. Rev.*, **86**, 563-612.
- Nemecek, Z., Safrankova, J., Zastenker, G. N., Pisoft, P., Paulerana, K. I., and Richardson, J. D.**, 2000: Observations of the radial magnetosheath profile and a comparison with gasdynamic model predictions, *Geophys. Res. Lett.*, **27**, 2801-2804.

- Ogilvie, K. W., and Fitzenreiter, R.**, 1989: The Kelvin-Helmholtz instability at the magnetopause and inner boundary layer surface, *Geophys. Res. Lett.*, **94**, 15113-15123.
- Ogino, T.**, 1993: Two-dimensional MHD code, *Computer space plasma physics: simulation and software*, Eds. H. Matsumoto and Y. Omura, Terra Sci., Tokyo, 161.
- Omidi, N., Blanco-Cano, X., Russell, C. T., Karimabadi, H., and Acuna, M.**, 2002: Hybrid simulations of solar wind interaction with magnetized asteroids: General characteristics, *J. Comput. Physics*, **107**, 12, 1-10.
- Omidi, N., Blanco-Cano, X., Russell, C. T., and Karimabadi, H.**, 2004: Dipolar magnetospheres and their characterization as a function of magnetic moment, *Adv. Space Res.*, **33**, 1996-2003.
- Omidi, N., Blanco-Cano, X., and Russell, C. T.**, 2005: Macrostructure of the bow shock and ion foreshock: 1. Scale lengths, *J. Geophys. Res.*, **110**, A12212, doi:10.1029/2005JA011169.
- Omidi, N., and Sibeck, D. G.**, 2007: Formation of hot flow anomalies and solitary shocks, *J. Geophys. Res.*, **112**, A01203, doi:10.1029/2006JA011663.
- Omidi, N.**, 2009: Personal communication
- Paschmann, G., G. Haerendel, N. Sckopke, E. Moebins, H. Luehr, and Carlson, C. W.**, 1988: Three dimensional plasma structures with anomalous flow directions near the Earth's bow shock, *J. Geophys. Res.*, **93**, 11279-11294.
- Quest, K. B.**, 1989: *Hybrid simulation, in tutorial courses: Third international school for space simulation*, Eds. Lembege, B. and Eastwood, J. W., Cepadues Ed., Toulouse, France, 177.
- Raeder, J.**, 2003: *Global magnetohydrodynamics -A tutorial in space plasma simulation*, Eds. J. Buechner, C. T. Dum, and M. Scholer, Springer Verlag, Heidelberg, Germany, 615.
- Rème, H., Aoustin, C., Bosqued, J. M., Dandouras, I., Lavraud, B., et al.**, 2001: First multi-spacecraft ion measurements in and near the Earth's magnetosphere with the identical Cluster Ion Spectrometry (CIS) experiment, *Ann. Geophys.*, **19**, 1303 – 1354.
- Roelof, E., and Sibeck, D. G.**, 1993: Magnetopause shape as a bivariate function of interplanetary magnetic field  $b_z$  and solar wind dynamic pressure, *J. Geophys. Res.*, **98**, A12, 21421-21450.
- Russell, C.T., Petrinec, S. M., Zhang, T.L., Song, P., and Kawano, H.**, 1997: The effect of foreshock on the motion of the dayside magnetopause, *Geophys. Res. Lett.*, **24**, 12, 1439-1441.
- Russell, C.T.**, 1999: Magnetic stress in solar system plasmas, *Aust. J. Phys.*, **52**, 733-751.
- Safrankova, J., Zastenker, G., Nemecek, Z., Fedorov, A., Simersky, M., and Prech, L.**, 1997: Small scale observation of magnetopause motion: preliminary results of the Interball project, *Ann. Geophysicae*, **15**, 562-569.

- Safrankova, J., Nemecek, Z., Santolik, O., Sibeck, D. G., Zastenker, G. N.,** 2000: The flank magnetopause: INTERBALL observations, *Adv. Space Res.*, **25**, 7-8, 1503-1510.
- Scholer, M., Gloeckler, G., Ipavich, F. M., Hovestadt, D., and Klecker, B.,** 1981: Leakage of magnetospheric ions into the magnetosheath along reconnected field lines at the dayside magnetopause, *J. Geophys. Res.*, **86**, 1299-1304.
- Scholer, M.,** 1985: In collisionless shocks in the heliosphere: Reviews of current research, Eds. B. T. Tsurutani and R. G. Stone, *Geophys. Monograph*, **35**, AGU, Washington DC, USA, 287-301.
- Schwartz, S. J., Kessel, R. L., Brown, C. C., et al.,** 1988: Active current sheets near the Earth's bow shock, *J. Geophys. Res.*, **93**, 11295-11310.
- Sibeck, D. G., McEntire, R. W., Lui, A. T. Y., Krimigis, S. M., Zanetti, L. J., and Potemra, T. A.,** 1987a: The magnetosphere as a source of energetic ions, *Geophys. Res. Lett.*, **14**, 1011-1014.
- Sibeck, D. G., McEntire, R. W., Lui, A. T. Y., Krimigis, S. M., Zanetti, L. J., and Potemra, T. A.,** 1987b: Energetic magnetospheric ions at the dayside magnetopause: leakage or merging?, *J. Geophys. Res.*, **92**, 12097-12114.
- Sibeck, D. G., and MacEntire, R. W.,** 1988: Multiple satellite observations of leakage of particles from the magnetosphere., *Adv. Space Res.*, **8**, 201-216.
- Sibeck, D. G., Baumjohann, W., and Lopez, R. E.,** 1989a: Solar wind dynamic pressure variations and transient magnetospheric signatures, *Geophys. Res. Lett.*, **16**, 13-16.
- Sibeck, D. G., Baumjohann, W., Elphic, R. C., Fairfield, D. H., Fennell, J. T., et al.,** 1989b: The magnetospheric response to 8-min-period strong-amplitude upstream pressure variations, *J. Geophys. Res.*, **94**, 2505-2519.
- Sibeck, D. G.,** 1990: A model for the transient magnetospheric response to sudden solar wind pressure variations, *J. Geophys. Res.*, **95**, A4, 3755-3771.
- Sibeck, D. G.,** 1995: The magnetospheric response to foreshock pressure pulses, in *Physics of the Magnetopause*, *Geophys. Monograph*, **90**, 293, AGU, Washington, DC.
- Sibeck, D. G., Borodkova, N. L., Schwartz, S. J., Owen, C. J., Kessel, et al.,** 1999: Comprehensive study of the magnetospheric response to a hot flow anomaly, *J. Geophys. Res.*, **104**, A3, 4577-4593.
- Sibeck, D. G., Kudela, K., Lepping, R. P., Lin, R. P., Nemecek, Z., et al.,** 2000: Magnetopause motion driven by interplanetary magnetic field variations, *J. Geophys. Res.*, **105**, 25155-25169.
- Sibeck, D. G., Decker, R. B., Mitchell, D. G., Lazarus, A. J., Lepping, R. P. and Szabo, A.,** 2001: Solar wind preconditioning in the flank foreshock: IMP 8 observations, *J. Geophys. Res.*, **106**, A10, 21675-21688.



- Sibeck, D. G., Phan, T. D., Lin, R., Lepping, R. P., and Szabo, A.,** 2002: Wind observations of foreshock cavities: A case study, *J. Geophys. Res.*, **107**, A10, 1271.
- Sibeck, D. G., Omid, N., Dandouras, I., and Lucek, E.,** 2008: On the edge of the foreshock: model-data comparisons, *Ann. Geophysicae.*, **26**, 1539-1544.
- Shue, J. H., Chao, J. K., Fu, H.C., Russell, C. T., Song, P., Khurana, K. K., and Singer, H. J.,** 1997: A new functional form to study the solar wind control of the magnetopause size and shape, *J. Geophys. Res.*, **102**, A5, 9497-9511.
- Smith, C. W., L'Heureux, J., Ness, N. F., Acuna, M. H., Burlaga, L. F., and Scheifele, J. L.,** 1998: The ACE magnetic fields experiment, *Space Sci. Rev.*, **86**, 613-632.
- Sommerer, T. J., Hitchon, W. N. G., Harvey, R. E. P., and Lawler, J. E.,** 1991: Self-consistent kinetic calculations of Helium RF glow discharges, *Phys. Rev.*, **43**, 4452-4472.
- Sommerer, T. J., and Kushner, M. J.,** 1992a: Numerical investigation of the kinetics and chemistry of rf glow discharge plasmas sustained in He, N<sub>2</sub>, O<sub>2</sub>, He/N<sub>2</sub>/O<sub>2</sub>, He/CF<sub>4</sub>/O<sub>2</sub>, and SiH<sub>4</sub>/NH<sub>3</sub> using a Monte Carlo-fluid hybrid model, *J. Appl. Phys.*, **71**, 1654.
- Sommerer, T. J., and Kushner, M. J.,** 1992b: A Monte Carlo-fluid model of Chlorine atom production in Cl<sub>2</sub>, HCl and CCl<sub>4</sub> radio frequency discharges for plasma etching, *J. Vac. Sci. Tech.*, B, **10**, 2179.
- Surendra, M., and Graves, D. B.,** 1991: Particle simulations of radio-frequency glow discharges, *IEEE Trans. Plasma Science*, **19**, **2**, 144-157.
- Thomas, V. A., and Brecht, S. H.,** 1988: Evolution of diamagnetic cavities in the solar wind, *J. Geophys. Res.*, **93**, 11341-11353.
- Turk F., Kaymaz, Z., and Sibeck, D. G.,** 2003: Search for plasma and magnetic field cavities in magnetosheath, *Adv. Space Res.*, **31**, 5, 1455.
- Url-1** <[http://www.nasa.gov/mission\\_pages/hinode/solar\\_020.html](http://www.nasa.gov/mission_pages/hinode/solar_020.html)>, accessed at 17.07.2010.
- Url-2** <[http://pluto.space.swri.edu/IMAGE/glossary/bow\\_shock.html](http://pluto.space.swri.edu/IMAGE/glossary/bow_shock.html)>, accessed at 17.07.2010.
- Url-3** <[http://en.wikipedia.org/wiki/Plasma\\_parameters](http://en.wikipedia.org/wiki/Plasma_parameters)>, accessed at 18.07.2010.
- Url-4** <[http://en.wikipedia.org/wiki/Plasma\\_parameters/Flux](http://en.wikipedia.org/wiki/Plasma_parameters/Flux)>, accessed at 19.07.2010.
- Url-5** <<http://hyperphysics.phy-astr.gsu.edu/hbase/kinetic/kintem#c4.html>>, accessed at 11.08.2010.
- Url-6** <<http://hyperphysics.phy-astr.gsu.edu/hbase/kinetic/kintem.html>>, accessed at 11.08.2010.
- Url-7** <[http://en.wikipedia.org/wiki/Maxwell's\\_equations](http://en.wikipedia.org/wiki/Maxwell's_equations)>, accessed at 1.08.2010.
- Url-8** <<http://hyperphysics.phy-astr.gsu.edu/hbase/electric/maxeq.html>>, accessed at 11.08.2010.

- Url-9** <<http://tide.gsfc.nasa.gov/Documentation/ProcessingSoftware/MomentsEquations.doc>>, accessed at 11.08.2010.
- Url-10** <<http://en.wikipedia.org/wiki/Magnetometers>>, accessed at 20.08.2010.
- Url-11** <<http://www.iki.rssi.ru/apetruko/kpprep5.html>>, accessed at 21.08.2010.
- Wilken, B., Axford, W. I., Daglis, I., Daly, P., Güttler, W., et al., 1997:** RAPID, The imaging energetic particle spectrometer on cluster, *Space Sci. Rev.*, **79**, 399 - 473.
- Winske, D., Wu, C. S., Li, Y. Y., Mou, Z. Z., and Guo, S. Y., 1985:** Coupling of newborn ions to the solar wind by electromagnetic instabilities and their interaction with the bow shock, *J. Geophys. Res.*, **90**, 2713–2726.
- Winske, D., and Omidi, N., 1993:** Hybrid codes: Methods and applications, *Computer space plasma physics: Simulation techniques and software*, Eds. H. Matsumoto and Y. Omura, Terra Sci., Tokyo, 103.
- Yan, M., and Goedheer, W. J., 1999:** A PIC-MC simulation of the effect of frequency on the characteristics of VHF S<sub>i</sub>H<sub>4</sub>/H discharges, *Plasma Sources Sci. Technol.*, **8**, 349.
- Yermolaev, Y. I., Fedorov, A. O., Vaisberg, O. L., Balebanov V. M., et al., 1997:** Ion distribution dynamics near the Earth's bow shock: first measurements with the 'D ion energy spectrometer CORALL on the INTERBALL/Tail-probe satellite, *Ann. Geophysicae.*, **15**, 5, 533-541.
- Young, F. F., and Wu, C. H., 1993:** Two-dimensional, self-consistent, three moment simulation of RF glow discharge, *IEEE Trans. Plasma Sci.*, **21**, 3, 312-321.
- Zelenyi, L. M., Triska, P., and Petrukovich, A., 1997:** Interball- dual probe and dual mission, *Adv. Space Res.*, **20**, 4-5, 549-557.

## **APPENDICES**

**APPENDIX A.1 :** DVD of “Modeling Simulations” is under separate cover at the end of thesis.



## CURRICULUM VITAE



**Candidate's full name:** Filiz Türk Katircioğlu

**Place and date of birth:** Uşak, 06.05.1976

**Permanent Address:** Istanbul Technical University, Faculty of Aeronautics and Astronautics, Department of Meteorological Engineering, 34469, Maslak, Istanbul-TURKEY

**E-mail Address:** katirciogluf@itu.edu.tr

**Universities and Colleges attended:** Istanbul Technical University

**Undergraduate:** Meteorological Engineering, 1999

**Master of Science:** Meteorological Engineering, 2002

### Publications:

- Ersavaş F., Kaymaz Z., **Katircioğlu F. T.**, and Sibeck, D. G., 2010: Plasma Depletion Layer Comparisons, *Geophysical Research Abstracts*, EGU 2010, 12, 2667, 2010.
- **Katircioğlu F. T.**, Kaymaz Z., and Sibeck, D. G., 2008: Magnetosheath Cavities: Case Studies Using the Cluster Observations, *Annales Geophysicae*, 27, pp. 3765-3780, 2009.
- **Katircioğlu F. T.**, Kaymaz Z., and Sibeck D. G., 2008: A Study for the Effects of High Energetic Particles in the Near-Earth Space by Using Polar Orbiting Satellites, *2<sup>nd</sup> National Aeronautics and Space Conference (UHUK)*, October 15-17, 2008, Istanbul, Turkey.
- **Katircioğlu F. T.**, Kaymaz Z., and Sibeck D. G., 2008: Investigation on the Effects of Energetic Particles in the Magnetosheath Using Cluster Data, *37<sup>th</sup> COSPAR Scientific Assembly*, July 13-20, 2008, Montreal, Canada.
- **Katircioğlu F. T.**, Kaymaz Z., and Sibeck D. G., 2007: Plasma Depletion Layer and Energetic Particles, *3th International Conference on Recent Advances in Space Technologies (RAST)*, June 14-16, 2007, Istanbul, Turkey.
- **Katircioğlu F. T.**, Kaymaz Z., and Sibeck D. G., 2006: Role of Energetic Particles on the Formation of Depletion Layer in the Magnetosheath and IMF Dependence: Case Studies, *36th COSPAR Scientific Assembly And Affiliated Space Science Exhibition*, July 16-23, 2006, Beijing, China.

- **Turk F.**, Kaymaz Z., and Sibeck, D. G., 2005: Energetic Particles in the Magnetosheath And Their Relation to IMF, *2nd International Conference on Recent Advances in Space Technologies (RAST)*, June 09-11, 2005, Istanbul, Turkey.
- **Turk F.**, Kaymaz Z., and Sibeck D. G., 2003: Search for Plasma and Magnetic Field Cavities in the Magnetosheath, *Adv. Space Res.* Vol. 31, No. 5, pp. 1455-1462, 2003.
- **Turk F.**, Kaymaz Z., and Sibeck, D. G., 2002: Energetic Particles in The Magnetosheath and Their Effects on Plasma Parameters, *11<sup>nd</sup> Annual Conference of Doctoral Students – WDS 2002*, June 11-14, 2002, Prague, The Czech Republic.
- **Turk F.**, Kaymaz Z., and Sibeck, D. G., 2002: The Relationship between Energetic Particles and Plasma Parameters in The Magnetosheath, *COSPAR Colloquium: Plasma Processes in the Near-Earth Space: Interball and Beyond*, January 5-10, 2002, Sofia, Bulgaria.